

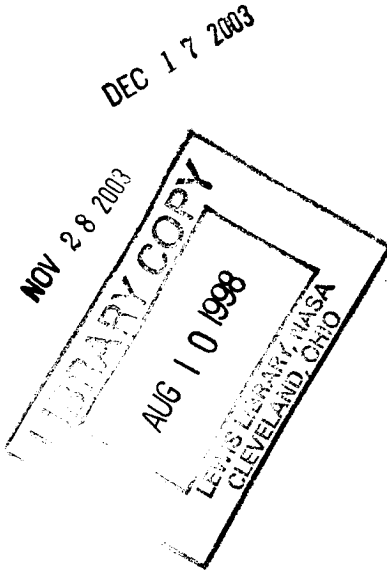
NASA - CP - 1998 - 207429

Dreslitt
106-1

NASA/CP—1998-207429



Thermal Barrier Coating Workshop, 1997



Proceedings of a workshop sponsored by the
TBC Interagency Coordination Committee
Cincinnati, Ohio
May 19-21, 1997

National Aeronautics and
Space Administration

Lewis Research Center

May 1998

Trade names or manufacturers' names are used in this report for identification only. This usage does not constitute an official endorsement, either expressed or implied, by the National Aeronautics and Space Administration.

Available from

NASA Center for Aerospace Information
7121 Standard Drive
Hanover, MD 21076
Price Code: A09

National Technical Information Service
5287 Port Royal Road
Springfield, VA 22100
Price Code: A09

NASA/CP—1998-207429



Thermal Barrier Coating Workshop, 1997

May 1998

The NASA STI Program Office . . . in Profile

Since its founding, NASA has been dedicated to the advancement of aeronautics and space science. The NASA Scientific and Technical Information (STI) Program Office plays a key part in helping NASA maintain this important role.

The NASA STI Program Office is operated by Langley Research Center, the Lead Center for NASA's scientific and technical information. The NASA STI Program Office provides access to the NASA STI Database, the largest collection of aeronautical and space science STI in the world. The Program Office is also NASA's institutional mechanism for disseminating the results of its research and development activities. These results are published by NASA in the NASA STI Report Series, which includes the following report types:

- **TECHNICAL PUBLICATION.** Reports of completed research or a major significant phase of research that present the results of NASA programs and include extensive data or theoretical analysis. Includes compilations of significant scientific and technical data and information deemed to be of continuing reference value. NASA's counterpart of peer-reviewed formal professional papers but has less stringent limitations on manuscript length and extent of graphic presentations.
- **TECHNICAL MEMORANDUM.** Scientific and technical findings that are preliminary or of specialized interest, e.g., quick release reports, working papers, and bibliographies that contain minimal annotation. Does not contain extensive analysis.
- **CONTRACTOR REPORT.** Scientific and technical findings by NASA-sponsored contractors and grantees.
- **CONFERENCE PUBLICATION.** Collected papers from scientific and technical conferences, symposia, seminars, or other meetings sponsored or cosponsored by NASA.
- **SPECIAL PUBLICATION.** Scientific, technical, or historical information from NASA programs, projects, and missions, often concerned with subjects having substantial public interest.
- **TECHNICAL TRANSLATION.** English-language translations of foreign scientific and technical material pertinent to NASA's mission.

Specialized services that complement the STI Program Office's diverse offerings include creating custom thesauri, building customized data bases, organizing and publishing research results . . . even providing videos.

For more information about the NASA STI Program Office, see the following:

- Access the NASA STI Program Home Page at <http://www.sti.nasa.gov>
- E-mail your question via the Internet to help@sti.nasa.gov
- Fax your question to the NASA Access Help Desk at (301) 621-0134
- Telephone the NASA Access Help Desk at (301) 621-0390
- Write to:
NASA Access Help Desk
NASA Center for AeroSpace Information
7121 Standard Drive
Hanover, MD 21076

Foreword

Thermal Barrier Coatings (TBC's) in current gas turbine engines routinely deliver metal temperature reductions of 50-80°C under normal conditions and as much as 140 °C temperature reductions in hot spots. With potential benefits estimated to be greater than 170 °C, TBC's offer a huge potential boost to the operating temperature capability of turbine components, roughly equivalent to 40 years of superalloy improvements. The high potential for increasing operating temperatures, and for deriving the associated efficiency increases, has fueled an explosion of TBC research.

While the potential of TBC's is great, TBC development has necessarily followed the path of other new materials. Following a period of R&D, TBC's are now serving in the conservative function of increasing metallic component life at current engine temperature levels. As the level of experience, and comfort, with the use of TBC's in these conservative applications has increased, the willingness to consider more aggressive use of TBC's in engines has also increased. TBC's are now viewed as one of the most viable means to achieve significant increases in engine efficiency.

While current TBC applications have been developed in spite of large gaps in knowledge of TBC behavior, the step up to higher risk applications requires a higher level of understanding. Specifically, designers must have the confidence that the coatings will behave predictably before the coatings will be used in critical applications. Unfortunately, gaps in knowledge span the range from a lack of detailed understanding of processing and how processing affects coating structure and properties, to a sketchy understanding of the processes leading to failure of a coating. Interestingly, even the basics of heat transfer through a coating are at a rudimentary stage of understanding.

Filling in these gaps is a substantial challenge but a challenge that must be met to take the next step in TBC technology. There are notable efforts in virtually all areas of TBC research that are working to fill these gaps. The papers contained in this volume provide some insights on current work addressing the two most critical properties of TBC's, heat transfer to and through the coating and coating durability. These papers were presented at the 1997 TBC Workshop, held in Cincinnati, Ohio, May 19-21, 1997. The workshop was sponsored by the TBC Interagency Coordination Committee. Committee members include Air Force Office of Scientific Research, Air Force Materials Directorate, The Department of Energy, DARPA, National Aeronautics and Space Administration, National Institute of Standards and Technology, Navy and Office of Naval Research. Significant organizational assistance and the funding to make this workshop a reality were provided by Capt. C.M. Ward and Dr. A. Pechenek of the Air Force Office of Scientific Research. I am also grateful to Drs. S.J. Dapkunas of NIST and W.Y. Lee of Oak Ridge National Laboratory for organizational assistance. Special thanks are due to Ms. Renee Madden of DTC, Inc., who did an excellent job in making all the arrangements of this workshop and compiling the papers contained in this volume.

William J. Brindley
Chair TBC Workshop

Table of Contents

HEAT TRANSFER/CONDUCTIVITY

<i>Thermal Conductivity of Thermal Barrier Coatings</i>	1
P. Klemens and M. Gell; University of Connecticut	
<i>Analysis of Thermal Radiation Effects on Temperatures in Turbine Engine Thermal Barrier Coatings</i>	17
R. Siegel and C. Spuckler; NASA Lewis Research Center	
<i>Thermal Conductivity Determinations of Thermal Barrier Coatings</i>	27
R. Taylor; Thermophysical Properties Research Laboratory (TPRL, Inc)	
<i>Thermal Conductivity of Functionally Graded Thermal Barrier Coatings</i>	33
A. Slifka, B. Filla, and J. Phelps; NIST	
<i>Development of Low Thermal Conductivity Thermal Barrier Coatings</i>	41
M. Maloney, H. Achter and B. Barkalow; Pratt & Whitney	

FAILURE MECHANISMS

<i>Degradation Modes of Thermal Barrier Coatings: Experience in High Thrust Experimental Engines at Pratt & Whitney</i>	43
S. Bose and J. Marcin; Pratt & Whitney	
<i>Mechanism-Based Life Prediction Issues for Thermal Barrier Coatings</i>	45
A. Evans, J. Wang and D. Mum; Harvard University	
<i>Modeling Oxidation Induced Stresses in Thermal Barrier Coatings</i>	53
A. Freborg, B. Ferguson, G. Petrus; DCT, Inc and W. Brindley; NASA Lewis Research Center	
<i>Influence of Cyclic Strain on PVD TBC Life</i>	73
P. Wright; GE Aircraft Engines	
<i>Industrial Environment-Hot Corrosion-TBC-Interactions</i>	83
N. Bornstein, W. Allen; UTRC and M. Trubeljia, D. Nissley; Pratt & Whitney Aircraft Company	
<i>The Effect of Alumina Phase Transformations on Thermal Barrier Coating Durability</i>	99
J. Schaeffer; GE Aircraft Engines	
<i>Substrate and Bond Coat Compositions: Factors Affecting Alumina Scale Adhesion</i>	109
B. Pint, I. Wright, W. Lee, Y. Zhang, K. Pr�ußner and K. Alexander; ORNL	

CHARACTERIZATION/TEST METHODS

Developing NDE Methods for Coated Combustion Turbine Components.....127
P. Zombo; Westinghouse Electric Company

Investigation of Thermal High Cycle and Low Cycle Fatigue Mechanisms of Thick Thermal Barrier Coatings..... 139
D. Zhu and R. Miller; NASA Lewis Research Center

Intelligent Processing of Materials for Thermal Barrier Coatings.....151
Y. Lau, C. Johnson, D. Gray, P. Houpt, M. Penney and H. Wang; GE Corporate Research and Development

Dynamic Model for Simulation of Heat Transfer, Vaporization, Vapor Transport, and Deposition in EB-PVD Process..... 157
F. Azad; GE Corporate Research and Development

Poster Session Abstracts..... 171
Various Authors

THERMAL CONDUCTIVITY OF THERMAL BARRIER COATINGS

P.G. Klemens and M. Gell
Institute of Materials Science, University of Connecticut
Storrs, CT 06269-3136

In the absence of significant high temperature structural materials development over the last ten years, thermal barrier coatings (TBCs) have played an increasingly important role in enhancing gas turbine engine durability and performance. The material almost universally used has been yttria stabilized zirconia (7YSZ). This ceramic has performed admirably as a TBC because of its favorable combination of properties, including: low thermal conductivity, high thermal expansion coefficient, phase stability to 1400°C, and good erosion resistance. There is considerable interest in developing TBCs with even lower thermal conductivity to provide further improvements in engine performance. To assist in this effort, this paper will describe some of the fundamental concepts of thermal conduction and how thermal conductivity may be reduced by changes in microstructure and composition.

The theory of heat conduction by lattice waves in solids can help to understand how the conductivity is influenced by lattice defects, grain boundaries and extended imperfections. At high temperatures one must also consider conduction by electromagnetic radiation within the solid, which is governed by analogous considerations. The thermal conductivity by mobile carriers, waves or particles, can be expressed as

$$\kappa = \frac{1}{3} C v l$$

where C is their specific heat per unit volume, v their speed and l their mean free path. If the carriers are waves (lattice waves or e.m. waves) ranging over a spectrum of frequencies f , this must be generalized to

$$\kappa = \frac{1}{3} \int_0^{f_m} C(f) v l(f) df$$

where $C(f)df$ is the contribution to the specific heat per unit volume from waves in the frequency interval df , v is the group velocity of the waves and $l(f)$ their attenuation length, usually a function of frequency. Also, f_m denotes an effective upper limit to the spectrum because v or l become very small for $f > f_m$. Since the energy content of waves consist of quanta, phonons or photons respectively, these quanta can also be considered as heat carriers.

Lattice waves are just elastic or ultrasonic waves, but their spectrum extends to very high frequencies where their wavelength λ is of atomic dimensions, and the relation between f and the wavelength λ is modified. The displacement field of the wave still has the form of a progressive wave, varying as $\exp i(\mathbf{q} \cdot \mathbf{r} - 2\pi f t)$, where the wave-vector \mathbf{q} has magnitude $2\pi/\lambda$ and points in the propagation direction. The field of an electromagnetic wave has a similar form.

The Debye theory of lattice vibrations makes the simplification that v is constant, but that the lattice wave spectrum is terminated at the Debye frequency f_D , chosen so that the number of normal modes agrees with the number of atoms. However, when the basic structural unit contains N atoms of varying mass, the spectrum divides into acoustic modes, of the progressive wave form, and optical modes, vibrations of the N atoms in each structural unit relative to each other. Only the former with upper frequency $f_m = f_D N^{1/3}$ have appreciable group velocity and transport heat. This approximation is used here. In the limit $T > hf_m/k$, which is the case of interest here, each wave or normal mode has energy kT , and $C(T) \propto f^2$. Here k and h are the Boltzmann and Planck constants, respectively.

The thermal conductivity is limited by various interaction processes, which transfer energy between the waves and establish thermal equilibrium. The intrinsic processes interchange energy between triplets of waves (three-phonon interactions). These satisfy frequency conservation, as in all non-linear processes, as well as wave-vector selection rules. The resulting intrinsic attenuation length is of the form [1]

$$l_i(f, T) = B f^{-2} T^{-1}$$

where $B \propto \mu \alpha^3 v f_m$, μ being the shear modulus. The intrinsic conductivity becomes then

$$\kappa_i = \frac{3}{4} N^{-2/3} \mu v^2 / (f_D T)$$

and this describes, reasonably well, the thermal conductivity of structurally perfect dielectric crystals near and above their Debye temperature hf_D/k . Weak binding, large atomic masses and structural complexity (large N) all tend to reduce the intrinsic conductivity. Note that if one writes $\kappa = \int k(f) df$, then in the intrinsic case the integrand $k_i \propto C(f)l_i(f)$ is independent of f , so that equal frequency intervals make equal contributions to the intrinsic conductivity. This contrasts to the specific heat, which for the acoustic modes is mainly due to their highest frequencies, since for $f < f_m$, $C(f) \propto f^2$.

Lattice imperfections further reduce the effective attenuation length. Different imperfections scatter with different frequency dependence. Point defects scatter as the fourth power of frequency, with an inverse attenuation length $1/l_p(f) = Af^4$, where A depends on their nature and concentration. Grain boundaries scatter independently of frequency with attenuation length L comparable to the grain size. The inverse attenuation length $1/l(f)$ is composed of the sum of these processes. Since point defects and grain boundaries scatter mainly in different frequency ranges, their conductivity reductions are approximately additive, so that

$$\kappa = \kappa_i - \delta\kappa_B - \delta\kappa_p$$

where $\delta\kappa_B$ and $\delta\kappa_p$ are the reductions due to boundaries and point defects. Point defects are small regions of volume α^3 in which the value of the wave velocity v is locally changed by δv .

Define f_0 by $l_i(f_0, T) = l_p(f_0)$ and f_B by $l_i(f_0, T) = L$, where L is the grain diameter, then

$$\begin{aligned}\delta\kappa_B &= \kappa_i (f_B / f_m) \arctan(f_m / f_B) \\ \delta\kappa_p &= \kappa_i [1 - (f_0 / f_m) \arctan(f_m / f_0)]\end{aligned}$$

For a substitutional atom of mass $\Delta M + M$ instead of M one finds

$$1/l_p(f) = c(\Delta M / M)^2 4\pi^3 \alpha^3 v^{-4} f^4$$

where c is the defect concentration per atom [2]. Effective values of $\Delta M / M$ can be obtained for other defects, including vacancies. If κ_i is known, one can deduce $l_i(f, T)$ and thus obtain $\delta\kappa_p$; this has been done for many systems [3], recently for cubic zirconia [4].

Cubic zirconia presents a further difficulty: it only exists if it contains stabilizing solutes and vacancies. Thus the intrinsic thermal conductivity and l_i must first be estimated in terms of its elastic and anharmonic parameters. The resulting uncertainty of perhaps 30% in κ_i translates into a 15% uncertainty in κ . There is rough agreement for various solutes and concentrations at room temperatures. At high temperatures the theoretical values are always less than the data. This will be shown for several compositions. This suggests the presence of a radiative component. Values of $\delta\kappa_B$ were calculated for various grain diameters, and the resulting lattice thermal conductivities are also shown. The reduction is greatest at low temperatures. At high temperatures any radiative component would not depend markedly on grain size.

Yttrium aluminum garnet, yttrium iron garnet and some solutions of the two materials were studied [5] over a wide temperature range. Point defect scattering is weaker here, since only one cation sublattice is affected, and there seem to be no oxygen vacancies. The grain size was 2 microns. Since $l_i(T)$ is larger in YAG than in ZrO_2 , reductions due to small grain size should be more pronounced. Calculated reductions are shown. Since the oxygen diffusivity is much smaller, YAG and perhaps some solutes may be of interest. In these materials there also seems to be a radiative component, significant above 600°C.

Since thermal barrier coatings operate mainly at high temperatures (in aircraft engines around 1,200°C), it is important to understand the factors controlling the radiative component. There is a difference between an engine environment and a thermal diffusivity measurement, where the sample is thicker and sandwiched between two opaque layers. In the latter case, for layer thickness L and index of refraction n , the radiative component of thermal conductivity, in the absence of absorption and scattering, is

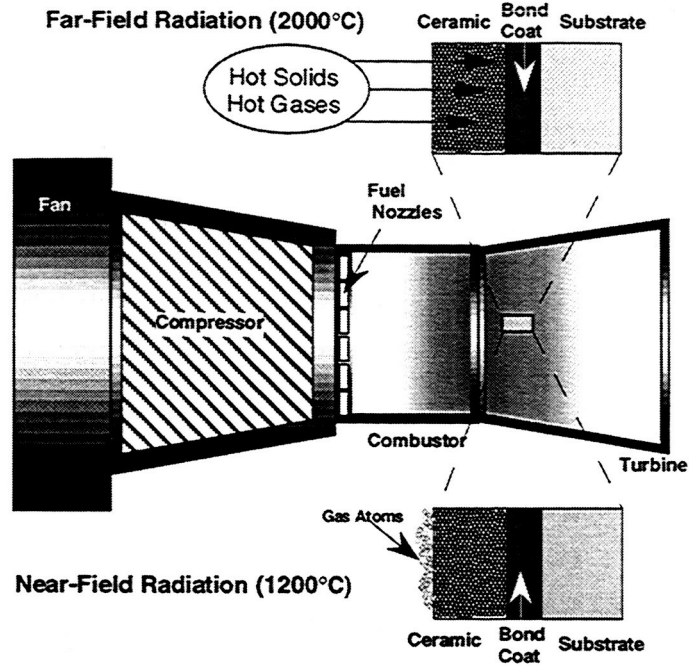
$$\kappa_r = 4\sigma T^3 n^2 L = 2.27 \times 10^{-7} T^3 n^2 L \quad (W - m^{-1} - K^{-1})$$

where σ is the Stefan-Boltzmann constant. For ZrO_2 , $n=2.7$. If $L=0.25\text{mm}$, κ_r would be $0.9 \text{ W}\cdot\text{m}^{-1}\cdot\text{K}^{-1}$ at $1,300^\circ\text{K}$. At temperature T , 75% of this radiative transfer occurs at frequencies $f > 3.1kT/h$, which is 8.1×10^{13} Hz. This can be reduced by porosity, provided the line-of-sight mean free path $l=4R/3p$ is well below L , where R is the (spherical) pore radius, p the porosity. However, the scattering cross-section of a pore falls off rapidly with decreasing f or wave-number q if $q < 1/R$. Since $q=2\pi mfc^{-1}$, where c is the light speed *in vacuo*, the diameter $2R$ must exceed 0.45 microns. Also $l=4R/3p$ should not exceed 0.025mm to keep the radiation for $f > 8 \times 10^{13}$ Hz at an acceptably low level. For this value of R , $p=0.012$ while larger pore sizes would require proportionally larger porosities. With these values of R and p and at $1,300^\circ\text{K}$, κ_r would be about $0.3 \text{ W}\cdot\text{m}^{-1}\cdot\text{K}^{-1}$. To benefit by reductions in the lattice thermal conductivity from nanometer sized grains, one would have to introduce pores of $\frac{1}{2}$ micron diameter with a fractional volume of 1-2%, in addition to any very small pores caused by the very fine grains.

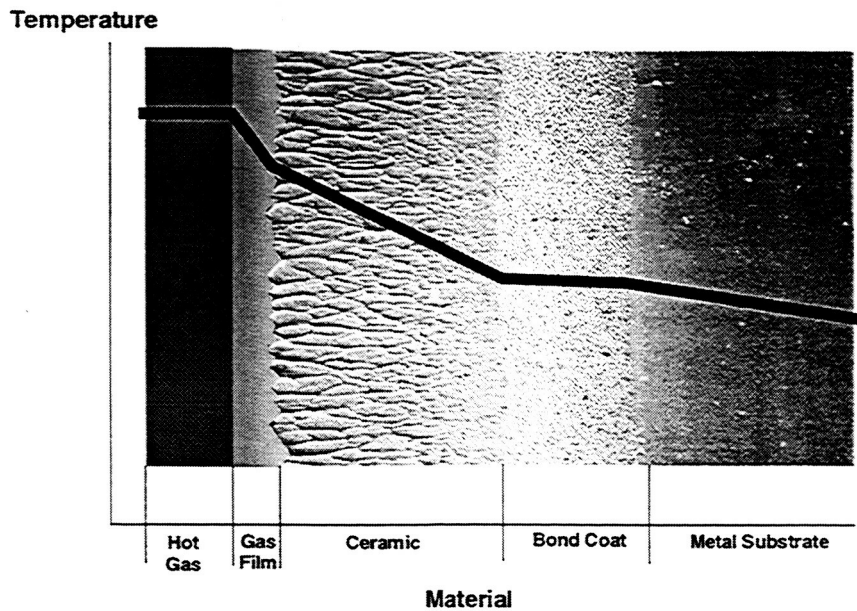
References:

- [1] P.G. Klemens, "Theory of Thermal Conductivity in Solids" in *Thermal Conductivity*, R.P Tye, ed., vol.1, 1-68, London, Academic Press, 1969.
- [2] P.G. Klemens, "Thermal Resistance due to Point Defects", *Physical Review* **119**, 507 (1960).
- [3] P.G. Klemens, "Theory of Heat Conduction in Non-stoichiometric Oxides and Carbides", *High Temperatures - High Pressures* **17**, 41 (1985).
- [4] P.G. Klemens, "Thermal Conductivity of Zirconia" in *Thermal Conductivity* **23**, K.E. Wilks, R.B. Dinwiddie, R.S. Graves, eds., 209 -220, Lancaster, PA: Technomics, 1996.
- [5] N.P. Padture, P.G. Klemens, "Low Thermal Conductivity in Garnets", *J. American Ceramic Society* **80**, No.4, 1997 in print.

Radiation Sources in Gas Turbine Engines



Temperature Across Thermal Barrier



Heat Transport and Thermal Conductivity

- Heat Transport Within Ceramic = Thermal Conductivity
- Thermal Conductivity has Two Components:
 - Lattice Waves ($f = 0$ to 10^{13} Hz, $\lambda \approx 10^{-9}$ m)
 - Infrared Electromagnetic Waves ($f = 0$ to 10^{13} hz, $\lambda \approx 10^{-6}$ m)
- Scattering from Structural Defects Can Greatly Reduce Thermal Conductivity, But Sources of Scattering Must Be Defined for Each Type of Wave
- Far-field Radiation from Hot Gas and Solids must also be included

Thermal Conductivity

Heat Conduction is a random motion of carriers of thermal energy. If the carriers are gas atoms, The Thermal Conductivity K is:

$$K = (1/3) C v l$$

C = specific heat per unit volume
 v = speed of carriers (gas atoms)
 l = mean free path

When heat is conducted by Waves, v becomes the wave velocity (group velocity), l is the attenuation length. Since $l(f)$ is usually a function of the wave frequency f , and the waves cover a wide spectral range, this is generalized to :

$$K = 1/3 \int C(f) v l (f) df$$

Where $C(f) df$ is the contribution to specific heat per unit volume from the frequency interval df , so that

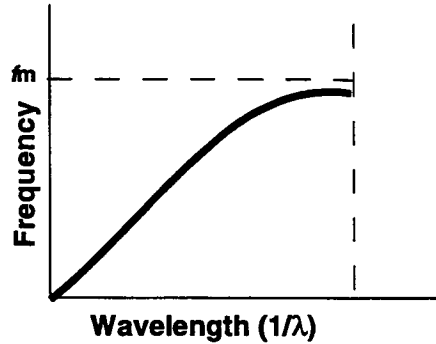
$$C = \int C(f) df$$

This expression of K holds for both elastic or lattice) waves as well as for electromagnetic waves

Lattice Waves

Lattice waves in solids are simply elastic waves with very high frequencies and very short (down to the range of interatomic spacing) wavelengths. Their maximum frequencies (f_m) are on the order of 10^{13} Hz, while ultrasonic elastic waves range from $10^5 - 10^9$ Hz. At the maximum frequencies, their wavelengths ($\lambda = v/f$) are about 10^{-9} m.

Dispersion:



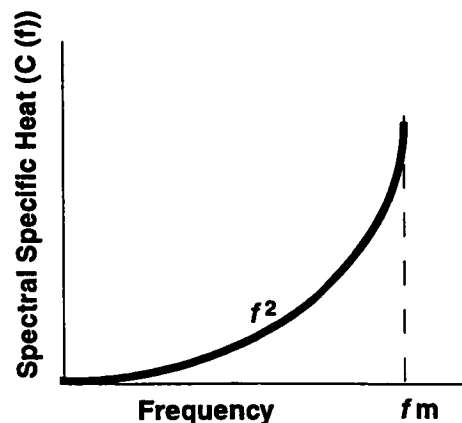
At the highest frequencies (shortest waves) f is no longer proportional to $1/\lambda$. The energy flow is proportional to the group velocity or slope of the curve.

Thermal Equilibrium and Specific Heat

In an ideal solid (perfectly regular and harmonic), the lattice waves are normal modes of vibration. No energy is exchanged between them. Real solids are not structurally perfect (lattice defects) and deviate slightly from linear elasticity (are slightly anharmonic). This causes a slow energy exchange amongst waves and thermal equilibrium. In thermal equilibrium at absolute temperature T , each wave has an energy of kT (k = Boltzmann constant) and each wave contributes amount k to the specific heat.

$$C = \int C(f) df$$

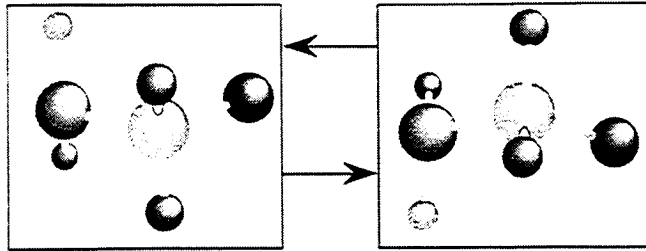
$$C(f) \propto f^2$$



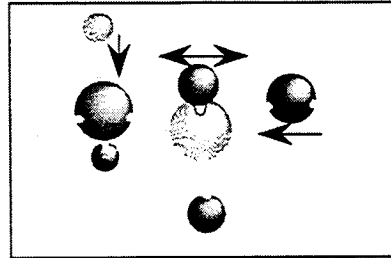
Lattice Wave Acoustic and Optical Branches

In crystals composed of molecular units (e.g. ceramic oxides), the waves are of two types:

- Acoustic
- Relative motion of molecular units

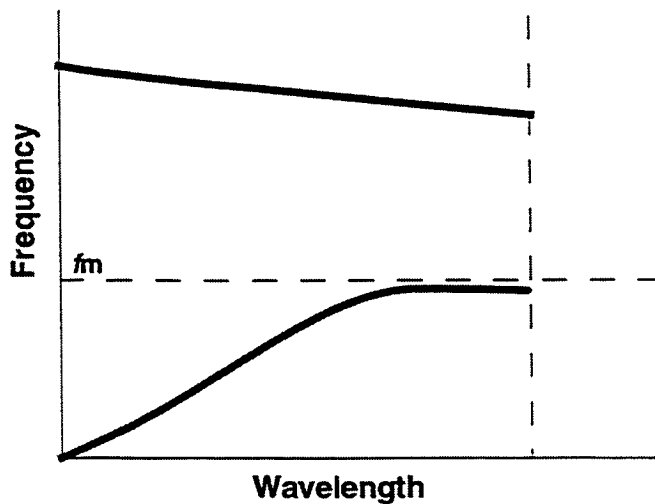


- Optical
- relative motion of atoms within each molecule



Acoustic and Optical Branches

The dispersion curve for lattice waves has two branches



To a good approximation, only the acoustic waves have significant group velocities and carry heat

Lattice Thermal Conductivity

Thus we have:

$$K = \frac{1}{3} \int_0^{fm} C(f) v l(f) df = \int k(f) df$$

where only acoustic branch waves are considered.

For ZrO_2 $N = 3$ $fm = 5.7 \times 10^{12}$ Hz

For $Y_3Al_5O_{12}$ $N = 3$ $fm = 5.4 \times 10^{12}$ Hz

$C(f)$ and v depend on the atom spacing, on the elastic moduli, and on density.

However, the attenuation length $l(f)$ is what really determines the lattice thermal conductivity. It is structure-sensitive, and also depends on absolute temperature T .

Attenuation Length (or Phonon Mean Free Path)

The attenuation length would be infinite if:

- a. Lattice forces were perfectly harmonic
i.e. strain energy quadratic in strains only
- b. Solid had no structural defects or imperfections
- c. there are no grain boundaries

However...

Real crystals have anharmonic force components, i.e. strain energy contains terms of 3rd power and higher in strain.

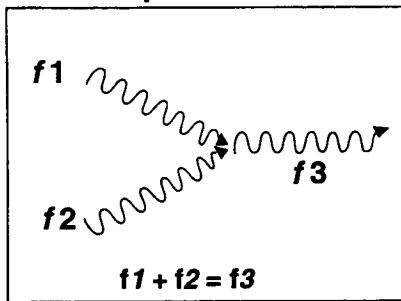
Real crystals have structural defects

Real crystals have grain boundaries

The realities limit the attenuation length $l(f)$ and the integrand $k(f)$, and cause thermal resistance. The interaction processes, exchanging energy between waves, establish thermal equilibrium. To calculate thermal conductivities, we need to know the strength of these interactions, that is the reciprocal of the attenuation length $l(f, T)$.

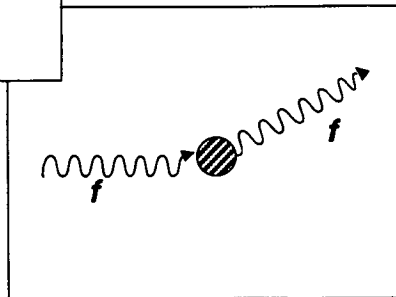
3 Types of Wave Interactions

Energy Exchange Between Wave Triplets



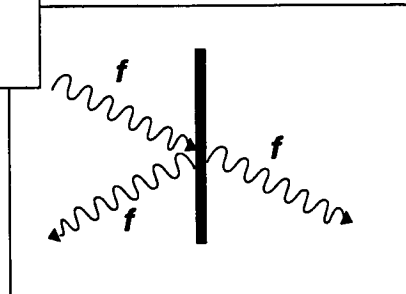
Conserves frequencies of participating waves

Scattering by Defects



Conserves frequency, but changes direction of wave

Scattering by Boundaries



Part of the incoming energy is transmitted, some is backscattered. Backscattered fraction independent of f

Potential Sources of Phonon/Photon Scattering and Conductivity Reduction

- **Boundaries**
 - Grain Boundaries
 - Interface Boundaries
 - Splat Boundaries (Linear Porosity)
- **Point Defects**
 - Vacancies
 - Solutes
- **Porosity**

Intrinsic Conductivity

$$K_i = \int k_i(f) df = (1/3) \int C(f) v l_i(f, T) df$$

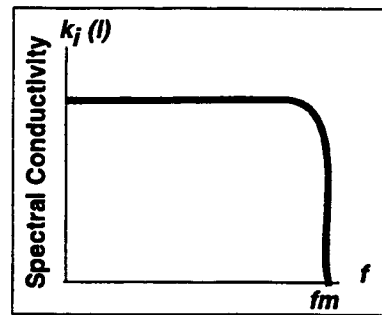
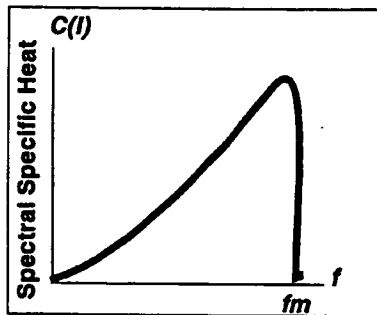
$$l_i(f, T) \approx (\mu a^3 / kT) v N^{1/3} fm / f^2$$

where μ = shear modulus, a^3 = volume per atom

Factor $kT/(\mu a^3)$ is mean square thermal strain

The mean square thermal strain for Zirconia at 1,300°K is about 0.03

$k_i \propto l_i C(f)$ is independent of frequency

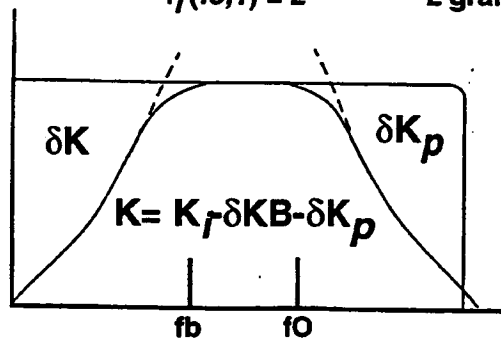


In thermal conductivity, equal frequency intervals contribute equally to K_i

Point Defects and Grain Boundary Reductions

Define f_0 by $l_i(f_0, T) = l_p(f_0)$

f_B by $l_i(f_0, T) = L$ L grain diameter



These reductions are independent of each other as long as $f_B \ll f_0$

For 7YSZ at 900°K $K_i = 1.85 \text{ W-m}^{-1} \text{-K}^{-1}$

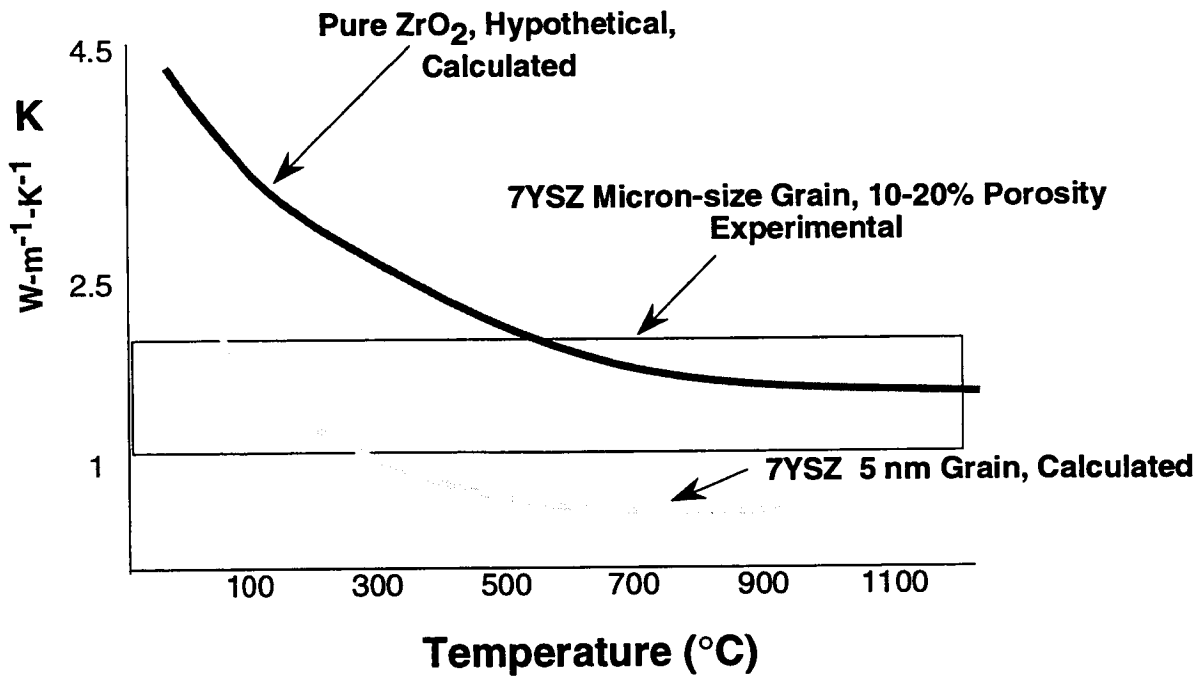
$$\delta K_p = 0.5 \text{ W-m}^{-1} \text{-K}^{-1}$$

and if $L = 1 \text{ micron}$ $\delta K_B = 0.07 \text{ W-m}^{-1} \text{-K}^{-1}$

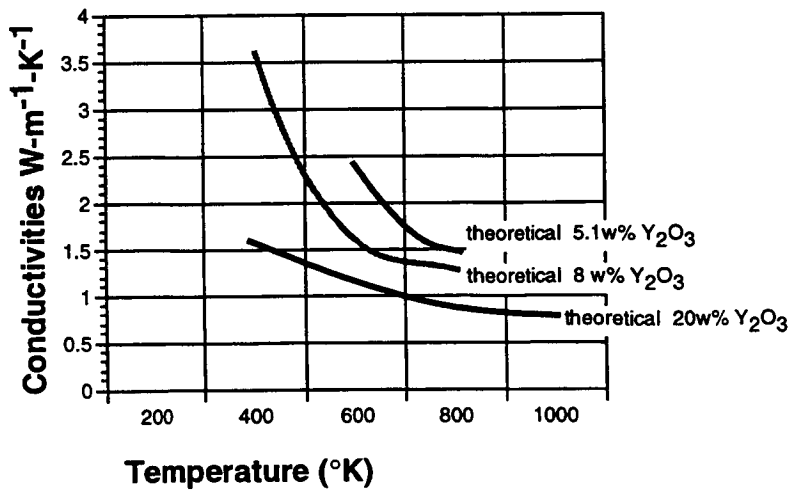
Theoretical $K = 1.3 \text{ W-m}^{-1} \text{-K}^{-1}$

Observed values 1.1 to 1.6 $\text{W-m}^{-1} \text{-K}^{-1}$

Thermal Conductivity of Zirconia

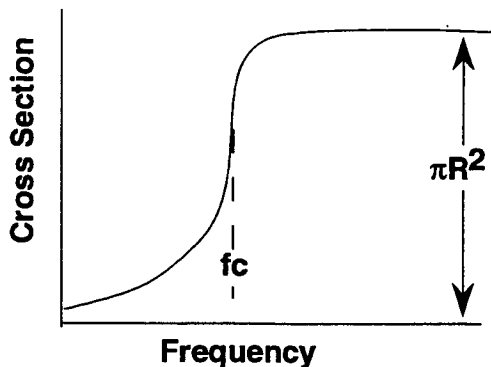


Conductivity of YSZ as a Function of Composition



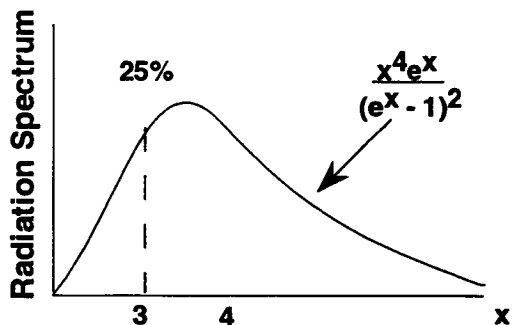
Radiative Component Reduction

Scattering by spherical pore radius R



$$fc = \frac{C}{2\pi n R}$$

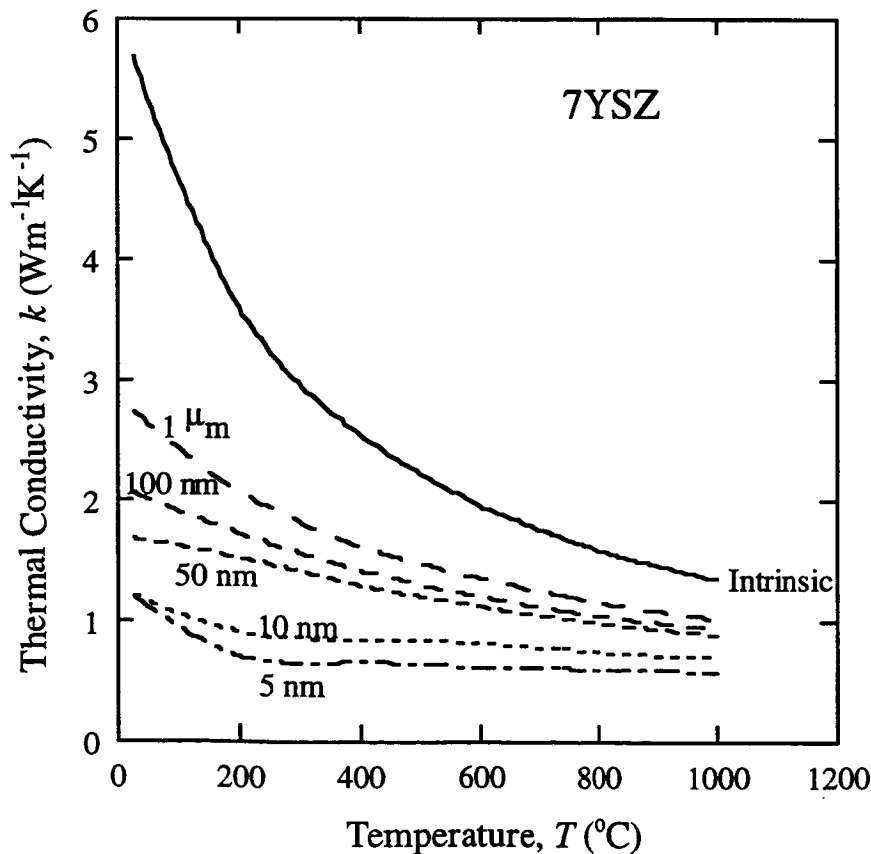
n- index of refraction
C - velocity of light in a vacuum



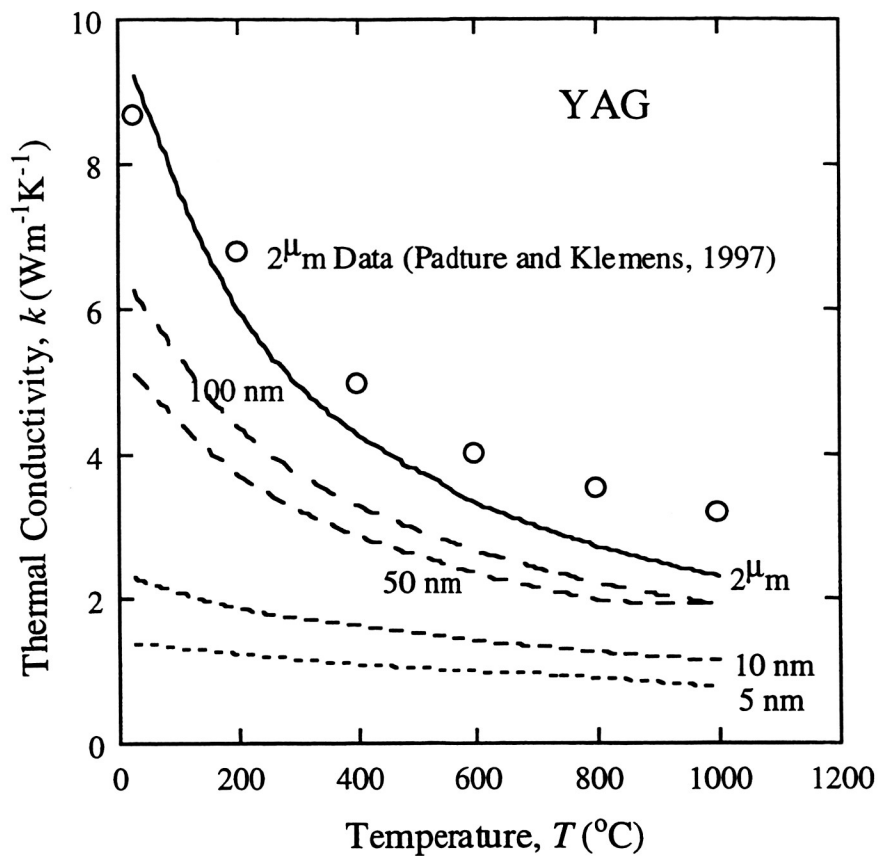
$$x = hp/RT$$

25% of Radiation below $x = 3$
Matching pc to $x = 3$ for minimum R
For 1,300K we need $R > 0.6$ micron
To reduce line of sight mean free path to $l = 25$ micron so that total radiation is 33% of black body
Since $l = 4R/3p$ p vol. fraction of pores, we need $p > 0.03 \mu$
Pores much smaller than 1 micron do not scatter radiation at the spectral peak

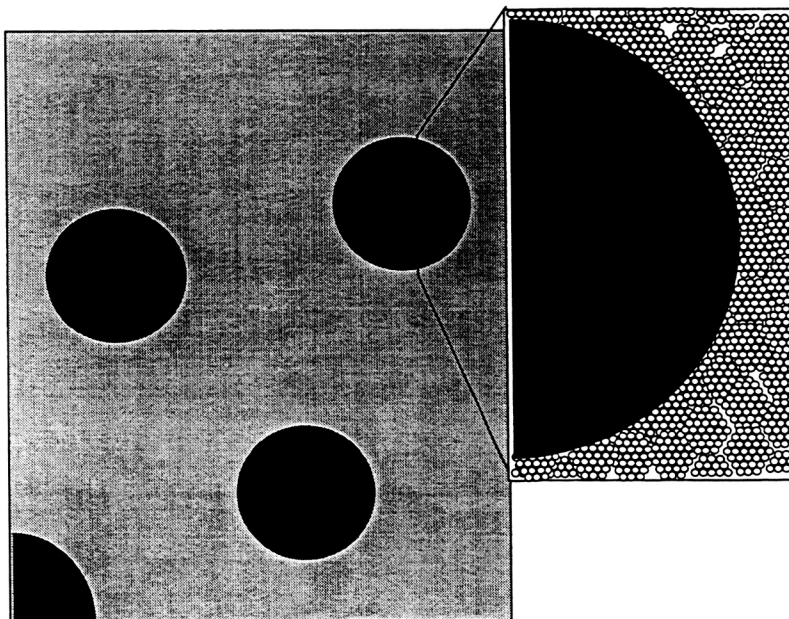
Thermal Conductivity for 7YSZ



Thermal Conductivity for YAG



Optimized Microstructure for Reduced Thermal Conductivity



Summary/Conclusions

- **Thermal Conductivity of TBCs can be understood based on lattice wave and electromagnetic wave theory**
- **Where theory and calculations differ, radiation effects and scattering from specific microstructural defects must be considered**
- **Thermal conductivity can be reduced compared to the current state-of-the-art TBCs by compositional and microstructural optimization**
- **For YSZ, a microstructure of nanometer-sized grains and micron-sized pores can provide reduced thermal conductivity**

ANALYSIS OF THERMAL RADIATION EFFECTS ON TEMPERATURES IN TURBINE ENGINE THERMAL BARRIER COATINGS

Robert Siegel and Charles M. Spuckler
NASA Lewis Research Center, Cleveland, Ohio 44135

Thermal barrier coatings are important, and in some instances a necessity, for high temperature applications such as combustor liners, and turbine vanes and rotating blades for current and advanced turbine engines. Some of the insulating materials used for coatings, such as zirconia that currently has widespread use, are partially transparent to thermal radiation [1-3]. The importance of radiation effects within thermal barrier coatings in a turbine engine was briefly discussed in [4]. A translucent coating permits energy to be transported internally by radiation, thereby increasing the total energy transfer and acting like an increase in thermal conductivity. This degrades the insulating ability of the coating. Because of the strong dependence of radiant emission on temperature, internal radiative transfer effects are increased as temperatures are raised. Hence evaluating the significance of internal radiation is of importance as temperatures are increased to obtain higher efficiencies in advanced engines.

In a combustor there is radiation from the flame, soot, and hot gases to the combustor liner, first stage turbine vanes, and to some extent to the first stage blades. When a thermal barrier coating is subjected to the combustion environment it will usually become covered with a thin layer of soot. Radiation is then absorbed by the soot, and is partially reradiated into the coating. Coatings in the combustor are considered with both clean and soot covered surfaces; for the turbine the results here are for clean surfaces. Within a hot coating there is internal radiant emission, absorption, and scattering. These mechanisms combine to provide a transport of radiative energy within the coating that acts in combination with heat conduction.

Internal radiative effects depend on the properties of the coating materials. If coatings can be made opaque then internal radiation is not a concern, and the only radiative exchange is at the exposed surface of the coating and, for some conditions, at the cooled side of the metal wall. However, some high temperature ceramic materials are somewhat translucent so internal radiation effects can occur, and their importance must be quantitatively evaluated to determine if they are a design consideration. Zirconia is somewhat translucent for radiation in the wavelength range below approximately 5 to 7 μm , and is often approximated as being opaque for wavelengths larger than 5 μm , [1]. Zirconia has large scattering compared with absorption, Fig. 2. At turbine engine temperatures a considerable portion of blackbody radiant energy is in the translucent wavelength range for zirconia.

In [1] a detailed heat transfer study was made of ceramic coatings for diesel engine cylinder liners. An analysis for zirconia coatings on a cooled metal wall in a turbine engine

environment was made in [5]. Radiative transfer computations can become complex for a coating with properties that depend on the radiation wavelength. Zirconia has high scattering relative to absorption, so the radiative equations must include the scattering component which adds to their difficulty. With wavelength dependent properties and large scattering, the solution of the exact radiative transfer equations becomes rather complex. It is desirable to use simplified mathematical models if these will yield good results. Approximate methods are usually adequate because the radiative contribution is found to be significantly smaller than heat conduction for turbine engine applications, and hence the radiative component is not required to high accuracy.

To investigate simplified models, some approximate techniques were applied in [6] to analyze composite layers of translucent materials, and the results were compared with solutions where the complete radiative transfer equations were solved. This showed that the two-flux method gave accurate results for layers with diffuse boundaries. Diffuse boundaries are a reasonable assumption for thermal barrier coatings since they have a somewhat rough exterior and a granular crystalline or columnar internal structure. A two-flux method was also used in [1] for coatings in a diesel engine environment. As a result, the two-flux method was further developed and applied in [5] for turbine engine conditions, and the results of additional calculations are given here. The two-flux method includes without difficulty, the large scattering that is characteristic of a semitransparent insulating material such as zirconia. To include spectral property effects the analysis in Ref. [5] and the calculations given here have approximated the zirconia transmission behavior by considering two spectral regions, one semitransparent and the other opaque.

For the radiative analysis, a mathematical description of the conditions at the boundaries is important, and must include emission and reflection at the interface of the coating and the metal wall. The reflection of a clean external interface must be quantified. The behavior must also be modeled of a soot coating that absorbs incident external radiation and reemits into the translucent coating. Some of these surface effects are difficult to define with assurance that they are quantitatively accurate. Within turbine blade rows away from the combustor, a blade is surrounded for the most part by other blades with the same radiative fluxes leaving their surfaces. Hence the incident and leaving fluxes at the coating surface are essentially equal and this reduces to zero the net radiative flux at the coating surface. The cooled side of the coating is bounded by the metal wall of the combustor or turbine vane or blade. The reflections characteristics of this interface must be included in the mathematical model. Cooling at the exposed side of the metal wall can occur by a combination of convection and radiative loss. Inside of a turbine blade cooling passage, radiative exchange is assumed negligible.

The figures given here illustrate typical temperature distributions and heat flows within zirconia coatings on a metal wall. Results are given for coatings on a combustor liner (Figs. 3, 4), a turbine blade subjected to combustor radiation (Figs. 5, 6), and a rotating blade away from the combustor surrounded by other cooled blades (Fig. 7). Results with radiation included within the coating are compared with heat conduction calculations with radiation neglected in the coating. For the limiting case of an opaque

coating with internal transfer of energy only by heat conduction, radiant absorption and emission occur only at the external surfaces. Thermal conductivity values for zirconia are in the literature [7,8,9] and can change as the coating is operated at high temperatures [7]. The effect of increased coating thermal conductivity in raising the metal temperature is shown in Fig. 6a.

It was pointed out in [4] and [6] that radiation trapping can occur in a coating because of multiple reflections between the metal substrate and the coating interface. This will occur for a clean coating, but not with a soot coating because there is then little reflection at the external interface. It will also be decreased if the absorptivity of the bond coat is large, but an increase in bond-coat absorptivity increases the temperatures in the metal wall as shown in Fig. 5b. Internal emission and internal reflections depend on the coating index of refraction, and there is uncertainty on the value of this parameter [1,10,11]. In some instances, as in Fig. 4b, the value of the refractive index is shown to have a significant effect on the temperature distribution in the coating.

From the present calculations, radiation effects were found to be most important when the exposed surface of the coating is subjected to incident radiation from the hot combustor. Depending on the properties assumed and the convective conditions, the magnitude of the radiative effects can be of some significance, although heat conduction is the more dominant heat transfer mechanism. The illustrative temperature distributions included here demonstrate the magnitudes of the temperature effects that can be caused by the coating being translucent, and being subjected to combustor radiation. Within the turbine blade rows away from the combustor, the blades are all cooled, and exchange of external radiation is expected to be negligible. For this condition, heat conduction was found to be the dominating heat transfer mechanism and radiation effects within the coating were found to be small as shown in Fig. 7.

References

1. S. Wahiduzzaman and T. Morel, "Effect of Translucence of Engineering Ceramics on Heat Transfer in Diesel Engines," Oak Ridge National Laboratory Report ORNL/Sub/88-22042/2, Oak Ridge, TN, (1992).
2. L. K. Matthews, R. Viskanta, R. and F. P. Incropera, "Combined Conduction and Radiation Heat Transfer in Porous Materials Heated by Intense Solar Radiation," *Journal of Solar Energy Engineering*, 107 (1985) 29-34.
3. T. Makino, T. Kunitomo, I. Sakai, I. and H. Kinoshita, "Thermal Radiative Properties of Ceramic Materials," *Transactions of the Japan Society of Mechanical Engineers*, 50 (1984) 1045-1052, *Heat Transfer - Japanese Research*, 13 (1984) 33-50.
4. Committee on Coatings for High-Temperature Structural Materials, "Coatings for

High-Temperature Structural Materials," National Academy of Sciences, National Academy Press, Washington, D.C., Appendix B, (1996) 65-66.

5. R. Siegel, "Internal Radiation Effects in Zirconia Thermal Barrier Coatings," *Journal of Thermophysics and Heat Transfer*, **10** (1996) 707-709.
6. R. Siegel and C. M. Spuckler, "Approximate Solution Methods for Spectral Radiative Transfer in High Refractive Index Layers," *International Journal of Heat and Mass Transfer*, **37**, Suppl. 1 (1994) 403-413.
7. H. E. Eaton, J. R. Linsey and R. B. Dinwiddie, "The Effect of Thermal Aging on the Thermal Conductivity of Plasma Sprayed Fully Stabilized Zirconia," *Thermal Conductivity 22*, ed. by T. W. Tong, Technomic Pub. Co. Inc., Lancaster, PA, (1994) 289-300.
8. L. Pawlowski, "Applications and Properties of Thermally Sprayed Oxide Ceramics," *Powder Metallurgy International*, **23** (1991) pp. 357-362.
9. K. S. Ravichandran, R. E. Dutton, S. L. Semiatin and K. An, "Microstructure and Thermal Conductivity of Thermal Barrier Coatings Processed by Plasma Spray and Physical Vapor Deposition Techniques," Materials Research Society Symposium Proceedings, **434** (1996) pp. 27-32.
10. D. L. Wood and K. Nassau, "Refractive Index of Cubic Zirconia Stabilized with Yttria," *Applied Optics*, **21** (1982) 2978-2981.
11. R. C. Buchanan and S. Pope, "Optical and Electrical Properties of Yttria Stabilized Zirconia (YSZ) Crystals," *Journal of the Electrochemical Society: Solid-State Science and Technology*, **130** (1983) 962-966.

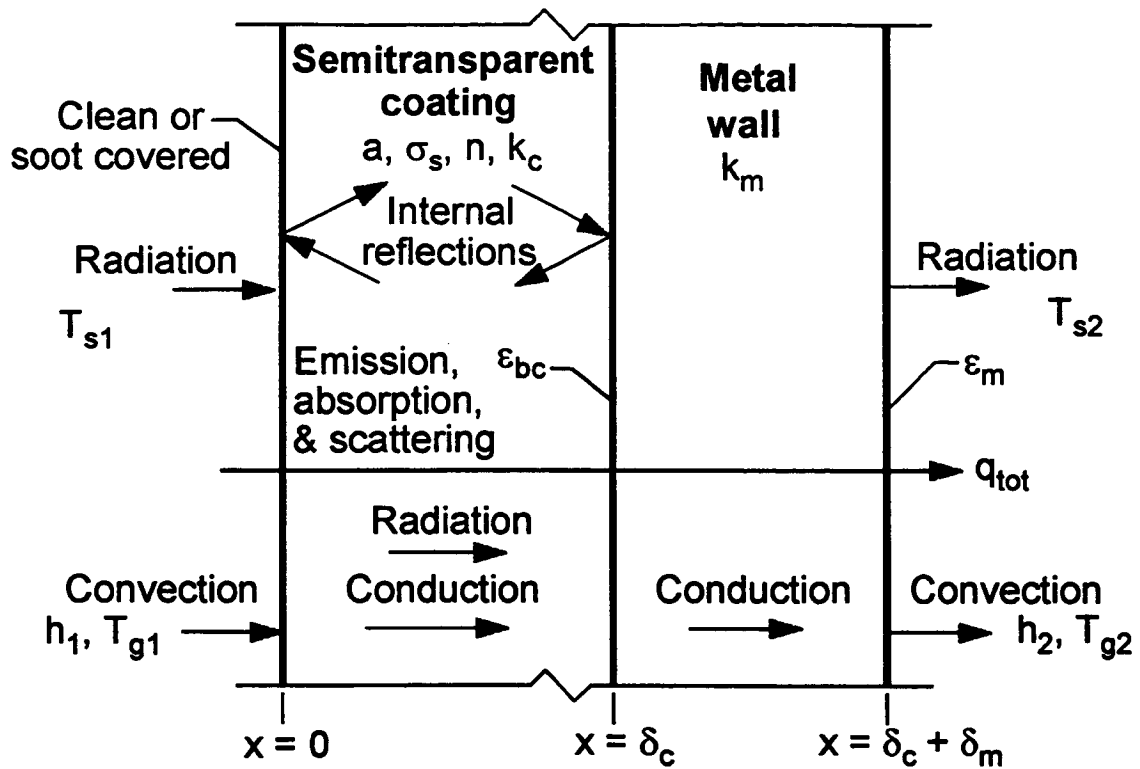


Figure 1. Geometry and nomenclature for semitransparent thermal barrier coating on metal wall.

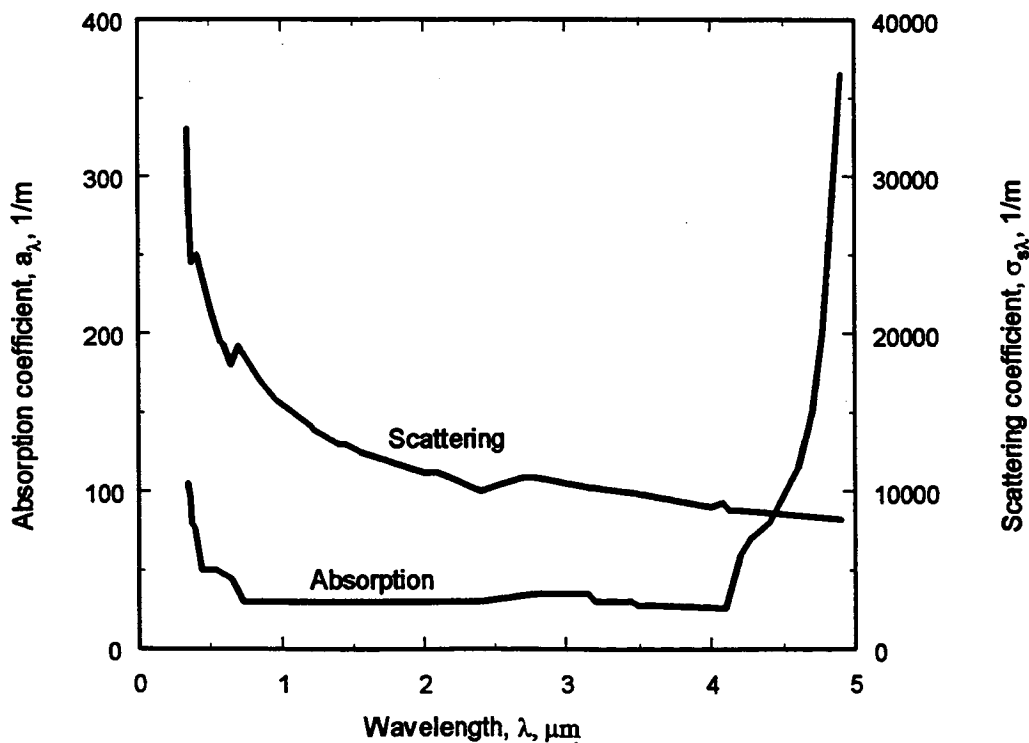


Figure 2. Typical radiative absorption and scattering coefficients for zirconia [1].

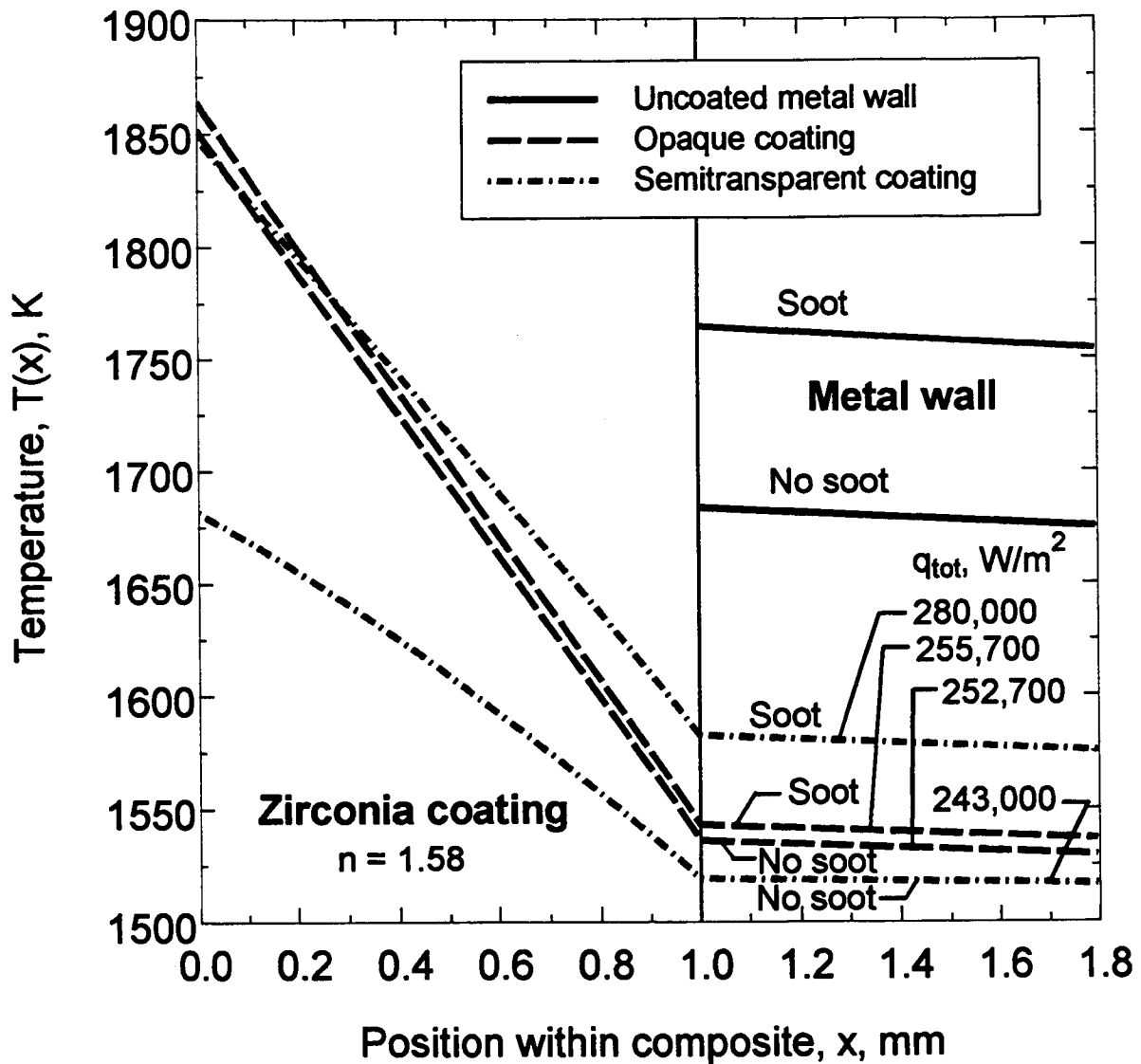
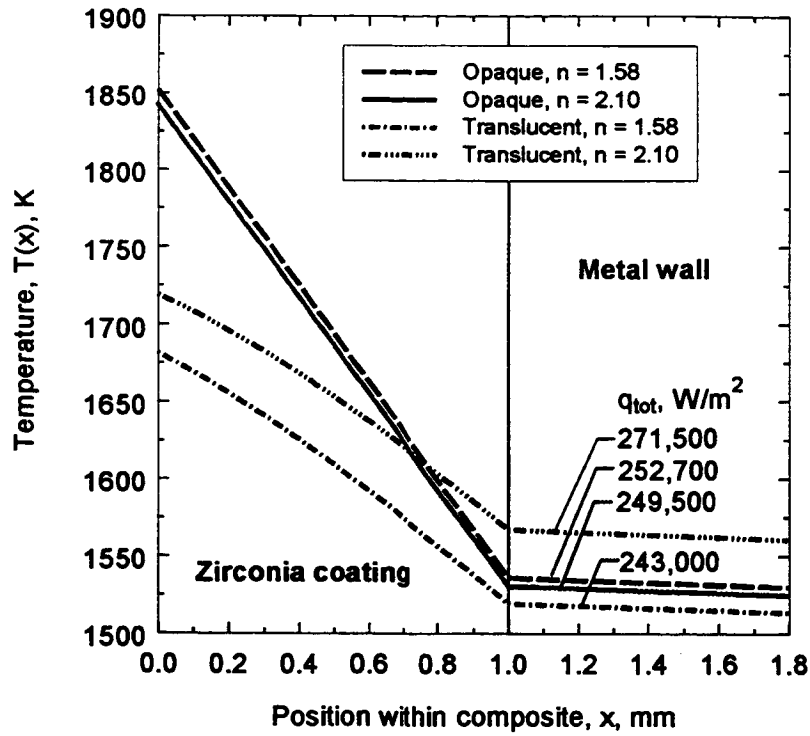
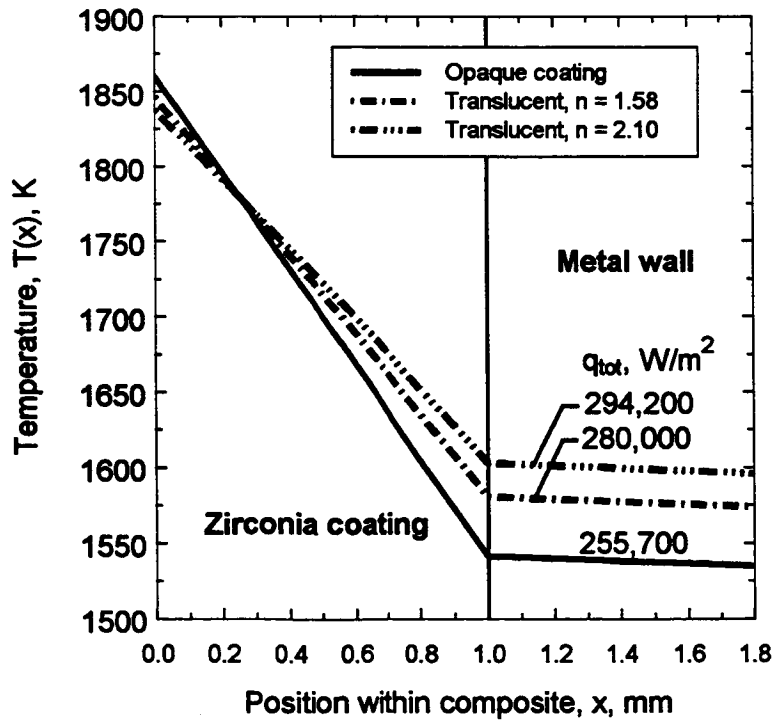


Figure 3. Temperature distributions in a zirconia coating on a combustor wall, compared with an opaque coating. Temperature distributions for oxidized metal without a coating, with an opaque coating, and with a semitransparent coating with and without soot on its exposed surface (on cooled side radiation is to large surroundings). Parameters (units are in W m K): $h_1 = 250$, $h_2 = 110$, $k_c = 0.8$, $k_m = 33$, $\delta_c = 10^{-3}$, $\delta_m = 0.794 \cdot 10^{-3}$, $n = 1.58$, $a = 30$ and $\sigma_s = 10^4$ for $\lambda < 5 \mu\text{m}$, $T_{s1} = T_{g1} = 2000$, $T_{s2} = T_{g2} = 800$, $\epsilon_{bc} = 0.3$, $\epsilon_m = 0.6$, $\epsilon_{soot} = 0.97$.

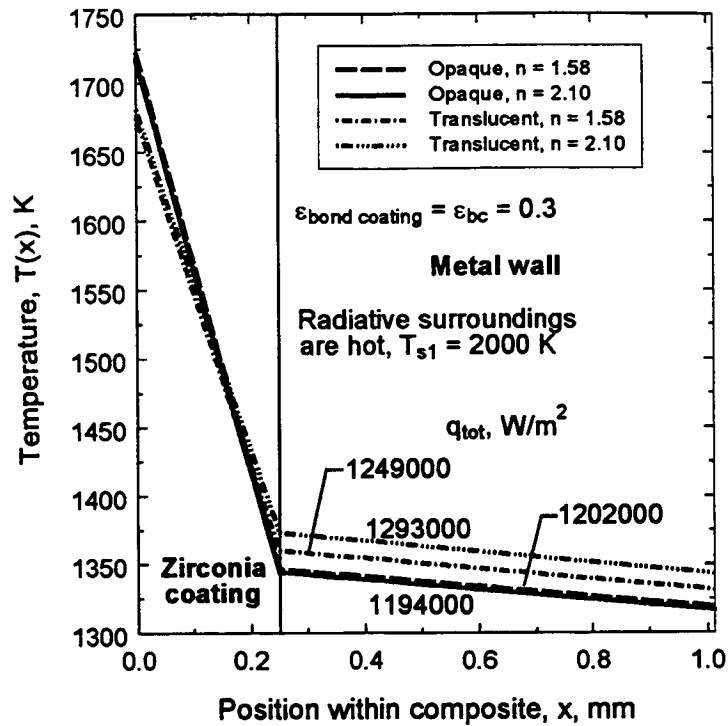


(a) Coating surface is clean.

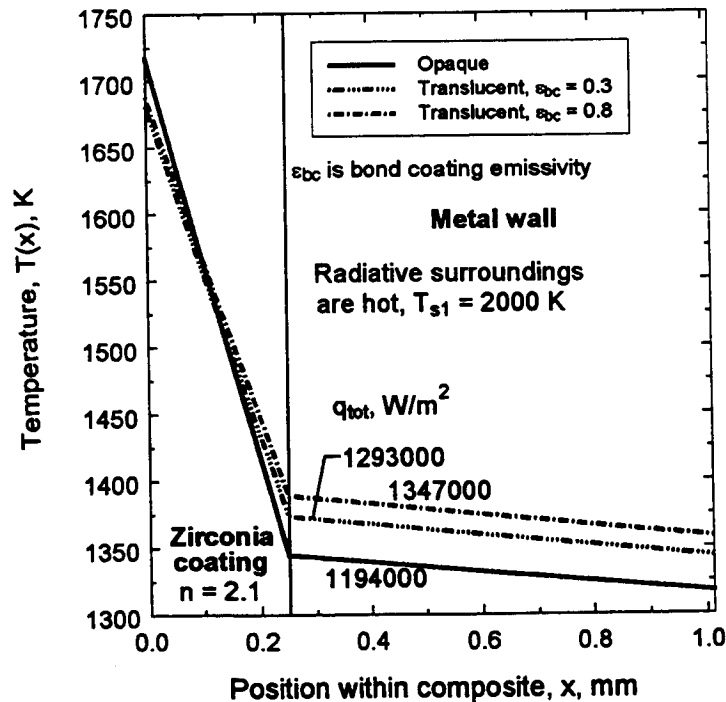


(b) Coating surface is covered with soot.

Figure 4. Effect of zirconia refractive index on temperatures in a coating on a combustor wall. Parameters are the same as for Fig. 3, with additional results for $n = 2.10$.

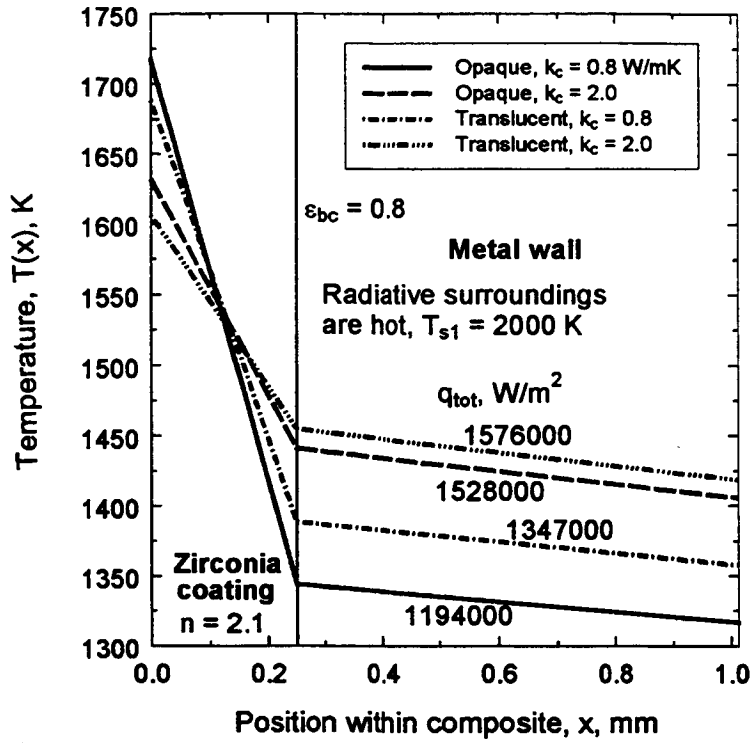


(a) Coating refractive index, $n = 1.58$ and 2.10 , for $\epsilon_{bc} = 0.3$.

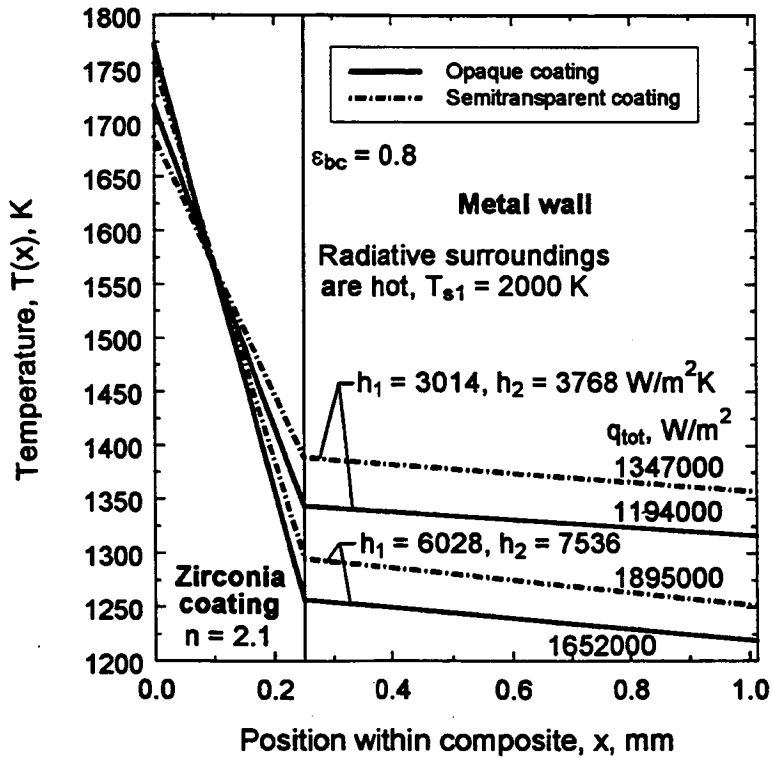


(b) Effect of bond-coat emissivity, $\epsilon_{bc} = 0.3$ and 0.8 for $n = 2.10$.

Figure 5. Turbine blade temperature distributions for blade exposed to combustor radiation. Temperatures for an opaque coating and a semitransparent coating with clean surfaces. Parameters (units are in $W m K$): $h_1 = 3014$, $h_2 = 3768$, $k_c = 0.8$, $k_m = 33$, $\delta_c = 0.25 \cdot 10^{-3}$, $\delta_m = 0.762 \cdot 10^{-3}$, $a = 30$ and $\sigma_s = 10^4$ for $\lambda < 5 \mu m$, $T_{s1} = T_{g1} = 2000$, $T_{s2} = T_{g2} = 1000$.



(a) Effect of coating thermal conductivity.



(b) Effect of doubling the values of h_1 and h_2 .

Figure 6. Turbine blade wall temperature distributions for blade exposed to combustor radiation. The parameters are the same as Fig. 5b with $\epsilon_{bc} = 0.8$.

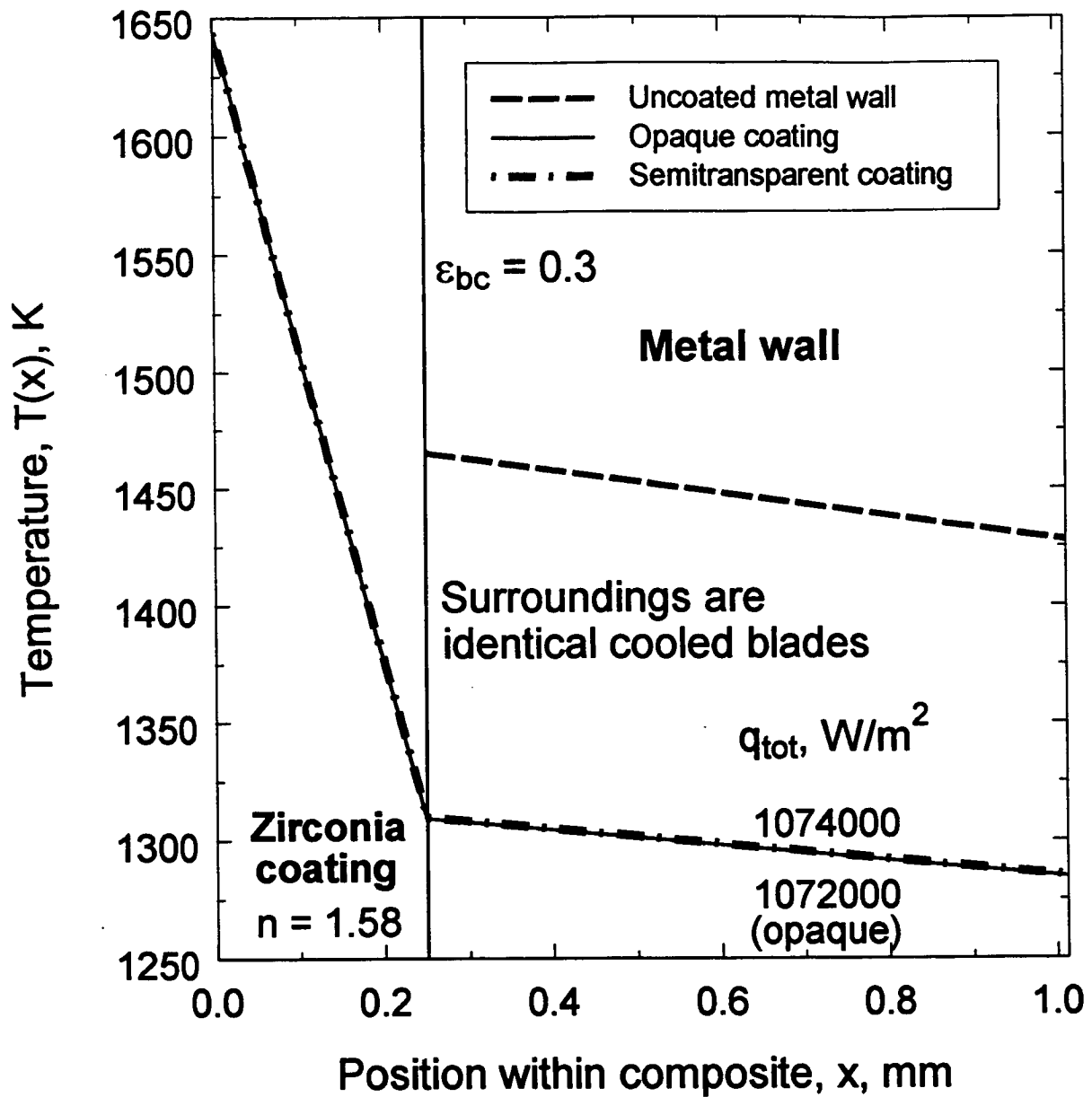


Figure 7. Turbine blade wall temperature distributions for blade surrounded by identical cooled blades. Temperatures for clean metal without a coating, with an opaque coating, and with a semitransparent coating with a clean surface. Parameters (units are in W m K): $h_1 = 3014$, $h_2 = 3768$, $k_c = 0.8$, $k_m = 33$, $\delta_c = 0.25 \cdot 10^{-3}$, $\delta_m = 0.762 \cdot 10^{-3}$, $n = 1.58$, $a = 30$ and $\sigma_s = 10^4$ for $\lambda < 5 \mu\text{m}$, $T_{g1} = 2000$, $T_{g2} = 1000$, $\epsilon_{bc} = 0.3$.

THERMAL CONDUCTIVITY DETERMINATIONS OF THERMAL BARRIER COATINGS

R.E. Taylor
TPRL, Inc.
2595 Yeager Road
West Lafayette, IN 47906 U.S.A.

Most determinations of the thermal conductivity of TBC's have been made using the laser flash method to measure diffusivity (α) and differential scanning calorimetry (DSC) to measure specific heat (C_p). Bulk density (ρ) values are calculated from sample geometry and mass. Thermal conductivity values are calculated as the product of these quantities, i.e. $\lambda = \alpha C_p \rho$. This approach enjoys the advantages of using small samples of simple shapes, ability to measure over wide temperature ranges rapidly (and hence being cost-effective) and enjoys a relatively high degree of accuracy when properly performed with suitable geometry samples. Computer programs which calculate the thermal diffusivity of one layer of a two-layer or three-layer composite from the half-time, $t_{1/2}$, measured in the conventional manner by the flash technique have been developed.

Even though samples of free-standing TBC's have been measured, it was often necessary to add thin coatings to the front surface to prevent laser beam penetration. In addition, we usually had to apply a very thin coating on the rear surface to prevent our i.r. detector from viewing into the sample and thus not giving an accurate temperature rise curve for the rear surface. In general, the presence of a rear surface coating did not have to be accounted for because it only takes a very thin layer to prevent the i.r. detector from viewing into the sample interior. However, preventing a relatively severe laser burst from penetrating into the samples may require a significant protective coat, depending upon the translucency of the TBC. In cases of a substantial front layer, the presence of the protective coat must be accounted for and the experiment becomes a two-layer case. It should be noted that in the case of TBC's mounted on a metal substrate, there is no need for a protective front layer, since the metal substrate provides this, i.e. we always have the substrate side positioned towards the laser.

Figure 1 shows the results for free-standing coatings of Al_2O_3 of ZrO_2 and of composites consisting of 4 (AZ41) or 8 (AZ81) alternating layers of Al_2O_3 and ZrO_2 . The conductivity values for AZ41 are somewhat larger than those for

AZ81. The ordering is as expected, with the multilayer composites having conductivity values inbetween those of the constituents. In fact, since the alternate layers could be represented by a series model, the conductivity of the layered samples can be calculated from constituents, i.e.

$$\lambda_{composite} = \lambda_1 \lambda_2 / (.5 \lambda_1 + .5 \lambda_2), \quad (1)$$

assuming that the layer have equal thicknesses. Using the data of Fig. 1, conductivity values for the layered composites at 200 and 700 are 0.0270 and 0.0232 W cm⁻¹K⁻¹, respectively. These results are within 1% of the measured values for AZ41 of 0.0270 and 0.0228 W cm⁻¹K⁻¹. These results show that many thin layers of alternating ceramics may often be treated as though there was one homogeneous layer.

While we routinely determine the thermal conductivity of one layer bonded to another, the accuracy strongly depends upon the absolute and relative values of the individual layers. An example of the results obtained on two-layer and three-layer samples is shown in Fig. 2. Samples of 13 mil Al₂O₃ and ZrO₂ each bonded to a 110 mil substrate were used to obtain conductivity values for the Al₂O₃ (Al₂O₃-A1) and ZrO₂ (ZrO₂-Z1) layers. Then a three layer sample consisting of 110 mil substrate, 7 mil Al₂O₃ and 7 mils ZrO₂ was measured. Using the substrate and Al₂O₃ results, conductivity values for the ZrO₂ layer were determined (ZR02-AZ11) and are compared to the previously determined values (Fig. 2). The results are in good agreement.

The input parameters which enter into a two-(or three) layer calculation are the thicknesses, densities and specific heat of each layer, the diffusivity of one (or two) layers, and the measured half rise times. The sensitivity of each of these parameters also depends on the relative values between these parameters for the various layer, i.e. the relative magnitudes of the layer thicknesses, the relative magnitudes of the diffusivity/conductivity values, etc. The situation is further complicated by the fact that the calculations of the diffusivity/conductivity value of the unknown layer is based upon parameter estimation (i.e. interative) procedures. Therefore several cases we were faced with experimentally were examined. These cases all involve superalloy substrates whose conductivity/diffusivity values increased substantially with increasing temperature and TBC's of relatively low diffusivity/conductivity values which were relatively temperature-independent. This means that the relative magnitudes of the diffusivity/conductivity values for the substrate and coating increases substantially with increasing temperature. For example, the conductivity ratios of substrate to coating were of the order of 10:1 at 100°C

and greater than 20:1 at 1000°C.

The effects of uncertainties in the input parameters for the case of a 11 mil coat bonded to a 25 mil substrate at 500°C are examined in Fig. 3. The calculated conductivity values are most sensitive to the uncertainty in the coating thickness and the measured half-times. However, it should be possible to obtain sufficiently accurate input parameter values to obtain reasonable results for this case.

However, when we consider a 3.3 mil coat on a 120 mil substrate at 500°C (Fig. 4), the extreme sensitivities of the calculated conductivity value to errors in substrate thickness, diffusivity and to half-rise times precludes meaningful results. For example, a $\pm 1\%$ change in the value assigned to substrate thickness results in changes of +60 and -28% change in the conductivity values. A $\pm 2\%$ change in the measured half-time value from 0.34089 seconds (i.e. 0.34087 ± 0.00682 sec) results in change in the calculated conductivity values of +65 to -30%.

These sensitivities also depend upon the relative magnitudes of the diffusivity/conductivity values of the substrate and TBC. The bigger this ratio, the better the experiment. This is the reason that the conductivity values for the layered composites often approach those for the free-standing coatings at higher temperatures. It is interesting to note that coating conductivity values could be determined fairly accurately under the conditions of Figure 4 if their values were one-tenth of the value normally encountered.

To summarize our experiences with the laser flash technique applied to TBC coatings, we routinely obtain very good results for 20 mil coatings, fair results for 10 mil coatings and fair to terrible results for 5 mil or thinner coatings, depending upon the manufacturer's ability to furnish accurate information on layer thicknesses and densities.

Other techniques which we have used to determine thermal conductivity of TBC's involve our multi-property apparatus, which uses samples of TBC's bonded to their tubes, and the photo-acoustic technique, which is limited to near room temperature measurements.

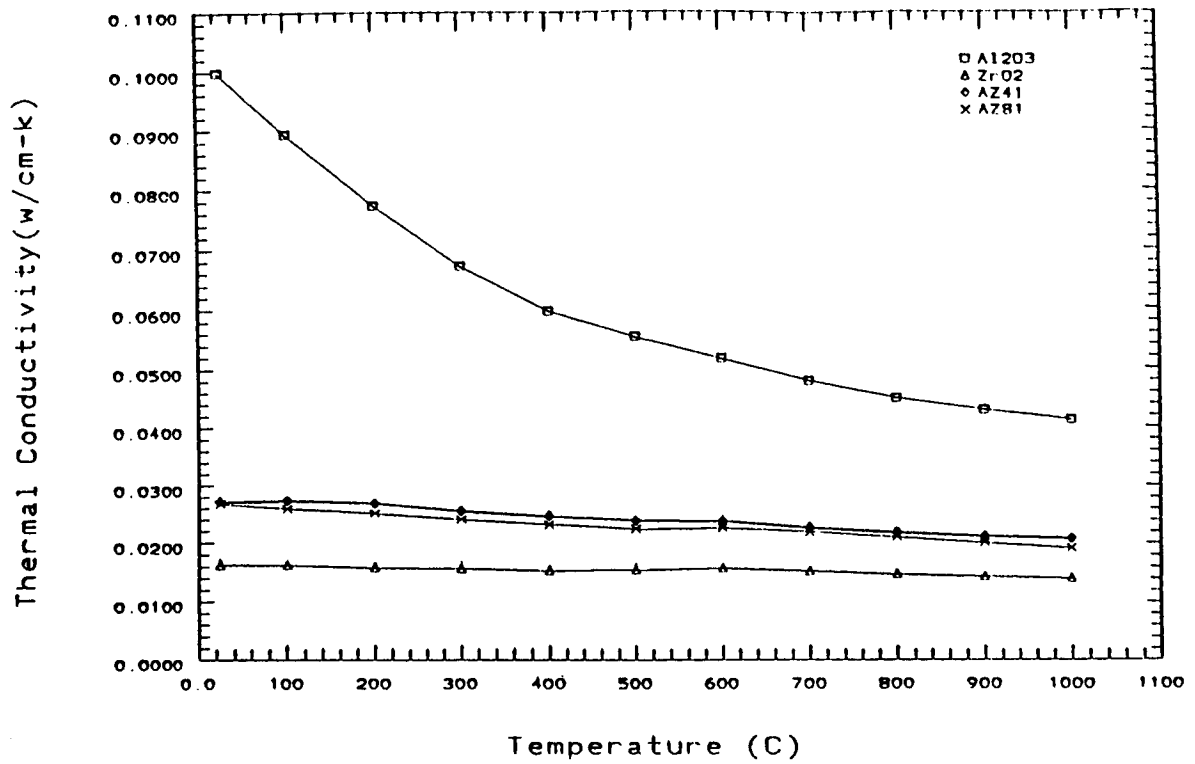


Figure 1 Thermal Conductivity Free-Standing Layers

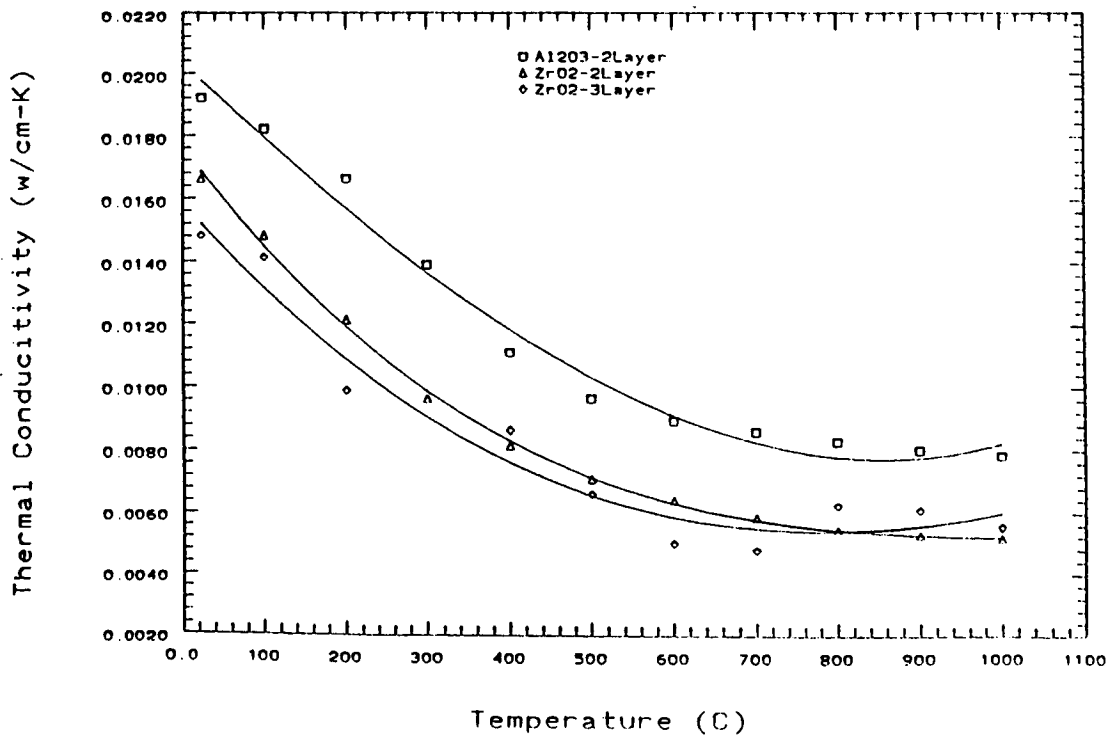


Figure 2 Thermal Conductivity (2 and 3 Layer Samples)

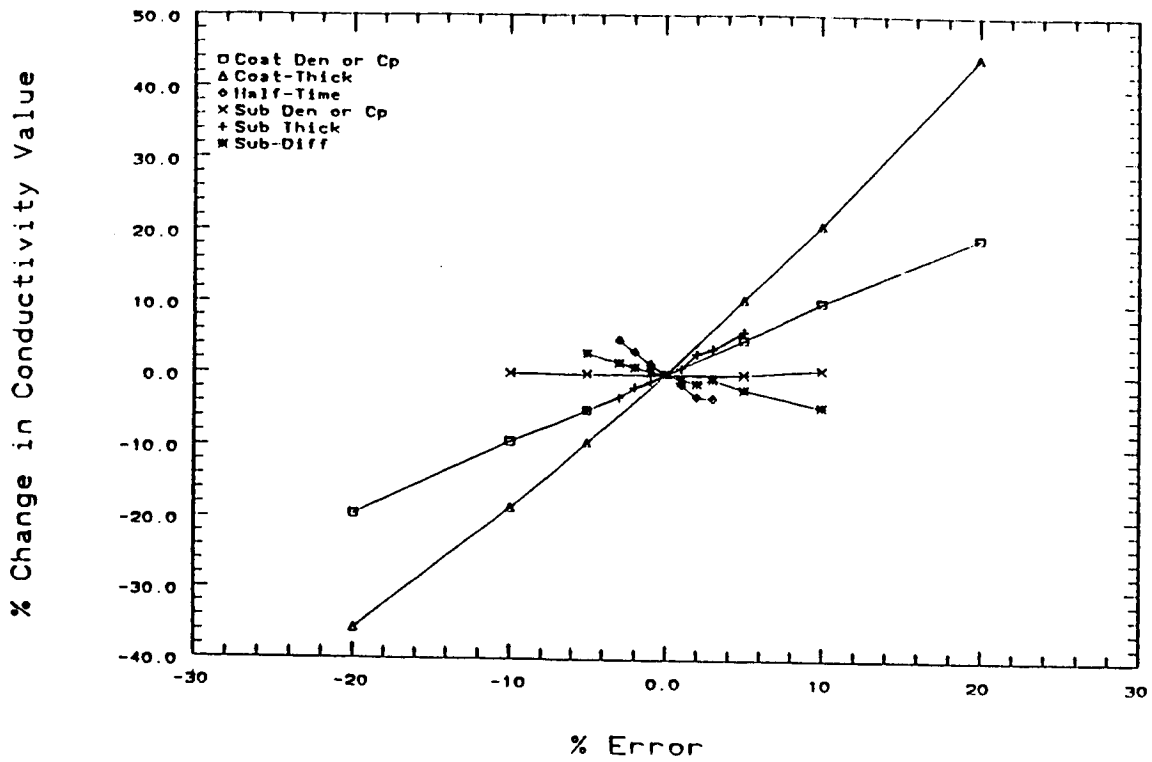


Figure 3
11 Mil Coating on 25 Mil Substrate

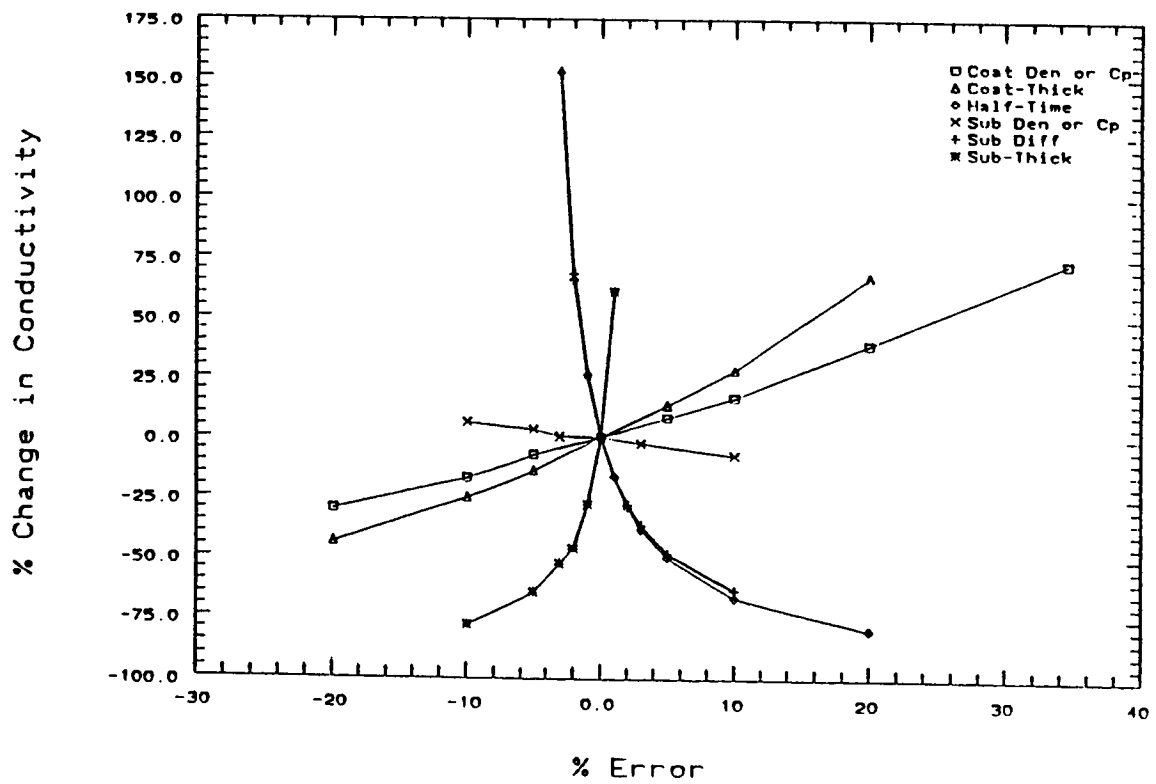


Figure 4
3.3 Mil Coating on 120 Mil Substrate

THERMAL CONDUCTIVITY OF FUNCTIONALLY GRADED THERMAL BARRIER COATINGS

ANDREW J. SLIFKA, B. James Filla, and John M. Phelps
NIST, Materials Reliability Division
325 Broadway
Boulder, CO 80303

Introduction

Functionally graded materials (FGMs) are being developed for high heat flux and large thermal gradient applications. The use of a compositional grading under high thermal load has been shown to reduce thermal stresses compared to a monolithic ceramic coating [1]. Applications are found primarily in aerospace, where this type of thermal loading is encountered by nose caps, leading edges, and engines [2]. The thermal properties of these coatings are needed for efficient design and development of thermal barrier and wear related systems. We have measured the thermal conductivity of two FGM coatings from 400 K to 1200 K using an absolute, steady-state technique. We did thermal conductivity testing only to 1200 K in order to remain below the sintering temperature of the coatings, which would have complicated interpretation of the results. One specimen is a 1.1mm thick Ni20Cr - 8% yttria-stabilized zirconia (YSZ) FGM with a linear grading from metal to ceramic. The second coating is a 1.8 mm thick NiCoCrAlY - 25% ceria-2.5% yttria-stabilized zirconia (CYSZ) FGM, also with a linear grading from metal to ceramic. Both coatings were obtained from commercial sources and deposited on 410 stainless steel substrates.

Experimental Method

The method used for the measurements described here is a modification of the ASTM C 177-85 test procedure for guarded-hot-plate measurements of thermal conductivity, modified for use at high temperatures [3]. A general description of the method, applied to measurements on FGM coatings, is given here, but details of the design of the apparatus can be found elsewhere [4, 5]. The method is a steady-state, absolute measurement of thermal conductivity done under computer control. Steady-state measurements of thermal conductivity are time-consuming, and a single test of a specimen in this apparatus takes over 130 hours to perform. This method is intended as a standards-quality measurement, and is not intended to compete with fast, convenient methods such as laser-flash thermal diffusivity, but to complement these and other techniques by providing measurement standards for the coatings community.

The main measurement stack is shown schematically in figure 1. The principle behind the guarded-hot-plate technique is to create steady-state, unidirectional heat flow through a specimen so that the simplified version of Fourier's conduction law can be used,

$$\frac{Q}{A} = k \frac{\Delta T}{\Delta x} \quad (1)$$

where Q is the power input, A is the metered cross-section area, k is thermal conductivity, ΔT is the temperature drop across the specimen, and Δx is the thickness of the specimen. The bottom and outer guard heaters are controlled to the same temperature

as the main heater plate, thus comprising an isothermal hot “cup”. The heat flux transducer replaces the lower specimen used in a typical guarded hot plate. This transducer is a 38-junction thermopile that ensures that no heat flows down from the main heater plate. The main heater plate is 70 mm in diameter, and because of the small physical size, there is no differential thermopile between the central main heater and surrounding inner guard heater, typically used to prevent radial heat flow. In this case, both heaters are powered to the same heat flux, resulting in uniform heating and no radial heat flow. Therefore, the power input to the main heater flows unidirectionally upward through the specimen and into the radiative heat sink. The heat sink weighs about 2 kg and provides a repeatable mechanical contact between the plates in the stack. Since we use a heat sink on the low-temperature side of the measurement, rather than the traditional controlled temperature plate, our control on the low-temperature side is open-loop. The open-loop condition does not allow us to accurately repeat the temperature difference across a given specimen during successive tests, but repeat tests on a few specimens have shown less than 0.5% variation of thermal conductivity values. An advantage of this open-loop control is rapid convergence to the final value of thermal conductivity, which increases the precision of the measurement.

Due to the temperatures seen in this system, we cannot use a thermally conductive grease or soft metal between the temperature sensor plates and the specimen. Therefore, there is a finite thermal resistance between each sensor plate and the specimen. Figure 2 shows the relevant thermal resistances of an FGM coating specimen. Since the coating adheres well to the substrate and is subjected to only a few thermal cycles during testing, we assume that the thermal resistance at the coating - substrate interface is negligibly small. There are four thermal resistances that we must consider, shown by the equation in figure 2. We obtain the thermal resistance of the substrate material and the substrate - sensor plate interfacial resistance from previous tests on blank substrate specimens. We use a functional form for the interfacial resistance between the coating and sensor plate from previous tests on a monolithic, 8% yttria-stabilized zirconia coating, which we modify to account for the surface roughness of the coating [6]. By using this information, we extract the thermal conductivity of the coating from our measurement of total conductivity across the specimen and interfaces.

Results and Discussion

The first coating we tested was the 1.1 mm thick Ni20Cr - 8% YSZ FGM coating produced by low-pressure-plasma spray. The spray atmosphere of 26.6 kPa has been shown to produce a coating of optimum density, which results in only 3.5 % porosity, measured from size and mass [7]. The coating is sprayed in a 6-step process to produce a linear grading in composition, shown in figure 3. We measured the thermal conductivity of this coating 5 times, with a moderate thermal shock between tests to induce microcracking. Figure 4 shows the thermal conductivity data for the 5 tests, with thermal conductivity ranging from 0.72 to 1.84 $W \cdot m^{-1} \cdot K^{-1}$. The thermal conductivity dropped an average of 9 % for each test.

The second coating tested was the 1.8 mm thick NiCoCrAlY - CYSZ FGM coating produced by air-plasma spray. The coating has 9 % porosity, measured by size and mass, and is also linearly graded, from a 10-step process. The coatings have similar laminar structures. Thermal conductivity data is shown in figure 5, with thermal conductivity ranging from 0.95 to 1.4 $W \cdot m^{-1} \cdot K^{-1}$. The curve has a similar shape to the FGM measurements of the first coating.

The general upward trend in both sets of data is due to the metallic component of the coatings. Figure 6 shows an optical micrograph of the CYSZ coating. The light areas are metallic, the grey areas are ceramic, and the dark areas show pores and microcracks, typical of plasma sprayed FGM coatings. The YSZ FGM coating had an initial thermal conductivity higher than that of the CYSZ coating, which was expected, since the YSZ FGM is thinner and less porous. The YSZ FGM coating showed a decrease in thermal conductivity upon successive thermal shock. This decrease is probably due to an increase in microcrack density caused by thermal cycling, the mechanism being the thermal expansion mismatch between the metal and ceramic components. We would expect the CYSZ coating to exhibit similar behavior if tested multiple times with moderate thermal shock between tests. On a microscopic scale, these coatings have many components, as shown by figure 7. The various phases of material allow for many different local thermal stresses to develop and induce microcracking. Both sets of thermal conductivity data also show a sharp upturn at high temperature, which is probably due to a radiative component of thermal conductivity. The most unusual result from these measurements was the observation of a significant drop in thermal conductivity, for both coatings, between 1050 and 1100 K. We are investigating three possible mechanisms for this repeatable, reversible, observed drop in thermal conductivity: splat separation due to thermal expansion mismatch; a magnetostrictive event in the substrate; and differential thermal expansion stresses inducing a phase change in the ceramic coating component.

References

1. R.L. Williamson, and B.H. Rabin, "Numerical Modeling of Residual Stress in Ni-Al₂O₃ Gradient Materials," *Ceramic Transactions*, **34** (1993) pp. 55-65.
2. R. Watanabe, A. Kumakawa, and M. Niino, "Fabrication of Panel Assembly of Functionally Gradient Material with Active Cooling Structures," *Ceramic Transactions*, **34** (1993) pp. 181-188.
3. ASTM Standard Test Method C 177-85, *Annual Book of ASTM Standards*, **4.06**, Plenum Press (1996) pp. 20-31.
4. B.J. Filla, "A Steady-State High-Temperature Apparatus for Measuring Thermal Conductivity of Ceramics," submitted to *Review of Scientific Instruments*, January (1997).
5. B.J. Filla, "Design and Fabrication of a Miniature High-Temperature Guarded-Hot-Plate Apparatus," *Thermal Conductivity*, **21** (1990) pp. 67-74.
6. A.J. Slifka, B.J. Filla, J.M. Phelps, G. Bancke, and C.C. Berndt, "Thermal Conductivity of a Zirconia Thermal Barrier Coating: A Technical Note," submitted to *Journal of Thermal Spray Technology*, October (1996).
7. N. Shimoda, H. Hamatani, Y. Ichiyama, S. Kitaguchi, and T. Saito, "Fabrication of PSZ / Ni-Alloy FGM by Applying Low Pressure Plasma Spray," *Advanced Materials '93, III / B: Composites, Grain Boundaries and Nanophase Materials*, M. Sakai et al. Ed., Trans. Mat. Res. Soc. Jpn., **16b** (1994) pp. 1263-1266.

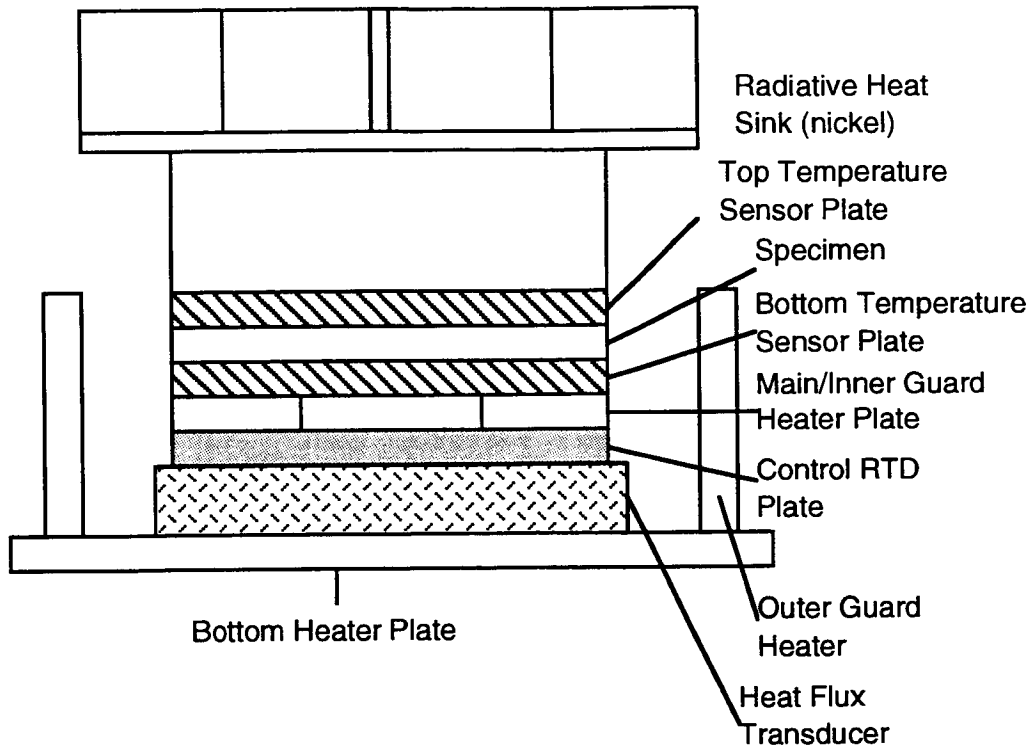
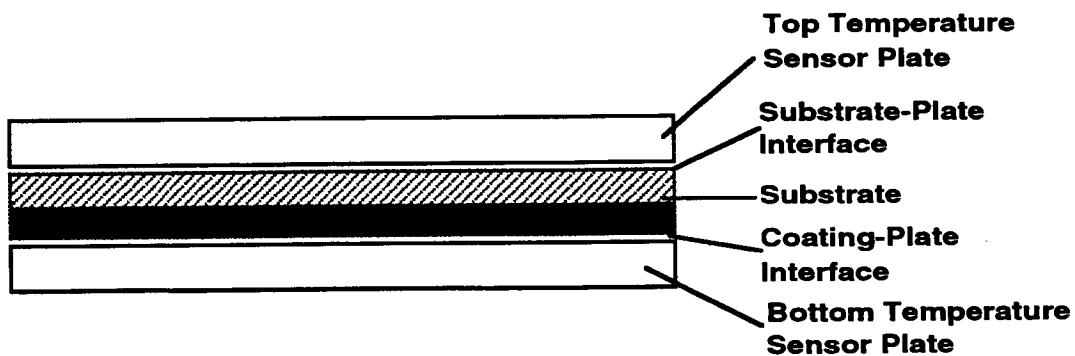


Figure 1. Schematic drawing of the measurement stack of the guarded-hot-plate apparatus.



$$\frac{\Delta T}{Q} = \frac{\Delta x}{k \cdot A} + R_{\text{substrate}} + R_{\text{substrate-plate}} + R_{\text{coating-plate}}$$

Figure 2. The relevant thermal interfaces for measurement of coating thermal conductivity.

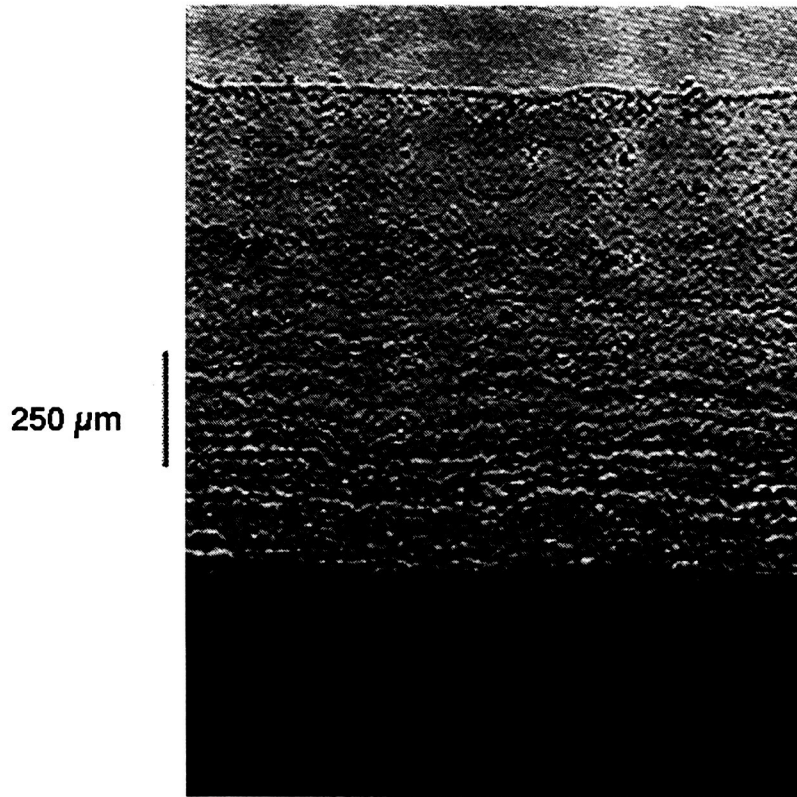


Figure 3. Optical micrograph (50x) of the 1.1 mm thick YSZ FGM coating.

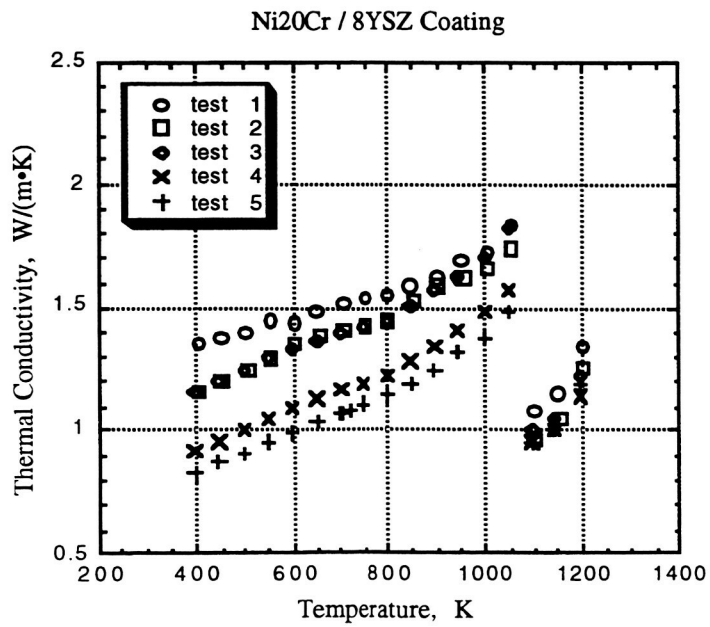


Figure 4. Thermal conductivity data for the five tests of the YSZ FGM coating.

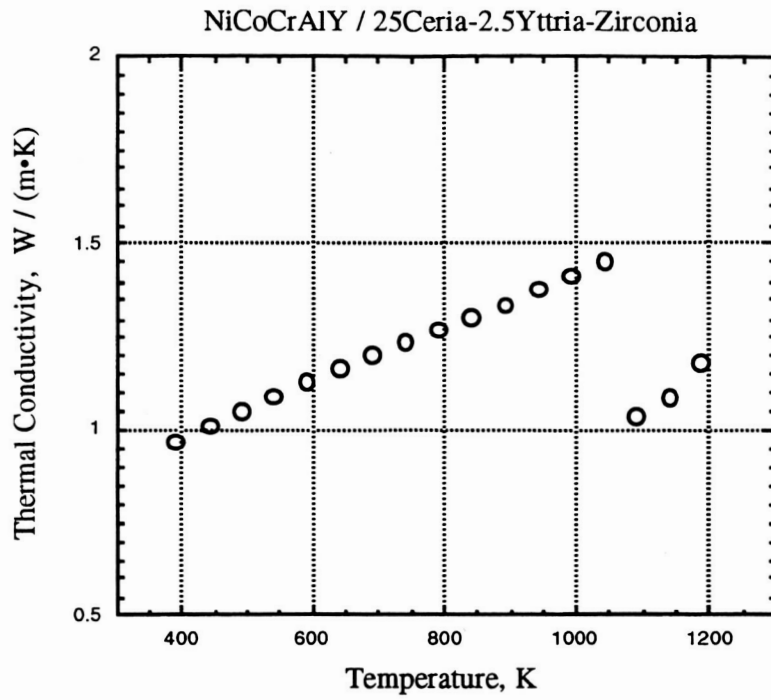
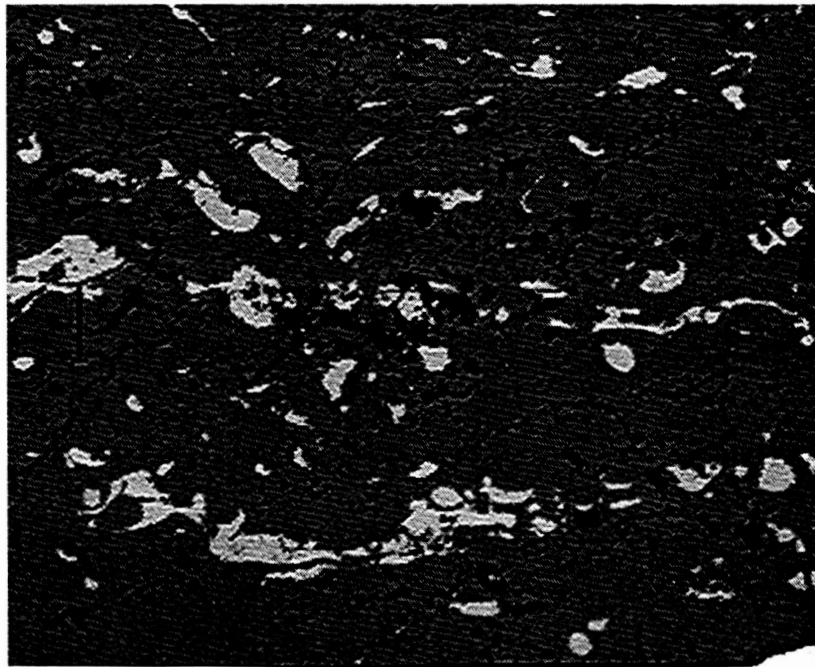


Figure 5. Thermal conductivity data for the CYSZ FGM coating.



Scale Bar = 50 μm

Figure 6. Optical micrograph of the CYSZ FGM coating, showing significant microcracking.

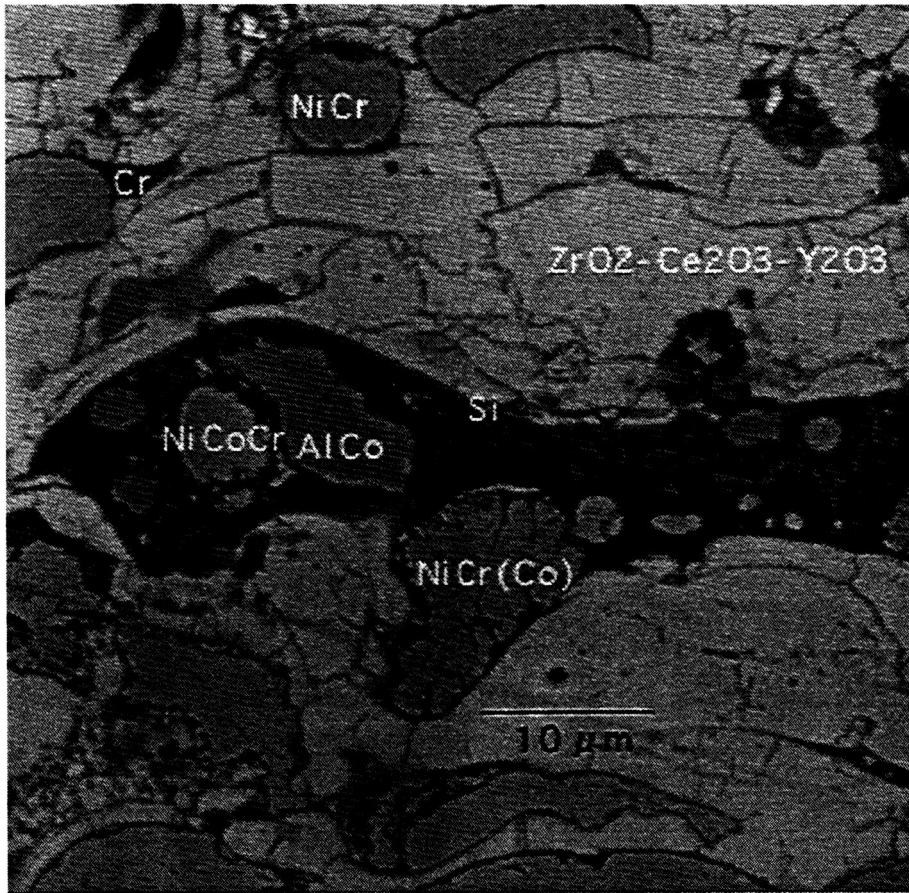


Figure 7. Backscatter electron micrograph of the CYSZ FGM coating, showing the complex chemistry and structure seen in these type materials.

Development of Low Thermal Conductivity Thermal Barrier Coatings

M.J. Maloney, H.S. Achter, and B.K. Barkalow

Pratt & Whitney, West Palm Beach, FL

Thermal barrier coatings are currently being employed in the turbine section of gas turbine engines on blades to provide insulation from the hot flow path environment and to provide a 170C increase in effective temperature capability. Turbine blade thermal barrier coatings typically utilize partially stabilized zirconia to provide thermal insulation. Under support from the NAVY, Pratt & Whitney has been evaluating the use of alternate ceramic compounds with improved thermal resistance over zirconia base systems. The use of low thermal conductivity thermal barrier coatings can have a significant impact on the performance of gas turbine engines in terms of increased efficiency and durability. Work is currently focused on development of a yttria-ceria thermal barrier coating processed by electron beam physical vapor deposition. Thermal resistance and performance of the ceria base thermal barrier coating relative to current systems will be discussed.

Degradation Modes of Thermal Barrier Coatings: Experience in High Thrust Experimental Engines at Pratt & Whitney

S. Bose and J.D. Marcin
Pratt & Whitney
400 Main Street
East Hartford, CT USA

The gas path temperatures in high pressure turbine section of today's high thrust engines far exceed the temperature capability of turbine materials. Thermal Barrier Coatings (TBC) in combination with innovative cooling schemes make it possible for the turbine components to survive. TBCs, consisting of a metallic bond coat and a thermally insulating ceramic top coat, are processed either by air plasma spray (APS) or Electron Beam Vapor Deposition (EB-PVD). The predominant degradation mode of TBCs is thermal spallation. In the EB-PVD system, failure generally occurs either within the thermally grown oxide (TGO) scale that forms at the ceramic - bond coat interface or at the TGO - bond coat interface. Oxidation, bond coat creep and other kinetic factors play varying roles in this spallation. Other degradation modes of lesser importance are impact damage and erosion. Examples of some of these degradation modes and their implications will be presented.

MECHANISM-BASED LIFE PREDICTION ISSUES FOR THERMAL BARRIER COATINGS

A.G. Evans, J.S. Wang and D. Mum
Harvard University, Cambridge, MA

1. INTRODUCTION

Thermal barrier coatings (TBCs) are susceptible to spalling from superalloy substrates with an intermediate bond coat. The event occurs upon cooling from an exposure that causes a thermally grown oxide (TGO), typically alumina, to form at the TBC/bond coat interface. Moreover, thermal cycling reduces the exposure time needed to form spalls. The mechanisms are dependent upon the TBC deposition method. For electron-beam deposited (EBPVD) coatings having a columnar grain structure, the low in-plane modulus imparts sufficient strain tolerance that the failure comprises separation of the TGO from the bond coat. This occurs by formation and initial propagation of a separation along the interface, followed by deflection into and through the TBC. Elucidation of the mechanisms is contingent on an understanding of interface cracking in compressed films. Plasma spray deposited TBCs spall more readily by crack evolution within the oxide layers. The fracture properties of both the TGO and the TBC are involved.

The compressive stress in the alumina is crucially important. It is the primary source for the energy release rate that motivates cracking and spalling. Recent measurements of this stress provide insight. The growth stresses, while relatively small, 0.2-1GPa (dependent on composition), nevertheless dictate the interface separation dynamics. These stresses can be partially relieved by creep or wrinkling. The thermal expansion mismatch stresses are much larger, of order 3-5GPa, dependent on the alloy. They dominate crack growth and spalling.

The time and cycle dependence of these stresses, combined with the fracture toughnesses of the oxides and the interfaces, underlie a mechanistic interpretation of the life. Measurements of these properties made in conjunction with mechanics solutions for the prospective crack trajectories comprise the principal content of a mechanism-based life prediction methodology. Fracture measurements made on interfaces produced by diffusion bonding provide relevant background. The Ni/alumina interface is susceptible to stress corrosion caused by moisture, with a relatively low effective toughness, $\Gamma_i \sim 10\text{Jm}^{-2}$. Segregation to this interface, particularly of C, activates the mechanism. Alloying with a small amount of Cr eliminates the problem. It enables the interface to be so tough that cracks blunt, causing fractures to extend in the oxide, rather than along the interface. This effect has been attributed to the ability of Cr to getter the C as Cr carbides, thereby inhibiting its segregation to the interface. S segregation to the TGO/bond coat

interface may have an analogous (perhaps, even more profound) consequence for interface toughness.

TBCs have anisotropic fracture properties. Measurements on plasma spray TBCs indicate an exceptionally low toughness on planes parallel to the interface ($K_{Ic} \sim 0.2 \text{MPam}^{1/2}$), caused by deposition defects. This compares with, $K_{Ic} \sim 2 \text{MPam}^{1/2}$ for bulk cubic zirconia. There are no data for EBPVD coatings.

2. SPALL MECHANICS

Two fundamentally different mechanisms have been proposed for the defoliation of compressed oxides from superalloys. (i) One derives from thin film mechanics. It involves buckling and spalling (fig 1). (ii) The other comprises compressive crumbling found in rocks and minerals (fig 2). These two phenomena are elaborated, enabling their key features to be compared and contrasted. A key test of the mechanistic description is its embodiment of physical parameters affected by S segregation to the interface.

2.1 Thin Film Spalling

Compressive spalling of thin films requires that five phenomena occur *in sequence* (fig 1). (a) A separation develops either at the interface or within the film. (b) The film above the separation buckles, causing an energy release rate at its perimeter. (c) The energy release rate exceeds the fracture toughness, enabling the buckle to propagate. (d) The crack deflects across the oxide, resulting in a spall. In some cases, (c) and (d) can be simultaneous. (e) When deflection begins, the process becomes dynamic and an additional energy release rate develops at the still attached regions of the film. These effects often cause the film to completely eject from the substrate.

Each of these events involves a characteristic stress and a characteristic size. These characteristics, when fully defined, provide a basis for experimental elucidation of the mechanisms. Inserting characteristic values for the oxide thickness provides an initial assessment of the applicability of the mechanism. For such analysis, two estimates for the interface fracture energy have been used. One is the value measured for diffusion bonded Ni/alumina interfaces at room temperature (10Jm^{-2}). The other is an estimate for an interface with diminished toughness caused by S segregation (1Jm^{-2}). The critical stresses found for buckle propagation and spalling (2-6GPa) bound the thermal expansion misfit stress ($\sim 3.5 \text{GPa}$). This aspect of the mechanism is thus consistent with observations, provided that segregation indeed enables a diminished toughness. The critical radii for propagation range from 16 to 27 μm (the latter referring to the lower interface toughness). The corresponding spall sizes vary from 16mm to 3mm.

The analysis also reveals that, for buckling to occur, separations of order 20 μm must exist at the interface. An understanding of the initial formation of such separations is essential to a self-consistent mechanistic model. Presently, this does not exist.

2.2 Compressive Defoliation

Compressive crushing is predicated on shear faults that pre-exist in the material. Sliding along these faults induces cracks which extend parallel to the direction of compression. A manifestation for oxide scales is depicted on fig 2. Inserting typical values for the misfit stress and the elastic properties and again bounding the interface toughness by 10 and 1Jm^{-2} , indicates crack lengths of order 1.5 to 15 μm . The latter are in the range of spall sizes reported in the literature. Further development is contingent on observation of the implied shear faults, coupled with an understanding of the mechanism that cause them to form. Such faults, if present, would be manifest as slip steps on the oxide surface (fig 2) accompanied by wedge-shaped cracks at the interface.

2.3 Separation Dynamics

When the oxide/metal interface is planar, there are no normal stresses to motivate interface separation. Non-planar morphologies are required. Four categories of oxide morphology (fig 3) are potential sources of the requisite stress: three periodic and one aperiodic. All of the periodic morphologies lead to interface stresses having the form:

$$\sigma_{ij} = \sigma_o(A/L)Q_{ij} \quad (1)$$

where σ_o is the compressive stress in the oxide, A is the amplitude and L the wavelength of the undulations. The function Q_{ij} is insensitive to the film thickness (fig 3), except for the out-of-phase morphology. The tensile stresses, σ_n , occur at the locations where the oxide is concave (fig 3). Among the three morphologies, the greatest stresses arise at the thinnest sections of the out-of-plane morphology, when h/L is small ($< 1/10$). For elastic properties representative of Ni and alumina, these stresses are characterised by: $Q_n \sim 2.2$.

For separations that develop from the regions of normal tension, the opening mode energy release rates, G_I , approach zero when the separation length approaches the wavelength. Consequently, for all realistic wavelengths ($< 10\mu\text{m}$), separations large enough to cause buckling ($> 20\mu\text{m}$) are unlikely to develop. This paradox is resolved if the interfaces have local penetrations of the type indicated on fig 4. These penetrations are centers of dilatation that motivate the growth of separations over dimensions many times the oxide thickness. They are analagous to lateral cracks that form from indentations in brittle solids. Observations have indicated sulfide, carbide and ternary oxide particles on TGO interfaces having this morphology. The energy release rates for such features are essentially identical to that identified above for the shear faults, with the same

implications for crack growth. But now, the physical features are in accordance with findings that spalls originate from regions of the interface containing sulfide particles.

The initial separations develop with time during the high temperature dwell. Under these conditions the stresses in the oxide are relatively low ($<1\text{GPa}$), with correspondingly small energy release rates. The remaining challenge is to identify a mechanism that operates at elevated temperatures, subject to the prevailing stresses. A likely candidate comprises crack-like voids growing by coupled interface and surface diffusion. Such voids have been recorded at spall locations. Analysis of their steady-state propagation provides insight. It is characterized by *two major features*. (i) A threshold condition below which the voids are unable to propagate. (ii) Steady-state power law growth above the threshold. The former is dictated by the work of adhesion, W_{ad} : voids are unable to grow when $G_I < W_{ad}$. Consequently, by equating G_I to W_{ad} , the likelihood of growing separations up to the magnitude needed for buckling, upon subsequent cooling, can be determined.

For "clean" Ni/alumina interfaces, the work of adhesion ($\sim 1\text{Jm}^{-2}$) is such that $20\mu\text{m}$ separations could only develop if the stress in the oxide were: $\sigma \sim 3\text{GPa}$. Such stresses are larger than values measured during growth. However, if S segregation to the interface reduced W_{ad} to $\sim 0.01\text{Jm}^{-2}$, the stresses needed for crack growth would diminish to $\sim 300\text{MPa}$, within the measured range. An essential role of S segregation is implied. These ideas, if conceptually correct, could be assembled into a life prediction model.

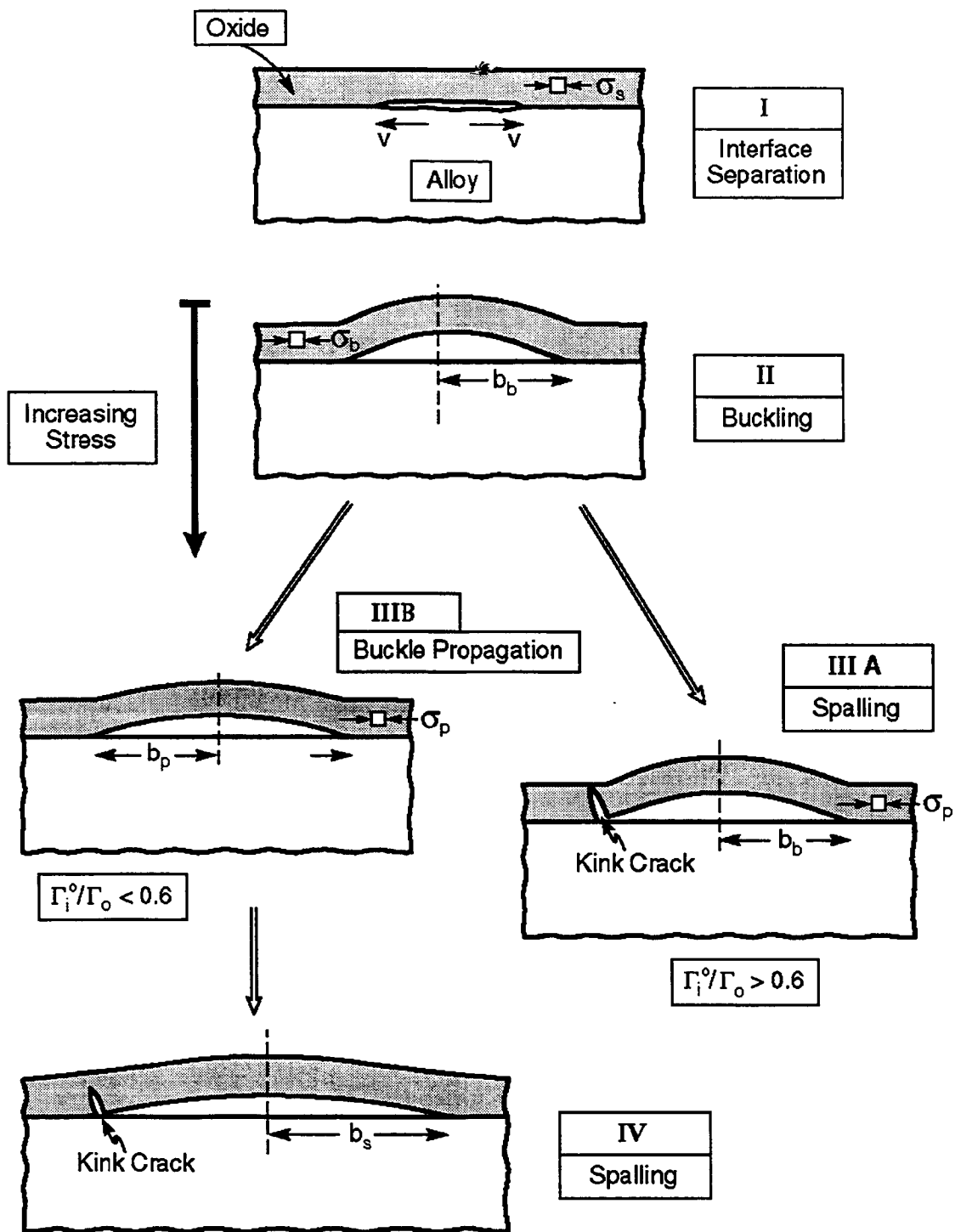
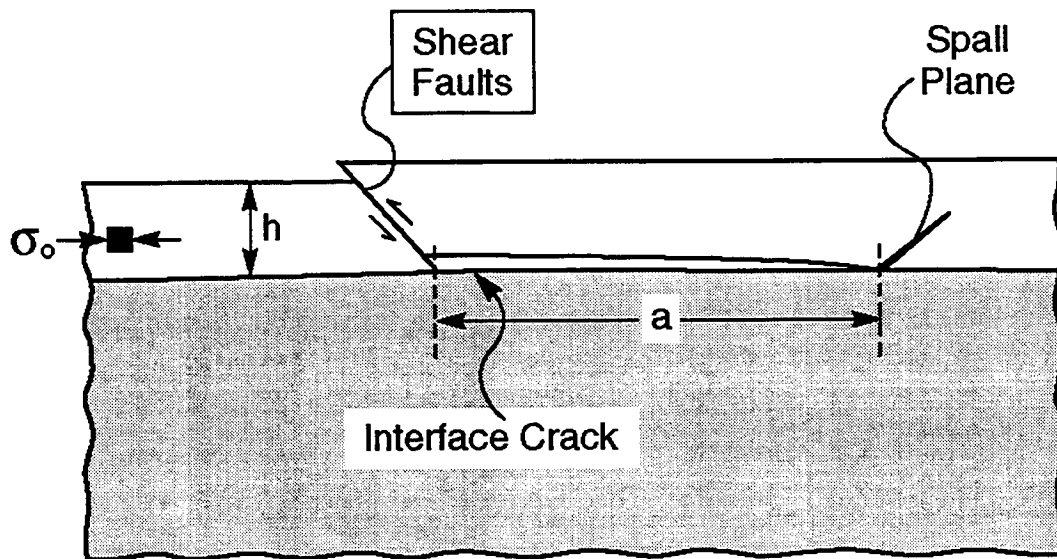


Figure 1. A schematic indicating the sequence of events that occur during the spalling of thin compressed, brittle films. Following formation of an initial separation, buckling is a necessary precursor to either interface crack growth or spalling



$$a/h = \sigma_0^2 h / \pi E \Gamma_i$$

Figure 2. Interface cracks caused by shear faults in the oxide.

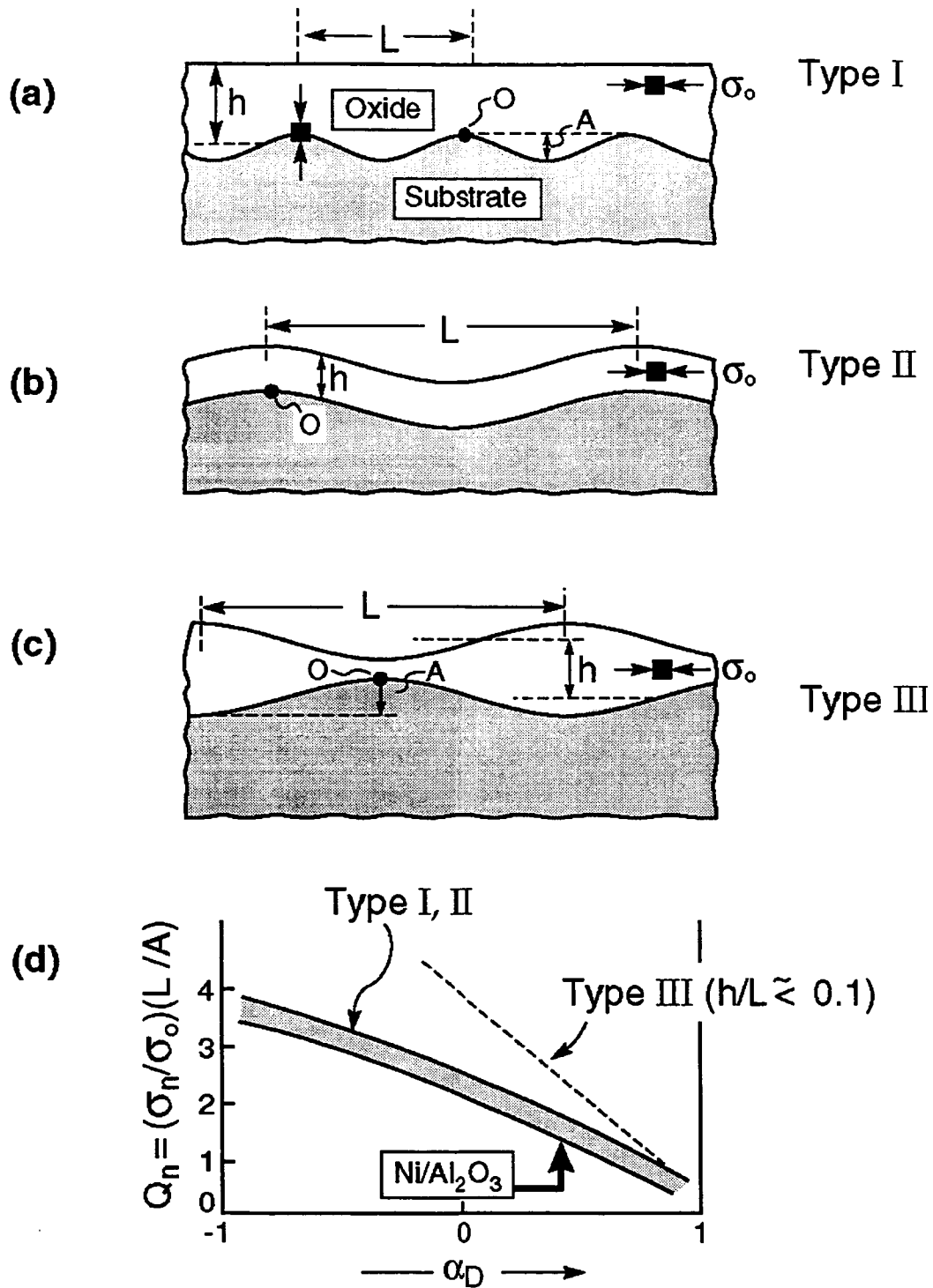


Figure 3. (a-c) Three periodic morphologies for oxide scales. (d) The maximum normal tensile stresses (at sites O in a to c) as a function of the Dundurs parameter, α_D . The values expected for the Ni/alumina system are indicated. All results reside within the band, except for thin out-of-plane undulations.

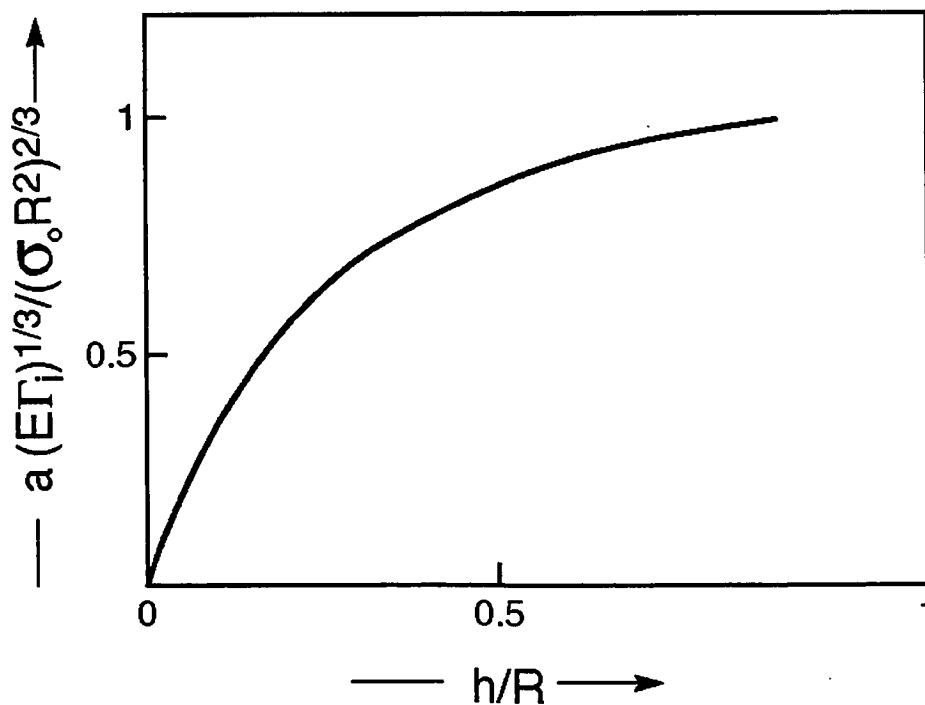
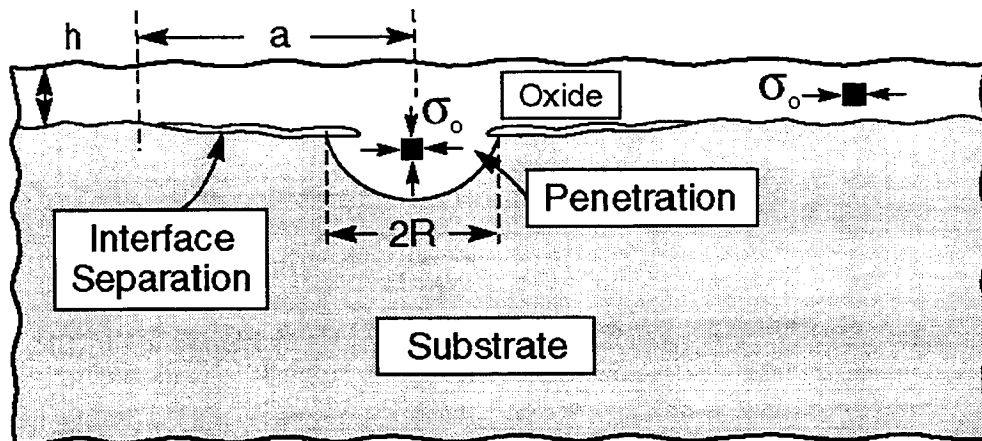


Figure 4. A penetration into the bond coat from the oxide scale, indicating the expected crack location and the associated energy release rate.

MODELING OXIDATION INDUCED STRESSES IN THERMAL BARRIER COATINGS

A. M. Freborg, B. L. Ferguson and G. J. Petrus
Deformation Control Technology, Inc.
Cleveland, Ohio

W. J. Brindley
NASA-Lewis Research Center
Cleveland, Ohio

INTRODUCTION

The use of thermal barrier coatings (TBC's) in gas turbines has increased dramatically in recent years, due mainly to the need for component protection from ever increasing service temperatures. Oxidation of the bond coat has been identified as an important contributing factor to spallation of the ceramic top coat during service [1]. Additional variables found to influence TBC thermal cycle life include bond coat coefficient of thermal expansion, creep behavior of both the ceramic and bond coat layers, and modulus of elasticity [2, 3]. The purpose of this work was to characterize the effects of oxidation on the stress states within the TBC system, as well as to examine the interaction of oxidation with other factors affecting TBC life.

APPROACH

Finite element analysis was specifically applied to characterize stresses in a TBC system undergoing thermal fatigue testing in a burner rig. The model incorporated realistic thermal transients based on measured burner rig surface temperatures (Fig. 1) and modeled thermal gradients. The stresses generated as a result of the thermal cycling were modeled using a NIKE 2-D stress model for the system geometry shown in Figure 2. The model examined the effect of the five factors shown in Figure 3 on the stresses in the TBC, incorporating temperature and time dependent properties for the bond coat and top coat, as well as a sinusoidal interface to simulate the rough bond coat interface. Oxidation was incorporated into the model via the empirical growth rate equation of DeMasi, et al. [1] (Fig. 4). The method of implementing oxidation in the model involved replacing bond coat elements with oxide elements at time intervals as determined by the oxidation rate equation. Volumetric expansion due to oxidation was simulated by use of an artificially high oxide coefficient of thermal expansion (CTE) during the steady state hold of the imposed burner rig cycle.

For this study, the effects of the five system variables (Fig. 3) on thermal stresses generated for up to five thermal cycles were analyzed at two levels, high and low, in a $1/2 \cdot 2^5$ factorial design of experiment. A Yate's analysis was then used to statistically rank and compare the effects of these variables on resulting thermal stresses. Stress results as a function of the number of thermal cycles (limited study), cycle duration, as well as the growth stress of the oxide were also analyzed.

RESULTS

General Analysis

A Yate's Analysis [5] was used to compare and rank the effects of 5 system variables, each occurring at 2 possible levels, on resulting cool-down stresses at the bond coat - ceramic interface. Review of the resulting stress contours indicated the interface region during the cool down period to be the location and time frame in which the highest stresses are generated. The effect of top coat creep within the property range used in this evaluation was shown to be negligible during the early stages of oxidation, and is not included in this paper. In both the ceramic and oxide layers, the relative impact of each system variable was found to vary by position along the interface. The complexity of the interactions can be seen in examining radial stress response along the interface. Figures 5, 6 and 7 illustrate the relative effect of each system variable on stress response in terms of a "percent influence," obtained through comparison of the Yates coefficients. The "percent" value indicates the degree of influence of each variable (pos. or neg.) on resulting stress response relative to the other variables. As most TBC cracking is observed at the interface peak position, interpretation of the interactions revealed by the models will concentrate on this area. The data clearly indicate the importance of variable interaction, and that one cannot define system behavior in terms of a single controlling variable. However, examination of the interactions becomes easier by dividing the data into cases based on the ranking obtained in the Yate's analysis, as shown in Figure 8. Case 1 examines the general impact of oxidation, with Figure 9 showing a portion of the burner rig time history comparing radial stress response at the ceramic peak in both oxidizing and nonoxidizing cases. The oxide layer is formed during heat-up in "cycle #3", with the plot clearly showing an overall increase in radial tension in the ceramic with bond coat oxidation.

A multiple cycle scenario (51 cycles) incorporating oxidation is shown in Figure 10, and illustrates the impact of an oxide layer gradually growing to approx. 1 μm in thickness. Interactions have yet to be quantified for 51 cycles. Growing an oxide to the same 1 μm thickness during a single cycle (the equivalent of increasing cycle time) greatly increases resulting ceramic layer radial stress as shown in Figure 11. Case 2 illustrates the general influence of bond coat CTE, with the time-history and response curves in Figures 12 and 13 indicating the combined impact of CTE variation with and without oxidation on ceramic radial stress. The added influence of bond coat creep is examined in Case 3, where it is seen that higher creep resistant bond coats also act to increase resulting ceramic radial stresses (see Figures 14 and 15). The oxidation effect is the same for both high and low CTE bond coats (no interaction). Case 4 illustrates the impact of surface roughness on radial stress, with the higher roughness model also showing an increased radial stress in the ceramic peak. Time history and response curves are given in Figures 16 and 17.

Additionally, details regarding stress behavior in the oxide layer were also studied. Two variables were assessed in terms of their impact on the stress gradient across the ceramic-oxide-bond coat interface: oxide volumetric expansion and interface roughness. Oxide growth stress, evaluated by comparing the behavior of bond coats which expand and do

not expand when oxidized, was found to relax during steady heating in the burner rig cycle. Thus growth stresses probably have little impact on the TBC system. See Figure 18. Figures 19 and 20 compare the observed gradients across the TBC peak and mid-slope interface regions for both low and high roughness interfaces. Notice the slightly larger spread in radial tension in both the ceramic and oxide in the high roughness model, as well as the lower off-peak gradient in the oxide. At the mid-slope position, both cases display huge stress gradients across the oxide layer (1800.0 MPa compressive to 0.0 MPa).

SUMMARY AND CONCLUSIONS

A finite element method has been used to model stresses within a TBC system in which five variables were closely examined. Though ceramic stress levels appear too high, these will be reduced upon implementation of a future failure criterion. Modeling results indicate the following:

- TBC's represent a highly complex system not amenable to simple rule building. Modeling is required to capture the complex interaction behavior.
- Bond coat CTE and oxidation have the greatest impact on TBC stresses, however variable interactions are also important. The model captures important essential experimental observations
- Duration of thermal cycles, as modeled by high oxide thickness, is important to ceramic stress levels.
- Amount of oxidation per cycle appears more important than pure number of thermal cycle in affecting ceramic stresses.
- Growth stresses due to bond coat oxidation appear unimportant due to bond coat relaxation.

REFERENCES

- [1] J. T. DeMasi, et al., "Thermal Barrier Coating Life Prediction Model Development: Phase I Final Report," NASA Contract Report 182230, December 1989.
- [2] B. L. Ferguson, G. J. Petrus and M. Ordillas, "A Software Tool to Design Thermal Barrier Coatings," NASA Phase I Final Report - Project No. 93-1-04.23-477, 1994.
- [3] W. J. Brindley, "Properties of Plasma Sprayed Bond Coats", Thermal Barrier Coating Workshop Proceedings, NASA Publication No. 3312, 1995.
- [4] R. D. Krieg, "Numerical Integration of New Unified Plasticity - Creep Formulations," SMiRT-4, M 6/4, 1977.
- [5] M. G. Natrella, Experimental Statistics, National Bureau of Standards Handbook 91, U. S. Department of Commerce, 1963.

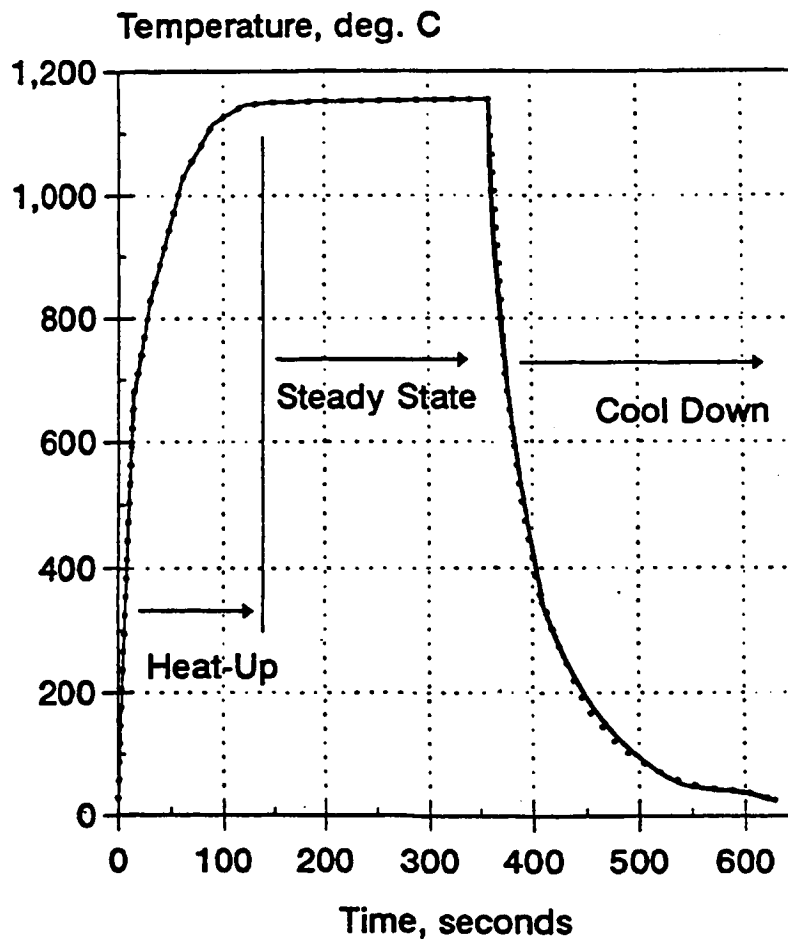
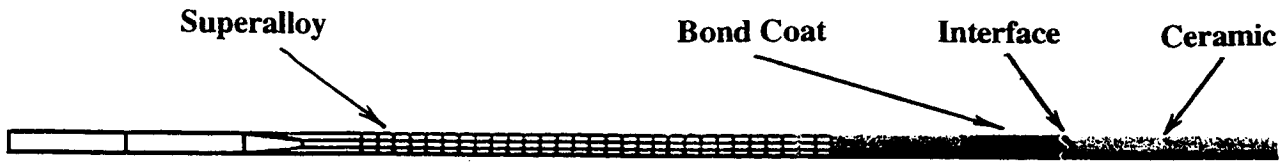


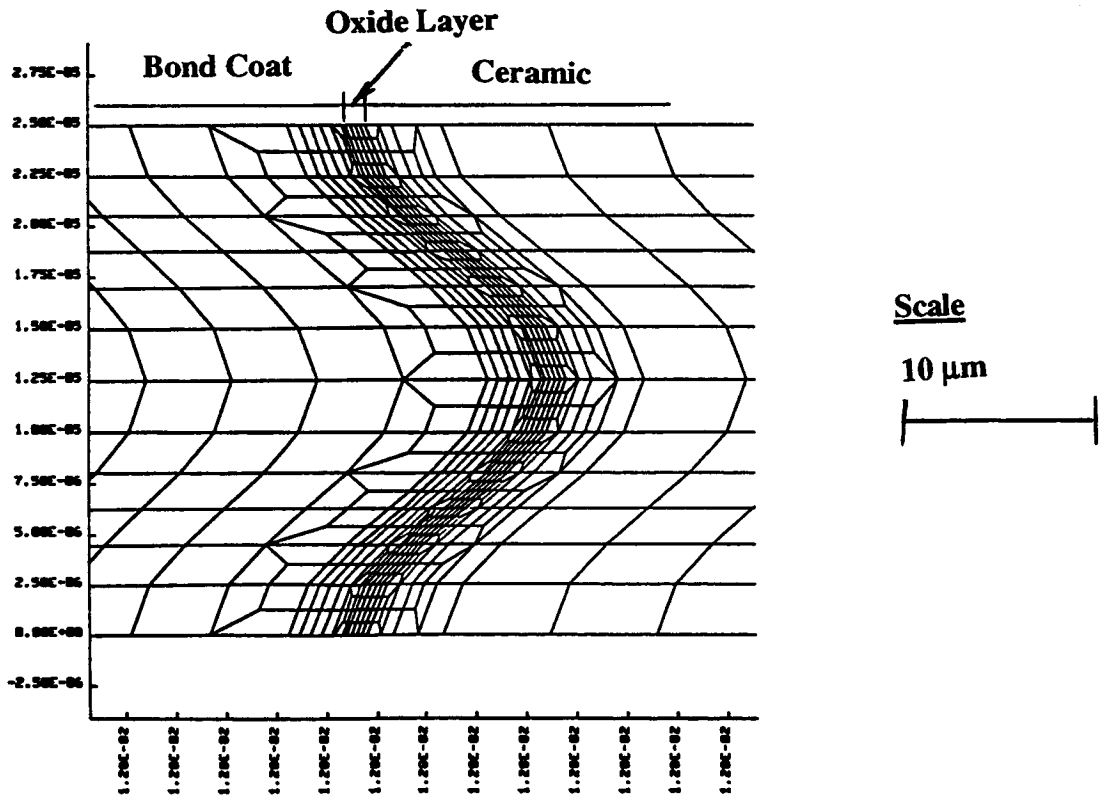
FIGURE 1 Burner Rig Test Cycle Thermal Profile used in Finite Element Model



Dimensions

- Superalloy Bar Radius: 0.0127 m (0.5in)
- Average Bond Coat Thickness: 130 μm (5.1 mils)
- Average Ceramic Coat Thickness: 250 μm (9.8 mils)

a) Overall Mesh



b) Interface Region

FIGURE 2 Mesh Geometry for TBC Oxidation Model: a) Overall
b) Interface Region

FIGURE 3

TBC Finite Element Study Parameters

5 Variables at 2 Levels

Oxidation -

1) None

2) Growth ----->

$$\text{Thickness } (\mu\text{m}) = 1.200\text{E-}04 \times (5.714\text{E}+11 \times e^{104856/RT} \times t)^{0.5}$$

Top Coat Creep Strength

1) Low -----> $\epsilon = 2.57\text{E-}08 \sigma^{1.3}$ at 1000 °C

2) High -----> $\epsilon = 2.57\text{E-}09 \sigma^{1.3}$ at 1000 °C

Bond Coat CTE -

1) Low -----> 1.400E-05 °C at 1000 °C

2) High -----> 2.000E-05 °C at 1000 °C

Bond Coat Creep Strength

1) Low -----> $\epsilon = 1.39\text{E-}07 \sigma^{3.0}$ at 1000 °C

2) High -----> $\epsilon = 1.39\text{E-}16 \sigma^{3.0}$ at 1000 °C

Roughness - (Sine Wave)

1) Low -----> Amp = 5 μm
Wavelength = 30 μm

2) High -----> Amp = 20 μm
Wavelength = 100 μm

NASA TBC - Bond Coat Oxidation Growth Curve

(Oxidation at 1433 K, Held 240 sec/cycle)

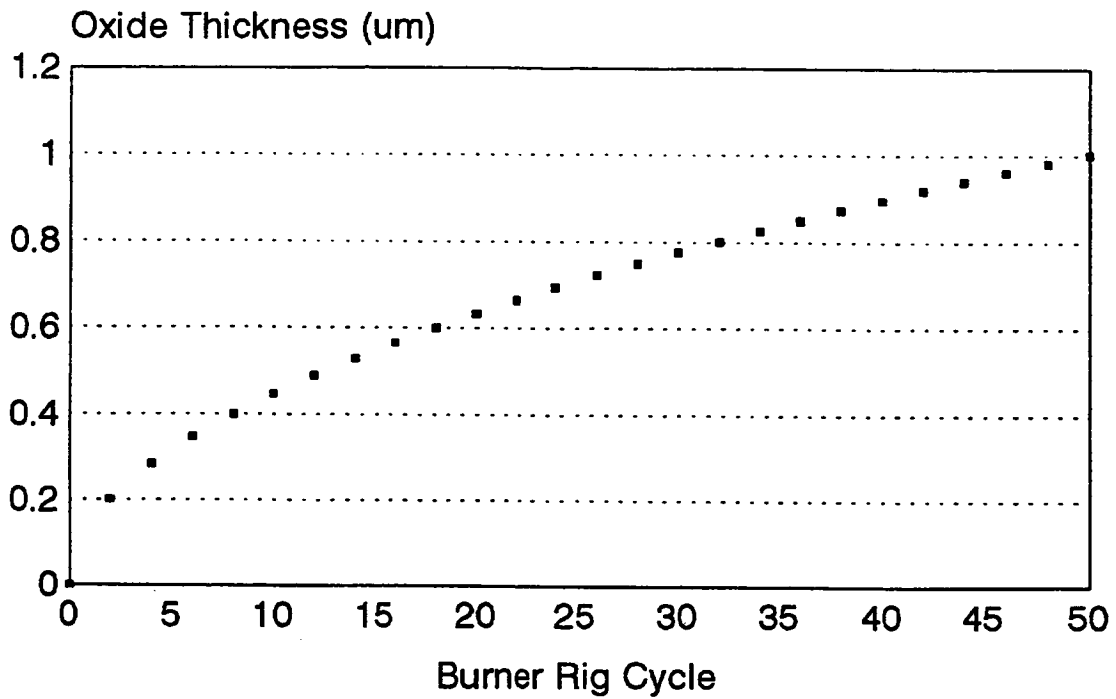


FIGURE 4 Bond Coat Oxidation Growth Curve for Al₂O₃, Held at 1433 K for 240 sec/cycle [1]

Bond Coat CTE and Oxidation Have Greatest Impact on TBC Radial Stresses at the Peak Position

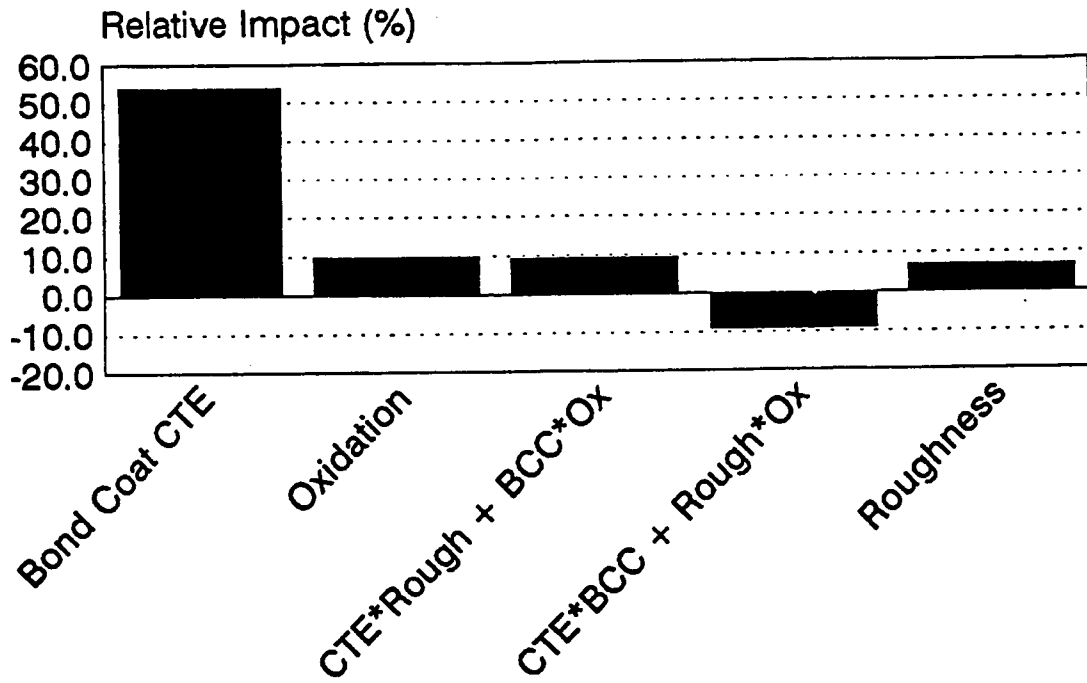


FIGURE 5 Degree of Influence of TBC System Variables on Radial Stress Response in the Ceramic at the Interface Peak

CTE Has Greatest Impact on TBC Radial Stresses at the Mid-Slope Position

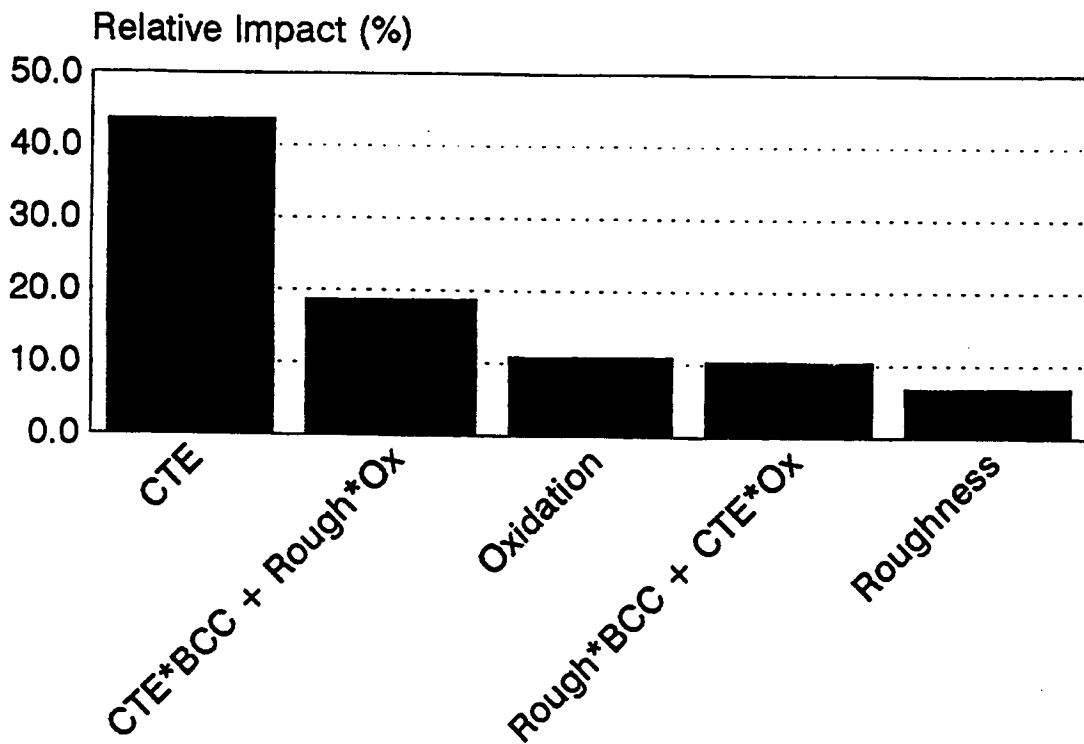


FIGURE 6 Degree of Influence of TBC System Variables on Radial Stress Response in the Ceramic at the Mid-Slope Interface Position

Bond Coat CTE, Oxidation and Bond Coat Creep Have Greatest Impact on TBC Radial Stress at the Valley Position

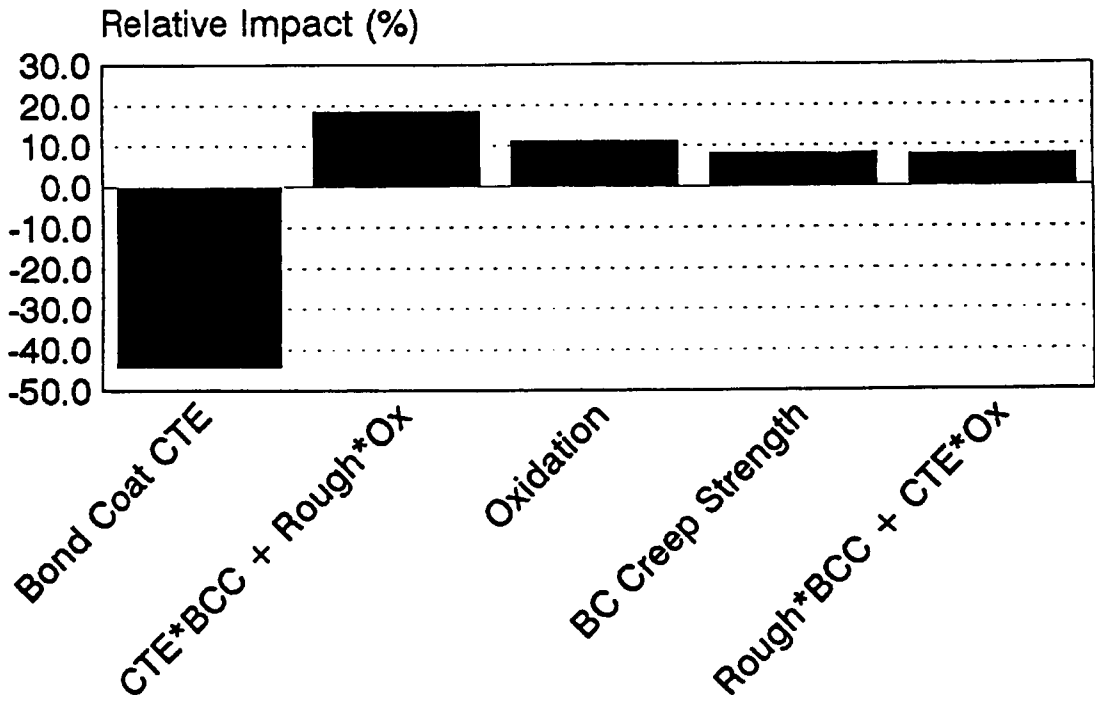


FIGURE 7 Degree of Influence of TBC System Variables on Radial Stress Response in the Ceramic at the Interface Valley Position

FIGURE 8

INVESTIGATION INTO TBC VARIABLE INTERACTIONS AND RESULTING IMPACT ON CERAMIC RADIAL STRESS

CASE 1 - OXIDATION

With and Without (Base Case Comparison)

Multiple Cycles

Birth of Single "Thick" Layer in 1 Cycle

CASE 2 - CTE

CASE 3 - BOND COAT CREEP

CASE 4 - ROUGHNESS (Single Definition)

ADDITIONAL ISSUES

GROWTH STRESS

GRADIENTS

Oxidation Increases TBC Radial Stress (Peak Position)

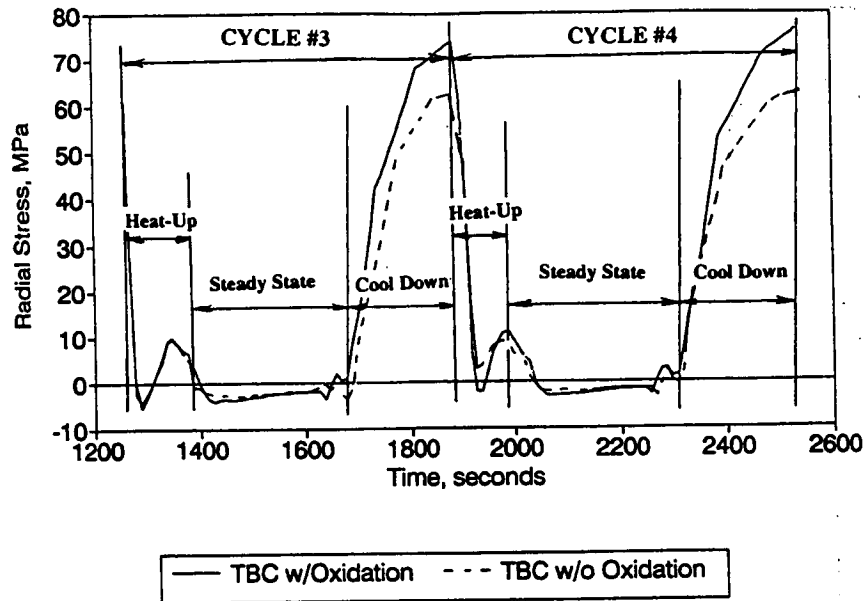


FIGURE 9 Radial Stress Time History, Comparing Ceramic Stress at the Peak in both Oxidizing and Non-Oxidizing Scenarios

Radial Stresses at Interface Peak Multiple Thermal Cycles

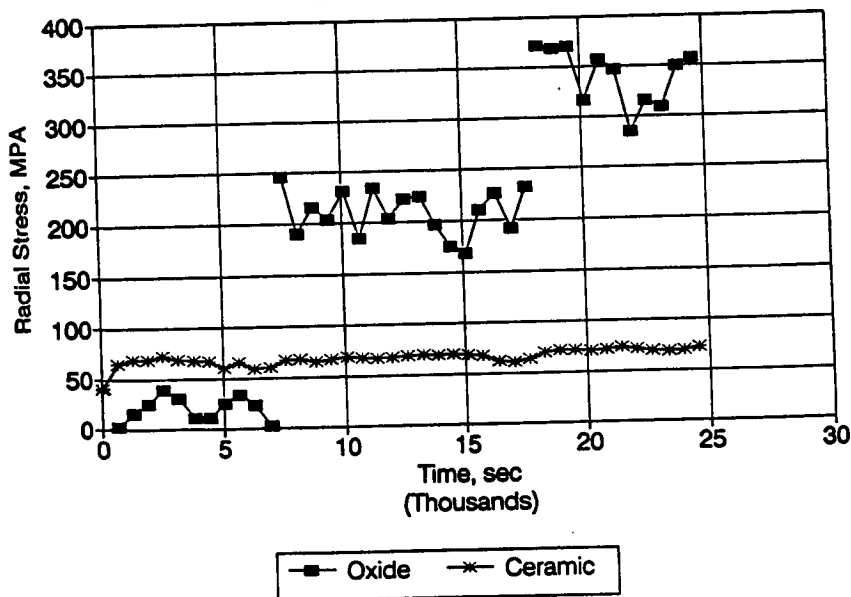


FIGURE 10 Radial Stress Behavior During Burner Rig Cool Down for Multiple Cycle Scenario

Growth of "Heavy" Oxide Layer in Single Thermal Cycle is More Detrimental than Gradual Growth

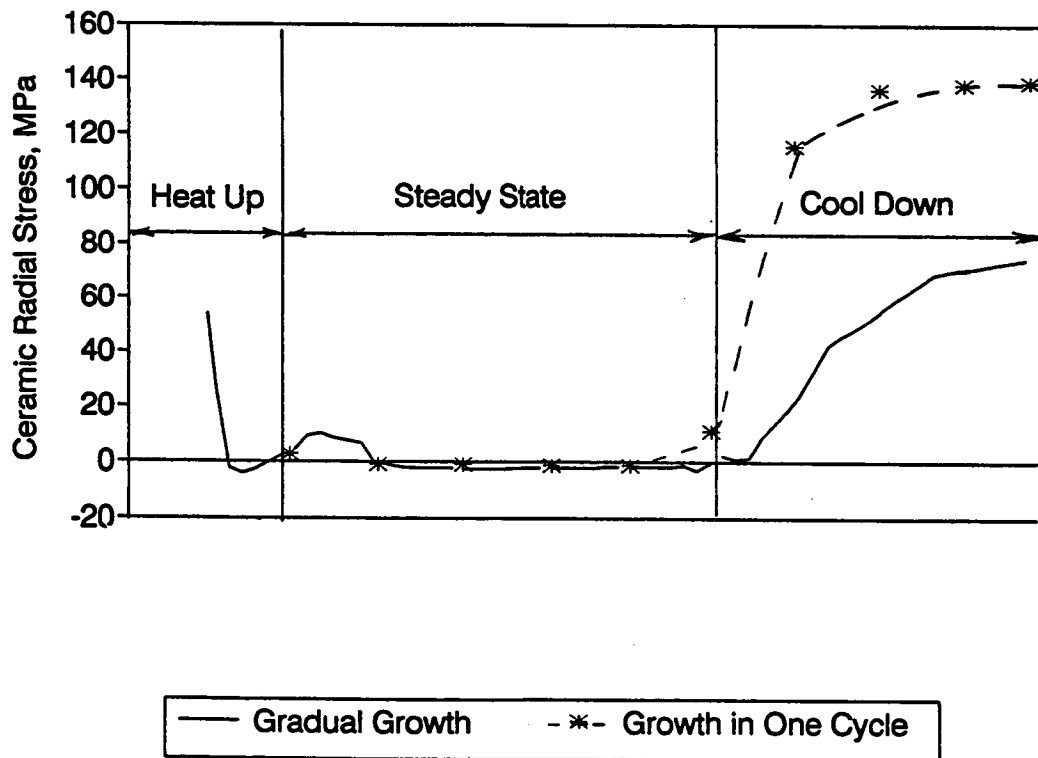


FIGURE 11 Comparison of Radial Stress Behavior at the Ceramic Peak for Multi Cycle (51) and Single Extended Cycle - Oxide Thickness is the Same ($1.0 \mu\text{m}$) in Both Cases

Increasing Bond Coat CTE Increases Ceramic Radial Stress at Peak

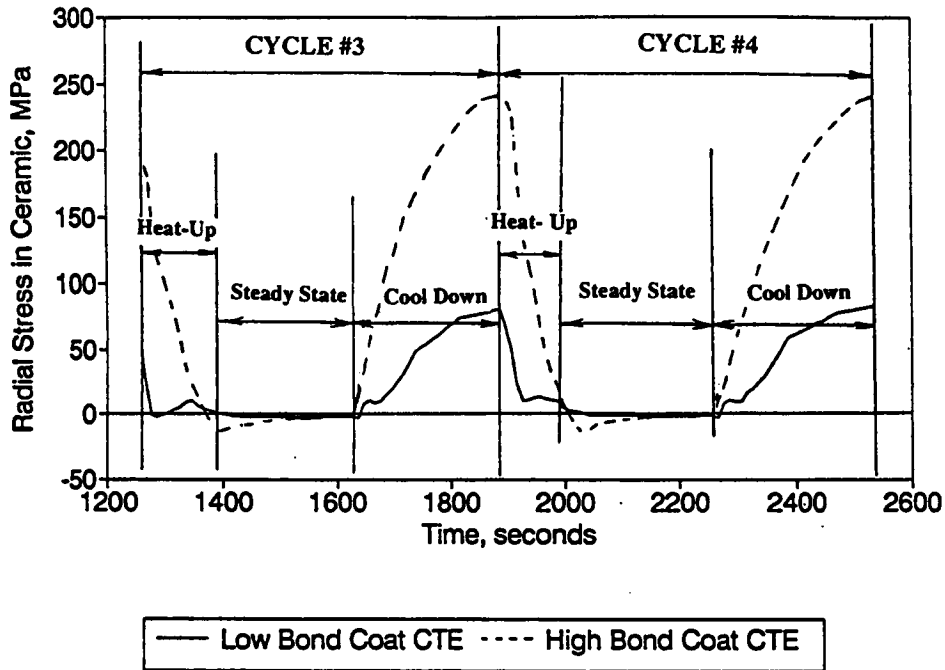


FIGURE 12 Effect of Increasing Bond Coat CTE on Radial Stress Response at the Ceramic Peak

Bond Coat CTE & Oxidation Combined Effect on Peak Radial Stress

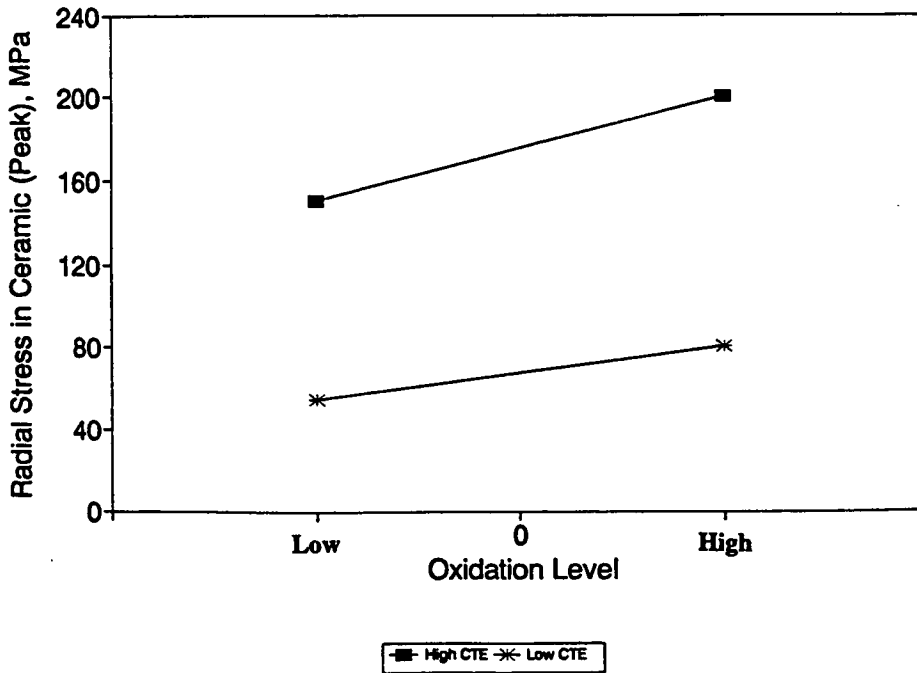


FIGURE 13 Response Curves Showing Combined Influence of Bond Coat CTE and Oxidation

**Bond Coat Plasticity Decreases
Ceramic Layer Stress at Peak Position**

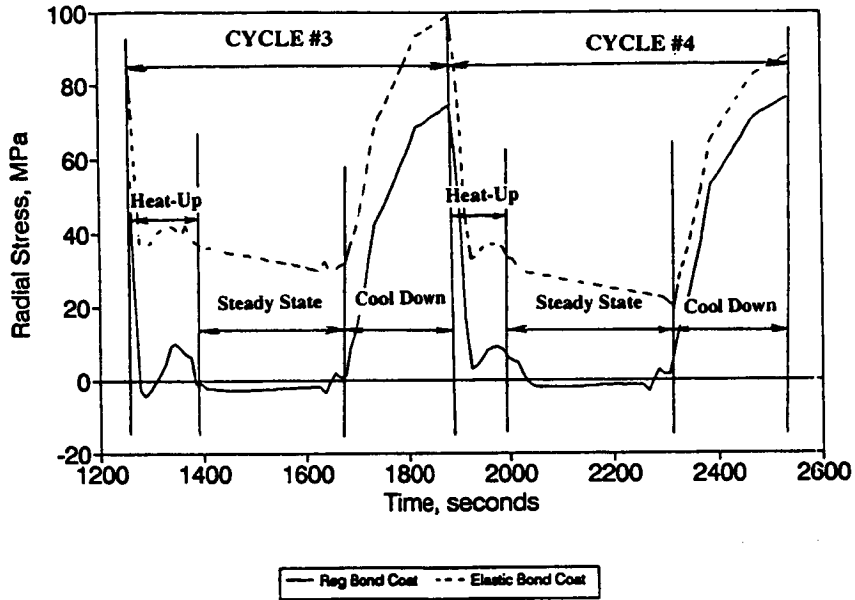


FIGURE 14 Effect of Bond Coat Creep on Radial Stress Response at the Ceramic Peak in an Oxidizing System

**Bond Coat Creep & Oxidation
Combined Effect on Peak Radial Stress**

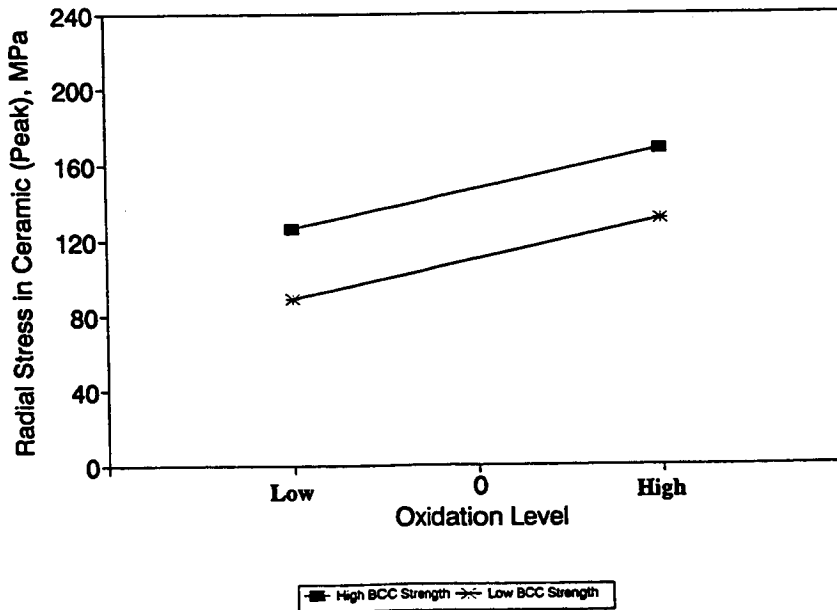


FIGURE 15 Response Curves Showing Combined Influence of Bond Coat Creep and Oxidation

High Roughness Increases TBC Radial Stress (Peak Position)

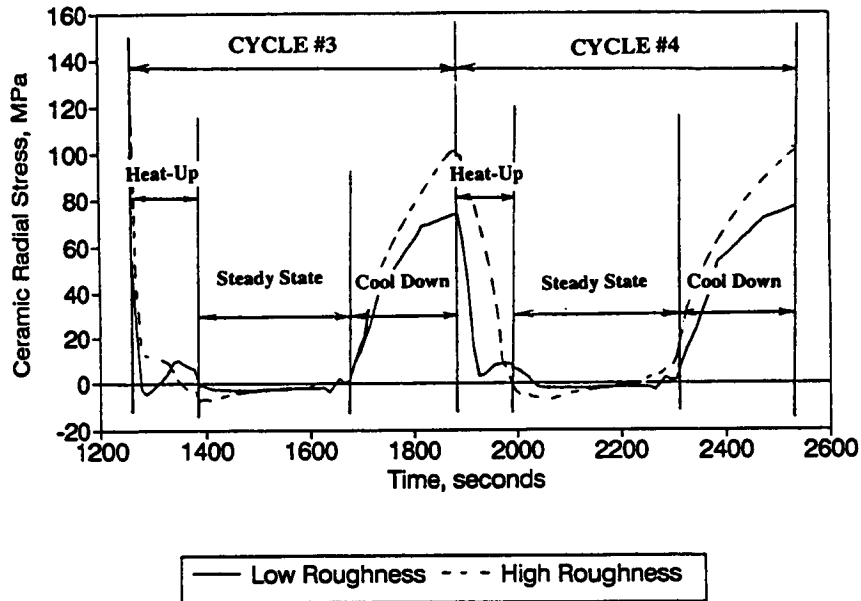


FIGURE 16 Effect of Increasing Interface Roughness on Radial Stress Response at the Ceramic Peak in an Oxidizing System

Interface Roughness & Oxidation Combined Effect on Peak Radial Stress

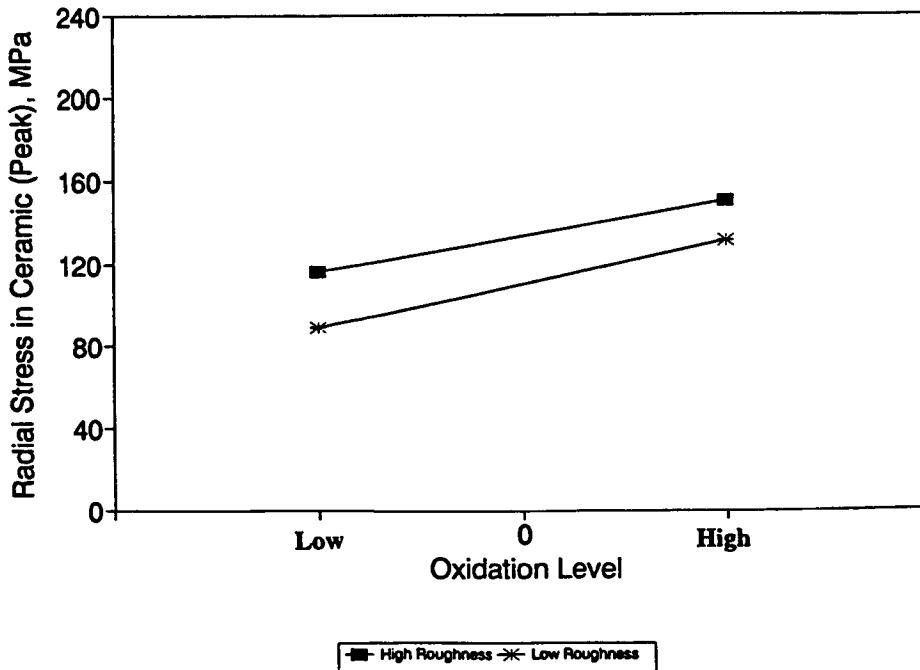
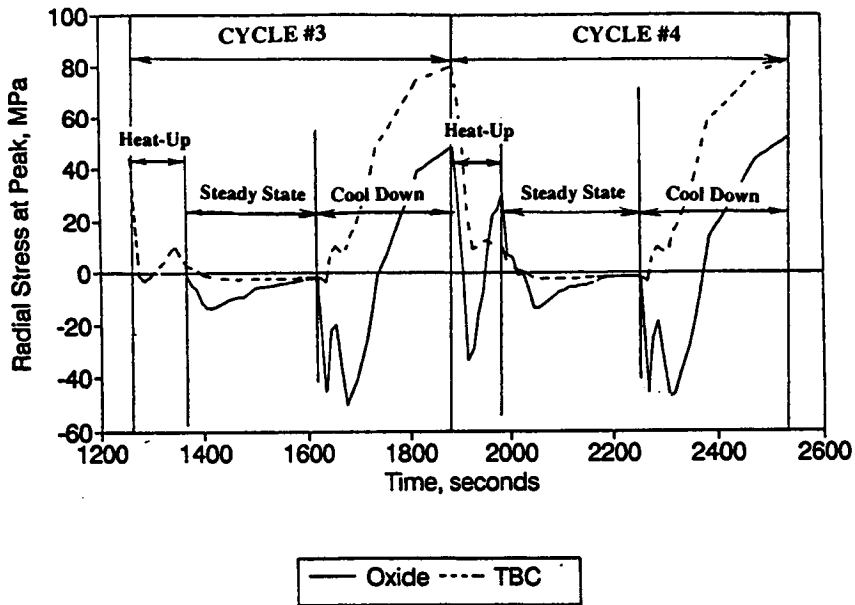


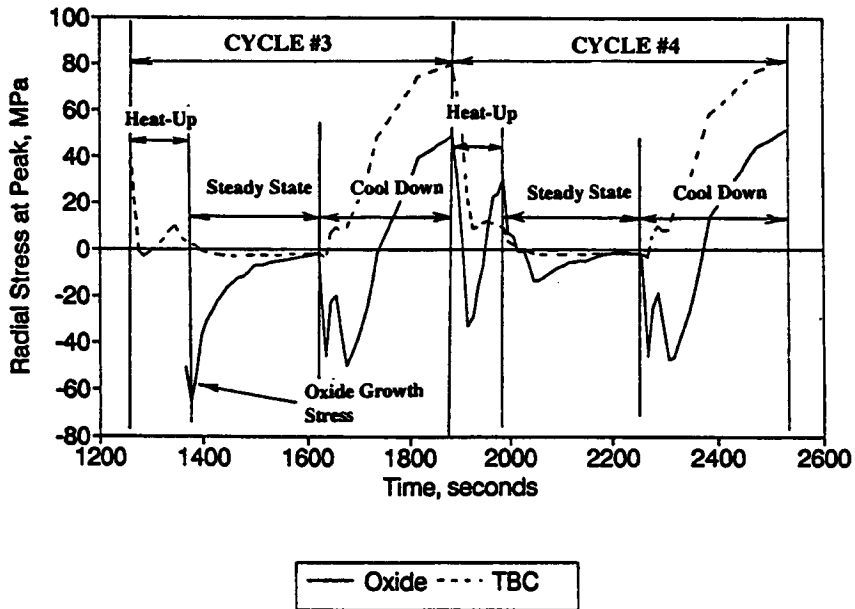
FIGURE 17 Response Curves Showing Combined Influence of Interface Roughness and Oxidation

Low Roughness Oxidation Model
Bond Coat/Oxide Same Expansion



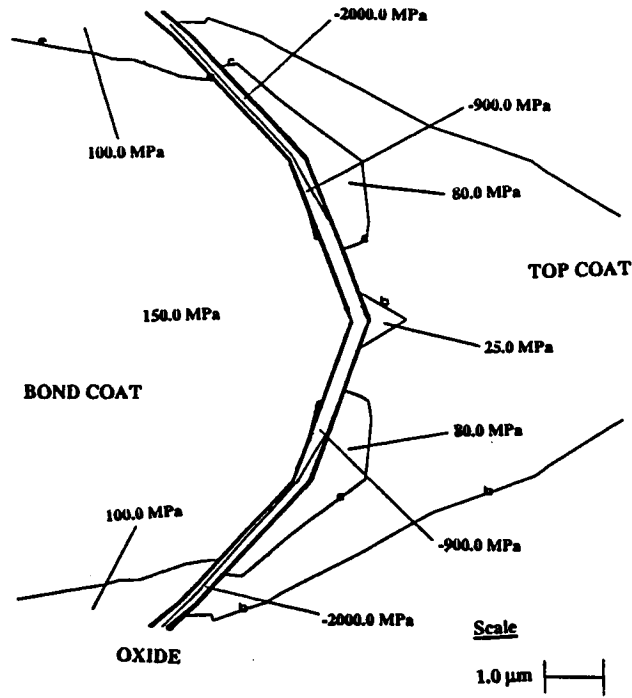
a) Bond Coat/Oxide with Same Expansion

Low Roughness Oxidation Model
Oxide Expands During Formation

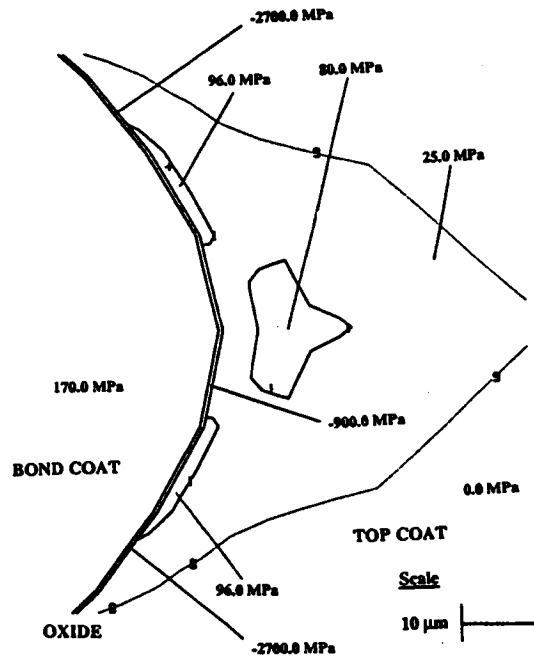


b) Oxide Expands During Formation

FIGURE 18 Effect of Bond Expansion during Oxidation on Ceramic Stress at the Peak

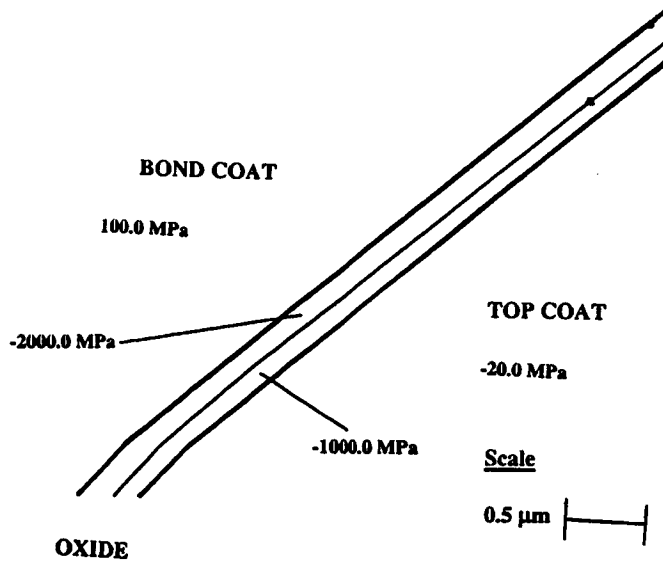


a) Low Roughness

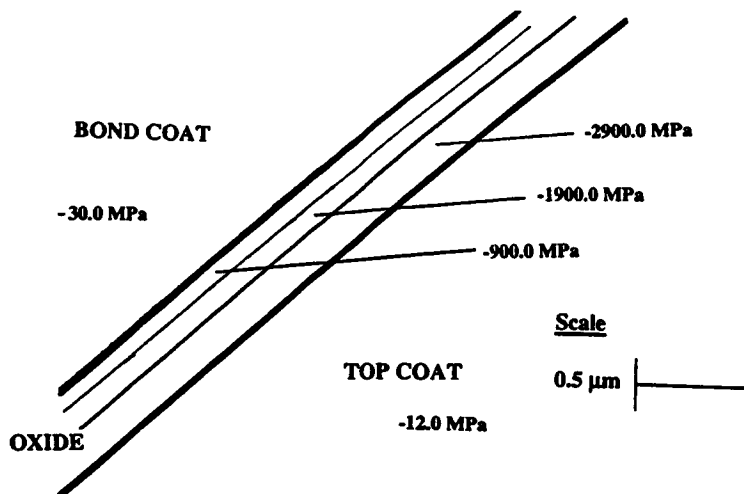


b) High Roughness

FIGURE 19 Ceramic-Oxide Radial Stress Gradients at the Interface Peak



a) Low Roughness



b) High Roughness

FIGURE 20 Ceramic-Oxide Radial Stress Gradients at the Mid-Slope Interface

INFLUENCE OF CYCLIC STRAIN ON PVD TBC LIFE

P. Kennard Wright
GE-Aircraft Engines
Cincinnati, OH

Introduction

Thermal barrier coatings are increasing in application in turbine engines because of their ability to reduce the temperature and extend the life of air cooled parts. However, if the coating does not remain adherent to the part, but spalls off, then its function is lost. As turbine designers grow increasingly reliant on TBC's, the consequence of such spalling increases. The factors contributing to spalling have been studied for many years, and significant efforts have been directed at developing quantitative models for predicting when spalling is likely to occur [1, 2, 3, 4]. These models involve the oxidation which occurs at the interface between the ceramic and its bond coat, and the stress or strain developed in the coating from several sources. However, the effect of such strains has never been directly quantified, but only inferred from thermal analyses of laboratory specimens tested without external stress. The objective of this study was to directly determine the effect of strain on life of an EB-PVD thermal barrier coating so that strain effects could be incorporated into coating life models.

Approach

The approach adopted was to develop and apply a test which simultaneously applied thermal and external mechanical strains to a TBC'd specimen. By independently varying the applied mechanical strain range in the presence of a fixed thermal strain and oxidation history, we were able to isolate the effect of strain under conditions which were felt to be reasonably representative of engine application.

This was accomplished by building a special thermal-mechanical fatigue (TMF) test rig (Figure 1) at a subcontractor, Martest, Inc. of Cincinnati. Features of this rig which were different from conventional TMF rigs were:

- a) Specimen heating was accomplished using a silicon carbide igniter furnace which delivered heat primarily to the outer surface of the TBC rather than to the metallic substrate, as would an induction heated system. The furnace was programmed to heat, hold at maximum temperature, and shut down, and open up to permit rapid cooling of the specimen.
- b) Monitoring of the coating surface using a video camera coupled with a system of mirrors to permit viewing both the front and back sides of the specimen. The specimen could be viewed during the cooldown portion of the cycle when the furnace was open. This permitted an accurate measurement of cycles to spall without continual manual inspection.

An extensometer was mounted on the gage section of the specimen to measure specimen strain, and cooling air was used to cool both the exterior and interior of the specimen. Specimens were fabricated from a single crystal superalloy, Rene N5, into a hollow cylindrical shape with a wall thickness of 30 mils, as shown in Figure 2. The samples were then coated with a bond coat of platinum aluminide and a ceramic top coat of yttria-stabilized zirconia using the physical vapor deposition facility at GE. The resulting final microstructure is shown in Figure 3. Some samples were given an additional 2000°F, 100hr. treatment in air prior to testing. Load was applied to the specimens through grips threaded onto the ends.

The thermal and mechanical strain cycles used are shown in Figure 4. The specimen was heated from minimum temperature (usually 170°F) to 2075°F in 2 minutes, held at 2075°F for 2 to 5 minutes, and then cooled to T_{\min} in 3 minutes. Two different types of mechanical cycles were applied in conjunction with this thermal cycle. One type of cycle was in-phase, that is, the strain increased from maximum compression as the temperature increased, was held at zero as temperature was held at its maximum, and decreased again (into compression) as temperature decreased. Note that this cycle produces maximum compression at minimum cycle temperature. The other cycle type was out-of-phase, with the strain changing in opposite direction to the temperature. This produced maximum compression at maximum cycle temperature, with no compression at minimum temperature. Both cycle types were performed with several different mechanically applied strain ranges for a constant thermal cycle. A few tests were also performed with no applied strain (thermal cycling only) and with higher minimum cycle temperatures (300, 450 and 1000°F). In addition to the TMF tests, a few isothermal compression tests were performed at 170°F, the minimum cycle temperature. These tests were intended to determine the one-cycle spalling strain capability of the coating.

Results

Most of the tests produced coating spalling after various numbers of cycles (or hours). A variety of spall geometries were observed, a sampling of which are shown in Figures 5 and 6. Some of the spalls, as shown in Figure 5, had a splintered appearance with cracking in both the axial and circumferential directions. Others, as shown in Figure 6, had no particular preferred directions. No trend of spall appearance vs. test conditions could be noted. In no cases were tests terminated by substrate failure.

As expected, the interface between the ceramic and the bond coat developed an oxide scale during testing, as shown in Figure 7. It was typically cracked, both within the scale itself and at the interfaces with the ceramic and the bond coat. Oxide scale thickness were measured after coating spalling and these are shown in Figure 8. The scale thickness appeared to increase with a $t^{1/2}$ dependence as expected. Samples which were pre-oxidized followed the same trend as those which were not, indicating that the oxidation process was not dependent on the mechanical cycling or its details. No critical oxide thickness for spalling could be identified.

The dependence of coating life (cycles to spall) on applied mechanical strain is shown in Figure 9. For reasons to be shown below, the in-phase (max. compression at min. temperature) tests have been plotted as negative strain range, tests without applied strain as zero, and out-of-phase tests as positive strain range. The 1 cycle compression tests at minimum temperature are also plotted on the same graph. There is a clear trend that with increasing compressive (negative) strain range the coating life is shortened. Samples which received prior exposure exhibited shorter life (about 1/2) than the unexposed samples. Several of the longer tests failed for other reasons than coating spalling (thermocouple and thread failures) and so they are plotted with arrow indicating longer life. The compression test (1 cycle) of the unexposed sample (filled circle) failed by specimen buckling before the coating spalled, so it also is indicated with an arrow pointing to higher strain.

The reason for the strain sign convention above is that in addition to the mechanical strain, $\Delta\epsilon_m$, being imposed on the coating, there is a thermal expansion mismatch strain, $\Delta\epsilon_{th}$, being applied as well, due to the difference in thermal expansion coefficient between the various coating constituents and the superalloy substrate. Since the thermal expansion of the ceramic and the oxide are smaller than that of the superalloy, during cooldown from a

relatively low stress high temperature condition, the strain or stress imposed on the coating will be compressive. During in-phase TMF cycling, the compressive mechanical strain being applied at low temperature adds to the thermal strain (Figure 10), producing a larger total strain range, $\Delta\epsilon_{tot}$. Since the spalling of the ceramic is a buckling type failure, it should be sensitive to the maximum level of compression during thermal cycling, which is produced in this case at minimum temperature. During out-of phase cycling, Figure 11, the applied mechanical strain range is of opposite sign than the thermally generated strain range, so when the two are added to obtain the total strain range on the coating, the result is a lower total strain range. The maximum compression is still at minimum temperature, but its magnitude is smaller and so the coating withstands more cycles before spalling.

The results from the two types of TMF tests can be combined into one plot using this total strain concept. Figure 12 shows the total strain on the oxide scale in the direction of maximum strain, assuming it to have the thermal expansion properties of bulk alumina. Without any applied mechanical strain, this thermal expansion would produce about 0.8% strain (compression) when cooled from 2075°F to 170°F (indicated on the graph as "thermal mismatch strain"). In-phase cycling, as well as the 170°F compression tests, produce larger total strain levels, and lower coating lives. Out-of-phase cycling produces a maximum strain equal to the thermal strain in the transverse specimen orientation and did not lead to longer life. The effect of increasing the minimum cycle temperature is to reduce the thermal (and thus the total) strain range. The dependence of cycles-to-spall on total strain range appears to fit a simple power law form $N_f = k(\Delta\epsilon)^n$ reasonably well. The value of the exponent is between -3 and -4, not a very large value for a ceramic system.

Summary & Conclusions:

In summary, a TMF test has been developed which has permitted a direct measurement of the effect of strain on TBC life. Testing on EB-PVD coated single crystal superalloy samples was performed under a variety of imposed strain cycles, including in- and out-of phase cycling between fixed temperature extremes. An oxidizing pre-exposure was found to shorten life compared to unexposed samples. A distinct dependence of coating life on applied strain was seen, for which the governing factor appearing to be the extent of compression at minimum cycle temperature. Cyclic conditions which produced higher amounts of compression at minimum cycle temperature reduced the coating life. The results were evaluated in terms of the maximum total (thermal mismatch + applied mechanical) strain on the oxide scale and a power law dependence with an exponent of about -3 appears to describe the life capability.

References

1. Hillery, R.V., Pilsner, B.H., McKnight, R.L., Cook, T.S., and Hartle, M.S., "Thermal Barrier Coating Life Prediction Model Development", Final Report, NASA CR-180807, Nov, 1988.
2. Meier, S.M., Nissley, D.M., and Sheffler, K.D., "Thermal Barrier Coating Life Prediction Model Development", Phase II, Final Report, NASA CR 189111, July 1991.
3. Strangman, T.E., Neumann, J., And Liu, A. "Thermal Barrier Coating Life-Prediction Model Development", Final, Report, NASA CR-179648, Oct. 1987.
4. R. Miller, "Oxidation-Based Model for Thermal Barrier Coating Life", J. American Ceramic Society, Vol. 67, No. 8, Aug. 1984, pp. 517-521.

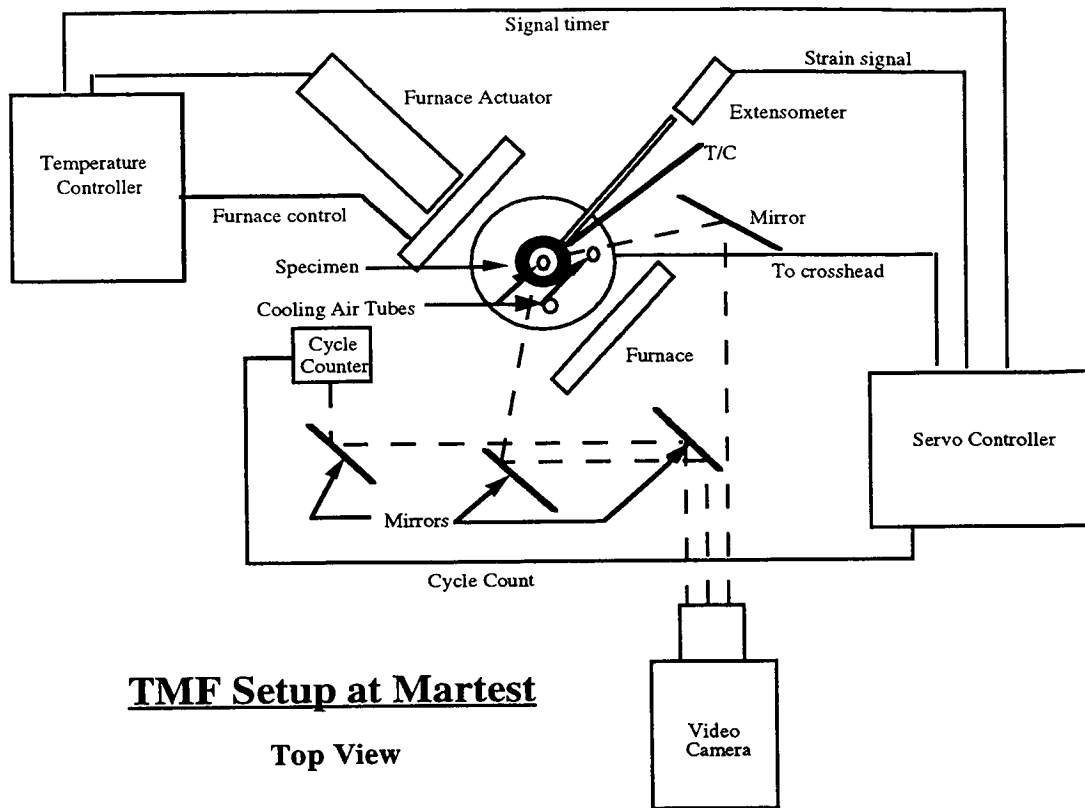


Figure 1 - Test setup developed at Martest, Inc., for use in thermal mechanical fatigue testing TBC coated specimens.

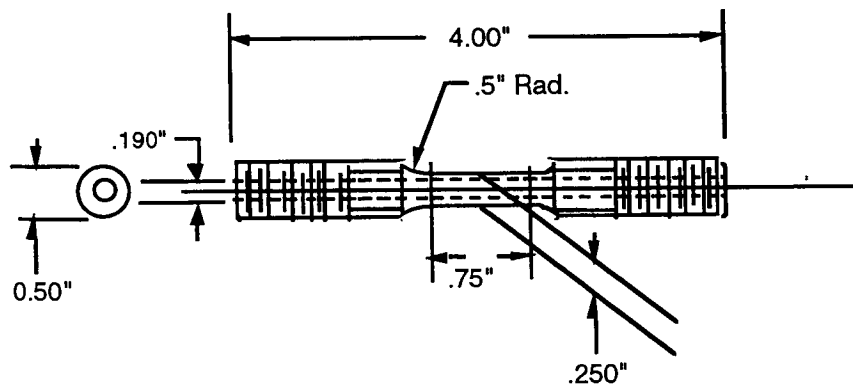


Figure 2 - Hollow cylindrical test specimen configuration used in establishing strain effects on TBC life.

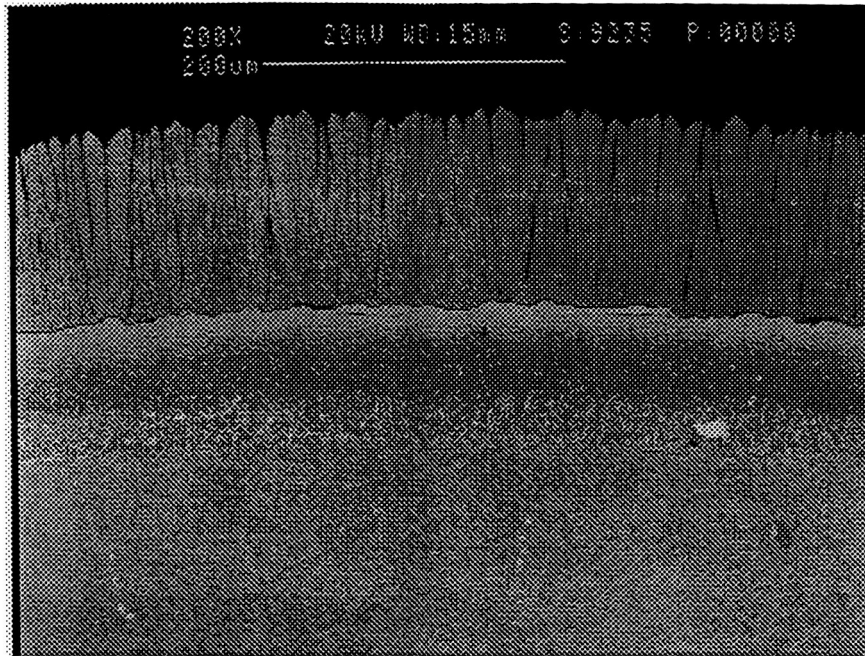


Figure 3 - Microstructure of EB-PVD coating on Pt-Al bond coat and Rene N5 substrate.

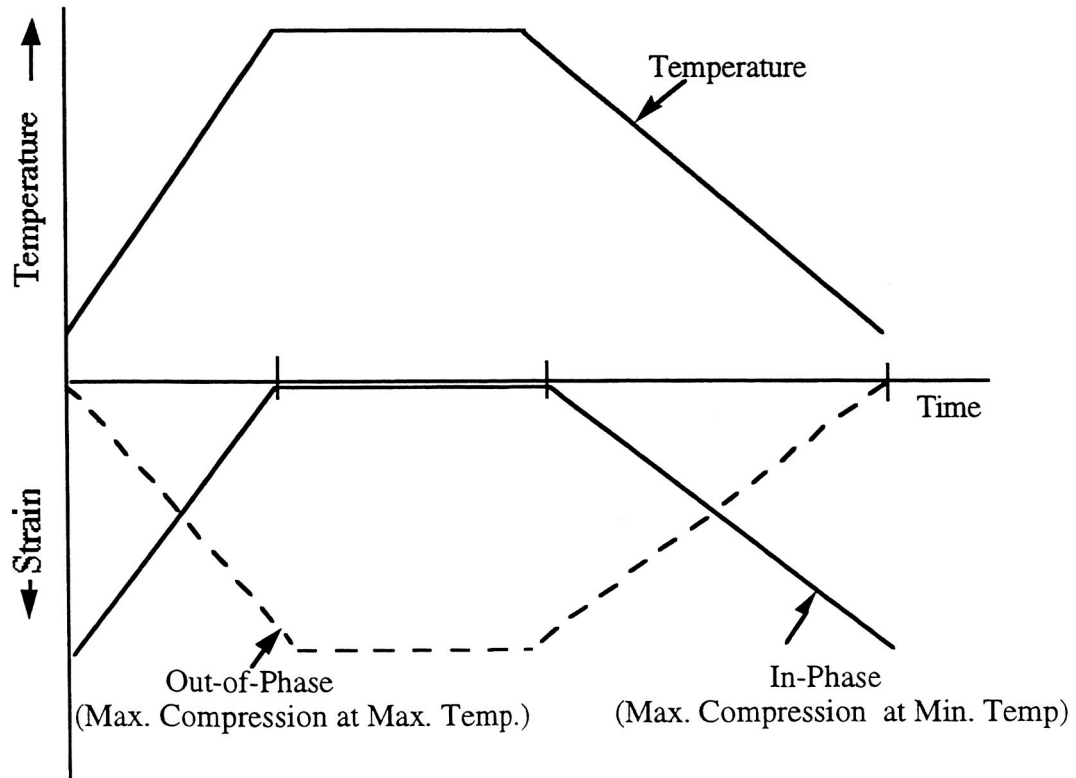


Figure 4 - In-phase and out-of-phase thermal and mechanical strain cycles were used in determining strain effects on TBC life.

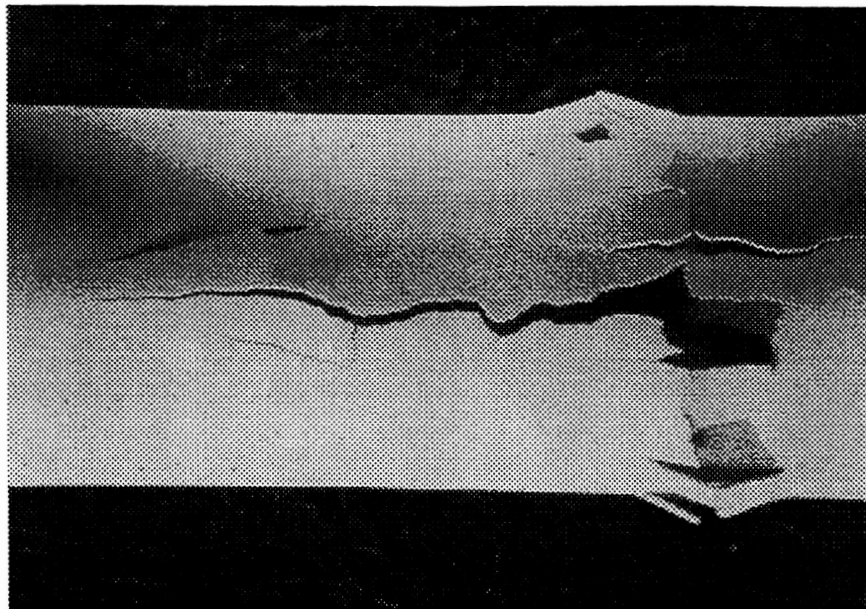


Figure 5 - A spall showing splintered appearance from multiple axial coating cracks. Splintering was absent on most spalls.

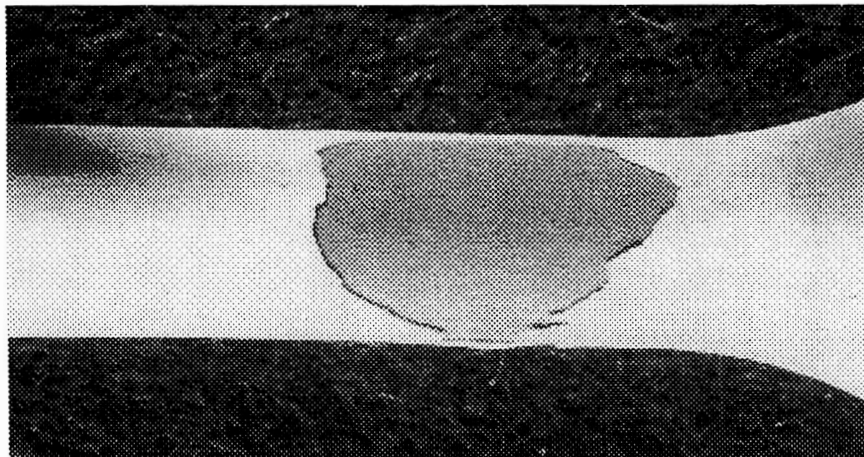


Figure 6 - Large, more typical irregularly shaped spall

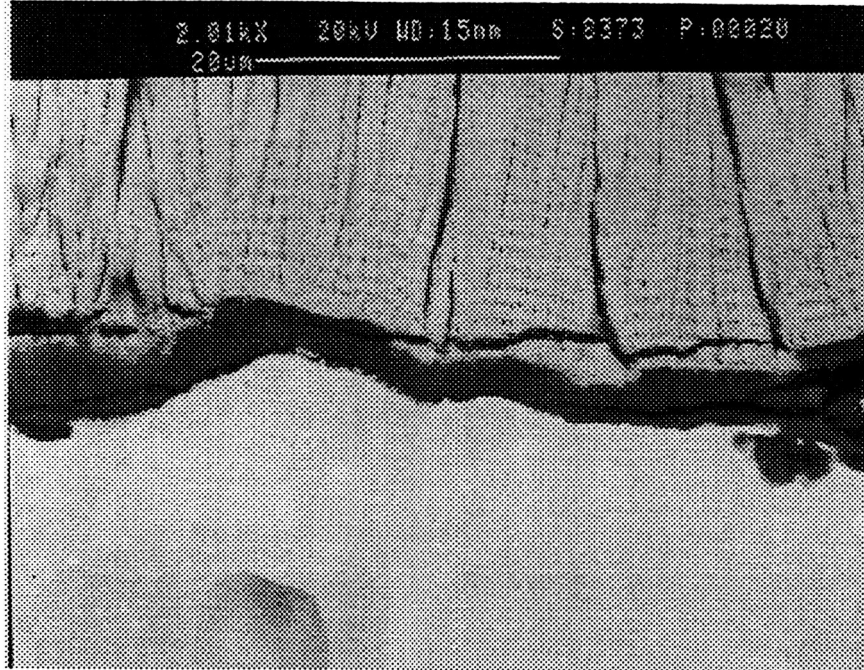


Figure 7 - Oxide scale formed at the interface between the top coat and bond coat. Scales were typically cracked internally as well as at both interfaces after testing.

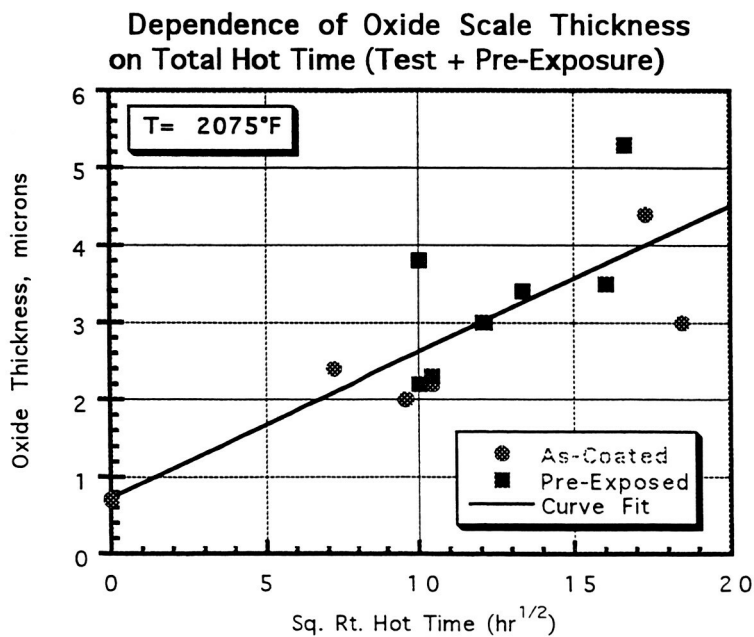


Figure 8 - Oxide scale thicknesses at spalling appeared to follow a parabolic time dependence, independent of strain history.

TMF of EB-PVD TBC on Rene N5
(165-2075°F)

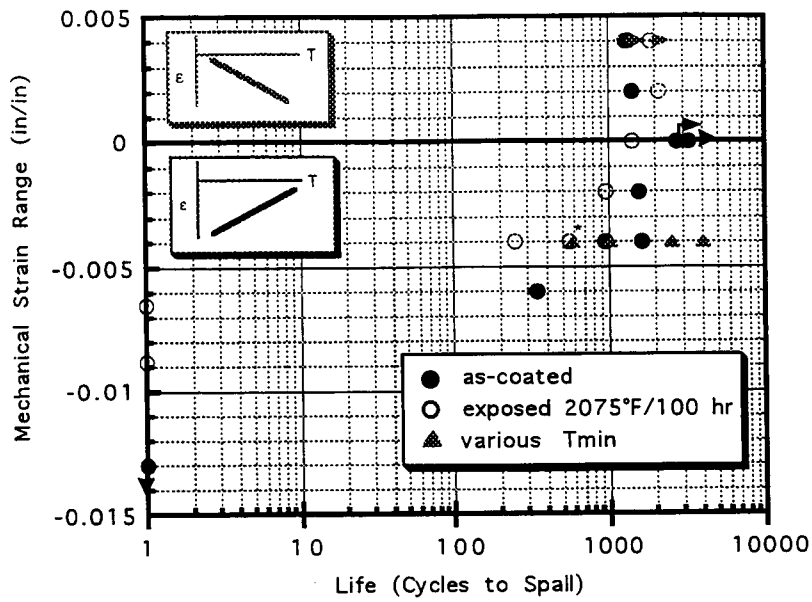


Figure 9 - Effect of applied mechanical strain range on PVD TBC life for a 170°F to 2075°F cycle.

Thermal + Mechanical Strain Summation in TMF Test

Maximum Compressive Strain at Minimum Test Temperature

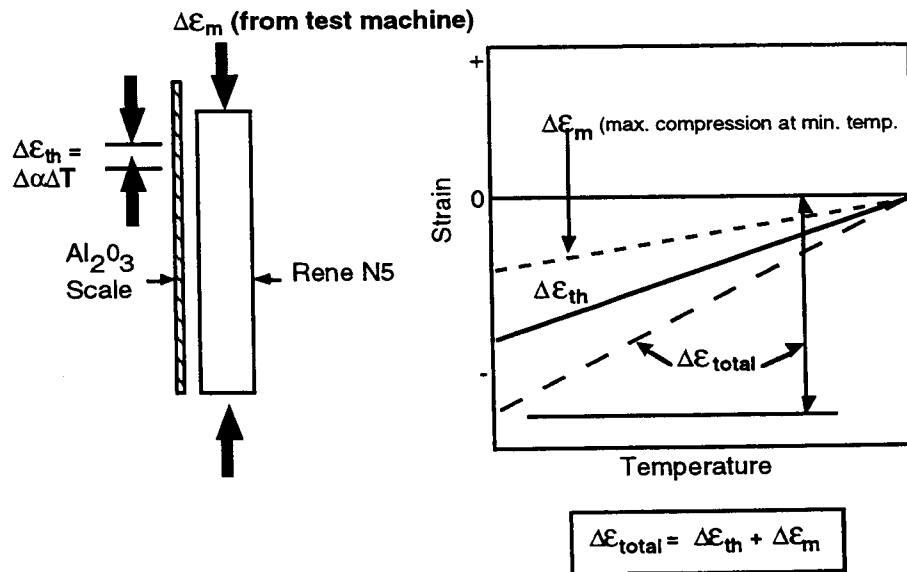


Figure 10 - Summation of thermal plus mechanical oxide scale strain ranges for in-phase TMF cycling to achieve total oxide scale strain range.

Thermal + Mechanical Strain Summation in TMF Test

Maximum Compressive Strain at Maximum Test Temperature

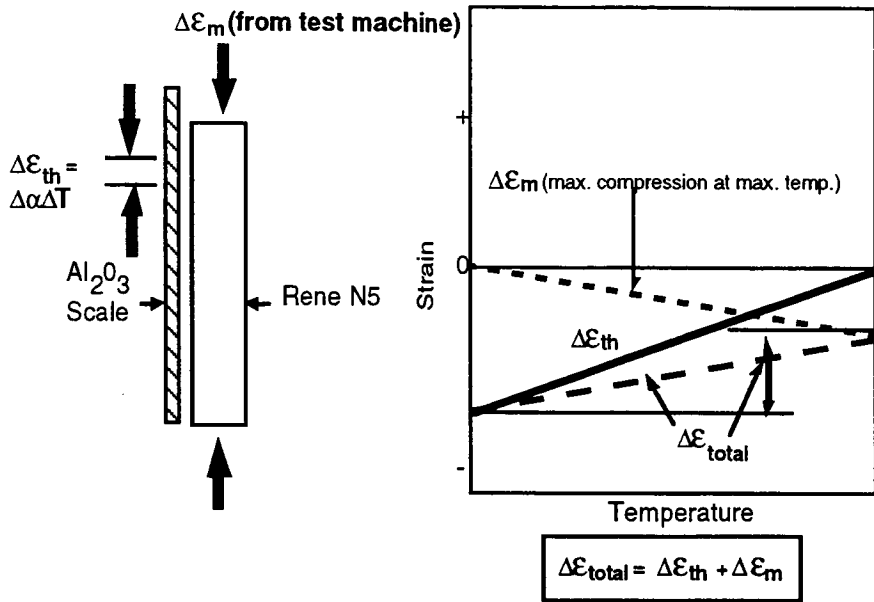


Figure 11 - Summation of thermal plus mechanical oxide scale strain ranges for out-of-phase TMF cycling to achieve total oxide scale strain range.

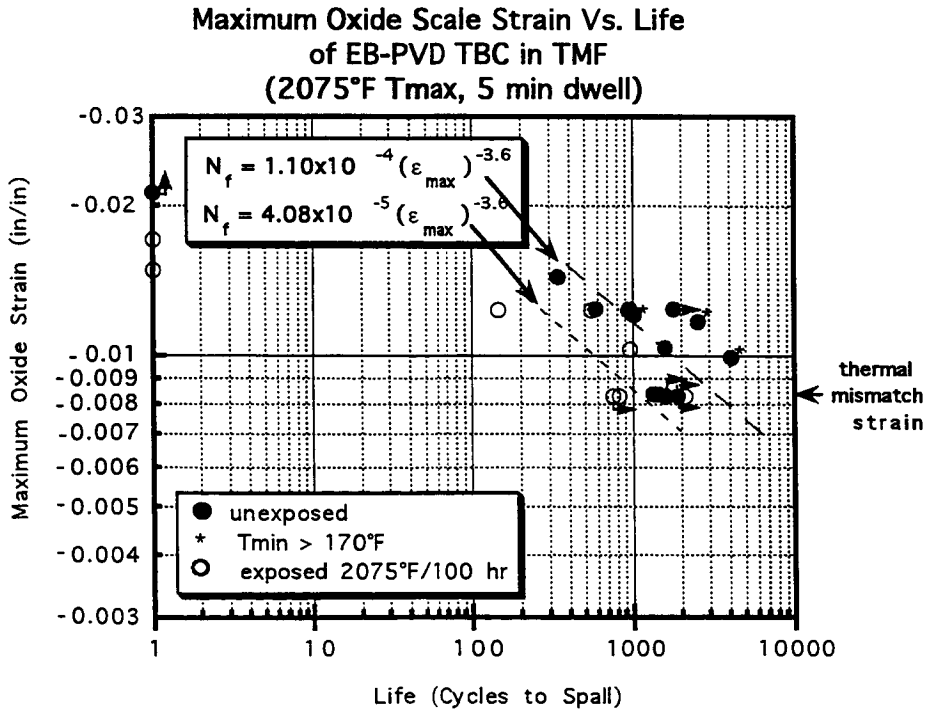


Figure 12 - Dependence of PVD TBC spalling life on maximum oxide scale strain.

Industrial Environment-Hot Corrosion -TBC- Interactions
Extended Abstract

Norman S. Bornstein, and William P. Allen,
United Technologies Research Center
Mladen Trubeljia and David M. Nissley
Pratt & Whitney Aircraft Company

Introduction

Thermal barrier coatings afford protection and allow turbine components to operate more efficiently. Historically the ranking of coating systems is based upon accelerated laboratory tests. The approach taken is that the environment and/or exposure conditions are made more aggressive than that expected in service. Acceptance implies a complete understanding of the processes that govern materials behavior. Without this knowledge there is no basis for prediction and no means for assessing or limiting the uncertainty of a prediction. This paper describes the strengths and weakness of the current test procedures, and outlines a procedure that duplicates field results.

Background

Sodium sulfate is the principle constituent of the corrosive salts found on the surfaces of industrial and marine gas turbine components [1]. The corrosion microstructure most frequently observed in the field (type I) is duplicated in the laboratory by (1) application of thin films ($0.1-1.0 \text{ mg/cm}^2$) of sodium sulfate (TGA studies), (2) doping of fuels with oil soluble sodium compounds (burner rig studies) or (3) the introduction of a sea salt solution into the air or the exit nozzle of a laboratory jet burner. The type II microstructure is reproduced in the salt laden burner rig tests by artificially increasing the partial pressure of the oxides of sulfur in the combustion gases. It is often stated that Type I is associated with high temperatures (800C and above), whereas Type II occurs primarily within the temperature range from 650 to 775C. Thus the two forms of corrosion are distinguished principally by the metallographic appearance of the corrosion.

Gupta et al [2] recently reviewed the factors controlling the gas turbine hot section environment and their influence on hot salt corrosion test methods. They concluded that laboratory test results do not correlate well with actual service experience, and often lead to damage morphologies that substantially differ from those experienced in engines. According to the authors "the understanding of the corrosion factors is an essential precursor to the development of realistic test methods for durability analysis of high temperature materials".

Bornstein and his associates [3,4] revisited the chemistry of gas turbine salt deposits. They examined that composition of the salts that adhere to the high compressor components as well as the composition of the salts on the interior and exterior surfaces of turbine components and measured the quantity of salts that deposited on the various turbine stages (table 1; figs 1,2). The authors concluded that the principle mode of

deposition of the corrosive salts is by impaction rather than equilibrium condensation. Supporting evidence is (1) the similarities in chemistry between compressor and turbine deposits; (2) identical chemistries for salts removed from internal passageways and the airfoil, (the interior cavities are not subjected to combustion air and are cooled by compressor air), and (3) the salt deposition pattern which clearly reveals that the deposition is independent of surface temperature, fig 3. Equally important but not explained is the observation that the ratio of sodium to potassium in the deposits differs significantly from the principle source of the salts. The molar ratio of sodium to potassium in sea salt is 0.003 while the ratios observed on compressor and turbine components are comparable and close to two orders of magnitude greater than that for sea salt. Most importantly however is the demonstration that the type I and type II morphologies are caused by the same salt, and the composition of the salt is unstable in common laboratory burner rig tests.

Experimental Procedure

The duplication of corrosion morphologies requires a working knowledge of the roles of each of the corrodents. Of particular importance is the role of magnesium sulfate. Based upon the available data, at the temperatures of interest, magnesium sulfate is not a stable compound. At elevated temperatures magnesium sulfate "roasts" to form magnesium oxide and the oxides of sulfur.

The equilibrium phase diagram for the ternary system $MgSO_4-CaSO_4-Na_2SO_4$ (13) is reproduced in Figure 4. Two phases are liquids within the temperature range of operation of industrial gas turbine engines. The ternary eutectic, applied as a thin film onto the surfaces of nickel base superalloy coupons, duplicates the corrosion morphologies of type I and type II. The type II corrosion morphology shown in figure 4, is produced when the specimens are exposed for 6hrs at 750C. In the field, both morphologies, type I and type II, can be found on the same component, fig 5.

Experimental Procedures and Results

The eutectic salt composition defined in figure 4, was applied, together with the indigenous oxides associated with industrial environments, onto various TBC compositions under consideration in the ATS program. The specimens were exposed for 6 hours at 1200C, after which they were cooled to room temperature. Many specimens exhibited spallation of the TBC and subsequent corrosion of the bond coat. The result of application and exposure of coated specimens is shown pictorially in figure 6. The "gob" of corrodent penetrated and caused the TBC to spall, fig 6a. The gob, liquid at the test temperature, penetrated through the TBC, fig 6b. The liquid corrodent also attacked the bond coat, figure 6c.

The liquid corrodent wets and attacks the yttria stabilized zirconia as shown in fig.7. Also shown are partial results of the on-going chemistry studies. In back scatter mode (BSE), the denser zirconia appears white while the darker area are the less dense solidified corrodent. Also shown are the characteristic x-rays for the elements zirconium

and yttrium. It appears that the corrodent leaches yttria from the zirconia matrix. Lastly, as shown in fig. 8, the corrodent attacks the bond coat. Surprisingly, although sulfur is a major component of the as applied corrodent, there is no optical evidence of sulfides present in the scale or the alloy depleted zone within the bond coat.

References

- 1 Bornstein, N. S. JOM Nov 1996 p37
- 2 Gupta, A. K., J. P. Immariegeon and P.C. Patnaik High Temperature Technology vol. 7 No 4 1989 p173
- 3 Bornstein, N. S. Deposition and Hot Corrosion Proceedings 13th International Corrosion Conference, Nov 1996, Melbourne Australia
- 4 Bornstein N. S. and William Allen Sulfidation Corrosion Revisited Proceedings 4th International Symposium On High Temperature Corrosion Elsevier Science Publishers 1996

Table I Salt Deposits Observed On Turbine Blade Surfaces

Airfoil Surface	Salt Constituent	First Stage Deposit Chemistry (mole%)	Second Stage Deposit Chemistry (mole%)
External (gas path)	Na ₂ SO ₄	40	28
	K ₂ SO ₄	4	3
	CaSO ₄	40	59
	MgSO ₄	13	8
Internal (cooling passages)	Na ₂ SO ₄	45	37
	K ₂ SO ₄	3.2	4.4
	CaSO ₄	41	46
	MgSO ₄	9.5	11.5

figure 1
compressor stage salt deposits

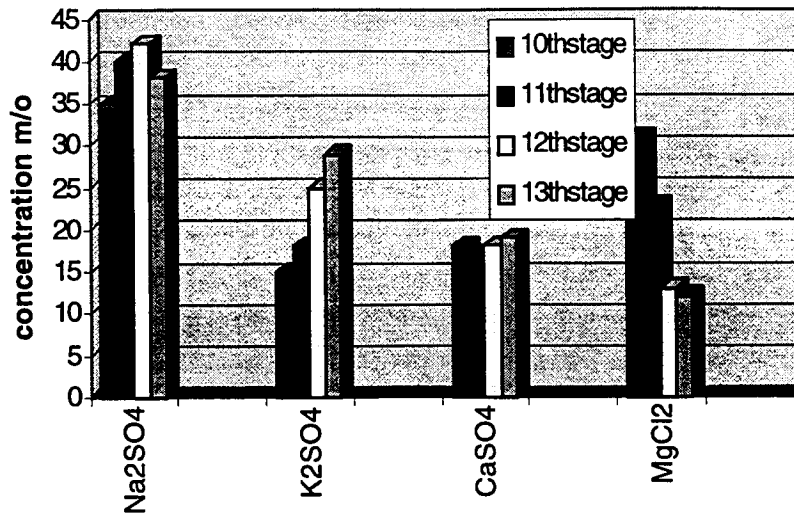


Figure 2
Quantity Of Salt Deposited Onto Turbine Components

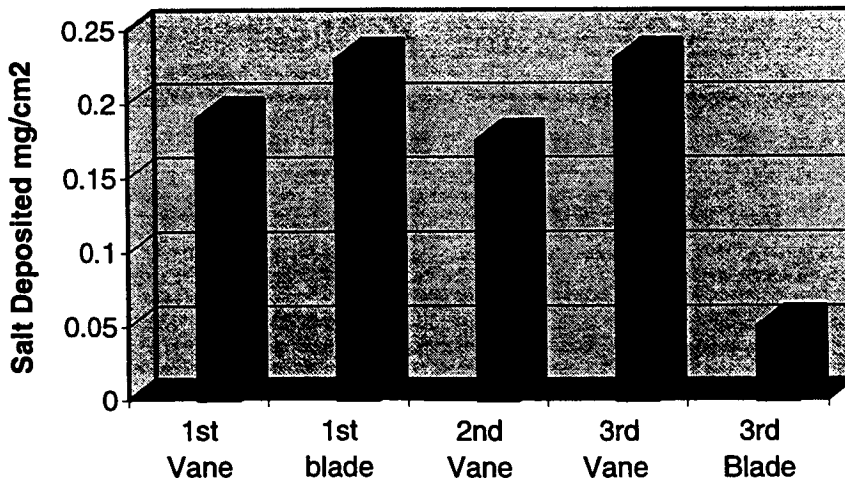
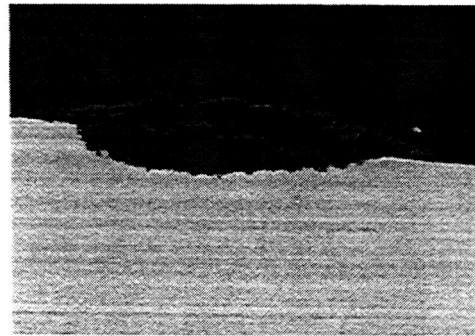
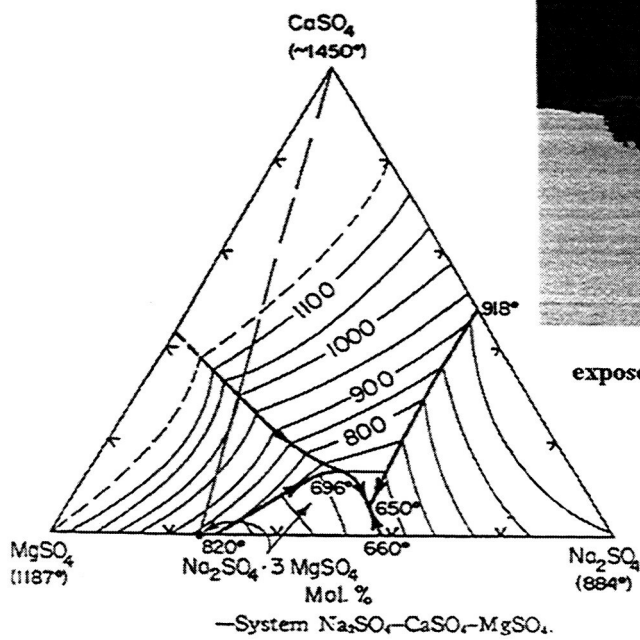


Figure 3

Salt deposits on Turbine Blades



Figure 4
Phase Equilibrium Diagram of Hot Corrosion Corrodent



exposed 6 hrs at 750C

Fig 5
Simultaneous appearance of Type I
and Type II Corrosion

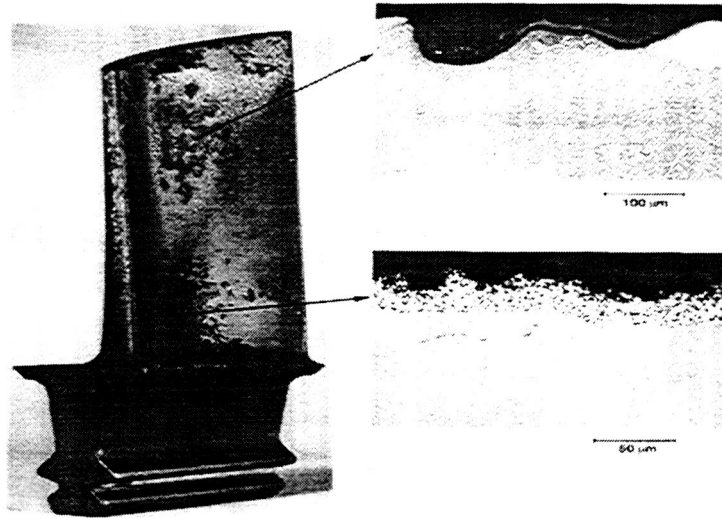
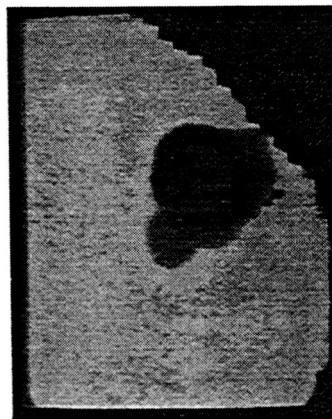


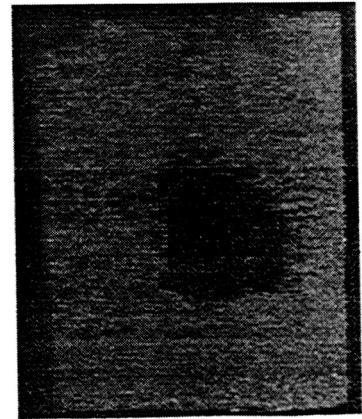
Figure 6
1200C Corrosion Test



exposed ceramic surface

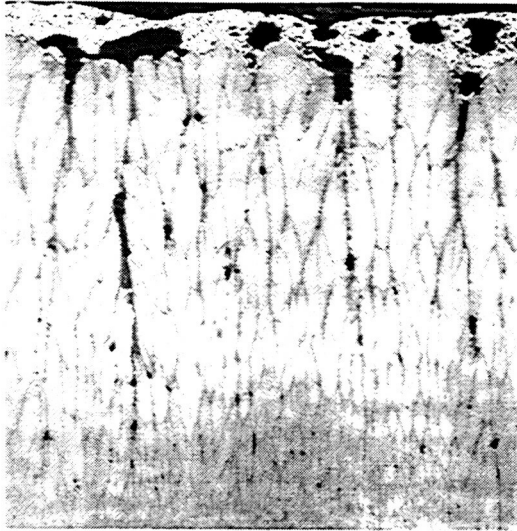


Back-side
corrodent penetrates ceramic

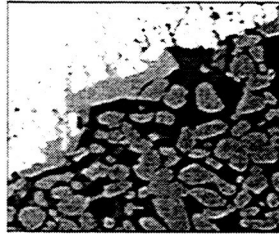


metallic surface
corrodent attack

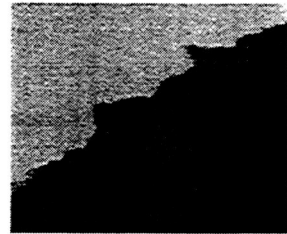
Figure 7
1200C Corrosion Test



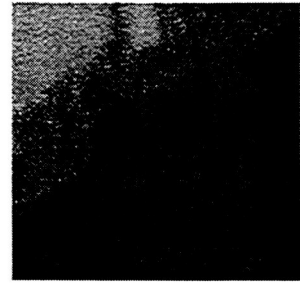
100X



BSE



Zr



Y

Figure 8
1200C Corrosion Test

corroded layer
depleted zone

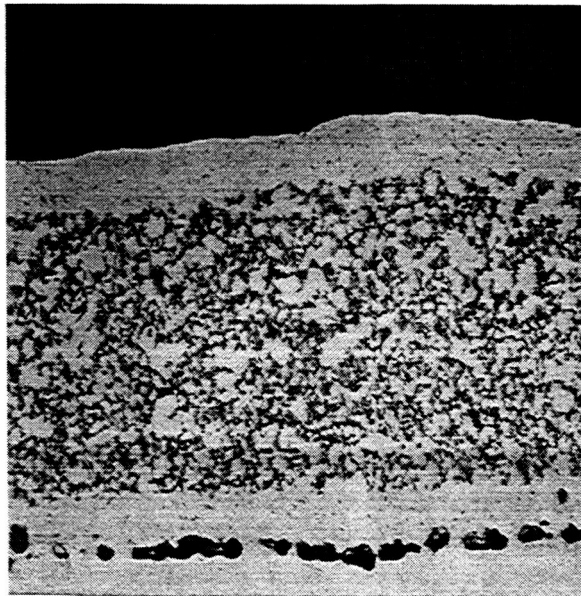


Figure 1
 compressor stage salt deposits

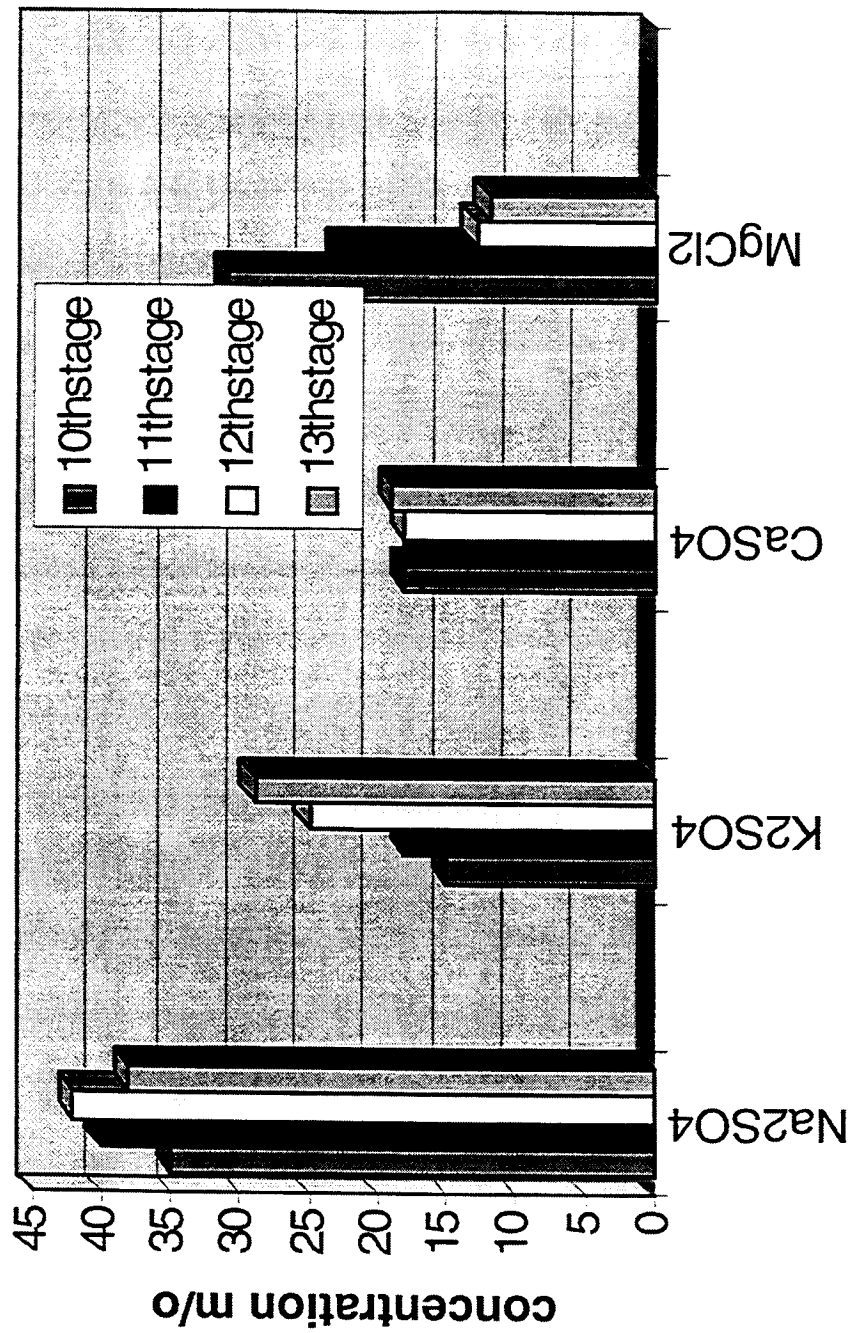


Figure 2
Quantity Of Salt Deposited Onto Turbine Components

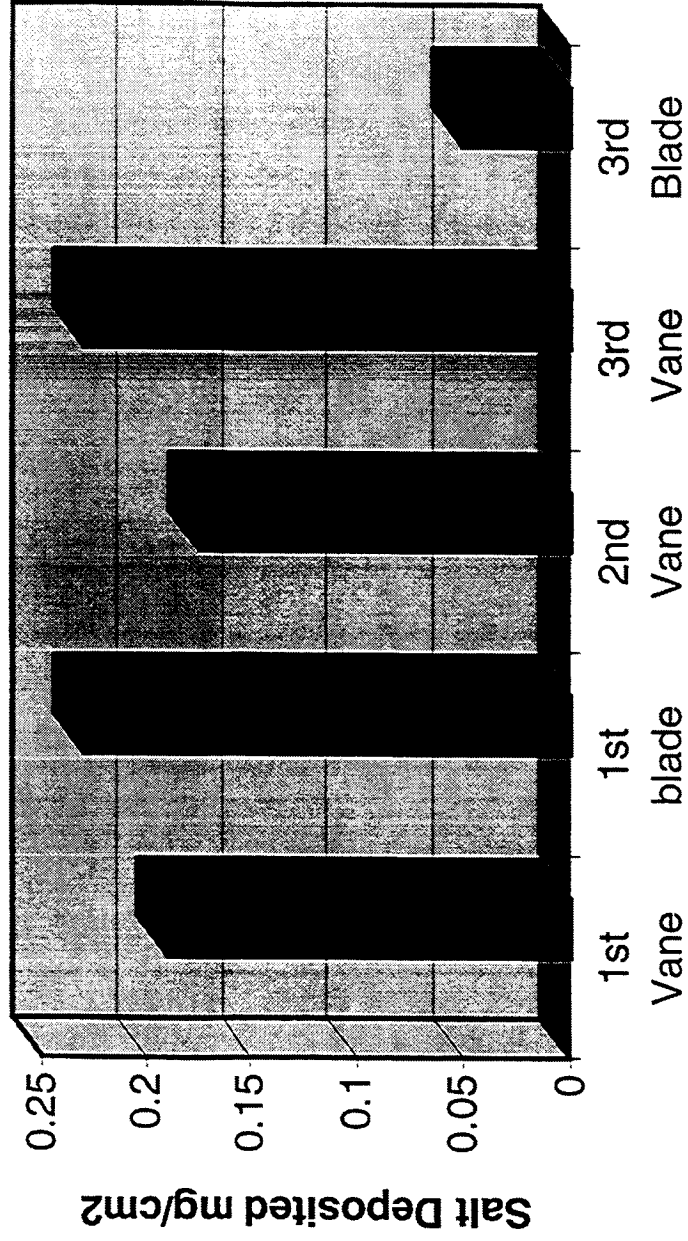


Figure 3
Salt deposits on Turbine Blades

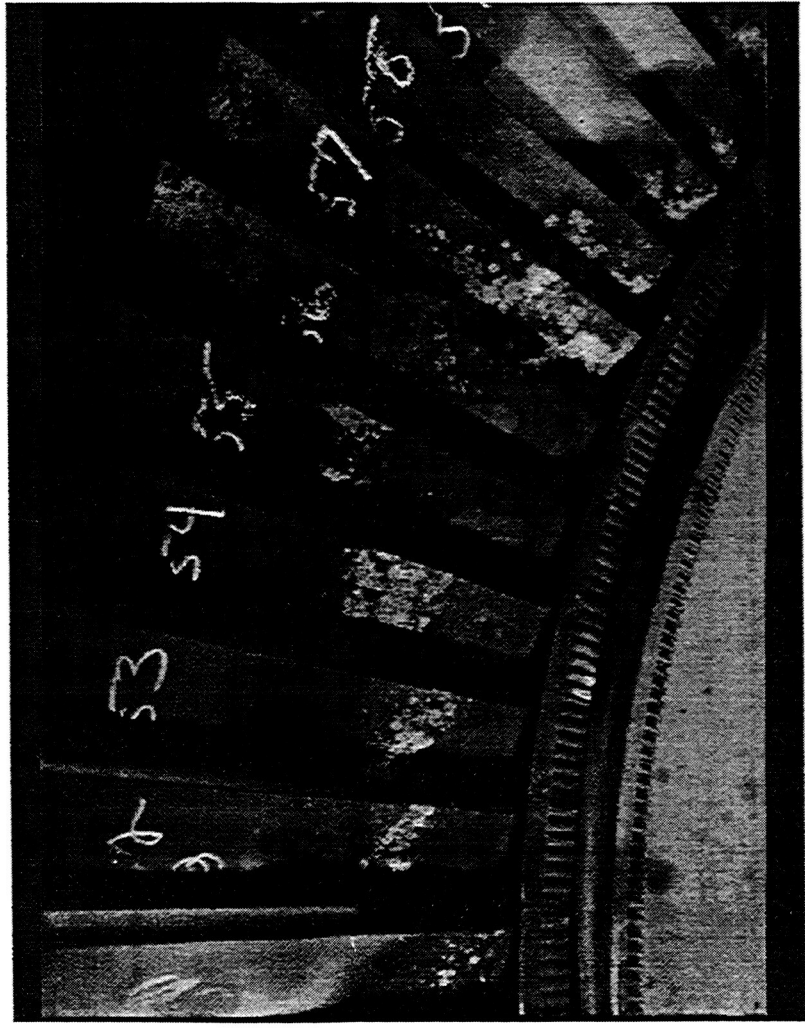


Figure 4
Phase Equilibrium Diagram of Hot Corrosion Corrodent

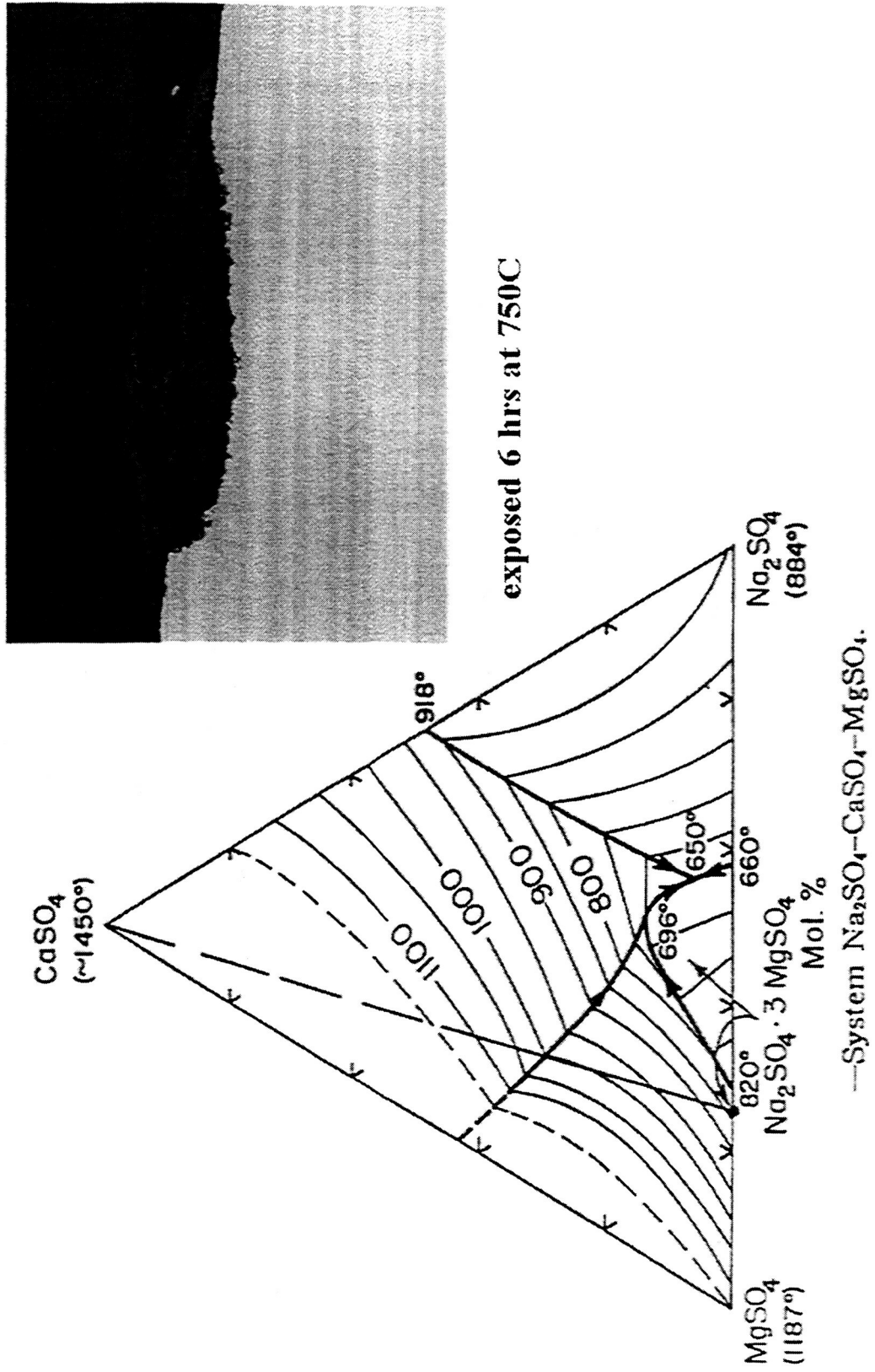


Fig 5
Simultaneous appearance of Type I
and Type II Corrosion

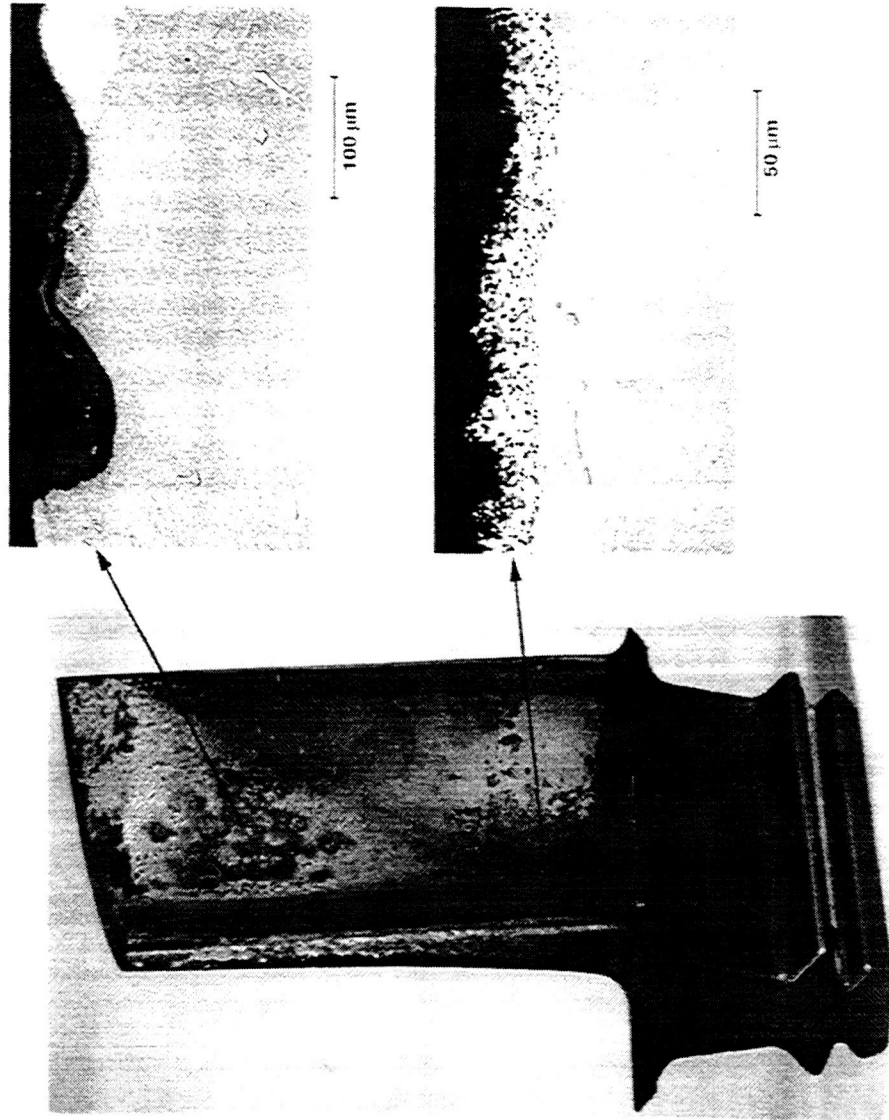
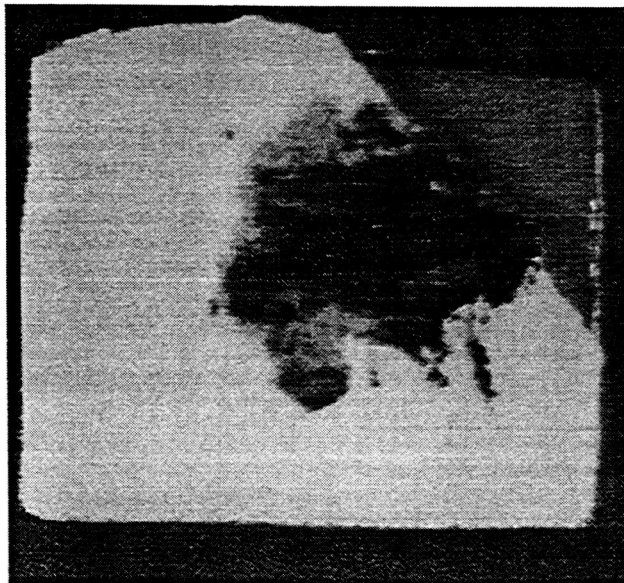
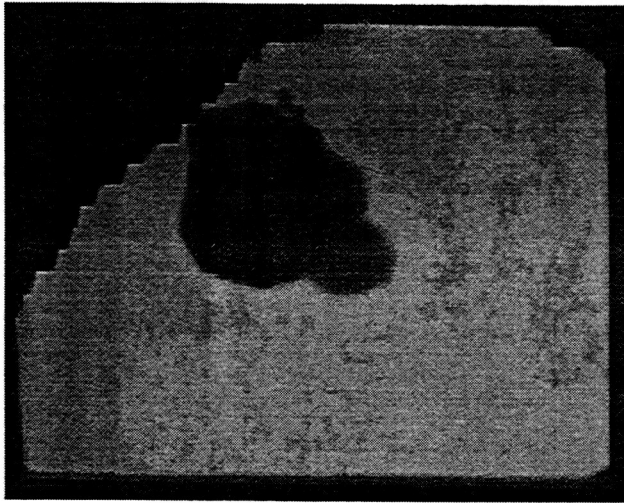


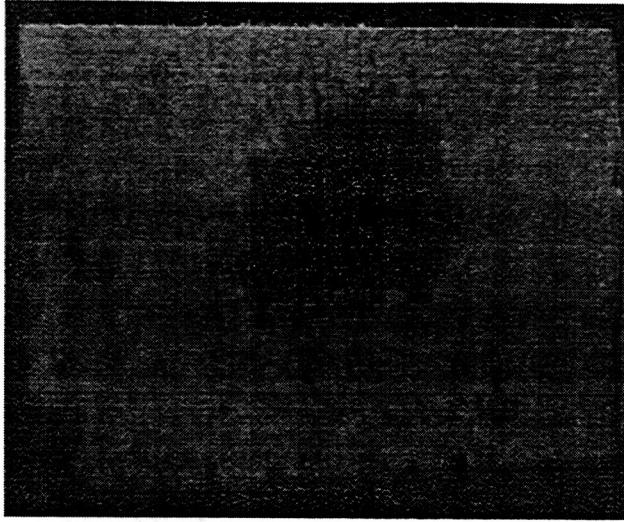
Fig 6
1200C Corrosion Test



exposed ceramic surface

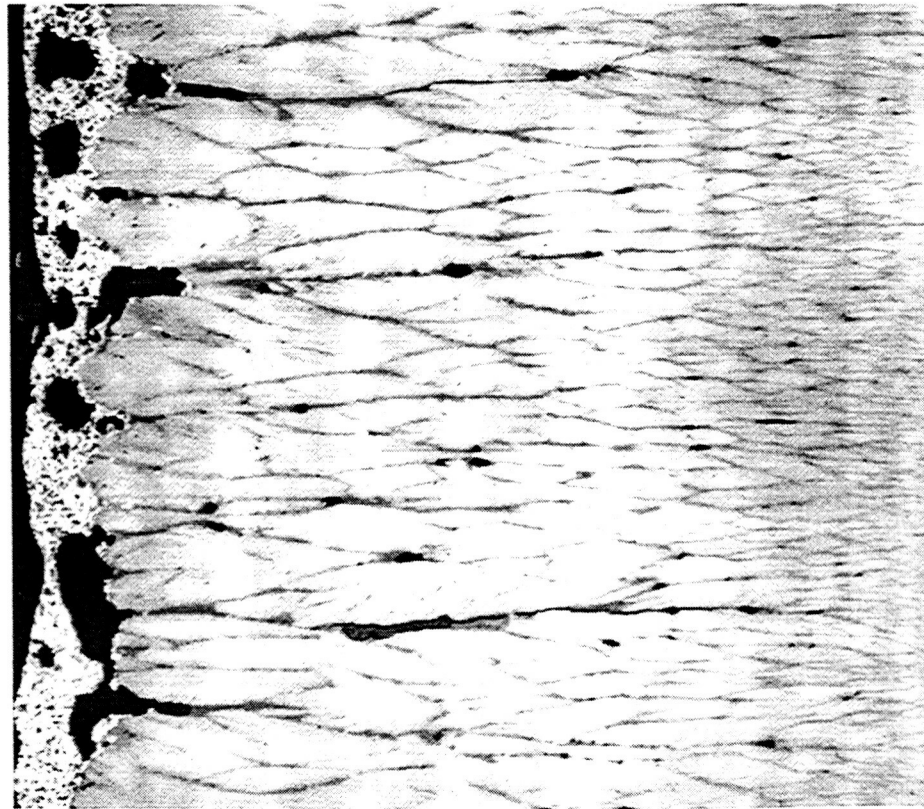


Back-side
corrodent penetrates ceramic

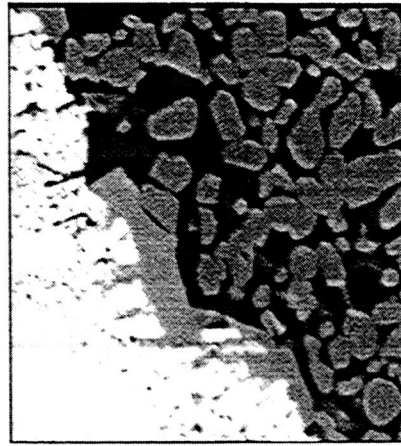


metallic surface
corrodent attack

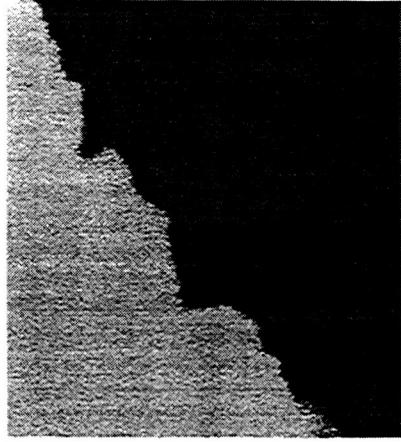
Figure 7 1200C Corrosion Test



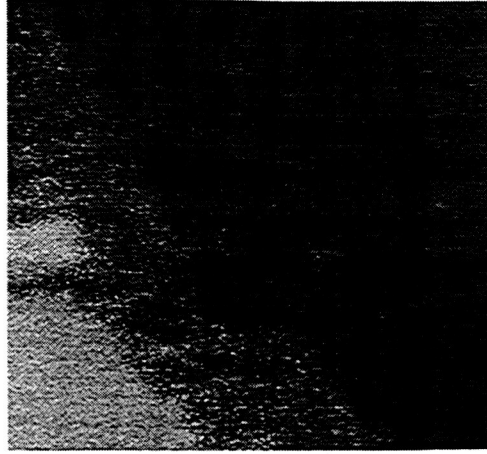
100X



BSE

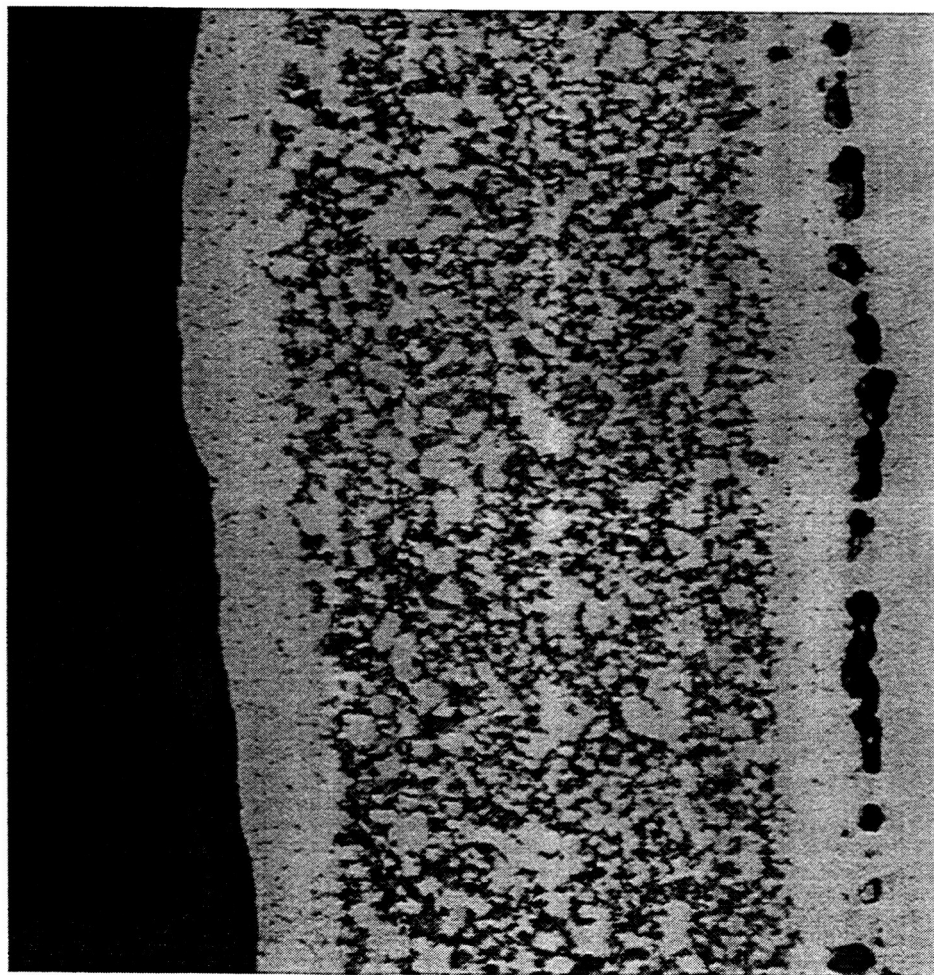


Zr



Y

Fig 8 1200C Corrosion Test



corroded layer

depleted zone

THE EFFECT OF ALUMINA PHASE TRANSFORMATIONS ON THERMAL BARRIER COATING DURABILITY

JON C. SCHAEFFER
General Electric Aircraft Engines
Evendale, Ohio

Introduction

The typical TBC system has a superalloy substrate, an alumina (Al_2O_3) forming bond coat and a 6-8 weight % yttria-partially stabilized zirconia ceramic top coat. Thermal barrier coating (TBC) adhesion and durability is dependent upon the characteristics of the interface to which it is bound. Surface preparation controls the morphology of the interface and bond coat chemistry combined with pretreatment determine the oxide that forms. The initial interface is mostly a thin alumina scale that forms during heat treatments and TBC deposition. Reviews are available in the literature concerning the microstructure, growth and adhesion of alumina scales on compositions representing aluminide and overlay bond coats.[1]

One interesting aspect is the formation of transitional alumina scales like θ , γ and δ on model bond coat compositions after exposures at relatively low temperatures and times. In a study on single crystal NiAl, low temperature oxidation at 800°C produced δ and γ -alumina scales with epitaxial relationships to the β -NiAl substrate. Final transformation of these scales to α -alumina occurs after 3-5Hr at 1100°C in air.[2] The γ to α -alumina transformation has a ΔV of -14.3% resulting in cracking and residual tensile stresses.[3] The impact of the phase transformation on TBC systems has not been studied, however, pretreatments prior to ceramic deposition that undoubtedly stabilize the alumina scale have been patented and reported.[4, 5]

This study shows that alumina transformations do occur during normal TBC processing and may impact durability as measured by a laboratory thermal cycle test. Additionally the study indicates that α -alumina stabilization should be considered prior to TBC deposition.

Experimental

Rene N5 buttons (1" O.D.) were grit blasted at 30-50 p.s.i. with 240 grit alumina and coated with a low pressure plasma sprayed (LPPS) BC51 coating to a thickness of 3-5mils. The composition of BC51 is shown in the following table:

	Ni	Co	Cr	Al	Re	W	Mo	Ta	Hf	Y
Wt.%	67.2	4	9	6	1.5	4.5	1.5	5	0.9	0.3
At.%	67.4	4	10.2	13	0.5	1.4	0.9	1.6	0.3	0.2

Prior to electron beam physical vapor deposited (EBPVD) TBC deposition, the buttons were divided into two groups:

- Group 1: ground with 400 grit SiC paper then heat treated at 1080°C/2Hr/Vac; and
- Group 2: heat treated at 1080°C/2Hr/Vac then ground with 400 grit SiC.

The EBPVD TBC was applied to a thickness of 5mils at Chromalloy in Orangeburg, N.Y. Post coating and final ages were given to the buttons consistent with typical RN5 processing.

After coating, three buttons from the two groups were cycled into the hot zone of a furnace. One cycle was a 45 minute soak at 1135°C in air followed by fan-cooling to room temperature. The samples are examined every day for TBC spallation and removed when 10% of the area is spalled. After furnace cycle testing, it was clear that the two groups had different lives. Cross sectional foils were made of the as-coated TBC systems and were analyzed on a Philips 400 analytical electron microscope (AEM).[6]

Results and Discussion

The thermal cycle test results of the samples characterized in this work are summarized with a bar chart in Figure 1. The LPPS BC51 samples from group 1 exhibited an average life of 1600 cycles while group 2 samples yielded 200 cycles.

Figure 2 is a representative micrograph of the spallation from a group 1 sample. The fracture was in the thick (10-15 μ m) α -alumina scale and did not have a preference for the bond coat/alumina or alumina/TBC interface. Deep pegs of alumina engloved hafnia (HfO₂) is a typical feature of BC51 and Hf-containing bond coat systems. The group 2 sample was similar in appearance but had a much thinner oxide scale (2-5 μ m) as a result of a shorter exposure. A better understanding of group difference was obtained by characterizing untested specimens.

Figure 3 shows a representative backscattered micrographs of the as-coated sample from group 1 and 2. The group 1 sample had a 175 μ m BC51 bond coat vs. 50 μ m bond coat for the group 2. The TBC thickness in each case is ~125 μ m. The difference in thickness between the groups was caused by variability in grinding and plasma spray thickness. The figure also shows the TBC/alumina/BC51 interface of each sample. The interfacial roughness of each sample was similar as expected from the surface grind preparation.

AEM of the samples showed a major difference in the alumina scale on the samples. Figure 4 shows a cross section bright field TEM micrograph of the scale on the group 1 sample. The Al₂O₃ scale is ~0.2 μ m thick and was confirmed to be the α -rhombohedral form of alumina by selected area diffraction. Figure 5 is a similar micrograph for the group 2 sample. In this case, the alumina scale was thinner, ~0.1 μ m and composed mainly of γ -Al₂O₃, which is cubic.

Additional phases found near or in the oxide were yttrium oxide, hafnia pegs and (Hf,Zr)O₂ particles. Table 1 lists some density and crystal system data for oxides possible on BC51.

The TBC in each sample was composed of 0.05 μ m equiaxed grains near the alumina scale which transition into columnar grains with a diameter of \sim 0.075 μ m about 0.2 μ m above the alumina scale. The BC51 bond coat grains appear to be large compared to the fine size of the oxide grains. Figure 6 shows a dark field (100) micrograph of a BC51 bond coat grain. The grain is a matrix of fcc γ with ordered domains (circular in the micrograph) of L1₂, γ' . The γ' is fine with a domain size of \sim 0.1 μ m. Group 1 samples show that γ - γ' bond coat compositions can provide excellent TBC durability.

The presence of γ -Al₂O₃ on group 2 samples makes sense because the bond coat was heat treated and then ground. The heat treatment forms a mature α -Al₂O₃ scale but subsequent grinding removed it forcing the alumina to reform during TBC deposition under conditions where a transitional alumina scale might form. This experiment illustrates that durable TBC systems may require an α -Al₂O₃ scale prior to TBC deposition.

The mechanism by which the alumina transformation might impact adhesion is not clear and deserves some study. One possibility is that the decrease in volume of a transforming segment would introduce tensile stresses to weak bond coat/alumina or alumina/TBC interfaces resulting in a loss of adhesion. The effect would be most pronounced when the volume fraction of the transforming scale exceeds a critical size and an interfacial crack starts and grows during thermal cycling. In any case, models for oxide scale adhesion and TBC life should take into account a new strain term if any major oxide transformations occur.[7, 8]

Another noteworthy observation is in Figure 7 which shows a HfO₂ peg in the as-coated group 1 long life sample. The hafnia peg is surrounded by γ -alumina and not the α -alumina at the interface. This morphology was common for hafnia pegs at the BC51/alumina interface showing that γ -alumina is stabilized when formed on a hafnia substrate. Diffraction patterns showed the hafnia to be in a tetragonal form similar to the TBC. Apparently epitaxy with these tetragonal oxide and cubic bond coat phases encourages γ -alumina formation. The kinetics and effect of the eventual transformation of the peg into α -Al₂O₃ is not known.

Summary

A processing variation on a R'N5/BC51/TBC system provided an excellent opportunity to observe the effect of a γ -alumina scale at the critical bond coat/TBC interface. The sample had low laboratory thermal cycle test results when compared to a sample with an α -alumina scale. It is postulated that the transformation from gamma to alpha alumina during subsequent processing and testing reduced the life of the TBC. These observations make the stabilization of an alpha alumina scale prior to TBC deposition an important processing consideration.

Acknowledgments

The author would like to thank Dr. R. D. Field and W. B. Connor for their collaboration in this work.

References

1. Graham, M. J. and R. Prescott, *The Formation of Aluminum Oxide Scales on High Temperature Alloys*. Oxidation of Metals, 1992. **38**(3/4): p. 233-253.
2. Doychak, J.K. and T.E. Mitchell, *High Temperature Oxidation of β -NiAl*. Mat. Res. Soc. Proc., 1985. **39**:p. 475.
3. Donlon, W.T., T.E. Mitchell, and A.H. Heuer, J. Mat. Sci., 1982. **17**: p. 1389.
4. Strangman, T.E., *Columnar Grain Ceramic Thermal Barrier Coatings*, 1982, United Technologies Corp., U.S. Patent 4,321,311.
5. Lih, W., *et al.*, *Effects of Bond Coat Preoxidation on the Properties of ZrO₂-8wt.% Y₂O₃/Ni-22Cr-10Al-1Y Thermal Barrier Coatings*. Oxidation of Metals, 1991. **36**(3/4): p. 221-238.
6. Field, R.D., *PVD/TBC AEM Data*, 1987, GE Aircraft Engines Letter Report.
7. Schutze, M. and A. Rahmel, *Mechanical Aspects of the Rare-Earth Effect*. Oxidation of Metals, 1992. **38**(3/4): p. 255-266.
8. Miller, R.A., *Life Modeling of Thermal Barrier Coatings for Aircraft Gas Turbine Engines* 1988, NASA TM-100283.
9. *International Centre for Diffraction Data 1995*, Newtown Square, Pa.

<u>Oxide</u>	<u>Calculated Density,</u> g/cc	<u>Molar Volume,</u> cc/mol	<u>Crystal System</u>
NiO	6.809	10.97	cubic
NiAl ₂ O ₄	4.502	39.24	cubic
α -Alumina	3.987	25.57	rhombohedral
γ -Alumina	3.674	27.75	cubic
δ -Alumina	3.654	27.90	tetragonal
θ -Alumina	3.689	27.63	monoclinic
HfO ₂	10.080	20.88	tetragonal
HfO ₂	10.111	20.82	monoclinic

Table 1. Table showing oxide phases that form on BC51 during processing and service. Oxide transformations result in volume changes which introduce strain to the critical bond coat/TBC interface.[9]

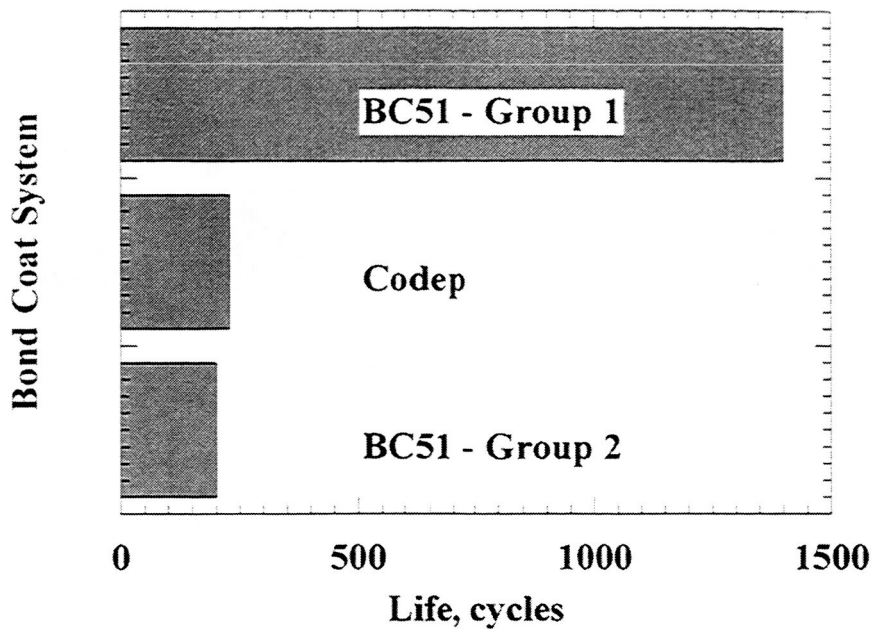


Figure 1. Bar chart comparing the average thermal cycle test life of a group 1 vs. group 2 R'N5/BC51/TBC samples. A R'N5/Codep/TBC average result from the same vintage is shown for comparison. The group 1 samples show that a γ - γ' bond coat system can produce a system with excellent durability.

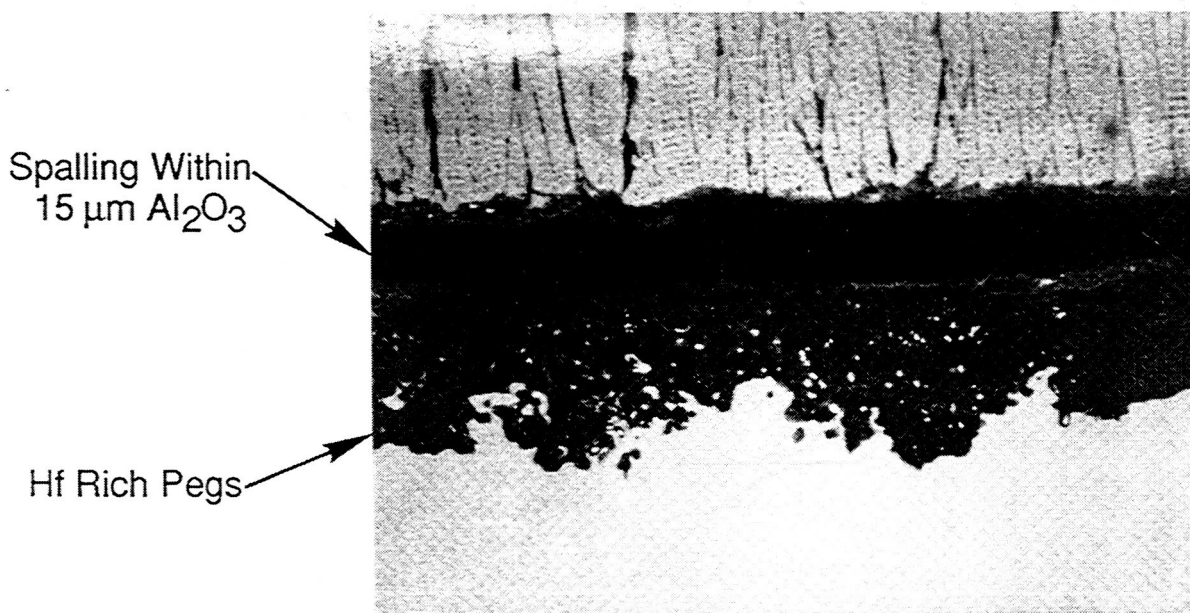
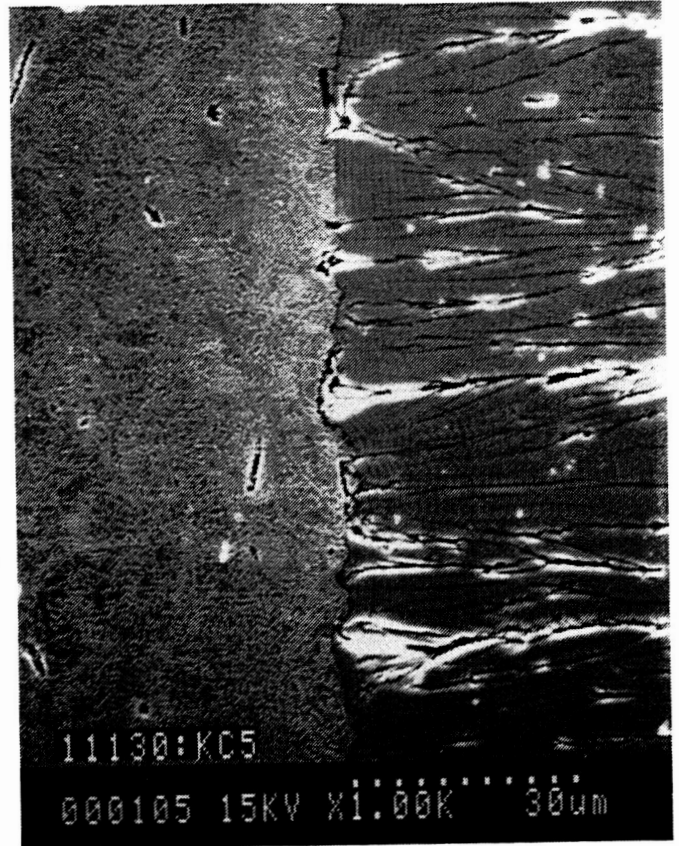
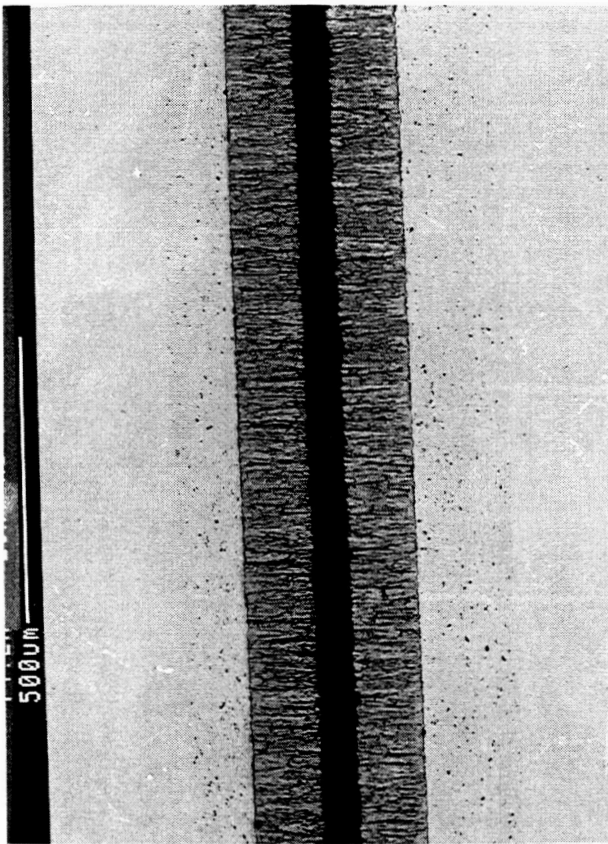


Figure 2. SEM micrograph showing a typical R'N5/BC51/TBC group 1 sample after thermal cycling. The fracture generally occurs in the alumina layer. Alumina encased hafnia pegs extend into the bond coat.

Group 1 - Long Life - Grind + HT



Group 2 - Short Life - HT + Grind

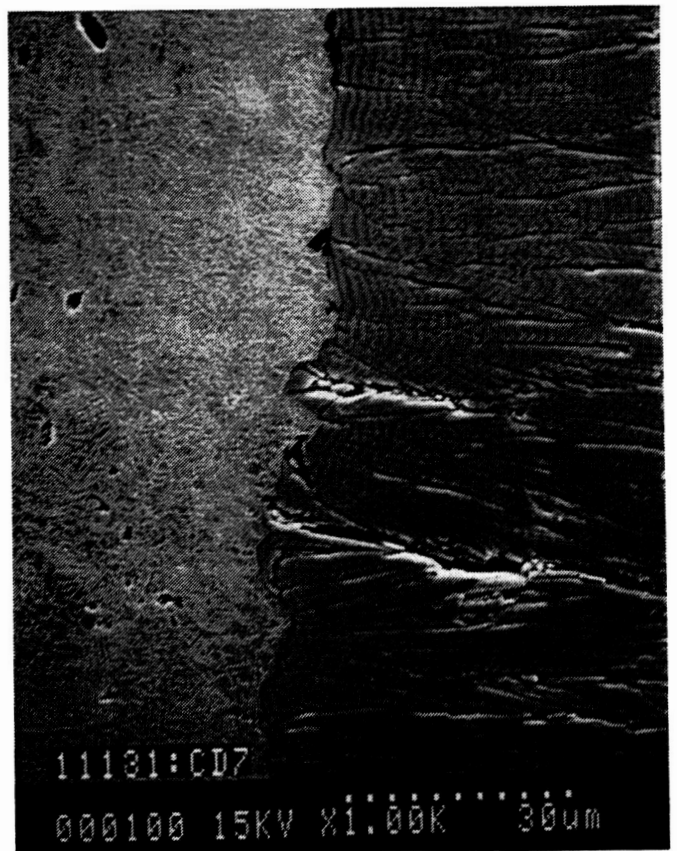
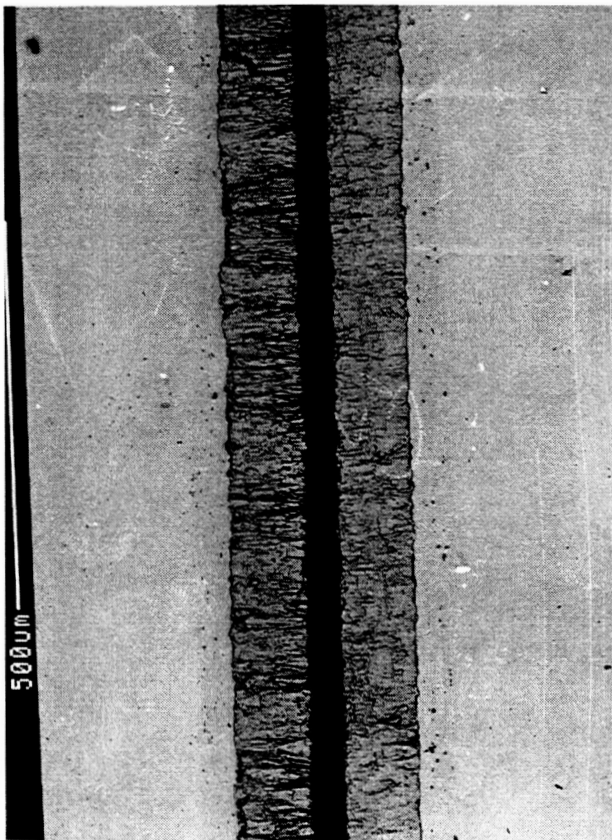


Figure 3. Backscattered micrographs showing R'N5/BC51/TBC group 1 and group 2 samples in the as-coated condition.

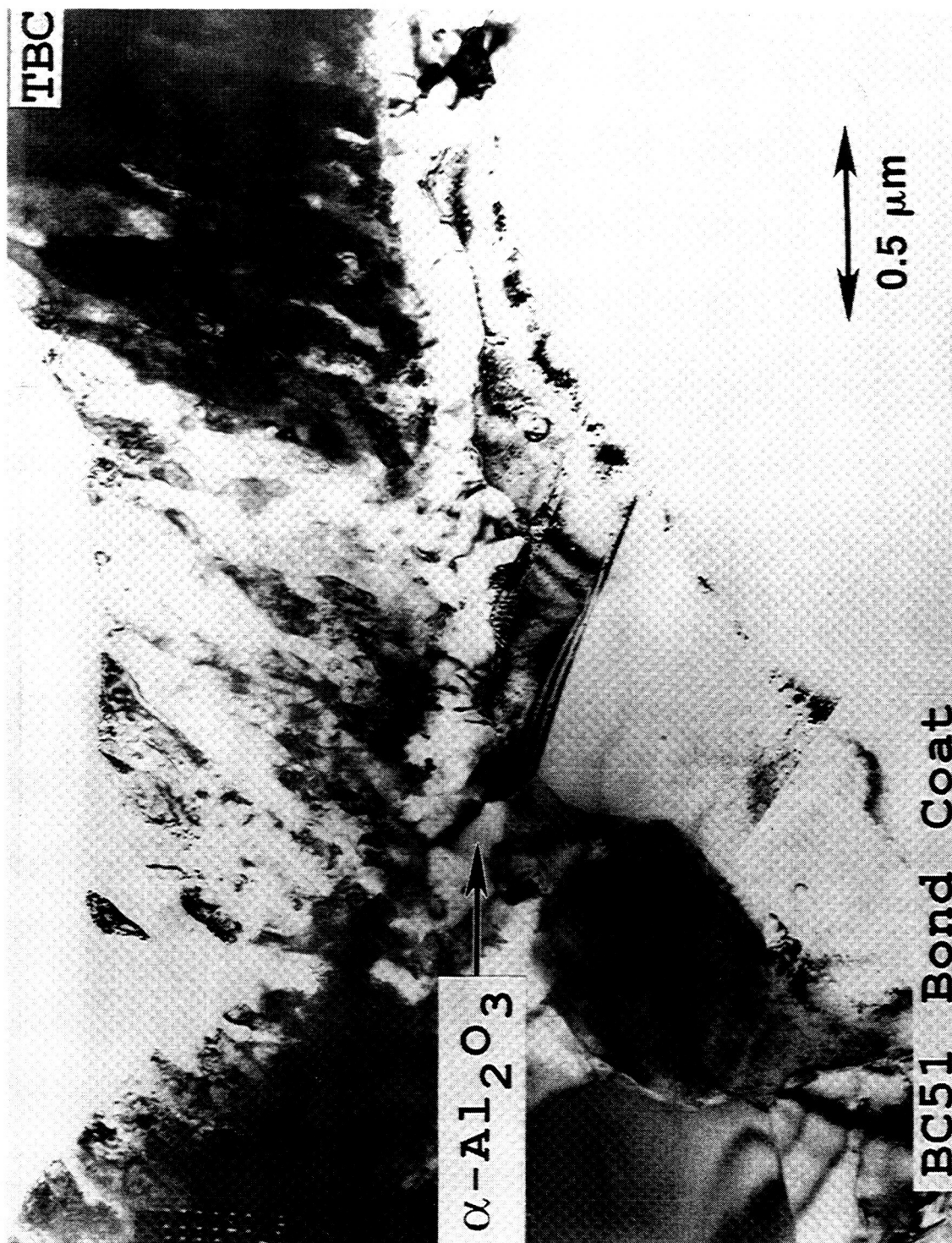


Figure 4. Cross sectional bright field micrograph of the BC51/TBC interface of an as-coated group 1 sample. An α -alumina scale is present at the interface.

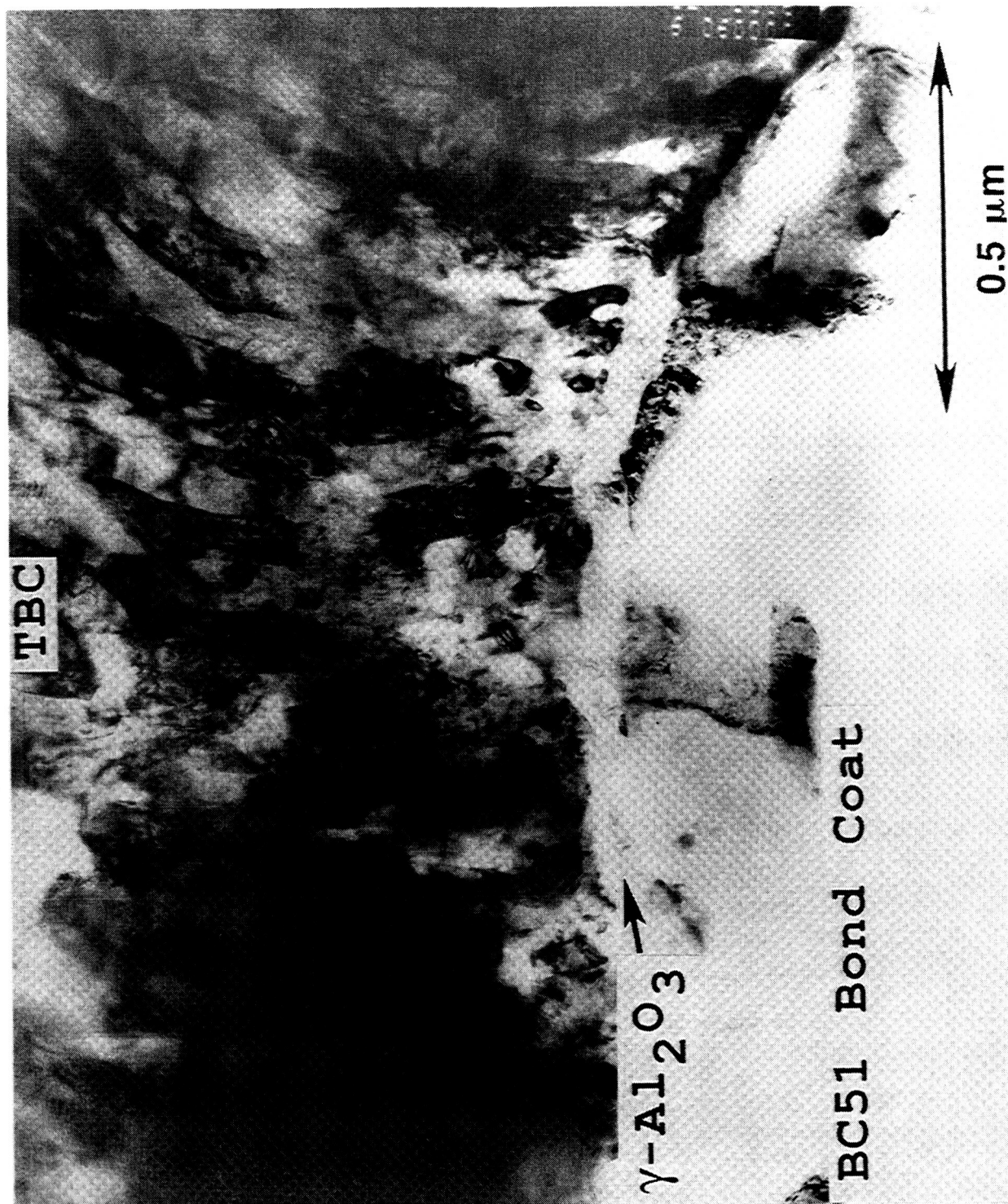


Figure 5. Cross sectional bright field micrograph of the BC51/TBC interface of an as-coated group 2 sample. A thin γ -alumina scale is present at the interface. XRD of samples after testing shows α -alumina, therefore, a transformation occurs.

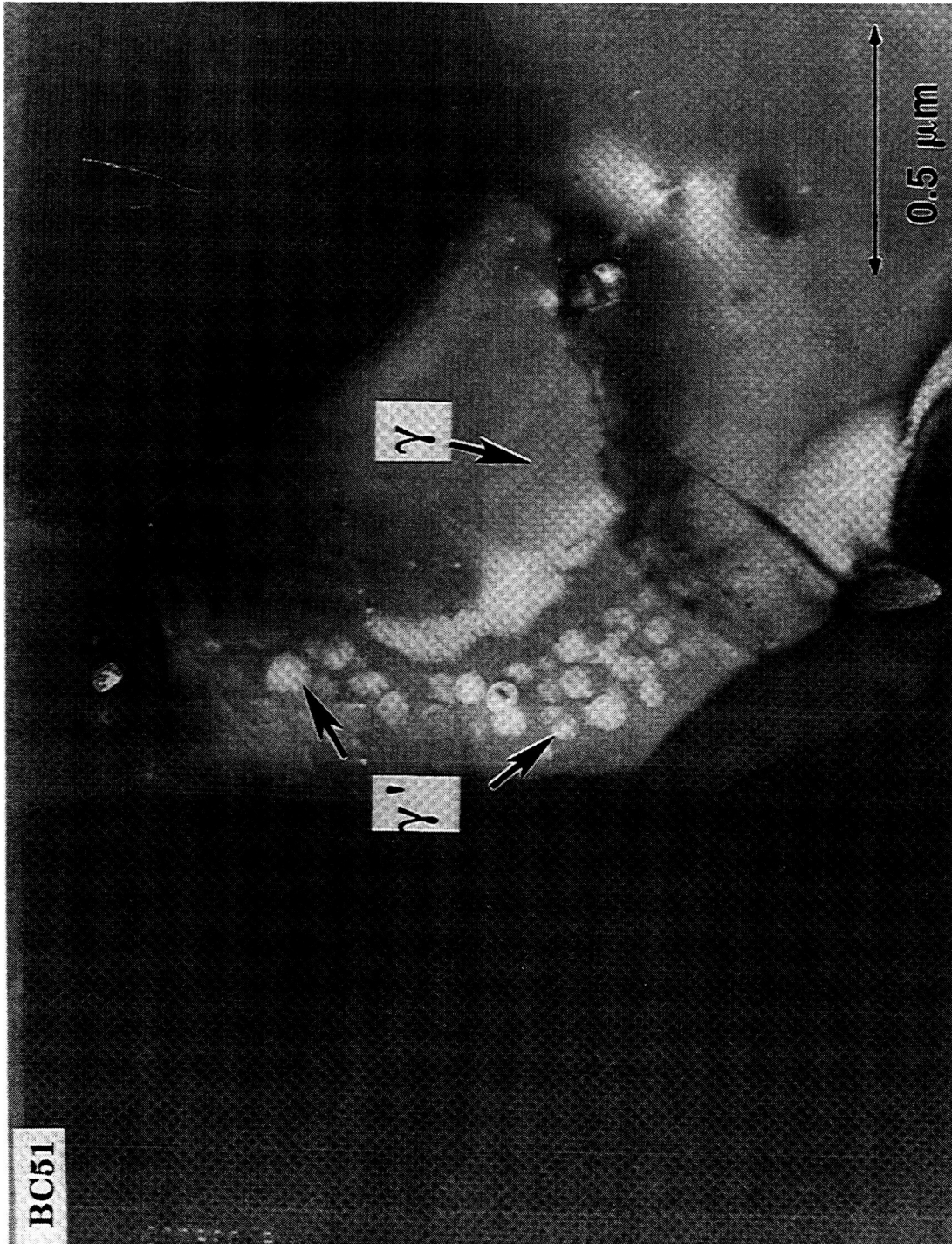


Figure 6. A dark field (100) micrograph of the BC51 bond coat showing circular γ' domains.

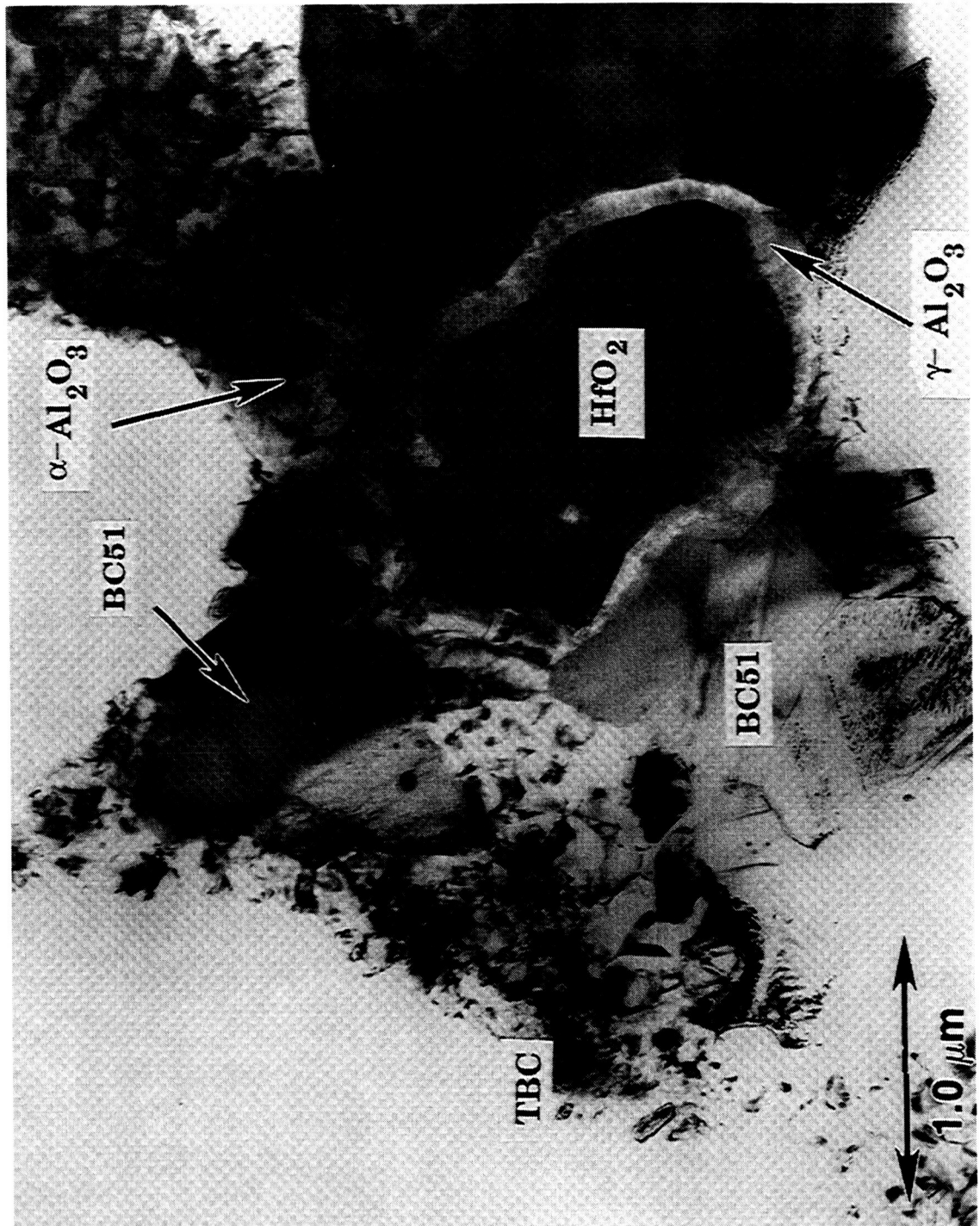


Figure 7. Cross sectional bright field micrograph of the BC51/TBC interface of an as-coated group 1 sample. An α -alumina scale is present at the interface, however, a γ -alumina scale encases a hafnia peg.

SUBSTRATE AND BOND COAT COMPOSITIONS: FACTORS AFFECTING ALUMINA SCALE ADHESION

Bruce Pint, Ian Wright, Woo Lee, Ying Zhang, Karin Prübner and Kathleen Alexander

Metals and Ceramics Division
Oak Ridge National Laboratory
Oak Ridge, TN 37831

Thermally-grown oxide scales that form beneath ZrO_2 top coats play an important role in determining the performance of a thermal barrier coating (TBC). Numerous factors, including the composition of both the alloy substrate and the bond coat, affect adhesion of the $\alpha-Al_2O_3$ scale to the metal substrate. In order to study the problem of oxidation-related failure, a model substrate was selected: cast, Zr-doped $\beta-NiAl$. With the addition of a reactive element (RE) like Zr, $\beta-NiAl$ is one of the most highly oxidation-resistant alumina-forming alloys. $\beta-NiAl+Zr$ substrates were coated with a 125 μm thick, electron beam, physical vapor deposited (EB-PVD), Y_2O_3 -stabilized ZrO_2 (YSZ) coating by GE Aircraft Engines¹ and furnace cycled at 1150°C (1h cycles at temperature) and 1200°C (2h cycles at temperature). The coating lifetime is >1650 cycles at 1150°C and >275 cycles at 1200°C. Neither coating has failed to date, except for chipping at the edge of the coupons. A similar-thickness, EB-PVD YSZ coating on René N5 (plus Pt aluminide bond coat) exhibited failure at 1150°C after 600 cycles and after 106 cycles at 1200°C, Figure 1. These results indicate that a significant improvement in TBC lifetime (≥ 3 fold) may be garnered from having a more oxidation-resistant substrate beneath the YSZ coating.

Three general factors are contributing to the "ideal" scale formation and adhesion on Zr-doped $\beta-NiAl$: (i) no major redistribution of alloying elements within the metal substrate, (ii) segregation of Zr to the metal-scale interface and the scale grain boundaries, and (iii) ability to tolerate stresses generated in the scale.

One clear advantage of the Zr-doped $\beta-NiAl$ substrate is that it has a plentiful supply of Al and no additional elements (except Zr) that may diffuse into the $\alpha-Al_2O_3$ scale. With a conventional metallic substrate of Ni-base superalloy and bond coat, it has long been recognized that there is significant diffusion of elements between these components. The concentration gradient drives Al from the bond coat into the Al-lean substrate. In the case of René N5, the uncoated substrate is already highly oxidation resistant and contains a sufficient Al content to form a protective alumina scale. However, there are indications that Ni-rich $NiAl$ is more prone to interfacial void formation², thus, although a minor Al depletion in the Pt aluminide bond coat on René N5 may not inhibit Al_2O_3 formation, it may result in a less adherent scale.

It is also known that Co, Ta, Hf, Re and other elements readily diffuse from the superalloy into the bond coat and scale. Results from a study of CVD aluminide coatings on René N5 indicate that a larger bond coat grain size shows better scale adhesion (without a top coat), Figure 2. Presumably grain boundaries are fast diffusion paths for elements such as Ta, Hf and Re. This outward diffusion of elements is aided by a second driving force - the oxygen potential gradient created during oxidation³. Just as Al diffusion is driven by the oxidation potential, other oxygen-active elements are drawn into the scale by the same mechanism. Analytical electron microscopy (AEM) results of the alumina scale formed on uncoated René N5 revealed an outer oxide layer containing Co and Ta and also showed Y, Ta, Hf and Re segregation on $\alpha-Al_2O_3$ grain boundaries, Figure 3. The oxygen potential gradient extends into the metal and affects all oxygen active elements, even those in "stable" oxides, nitrides, carbides and sulfides. The eventual result is an excess of additional elements in the alumina scale which is usually not beneficial to scale adhesion.

The second factor concerns the chemistry of the metal-scale interface and involves the effects of indigenous S and RE additions like Y, Zr, Hf and La. The Zr-doped β -NiAl substrates have a bulk S content of 47ppma. Any potentially negative effect of this nominally high S level is apparently easily overcome by the addition of 0.04at%Zr. Previous work has demonstrated that Zr segregates to the metal-scale interface^{4,5} and inhibits the interfacial segregation of S^{3,6}. In Ni-base superalloys, the detrimental role of S also can be reduced by de-sulfurizing the substrate^{7,8}. For the case of René N5, the substrate contains 34ppma Y and 7ppma S but the Pt aluminide coating does not contain any specific RE addition. In cyclic testing at 1150°C, the S and Y content of the substrate have been found to affect TBC lifetime on René N5, Figure 4. Both by adding Y or de-sulfurizing without Y there is an increase in coating lifetime.

The addition of Pt to the aluminide coating is recognized as being beneficial to scale adhesion^{9,10}. Comparing cast PtAl and NiAl + 10wt%Pt to cast, undoped NiAl there is a clear improvement in scale adhesion with the addition of Pt to the substrate, Figure 5. However, the additional RE effects of reducing the scale growth rate and changing the α -Al₂O₃ microstructure³ are not observed and in general, Pt is not as effective as Hf and Zr in improving scale adhesion, Figure 6. One potential mechanism for the benefit of Pt is that it changes diffusivities in the substrate which, in turn, inhibits void formation at the metal-scale interface, thus improving scale adhesion.

Several issues remain unresolved about the RE and S effects. For example, Hf is highly effective in improving the oxidation resistance of NiAl and yet it does not have the same strong effect in René N5. Also if S is gettered by Y, then it would appear that the amount of Y in a MCrAlY bond coat should be sufficient to getter indigenous S and de-sulfurizing the substrate should be unnecessary.

The third issue regards the generation of stresses in the scale. Numerous research groups are attempting to model and measure the stresses in alumina scales¹¹. For the purposes of this discussion, only a qualitative description is used. Stresses arise from two sources: growth stresses generated isothermally, and thermal stresses generated during thermal cycling due to the metal-oxide thermal expansion mismatch. While once considered smaller and ignorable, it has now become clear that growth stresses are of the same order of magnitude and play a significant role in determining scale adhesion. Both of these sources appear to generate large compressive stresses in the plane parallel to the metal-scale interface. It is proposed that maintaining stresses in the parallel plane, thereby limiting out-of-plane, tensile stresses, is the best method for maintaining an adherent scale. To test this assumption, a 125 μ m-thick, plasma-sprayed YSZ top-coat was deposited by NASA Lewis on a polished β -NiAl+Zr substrate¹². In cyclic testing at both 1150° and 1200°C, this coating had a longer lifetime than the EB-PVD coating on René N5, Figure 7.

Another apparent manifestation of growth stresses is in a temperature effect on scale adhesion. Testing uncoated Ni-base superalloys in 1h cycles at 1100°C-1200°C revealed that, as the temperature increased, neither RE doping nor de-sulfurization could inhibit scale spallation, Figure 8. No such temperature effect was noted for β -NiAl over the same temperature range even though it exhibited a similar oxidation rate. It is proposed that this difference is related to a stress effect of the scale acting on the substrate and that the mechanical properties of the substrate play a role in scale adhesion.

Having cited these three factors for improved scale adhesion, some potential strategies to form more adherent alumina scales in practical TBC systems would be:

- add more Al to aluminide coatings, possibly limiting interfacial void formation
- investigate bond coat microstructures or phases (e.g. Engel-Brewer compounds¹³) which may inhibit diffusion of elements from the substrate into the scale

- identify which elements (alone or in combination) are most detrimental to scale adhesion; for example, it appears that Hf can be disruptive and is very oxygen-active, Ta is very active but does not appear to be especially detrimental. The effect of Re is uncertain.
- add reactive elements to platinum aluminide coatings; RE-doping will give an added boost to the benefit provided by the Pt alone.
- for applications with higher bond coat temperatures, aluminides appear to be superior to MCrAlY-base bond coats.
- pursue techniques such as the studies at NASA Lewis¹² for depositing plasma-sprayed top coats on flatter (less rough) substrates. This strategy will allow the scale to grow thicker without failure by maintaining compressive stresses in the parallel plane.
- design TBC systems based on the natural limitation that alumina scales thicker than $\approx 10\mu\text{m}$ will not remain ideally adherent and thus cannot support a ceramic top coat. For relatively flat metal-scale interfaces the cooling strain of a thick scale will exceed the metal-oxide interfacial strength resulting in decohesion. For convoluted scales, repeated thermal cycling will cause tensile stresses that will eventually cause failure in the $\alpha\text{-Al}_2\text{O}_3$ scale, which is a brittle ceramic. This strategy implies limiting the bond coat temperature or the time between refurbishing the coating.

References

1. B. A. Pint, B. A. Nagaraj, and M. A. Rosenzweig, in *Elevated Temperature Coatings: Science and Technology II*, N. B. Dahorte, J. M. Hampikian, and J. J. Stiglich eds., p.163-74, TMS Symp. Proc., Warrendale, PA (1996).
2. M. W. Brumm and H. J. Grabke, *Corr. Sci.*, **34**, 547-61 (1993).
3. B. A. Pint, *Oxid. Met.*, **45**, 1-37 (1996).
4. B. A. Pint, A. J. Garratt-Reed and L. W. Hobbs, in *Microscopy of Oxidation 2*, S. B. Newcomb and M. J. Bennett eds., p.463-75, Institute of Metals, London, U.K., (1993).
5. E. Schumann, J. C. Yang, M. J. Graham and M. Rühle, *Mat. and Corr.*, **46**, 218-22 (1995).
6. K. Prüßner, J. Bruley, U. Salzberger, H. Zweggart, E. Schumann and M. Rühle, in *Microscopy of Oxidation 2*, S. B. Newcomb and M. J. Bennett eds., p.435-44, Institute of Metals, London, U.K. (1993).
7. J. G. Smeggil, A. W. Funkenbusch and N. S. Bornstein, *Met. Trans.*, **17A**, 923-32 (1986).
8. J. L. Smialek, *Met. Trans.*, **22A**, 739-52 (1991).
9. E. J. Felten, *Oxid. Met.*, **10**, 23-8 (1976).
10. J. G. Fountain, F. A. Golightly, F. H. Stott and G. C. Wood, *Oxid. Met.*, **10**, 341-5 (1976).
11. Mechanical Properties of Protective Oxide Scales, *Mat. High Temp.*, **12**(2-3) (1994).
12. R. A. Miller and W. J. Brindley, in *Proc. Int. Thermal Spray Conf.*, p.493-8 (1992).
13. L. Brewer and P. R. Wengert, *Met. Trans.*, **4**, 83-104 (1973).

Acknowledgments

The authors would like to thank P. F. Tortorelli, J. R. DiStefano A. Haynes, P. F. Becher and J. H. DeVan at ORNL for their comments. B. A. Nagaraj at GE Aircraft Engines assisted in providing coatings and substrates. NASA Lewis provided NiAl substrates (J. D. Whittenberger and J. Doychak) and coatings (W. J. Brindley). This research was sponsored by the U. S. Department of Energy, Assistant Secretary for Energy Efficiency and Renewable Energy, Office of Industrial Technologies, as part of the Advanced Turbine Systems Program and by the Division of Materials Sciences under contract DE-AC05-96OR22464 with Lockheed Martin Energy Research Corporation.

Substrate and Bond Coat Compositions: Factors Affecting Alumina Scale Adhesion

B. A. Pint, I. G. Wright, W. Y. Lee, Y. Zhang
K. Prübner and K. B. Alexander

Metals and Ceramics Division
Oak Ridge National Laboratory
Oak Ridge, TN 37831

An Oxidation Perspective

scale = thermally grown oxide "TGO"

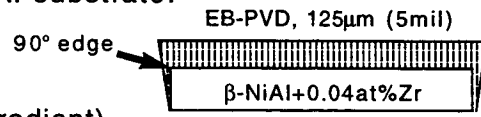
Important research topics in the oxidation community:

- reaction rates
- metal-oxide adhesion
- effect of minor-alloying "dopant" elements and tramp elements
e.g. reactive element and sulfur effects
- stress measurement and modeling
- hot corrosion
- lifetime prediction

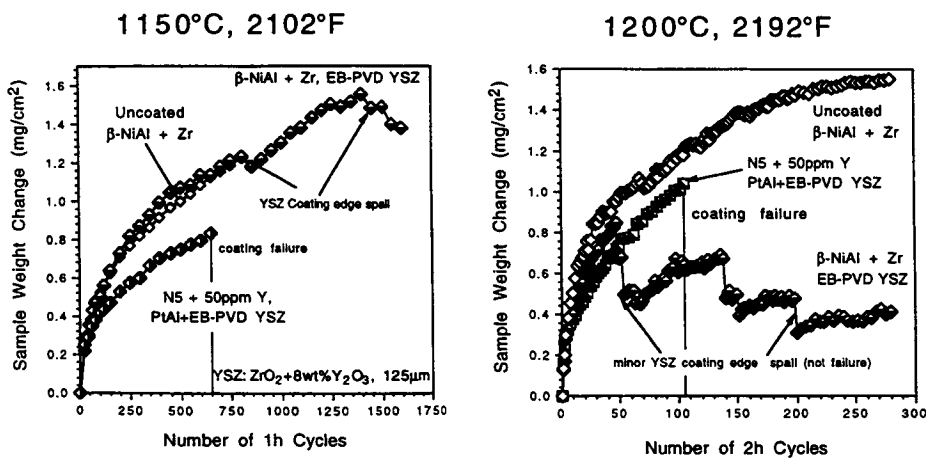
There is a strong overlap of topics important to TBC's

Experimental Approach

- focus on the alumina scale
not the only important factor but a potential weak link
- define the "ideal" scale
use a model system:
focus on NiAl + Zr which forms an adherent alumina scale
deposit TBC directly onto NiAl substrate:


- testing
furnace cycle (no temperature gradient)
cycle time is time at temperature, 10 min cooling between cycles
failure criterion: loss of 20% of coating from coupon
- compare to René N5:
General Electric single crystal alloy:
Ni-7.2wt%Co-6.8Cr-6.4Ta-6.3Al-5.0W-3.2Re-1.4Mo+Hf, Y, Zr
TBC: Pt aluminide bond coat + EB-PVD, 125 micrometers (5 mil) top coat

EB-PVD YSZ deposited on β -NiAl+Zr
longer life than TBC on René N5 (+Pt aluminide)
in furnace cycling at 1150° and 1200°C



N5+(Ni,Pt)Al bondcoat: life at 1150°C, = 650 x 1h, 1200°C, = 106 x 2h
 β -NiAl+Zr: life at 1150°C, >1650 x 1h, at 1200°C, >282 x 2h
 weight losses due to coating spallation at 90° edge of NiAl coupon

Figure 1 Factor of +3 increase in life

3 factors leading to an “ideal” scale on β -NiAl

1. No major redistribution of elements within the metal substrate

e.g., Al diffusing from bond coat to substrate
or Co, Ta, Hf, etc. diffusing into

2. Zr segregates to metal-oxide interface and the α - Al_2O_3 scale grain boundaries.

inhibits detrimental role of indigenous S on adhesion
lowers the scale growth rate by 2-3X

3. Ability to tolerate stresses generated in the scale

both thermal (metal-scale expansion mismatch: ΔCTE)
and isothermal (growth) stresses

Diffusion Problem

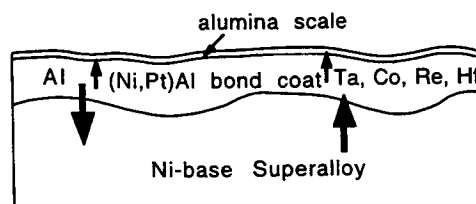
- Not an issue for the β -NiAl substrate, Al concentration remains flat in the substrate during oxidation

For generic Ni-base substrate and bond coat:

- concentration gradient drives Al into Al-lean substrate
- substrate elements also diffuse into bond coat and scale

For Pt aluminide coating on René N5:

- substrate already oxidation resistant
- but aluminide coating still loses Al to substrate
- elements such as Co, Ta, Re, W etc. may diffuse into bond coat



Loss of Al from bond coat

One potential outcome -

Al drops below critical Al level needed to form an alumina scale

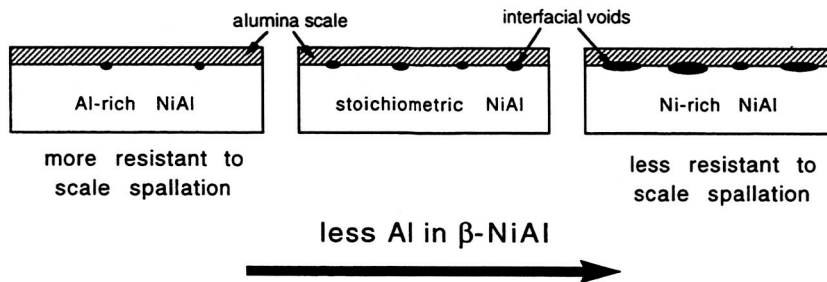
For Pt aluminide coating on René N5:

already sufficient Al in substrate for oxidation resistance

Al diffusion unlikely to cause a change to less stable oxides

However, loss of Al in Pt aluminide bond coat may result in the formation of a less adherent alumina scale

- Brumm & Grabke observed increasing interfacial void formation as Ni/Al ratio increased in β -NiAl. Linked change to a modification in Ni and Al diffusivities and a Kirkendall-type effect



Characterization of scale on uncoated René N5 formed after 100h at 1200°C

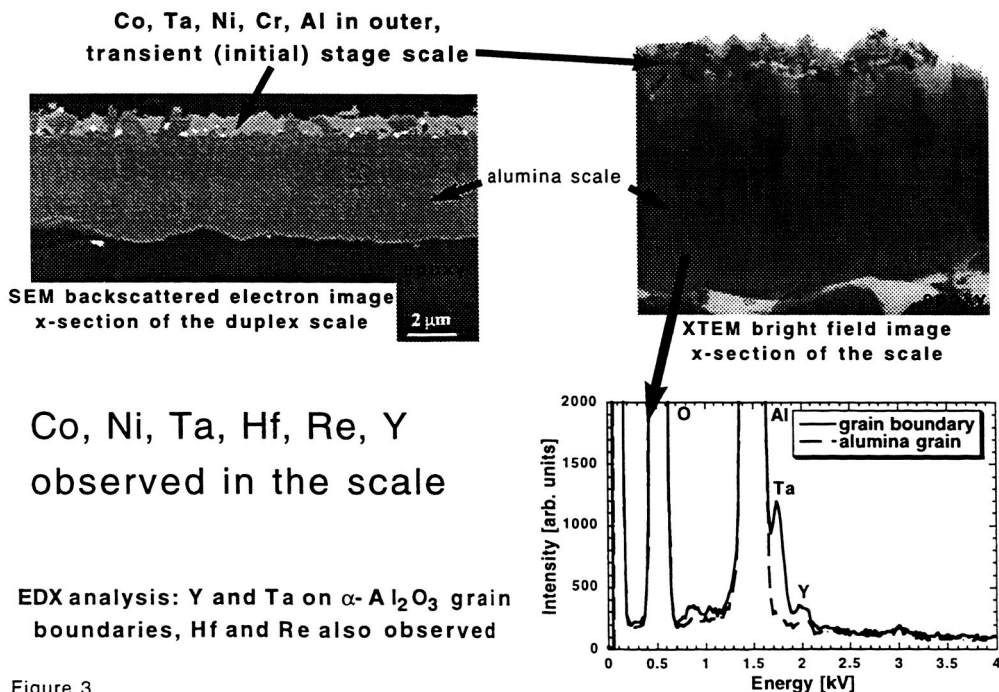
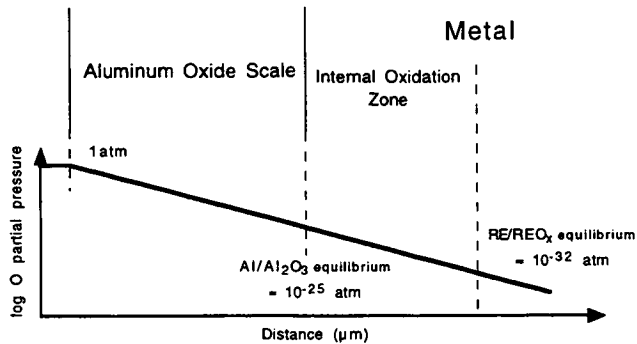


Figure 3

Second Driving Force for Diffusion

The oxygen potential gradient at high temperatures extends into the metal and drives the diffusion of oxygen-active elements into the scale.



for Al_2O_3 :

$$k_r = \frac{a_{\text{Al}_2\text{O}_3}^1}{a_{\text{Al}} p_{\text{O}_2}^{3/2}}$$

in general:

$$k_r = \frac{a_{\text{RE}_y\text{O}_x}^1}{a_{\text{RE}} p_{\text{O}_2}^{y/x}}$$

As the oxygen pressure increases, the activity of oxygen-active elements decreases. Thus, the oxygen gradient results in a chemical potential gradient which drives diffusion of oxygen-active elements.

The additional implication is that oxides, nitrides, sulfides, and carbides of oxygen active elements (Y, Hf, Ta, Zr, Ti, Re?, etc.) may not be stable in the presence of an oxygen potential gradient.

Indigenous S effect

Sulfur has an detrimental effect on scale adhesion

- Demonstrated that S segregates to the metal-scale interface
- Removing S to below 1ppma in alloys, improves scale adhesion

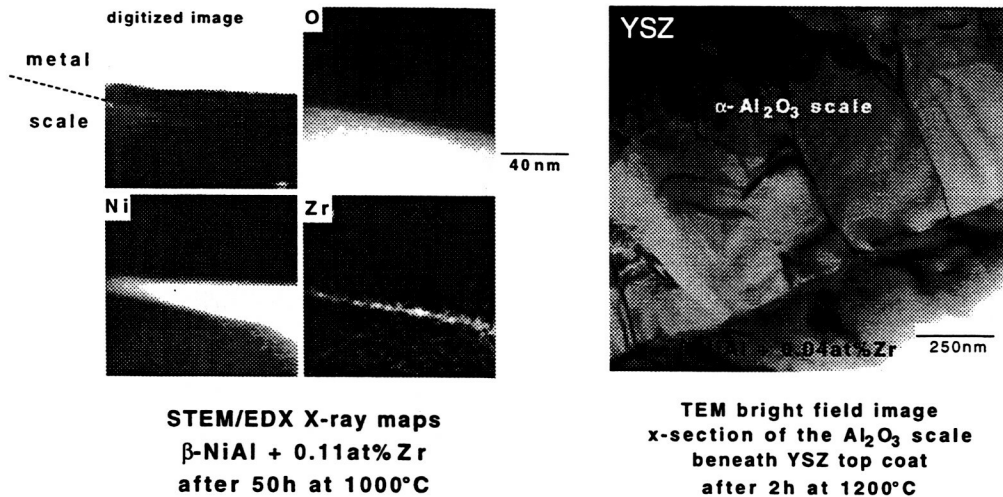
Reactive Element Effect

Additions of many elements improve scale adhesion

- RE ions segregate to metal-scale interface
- apparently inhibit the interfacial segregation of S
- RE's form stable sulfides
- RE's form stable oxides
- RE ions segregate to scale grain boundaries
- cation transport is inhibited by RE doping
- 2-4X reduction in parabolic rate constant at 1200°C
- RE doping changes the scale microstructure

Reactive element location: Zr (in β -NiAl) for this study

Zr ions observed segregated to the metal-scale interface
and the α -Al₂O₃ scale grain boundaries



Dopant effects in β -NiAl and René N5/Pt aluminide

β -NiAl+Zr

0.04at% (400ppma) Zr

47ppma S - bulk level in substrate

apparently Zr is able to overcome negative S effect

René N5

7ppma S in the substrate

not below the 1ppma level where tolerable

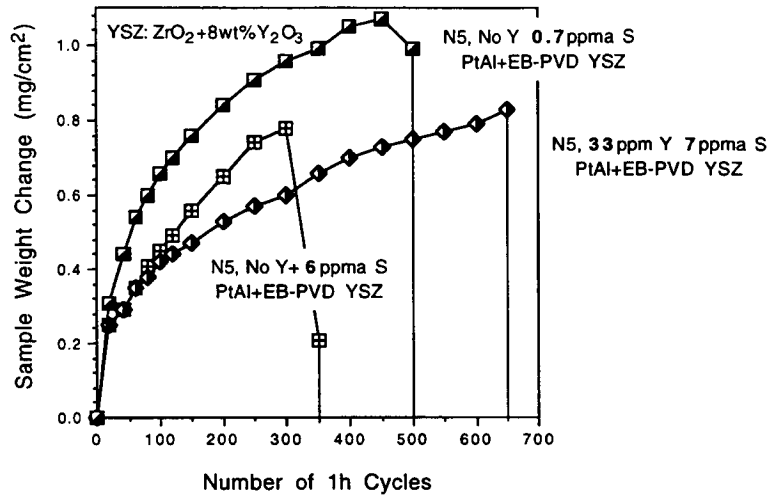
34 ppma Y (also 33ppma Zr and 540ppma Hf)

RE's in substrate, not added to Pt aluminide bond coat

Also - Pt in the aluminide bond coat - (10-20wt%)

known to be beneficial to alumina scale adhesion

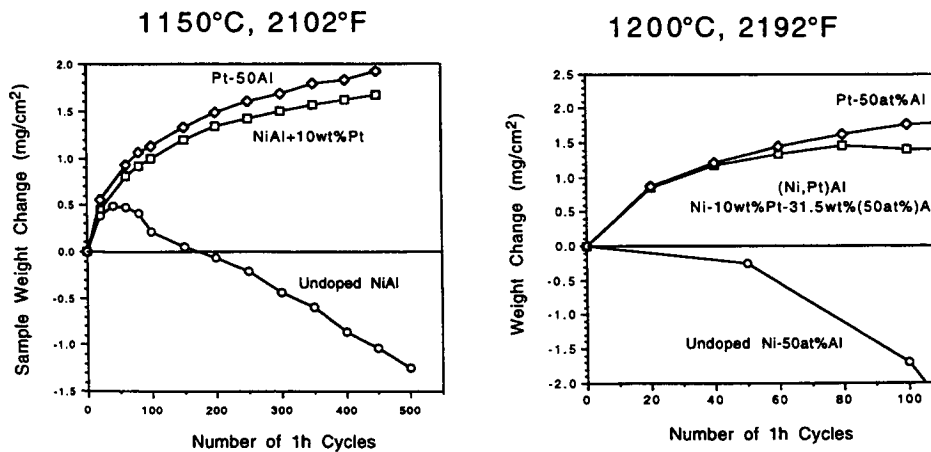
Effect of substrate on TBC lifetime changing Y and S altered performance in furnace cycling at 1150°C, 2102°F



René N5 substrates + (Ni,Pt)Al bond coat + 125 μ m EB-PVD YSZ top coat
de-sulfurization of substrate without Y and adding Y both increased
TBC lifetime at 1150°C

Figure 4

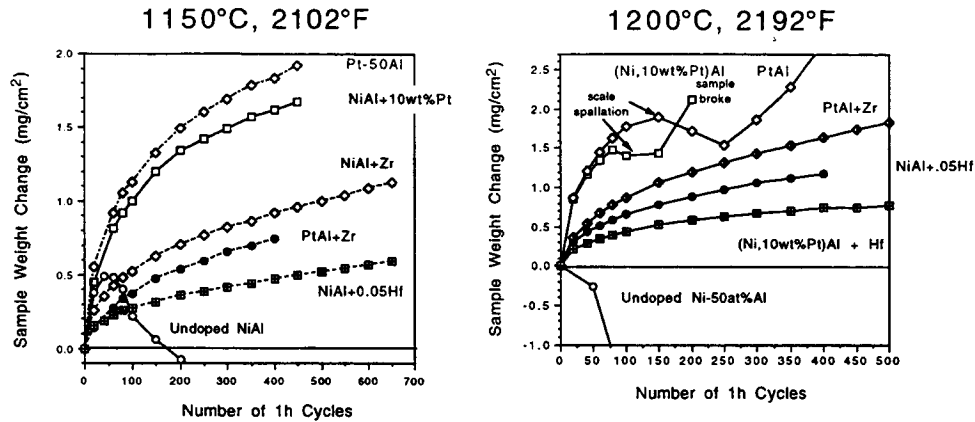
Effect of Pt on cast aluminides thermal cycling of uncoated coupons all contain $\approx 50\text{at}\% \text{Al}$



Comparing undoped (no RE additions) β -NiAl, PtAl and (Ni,Pt)Al(10wt%Pt):
The addition of Pt improves alumina scale adhesion in thermal cycling at
1150°C and 1200°C.

Figure 5

Effect of Pt on cast aluminides compared to Hf or Zr additions



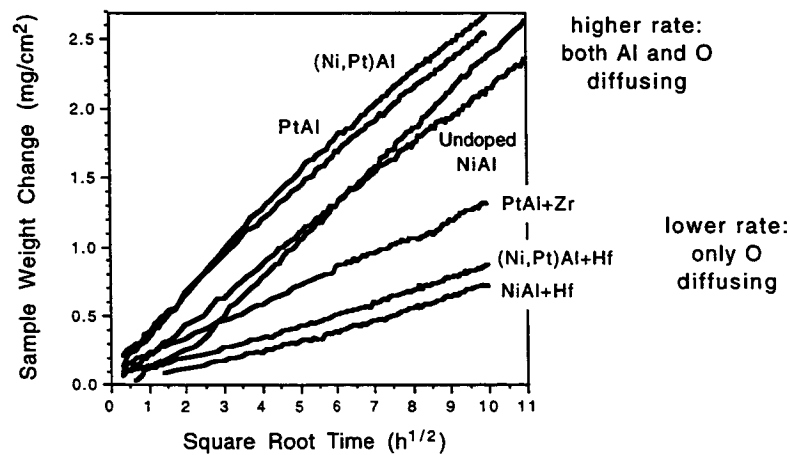
Higher weight gains on Pt aluminides because no RE doping
 Improvements associated with Pt additions begin to breakdown at longer times at 1200°C

RE additions such as Zr and Hf provide an additional benefit to Pt
 NiAl+0.05at%Hf - very adherent scale without Pt

Figure 6

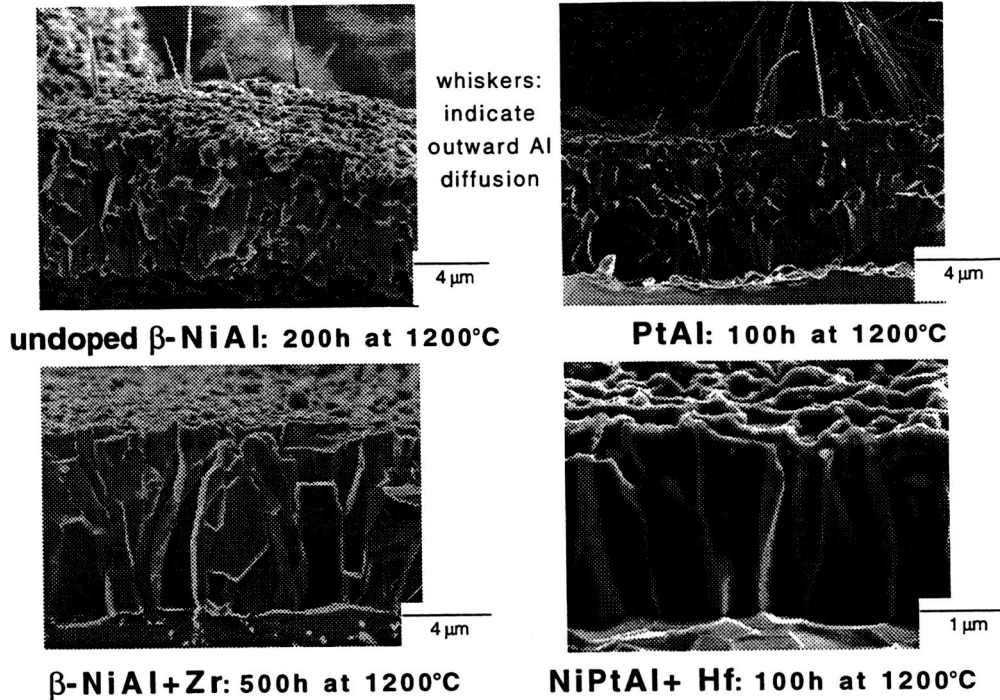
Effect of Pt on cast aluminides compared to Hf or Zr additions

Pt does not reduce the oxidation rate at 1200°C



RE doping reduces the reaction rate by changing the scale growth mechanism
 undoped α -Al₂O₃: grain boundary transport of both Al and O
 RE-doped α -Al₂O₃: growth primarily by O boundary diffusion
 RE (Zr, Hf, Y) ions segregated to the grain boundaries may inhibit Al diffusion

Little effect of Pt on α -Al₂O₃ microstructure isothermal exposures at 1200°C



Pt Effect vs. Reactive Element Effect (based on results from cast aluminides)

- Pt Effect
 - improves alumina scale adhesion
 - does not reduce the parabolic rate constant
 - does not change scale microstructure
- RE Effect
 - larger improvement in alumina scale adhesion
 - reduction in parabolic rate constant by 2-3X
 - change to a more columnar grain structure

Explanation of each effect is still a subject of debate

Both may strengthen the metal-oxide interface (e.g. by inhibiting S segregation) or inhibit the formation of interfacial voids

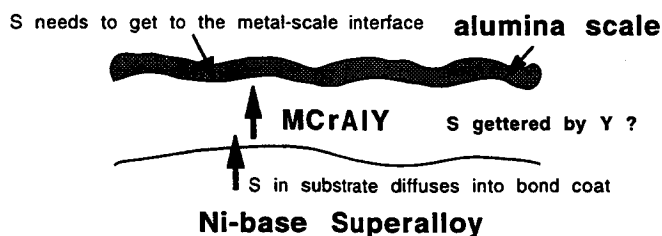
Unresolved RE-S Issues

Hf Effect

Hf is an extremely effect (best?) dopant in β -NiAl
 independent of nominal (3-30ppma) S contents
 comparable additions (0.05at%) in René N5 do not improve scale
 adhesion in the presence of 1ppma S

S Effect in presence of Y in MCrAlY

if Y getters S, then MCrAlY bond coat should getter S from
 substrate (?)



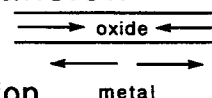
Why do scales spall?

(a few examples)

1. Cooling stresses

Difference in coefficient of thermal expansion
 between scale and metal, $\alpha_m > \alpha_{ox}$

- usually oxide in compression, substrate in tension
 but only in a perfect world



2. Growth stresses

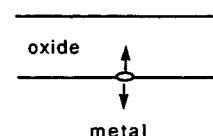
Isothermal stresses of uncertain origin

- deformation of substrate during oxidation
- convolutions in oxide lead to scale cracking

3. Defects

Prime example: Interfacial void formation

- limits contact between the metal and oxide
- stress concentrator - tensile stress
- crack initiator



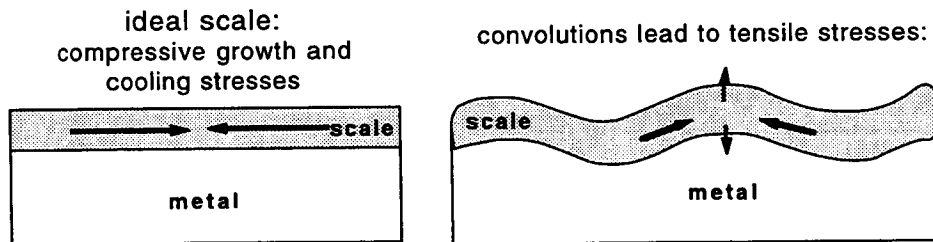
Dealing with Stress (a realistic approach)

Techniques such as functionally-grading do not work at high temperature due to oxidation

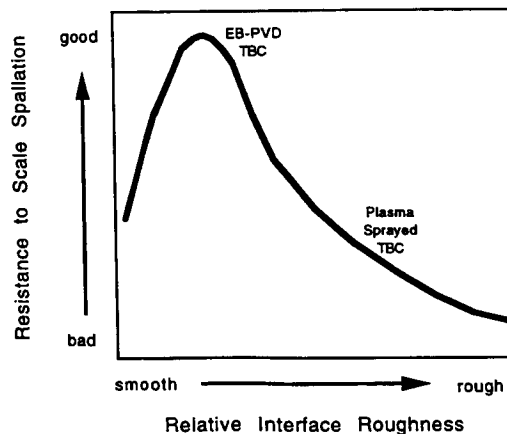
Alloys which have an adherent alumina scale generally have one common feature: a relatively flat, void-free, metal-scale interface

Mother Nature's strategy: maintain a flat, void-free, metal-scale interface

- maintains compressive stresses in the parallel plane and
- reduces out-of-plane tensile stresses
- RE-doping or de-sulfurizing to limit interfacial voids



Effect of surface roughness assuming all other variables constant



For a given:
oxidation temperature
substrate
scale thickness, etc.

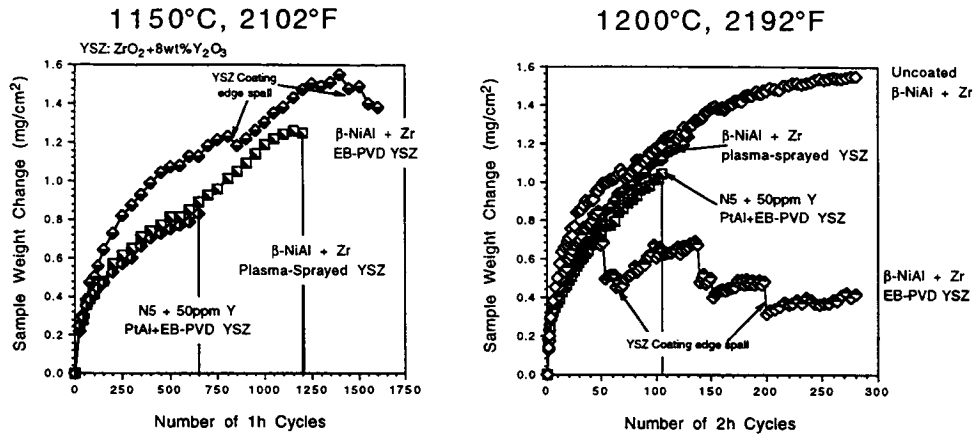
Predict that:

Rougher (less flat) surfaces produce convoluted scales with higher out-of-plane stresses which contribute to spallation

Very flat surfaces are subject to rapid propagation of interfacial cracks

One advantage of EB-PVD TBC's is depositing onto a flat substrate

Plasma-sprayed YSZ deposited on β -NiAl+Zr using NASA Lewis coating on "flat" substrate 1.25 μ m (5mil) coating in each case



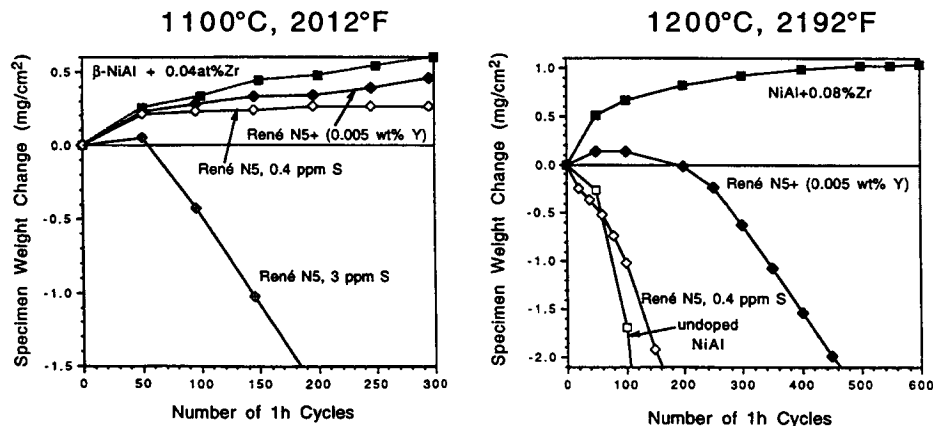
Typically, PS coatings on rough substrates for YSZ adhesion
also, EB-PVD lifetime > PS lifetime

In this case, PS on NiAl+Zr has longer lifetime than EB-PVD on René N5
However, EB-PVD on NiAl > PS on NiAl; still more defects in PS coating

Figure 7 Factor of 2 increase in life at 1150°C

Substrate Effects: NiCrAl-base vs. β -NiAl

1h cycles, in flowing O_2



At 1100°C, both RE additions and de-sulfurization improve the
alumina scale adhesion on uncoated René N5.

At 1200°C, neither technique achieves the same degree of scale
adhesion as observed on β -NiAl.

There appears to be a much greater temperature effect for René N5.

Figure 8

Mechanical effect of substrate on adhesion

Poorly understood area

Chemical effects (Cr, Al, S, RE) are well-studied

Mechanical effect (essentially unstudied) has numerous unresolved questions:

- which mechanical property is important?
 - creep strength? tension? compression? relaxation?
- can the substrate be too strong?
- is this directly related to scale growth stresses?
 - isothermal or cooling?

It is possible that very strong and very weak substrates are both less resistant to spallation

weak substrate - deformed by isothermal stresses, makes convoluted scale

Evans, et al. suggests that creep of substrate dissipates strain energy

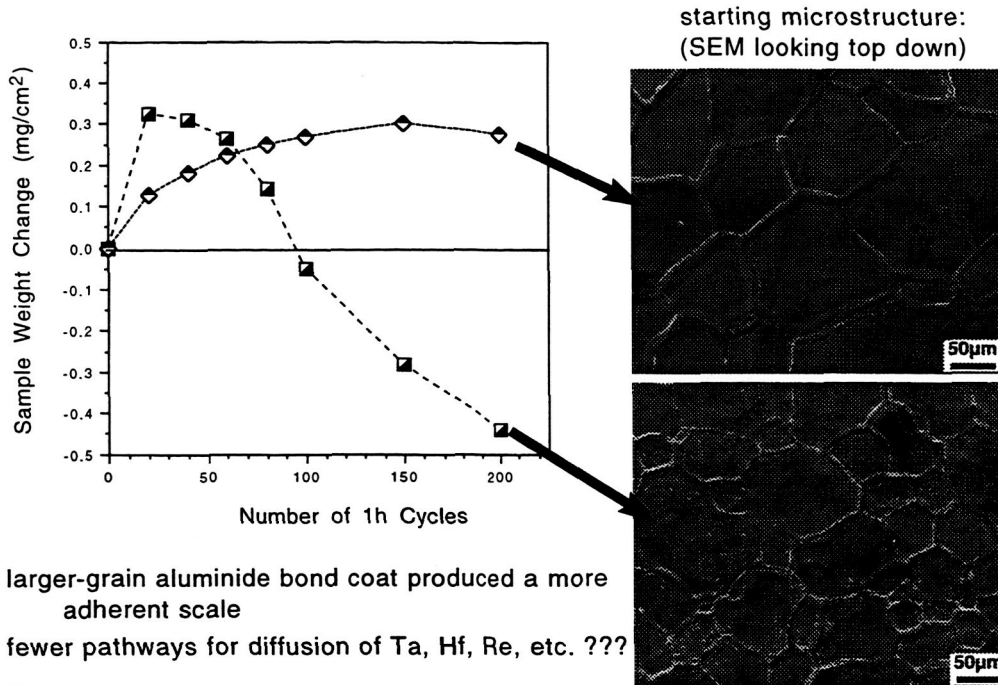
strong substrate - limited creep allows strain to build to failure

Possible implementation strategies

- * add more Al to aluminide coatings (at risk of embrittlement)
 - possibly limiting interfacial void formation
 - balance oxidation behavior with potentially more brittle coating
- * investigate bond coat microstructures or phases which may inhibit diffusion of elements from the substrate into the scale
 - grain size of bond coat
 - Engel-Brewer compounds
- * identify elements that are detrimental to scale adhesion
 - single elements or combinations
 - Hf: very oxygen active, bad in large quantities
 - Ta: active but not especially detrimental
 - Re: unknown effect
- * add REs to Pt aluminide coatings
 - RE doping will give an added boost to the benefits of Pt alone
 - slower growing scale, more adherent

CVD aluminide coating on René N5

larger bond coat grain size improves scale adhesion



Possible implementation strategies

- for higher temperature applications, aluminides appear to be superior to MCrAlY-based bond coats
 - at higher temperatures, observed more adherent scales on NiAl
- * pursue techniques (e.g. at NASA Lewis) for depositing plasma-sprayed top coats on flatter (less rough) substrates
 - a flatter metal-scale interface appears to be more adherent
- * design TBC systems based on the natural limitation that alumina scales thicker than $\approx 10\mu\text{m}$ will not remain ideally adherent and thus cannot support a ceramic top coat
 - flat scales: cooling strain of thick scale exceeds the metal-scale interface strength
 - convoluted scales: repeated thermal cycling will cause tensile stresses that will eventually cause failure
 - alumina is a brittle ceramic
 - if the $10\mu\text{m}$ goal is met, only lower bond coat temperatures will achieve longer TBC lifetimes

DEVELOPING NDE METHODS FOR COATED COMBUSTION TURBINE COMPONENTS

Paul J. Zombo, Westinghouse Electric Company

Ever-demanding performance improvements on the land based combustion turbine engines has increased combustion temperatures and placed a great demand on turbine blades. Coating systems have been developed to further protect the cooled blade base material from oxidation and creep damage. The coating systems discussed within this paper are comprised of a metallic coating, or a combination of metallic bond coat and a ceramic top coat. These coatings have a finite life and as the operating conditions increase in severity, the life of the coating decreases. As the coating deteriorates the potential for substrate degradation increases. After a predetermined operating time, the blades are striped, inspected and recoated for further use. This paper highlights the training sets manufactured as well as the comparison of a variety of NDE results from examination of the training set.

During interim examinations, when no blade replacement is planned, some blades exhibit local coating damage in the form of faint cracks, debonds, blisters or spalling, any of which leave the condition of the substrate in question. Previous field NDE methods have limited capabilities for through coating, substrate material evaluation. Eddy current methods have demonstrated some capabilities at sizing coating and substrate cracks but have not performed at differentiating between a coating crack that terminates into a debond and a coating crack that propagates into the substrate. Nor have eddy current methods been demonstrated to characterize substrate cracks or debonds that are not surface crack connected. The TBC coating adds a new complexity to the NDE of the coating system. Defects in ceramic TBC do not lend themselves to standard NDE methods and new possibilities for defects as well as substrate defect camouflage will be realized.

NDE methods are needed to characterize and size any combination of coating crack, substrate crack and debond. The method could be portable and allow examination of key areas of airfoil geometries, including the fillet radius at the base of the airfoil and airfoil edges. The system could perform an accurate assessment of the substrate, regardless of the coating on the bond integrity.

Test Specimen

Eight specimens were fabricated from each of the two superalloy materials chosen for study. The two alloys were Udimet 520 (Ni-18Cr-17Co-4Mo-3Al-3Ti) with a conductivity of 0.812 MS/m (1.4% IACS) and Inconel 738 (Ni-16Cr-8.5Co-3.5Al-3.5Ti-2.6W-1.8Mo-0.9Nb) with a conductivity of 0.724 MS/m (1.25% IACS). The specimens consisted of metallicly coated flat plates containing a variety of artificial defects. Each specimen contained a 3.175 or 6.350 mm long EDM slot and some of the specimens also contained a circular, simulated delamination. The EDM notches were introduced at various times in the fabrication process and their depths were varied to arrive at six different flaw types within the metallic coating and the substrate: coating only; coating and debond; coating and base; coating, debond and base; debond and base; and base only flaw. Figure 1 provides the overall dimensions of the specimens and illustrates the various flaw configurations used. TBC coatings were then applied to a select few of the

specimens with local artificial debonds under the TBC coating. Table 1 lists the attributes of each specimen.

Experimental Procedure

Prior to the TBC (top coat) application, three NDE methods were used to evaluate the training sets. The three methods were : surface wave ultrasonics at Pennsylvania State University under the guidance of Dr J. L. Rose [1], multi-frequency eddy current at Iowa State University under the direction of J. Moulder [2,3], and thermal wave imaging at Wayne State University under the direction of Dr. R. L. Thomas [4]. Refer to Table 2 for a qualitative comparison of all results.

Ultrasonic Experimentation

A surface wave contact pulse echo mode was used to evaluate the specimens. Throughout the experiment, all efforts were made to maintain constant interface conditions. Only the defect signals were acquired for each data set and all test scenarios were repeated four times. A frequency sweep was employed with the center frequency selected based on obtaining the maximum defect reflection. Seven incremental frequency data files were collected per specimen at increments of 0.1 MHz, about the center frequency (28 data sets per specimen). All data was then analyzed by neural networks with the following features: signal to noise ratio, average pulse width, average kurtosis, average skewness, power, and power ratio (selected).

Eddy Current Experimentation

Several measurement techniques were tried in hopes of achieving at least part of the stated objective. The measurements were carried out on an automated eddy current work station that consists of a computer-controlled 2-D scanner coupled with a Hewlett-Packard 4194A Impedance Analyzer. The measurement protocol consisted of performing a 2-D scan on each specimen at one frequency (usually 1 MHz) and then multi-frequency scans down the length of the flaw (a "flaw profile"). A conventional 2 MHz absolute surface probe was used to collect the 2-D scan and a multi-frequency scan consisting of ten frequencies from 0.1 to 1.0 MHz. The "flaw profile" scan was then repeated using a custom-designed uniform field probe which can operate over four decades in frequency, 10 kHz to 10 MHz. The scans using the uniform field probe typically covered a frequency of 100 kHz to 10 MHz, but some measurements from 10 kHz to 1 MHz were carried out as well.

Pulse-Echo IR Thermal Wave Imaging

Pulse-echo thermal wave imaging was used with a pulsed heat source on the surface of the sample to launch a plane thermal wave into the interior of the sample. High-power photographic flash lamps were used as a heat source, and an infrared video camera was used to monitor the time-dependent temperature contrast patterns on the surface of the sample. Images were acquired at the times after the flash which correspond to the transit times of the wave down to the defects and back. These images were recorded in a computer, and, after appropriate processing, were displayed on a monitor. Because of the short transit times through thin coatings, frame rates in the 100s of Hz and kHz ranges and an InSb focal plane array imager were used for the experiment.

Results and Discussion

The overall comparison of examination methods is shown in Table 2. The ultrasonic results were rather limited due to the fact that the cast Inconel base material did not lend itself well to ultrasonics because of coarse grain structure. As a result, only B,D and F combinations of flaw could be reviewed. The ultrasonic reporting was done exclusively with the use of neural networks with no human manipulation of the results. In all cases, two features dominated the recognition of type B, D and F flaws: average pulse width and average kurtosis, yielding an 83.3 percent recognition rate for a simultaneous 3 category sort. Figures 2a and b demonstrate a typical reference echo and crack echo as displayed.

Eddy current results were viewed in different forms throughout the frequency range of 100 kHz to 10 MHz. These included signal magnitude and phase vs. frequency, signal magnitude vs. phase. It was hoped that by collecting data over a wide range of frequencies, the technique would discriminate between the coating only cracks and cracks that had entered the base metal. Earlier work by Moulder and Nakagawa [3] has shown that buried cracks (such as the base metal cracks under an intact coating) have a characteristic impedance signature when plotted in a certain way, termed a McFetridge chart. The characteristic mentioned is the lack of an inflection point as the signal magnitude increases, and this was exhibited on subsurface defects that were not associated with a debond. Figures 3a and b demonstrate the McFetridge charts for these specimens.

Infrared examination results were reviewed simply as whole area images at increasing time intervals. The images clearly and simply demonstrate debonds, surface flaws and subsurface flaws independently. The reader is directed to a reduced set of Figures 4a-e to demonstrate this capability. Note that even subsurface flaws are distinguishable under debonds.

Summary

All methods had a degree of success at detecting and differentiating the targeted features. Only limited data was available to fully evaluate the ultrasonic method, however, due to our future direction toward cast substrates, ultrasonics was not pursued further at this time. Eddy current demonstrated excellent capabilities of clearly distinguishing subsurface flaws from surfaces flaws as long as debonds were not present. Unfortunately, our experience tells us that debonds are usually present in these situations. Thermal imaging demonstrated the best capabilities. Even in the presence of the debonds, all flaw types were distinguishable. Future work will be pursued in thermal imaging and electromagnetic methods.

References

1. J.L.Rose, K.M.Rajana, M.K.T.Hansch, P.J.Zombo : Base Metal Crack Detection Using Ultrasonic Guided Waves, Pennsylvania State University, 2/95.
2. B.Larson, J.Moulder, P.Zombo : Eddy Current Characterization of Flaws in NiCoCrAly-Coated Nickel Base Superalloys, Iowa State University, 3/95,presented at 1995 ASNT spring conference.
3. J.Moulder, Nakagawa,P.J.Shull, in review of progress in QNDE,Vol.7A,Edited by D.O.Thompson and D.E.Chimenti (Plenum Publishing Corp. 1988) pp.147-155 .
4. R.L.Thomas, L.D.Favro, L.Wang: Thermal Wave Imaging of coating Delaminations and Simulated Cracks, Wayne State University, 9/95

Table 1. Specimen Coating and Flaw Information

Specimen	Oxide Coating (mm)	Metallic Coating (mm)	EDM Length (mm)	EDM Depth (mm)	Flaw Type
I1	0.0127	0.152	3.175	0.152	C
I2	none	0.254	3.175	0.152	A
I3	0.0127	0.127	3.175	0.381	D
I4	0.0127	0.152	6.350	0.152	C
I5	none	0.254	6.350	0.152	A
I6	none	0.216	6.350	0.457	F
I7	0.0127	0.178	3.175	0.279	E
I8	0.0127	0.203	6.350	0.533	E
U1	0.0127	0.152	3.175	0.457	D
U2	none	0.152	3.175	0.432	B
U3	0.0127	0.152	3.175	0.483	D
U4	0.0127	0.152	6.350	0.762	D
U5	none	0.152	6.350	0.686	B
U6	0.0127	0.152	6.350	0.635	D
U7	none	0.152	3.175	0.279	F
U8	none	0.152	6.350	0.559	F

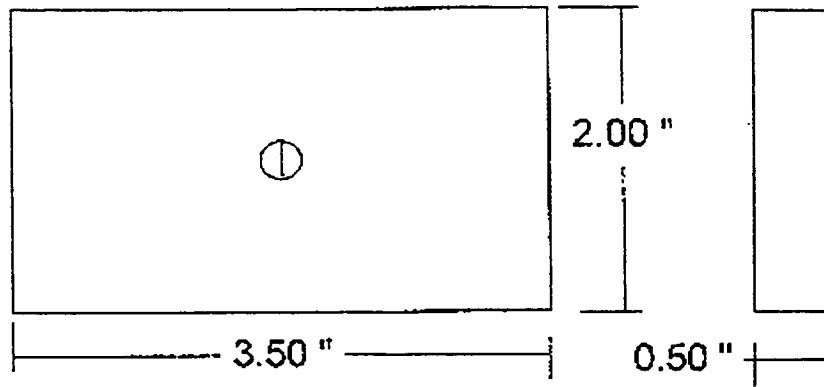
Flaw Type : A = Coating flaw, B = Coating Flaw with Debond, C = Coating Flaw with Base metal extension, D = Coating Flaw with debond and base metal extension, E = Debond and base flaw, F = base flaw only

Table 2 - Summary of Comparison of Three NDE Methods		Code	PSU UT Surf.		ISU MFET		WSU TWI	
Task	Sensitive		Separate	Sensitive	Separate	Sensitive	Separate	
Coating EDM from Coating/Base EDM	na	na	na	na	na	na	Y	N
Coating EDM from Coating with Debond	na	na	na	Y	Y	Y	Y	Y
Coating EDM from Coating/Base EDM & Debond	na	na	na	Y	Y	Y	Y	Y
Coating EDM from Base EDM & Debond	na	na	na	Y	Y	Y	Y	Y
Coating EDM from Base EDM	na	na	na	na	Y	Y	Y	n
Coating/Base EDM from Coating EDM & Debond	na	na	na	na	na	na	Y	Y
Coating/Base EDM from Coating/Base EDM & Debond	Y	Y	Y	Y	Y	N	Y	Y
Coating /Base EDM from Base EDM & Debond	na	na	na	na	na	na	Y	Y
Coating /Base EDM from Base EDM	Y	Y	Y	Y	Y	Y	Y	Y
Coating & Debond from Coating/Base EDM & Debond	na	na	na	Y	Y	N	Y	Y
Coating & Debond from Base EDM & Debond	na	na	na	na	Y	Y	Y	Y
Coating & Debond from Base EDM	na	na	na	na	Y	Y	Y	Y
Coating / Base EDM & Debond from Base EDM & Debond	na	na	na	na	Y	Y	Y	Y
Coating / Base EDM & Debond from Base EDM	Y	Y	Y	Y	Y	Y	Y	Y
Base EDM & Debond from Base EDM	na	na	na	na	Y	N	Y	Y

Upper Case - Good Result, Lower Case - Weak Result. Y - Yes, N - No, na - Not Applicable

A = Coating EDM
B = Coating EDM with Base EDM Extension
C = Coating EDM with Debond

D = Coating EDM with Base EDM Extension and Debond
E = Base Metal EDM with Debond
F = Base EDM



Flaw Types

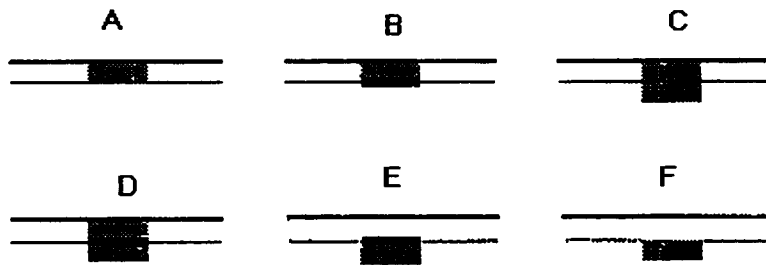
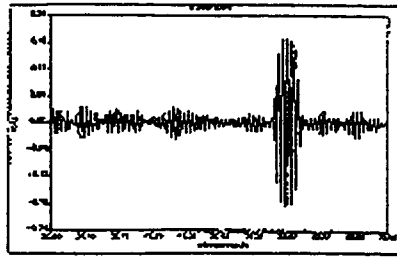
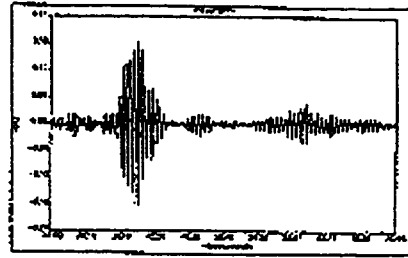


Figure 1. Overall Dimensions of Specimen and Flaw Types.
Specimen types are also cross-referenced in Table 1.



Specimen 1/1: Referencor echo



Crack echo $f = 2.23 \text{ MHz}$

Figure 2a and b [1] - Typical Pulse Echo results with and without flaw

In738 Samples
Comparison of Signal Magnitude vs. Phase
For a Frequency Range of 100 kHz to 10 MHz
 UFEC Probe Centered Over Flaw

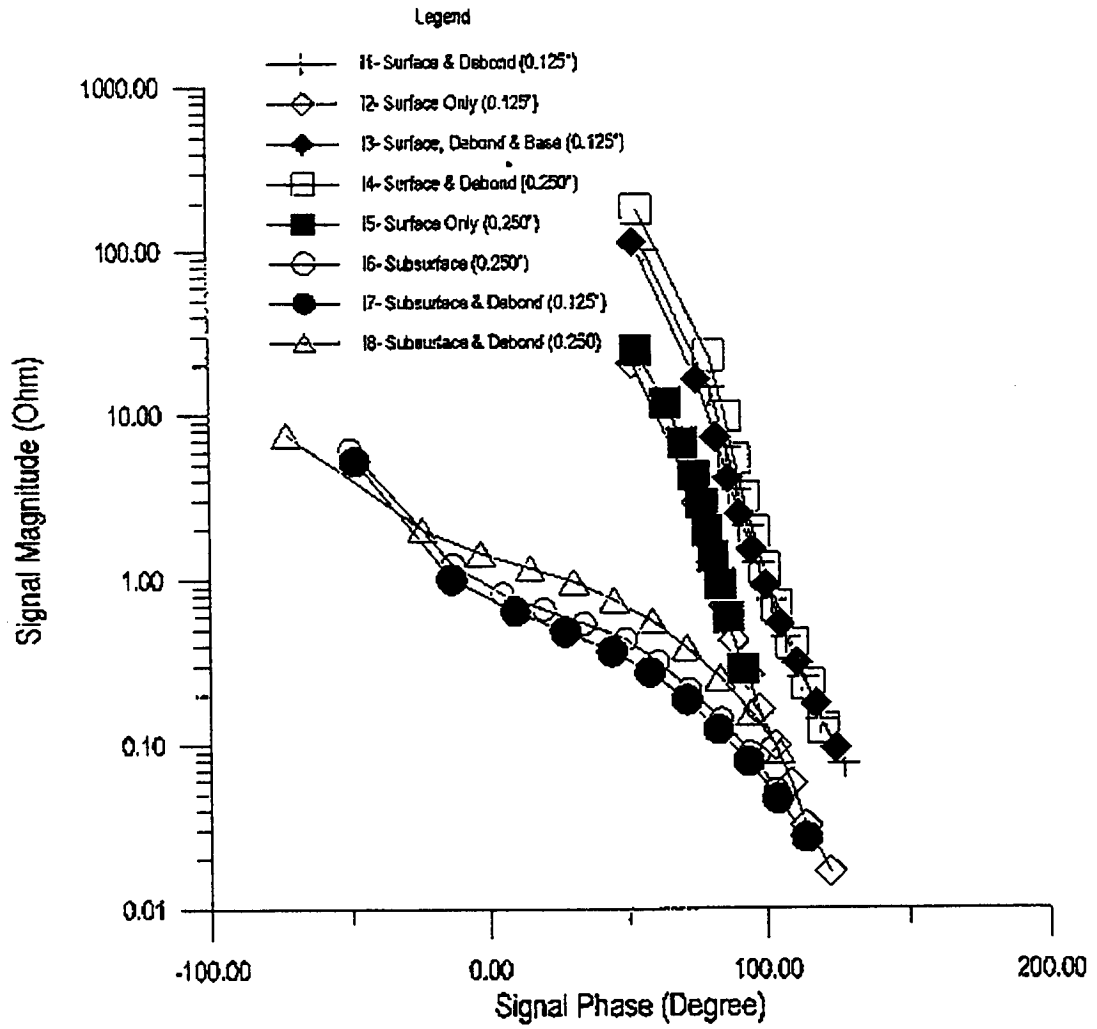


Figure 3a [2]

**U520 Samples
Comparison of Signal Magnitude vs. Phase
for a Frequency Range of 100 kHz to 10 MHz**

UFEC Probe Centered Over Flaw

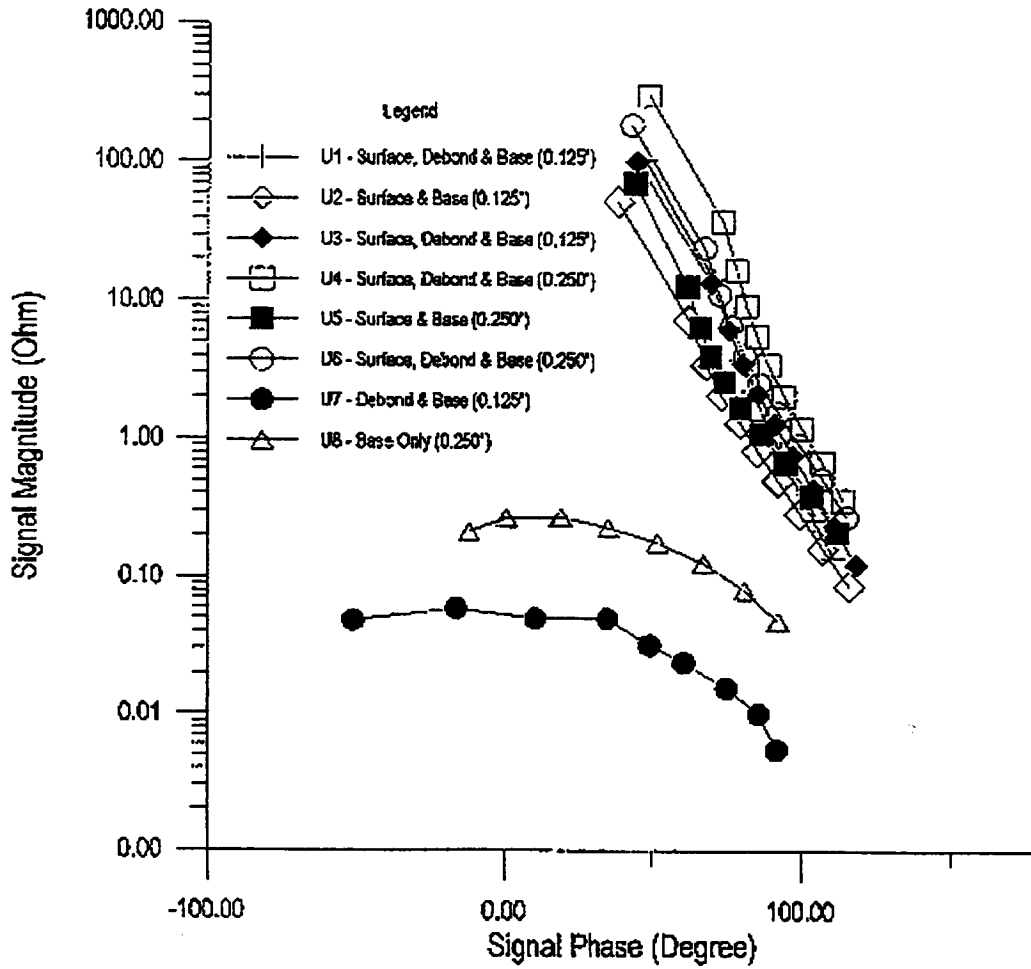
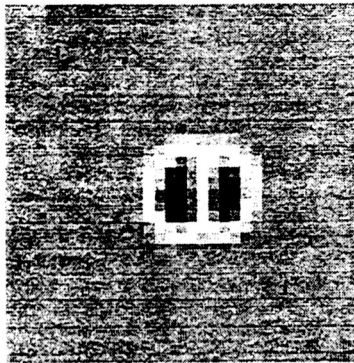


Figure 3b [2]

Figure 4a [4]- Coating Flaw with Base Metal Extension and Debond



■

Figure 4b [4] - Coating Flaw with Debond

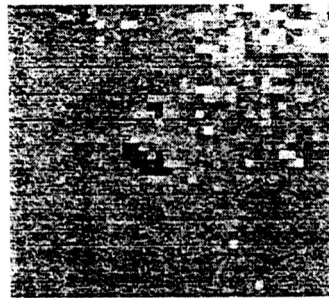


Figure 4c [4] - Coating Flaw

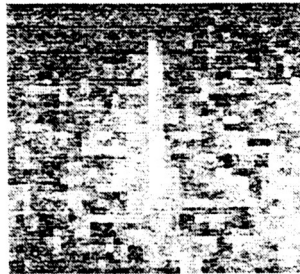


Figure 4d [4] - Base Metal Flaw under coating



Figure 4e [4] - Base Metal Flaw Under Debond



INVESTIGATION OF THERMAL HIGH CYCLE AND LOW CYCLE FATIGUE MECHANISMS OF THICK THERMAL BARRIER COATINGS

Dongming Zhu † and Robert A. Miller
National Aeronautics and Space Administration
Lewis Research Center, Cleveland, OH 44135

INTRODUCTION

Ceramic thermal barrier coatings have attracted increasing attention for diesel engine applications. The advantages of using the ceramic coatings include a potential increase in efficiency and power density and a decrease in maintenance cost. Zirconia-based ceramics are the most important coating materials for such applications because of their low thermal conductivity, relatively high thermal expansivity and excellent mechanical properties. However, durability of thick thermal barrier coatings (TBCs) under severe temperature cycling encountered in engine conditions, remains a major question. The thermal transients associated with the start/stop and no-load/full-load engine cycle, and with the in-cylinder combustion process, generate thermal low cycle fatigue (LCF) and thermal high cycle fatigue (HCF) in the coating system [1]. Therefore, the failure mechanisms of thick TBCs are expected to be quite different from those of thin TBCs under these temperature transients. The coating failure is related not only to thermal expansion mismatch and oxidation of the bond coats and substrates [2-4], but also to the steep thermal stress gradients induced in the coating systems [2, 4-8]. Although it has been reported [6, 9] that stresses generated by thermal transients can initiate surface and interface cracks in a coating system, the mechanisms of the crack propagation and of coating failure under the complex LCF and HCF conditions are still not understood. In this paper, the thermal fatigue behavior of an yttria partially stabilized zirconia coating system under simulated LCF and HCF engine conditions is investigated. The effects of LCF and HCF on surface crack initiation and propagation are also discussed.

EXPERIMENTAL

A ZrO_2 -8% Y_2O_3 ceramic coating and an Fe-25Cr-5Al-0.5Y bond coat were plasma-sprayed onto steel angle iron and rectangular bar substrates. The plasma spray conditions are listed elsewhere. [10] The thicknesses of the ceramic coating and the bond coat were about 1.6 mm and 0.28 mm, respectively. LCF and HCF tests were conducted using a 1.5 KW CO_2 laser. The CO_2 laser is especially suited for testing ZrO_2 -based thermal barrier coatings because it can deliver a well-characterized and well-controlled heat energy to the surface of the ceramic coating. Since ZrO_2 is opaque at the 10.6 μm wavelength of laser beam, the light energy is absorbed by the coating surface rather than penetrating into the coating. This test rig was controlled by a PC programmed to generate various LCF heating and cooling cycles. Backside air cooling was used to maintain the desired temperature gradient. The pure LCF cycles were generated by the continuous wave (CW) laser mode, and the HCF combustion cycles were simulated using the pulsed laser mode, as shown in Fig. 1. Because the high energy laser pulse was used, an HCF component was inherently superimposed on the LCF cycles. The laser pulse period and pulse width were fixed at 92 and 6 milliseconds (ms) respectively, as shown in Fig. 2. Laser power density distributions under the test conditions are shown in Fig. 3. Coating surface and backside metal temperatures were measured by an infrared pyrometer and an R-type thermocouple, respectively. The tested coating surfaces and cross-sections were examined under both optical and electron scanning microscopes to obtain information on crack density and depth.

When pulsed laser heating is used, a severe thermal transient will be induced even in the absence of LCF cycling. This temperature fluctuation under the HCF conditions was modeled by the one dimensional finite difference approach. In order to verify the validity of this model under the present laser beam conditions, the method was compared with analytical solutions for both a uniform, constant irradiance model and a Gaussian beam model in calculating the surface

† National Research Council — NASA Research Associate at Lewis Research Center.

Keywords: Thermal High Cycle and Low Cycle Fatigue, Ceramic Sintering and Creep, Fatigue Mechanisms

temperature swing [11]. The temperature swing predicted by all three approaches was essentially identical, implying that the Gaussian beam is sufficiently widespread to allow the use of the one-dimensional assumption. The modeled results indicate that the HCF transient occurs only at the surface of the ceramic coating. This layer may be defined as the HCF interaction depth at which appreciable temperature fluctuation (greater than about 10% the surface temperature swing) will occur. The temperature swing, generated by the pulsed laser, increases with increasing laser power density and pulse width. The HCF interaction layer depth, which is independent of laser power density, increases with laser pulse width. Under the HCF condition of 6 ms heating, the interaction depth is about 0.15 mm. The temperature profiles generated by the pulsed laser under peak heat fluxes of 3.38 and 4.95 MW/m² are illustrated in Fig. 4. The HCF stress distributions are shown in Fig. 5. It can be seen that this temperature fluctuation induces high-frequency cyclic stresses on the coating surface, with the predicted HCF stress amplitude of about 60 MPa at 3.38 MW/m² and 100 MPa at 4.95 MW/m². The dashed lines in Fig. 5 represent the ceramic surface stress values at the average steady state surface temperatures under the corresponding average heat fluxes 0.220 and 0.323 MW/m², respectively.

EXPERIMENTAL RESULTS

Surface cracking was observed for all specimens which were tested to a total heating time of 256 hours. Compared to the pure LCF tested specimen, the combined LCF and HCF tests produced higher crack densities. At the angle iron corners, nearly parallel cracks which run across the corners were formed. In contrast, equiaxial crack networks were generated by the laser tests at the rectangular specimen surfaces. At the edges of the rectangular specimens, parallel cracks similar to those found on the angle iron corners were observed with crack direction perpendicular to the edges. As shown in Fig. 6, the crack length in the ceramic coating increases with LCF cycle number. Also, higher surface temperature results in a longer crack length. The HCF component tends to increase the overall coating crack length, especially when crack branching is considered. As can be seen in Fig. 7, the fatigue crack growth rate, based on crack depth in the coating, increases with the characteristic HCF cycle number, N_{HCF}^* , which is defined as HCF cycle numbers per LCF cycle.

DISCUSSION

In plasma-sprayed ZrO₂-Y₂O₃ coatings, the primary creep stage is often observed due to the porous and microcracked nature of these coatings [12, 13]. This creep behavior is probably related to stress-enhanced ceramic sintering, splat sliding, and the stress redistribution around the splats and microcracks. The stress-dependent deformation can result in coating shrinkage and thus stress relaxation at temperature under the compressive stresses. The strain rate $\dot{\epsilon}_p$ can be generally written as

$$\dot{\epsilon}_p^i = A \cdot \exp\left(-\frac{Q}{RT}\right) \cdot \left(\sigma_{th}^0 - \epsilon_p^{i-1} \frac{E_c}{1-\nu_c}\right)^n \cdot t_i^{-s} \quad (1)$$

where $\dot{\epsilon}_p^i$ and ϵ_p^{i-1} are the creep strain rate at time t_i , and the total accumulated strain at the previous time step t_{i-1} , respectively, A , n and s are constants, Q is the activation energy, T is temperature, R is the gas constant, σ_{th}^0 is the initial thermal stress in the coating, and E_c and ν_c are the elastic modulus and Poisson's ratio of the ceramic coating. The stress relaxation effect on the creep strain rate is accounted for by the ϵ_p^{i-1} term in Equation (1).

The pulsed laser induced temperature swing can generate high compressive stresses that can result in the coating surface fracture. More importantly, the surface tensile stress, mainly generated by coating shrinkage due to coating sintering and creep at temperature, could also induce cracking during cooling. Fig. 8 shows that for a given heat flux, the HCF component will generate a higher creep rate at the coating surface compared to the pure LCF mode. Since the laser HCF component will promote both coating surface creep and surface compressive cracking, accelerated crack initiation and higher surface crack density at the coating surfaces are expected.

The LCF mechanism is closely associated with the relatively fast coating sintering and creep at high temperatures. These time and stress dependent strains in the ceramic coating will lead to a tensile stress state during cooling. Fig. 9 illustrates the modeled influence of coating creep behavior on LCF crack opening displacement and crack depth. The LCF mechanism is schematically shown in Fig. 10.

The HCF is associated with the cyclic stresses originating from the high frequency (typically about 10 Hz) temperature fluctuation at the ceramic coating surface. The HCF thermal loads act on the crack by a wedging mechanism, as schematically illustrated in Fig. 10. This wedging process can be further enhanced by crack face shifting and spalled particle intrusion. As shown in Fig. 11, the HCF stress intensity factor amplitude decreases with increasing crack length, but increases with increasing temperature swing. The HCF damage effect also increases with the interaction depth, the thermal expansion coefficient and Young's modulus of the ceramic coating [10]. It should be noted that, depending on the coating stress state at high temperature, the HCF may affect crack propagation far beyond the laser interaction depth. This has been demonstrated experimentally in pure HCF cycling where high temperature swings were generated near the surface of the ceramic coating [11]. In this case, the high surface thermal loads resulted in cracks that propagate deep into the coating.

CONCLUSIONS

The combined LCF and HCF tests induced more severe coating damage compared to the pure LCF tests. Significant coating sintering and creep are detrimental to the coating fatigue resistance. Strong interactions between LCF and HCF have been observed from the experiments. In the absence of severe interfacial oxidation, the LCF mechanism is closely related to coating sintering and creep phenomena at high temperatures. The stress relaxation at temperature induces tensile stresses in the coating after cooling. The HCF mechanism is associated with a surface wedging process. The HCF damage effect will increase with the temperature swing, the thermal expansion coefficient and the elastic modulus of the ceramic coating, as well as the HCF interaction depth.

ACKNOWLEDGMENTS

This work was performed while the first author held a National Research Council-NASA Lewis Research Center Research Associateship partially supported by the Army Research Laboratory. The authors are indebted to M. Brad Beardsley, Caterpillar Inc., for valuable discussions. The authors are grateful to George W. Leissler for his assistance in the preparation of TBC coatings.

REFERENCES

- [1] Miller, R. A., *NASA TM-103130, DOE/NASA/21794-1*, May, 1990.
- [2] Beardsley, M. B. and Larson, H. J., *DOE/NASA/0332-1, NASA CR - 190759*, 1992.
- [3] Zhu, D. and Miller, R. A., *NASA TM-107360, Army Research Laboratory Technical Report ARL-TR-1254*, November 1996.
- [4] Zhu, D. and Miller, R. A., *in preparation*, 1997.
- [5] Yonushonis, T. M., *NASA CR-187111*, August 1991.
- [6] Takeuchi, Y. R. and Kokini, K., *Journal of Engineering for Gas Turbines and Power*, **116**, 266-271, 1994.
- [7] Kokini, K., Choules, D. B. and Takeuchi, Y., in *Thermal Barrier Coating Workshop* (ed. Brindley, W. J.), 235-250, Cleveland, Ohio, March 27-29, 1995.
- [8] Sidewell, C. V. and Cruse, T. A., *Report 960801*, 1996.
- [9] Kokini, K., Takeuchi, Y. R. and Choules, B. D., *Surface and Coating Technology*, **82**, 77-82, 1996.
- [10] Zhu, D. and Miller, R. A., *NASA Technical Paper TP-3676, Army Research Laboratory Technical Report ARL-TR-1341*, March 1997.
- [11] Zhu, D. and Miller, R. A., in *International Conference on Metallurgical Coatings and Thin Films, ICMCTF 97* San Diego, California, April 21-23, 1997.
- [12] Johnsen, B. P., Cruse, T. A., Miller, R. A. and Brindley, W. J., *Journal of Engineering Materials and Technology*, **117**, 305-310, 1995.
- [13] Thurn, G., Schneider, G. A. and Aldinger, F., *Materials Science and Engineering*, to be published, 1996.

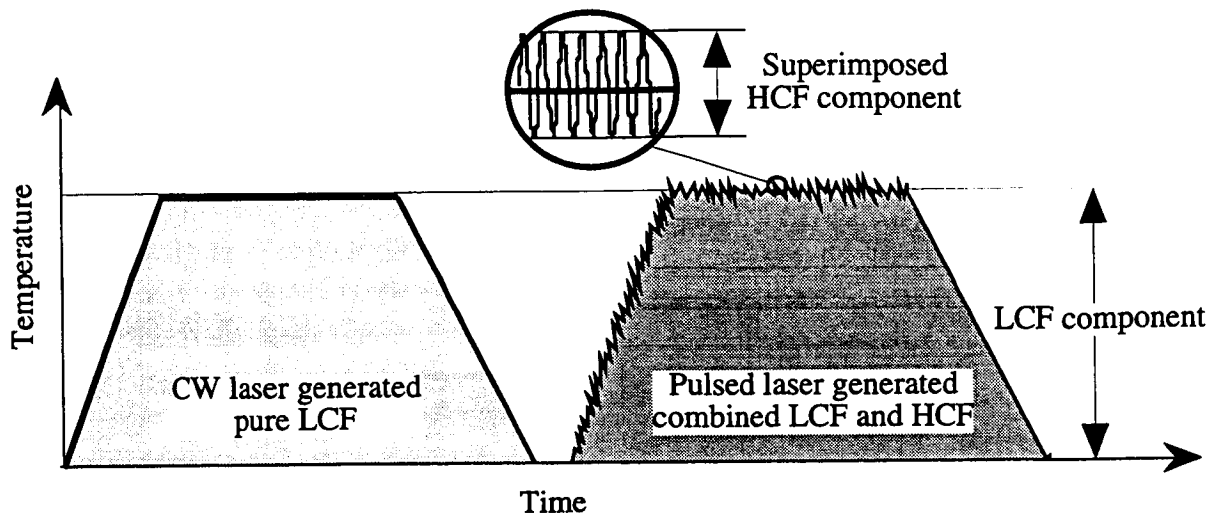


Fig. 1 Schematic diagram showing laser induced pure LCF and combined LCF and HCF cycles.

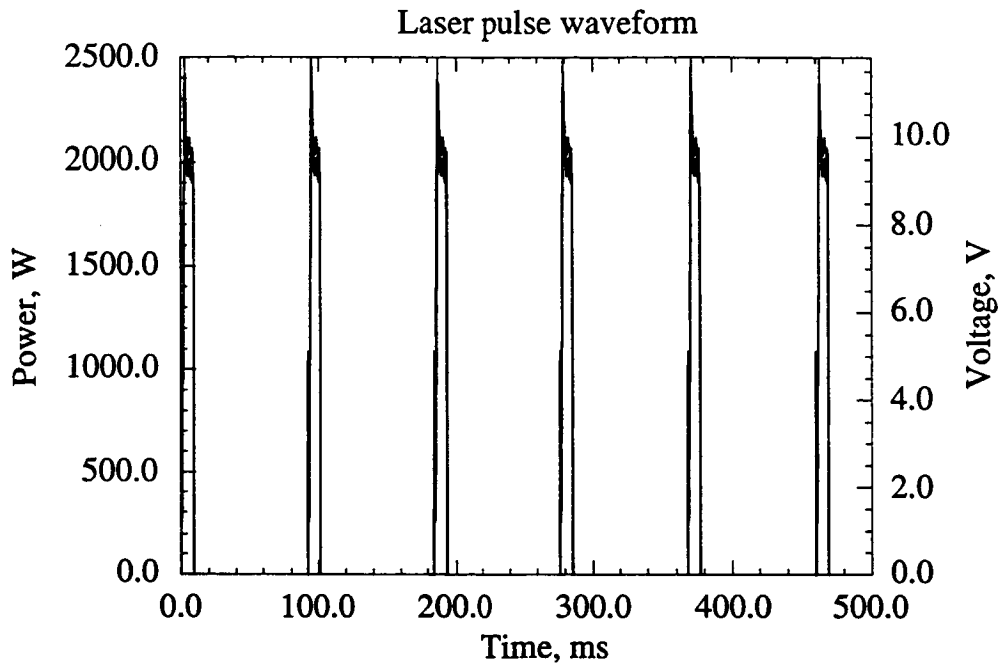


Fig. 2 Laser pulse waveform recorded from the laser pulse signal by an oscilloscope (Tektronix THS 720 Tekscope).

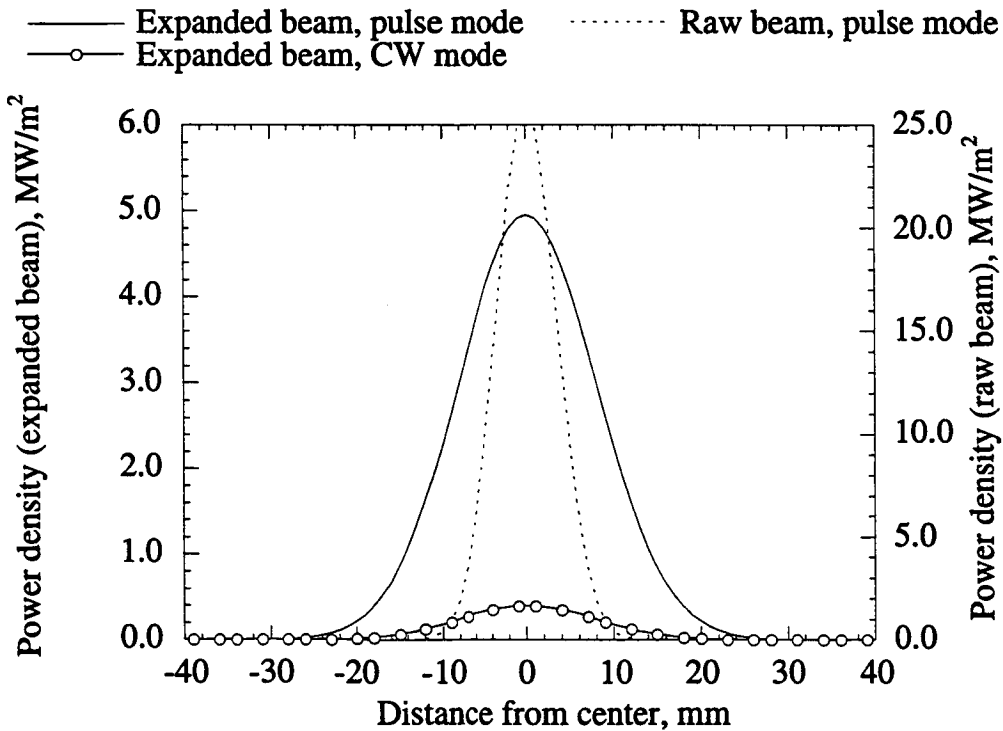


Fig. 3 Laser power density distributions estimated from the measured laser waveform and total power output. The peak power density from the pulsed laser beam at the beam center is 4.95 MW/m², corresponding to the average or equivalent continuous wave (CW) laser power density 0.323 MW/m². Minor beam non-uniformity observed is neglected.

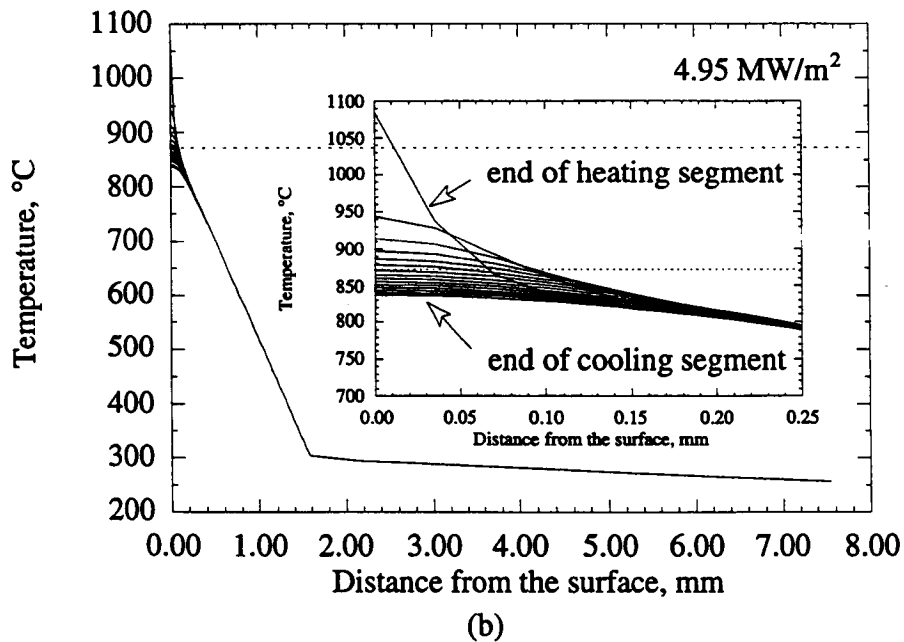
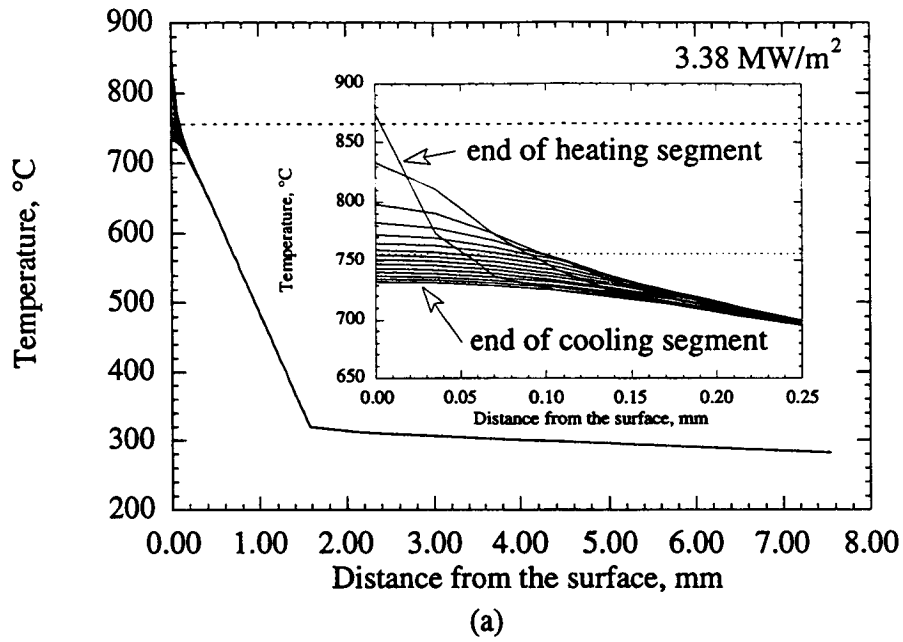
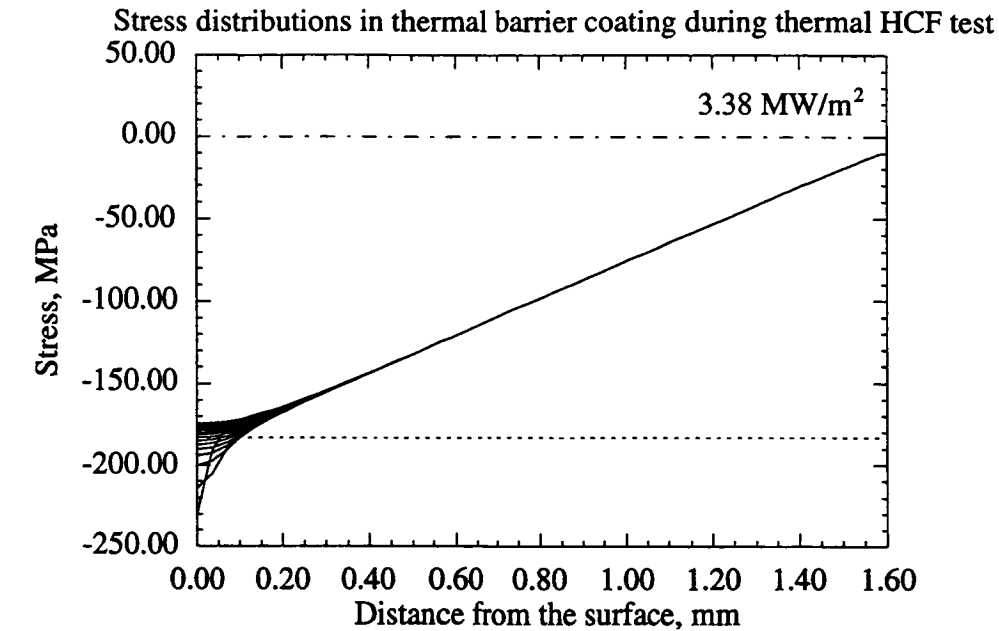
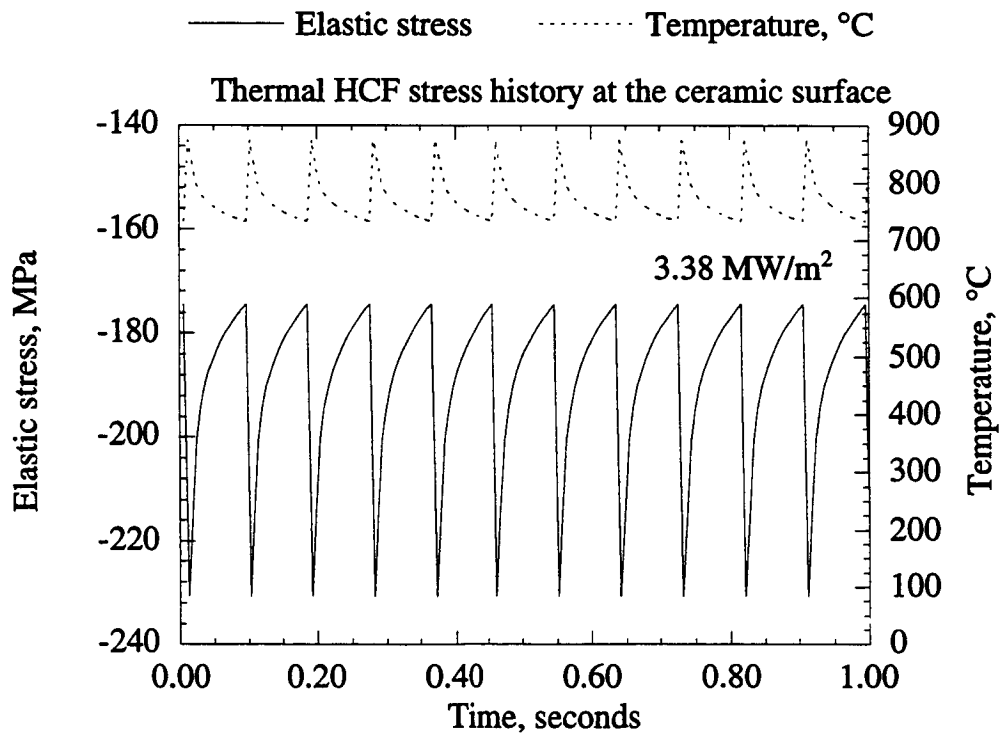


Fig. 4 Predicted temperature profiles generated by pulsed laser heating (pulse width 6 ms). A higher heat flux produces a higher temperature swing and average surface temperature (dashed line represents the average temperature).



(a)



(b)

Fig. 5 Predicted thermal stresses induced by pulsed laser heating. Besides a constant stress gradient generated by the steady state heating, high frequency HCF cyclic stresses are present near the ceramic coating surface. Peak power density 3.38 MW/m².

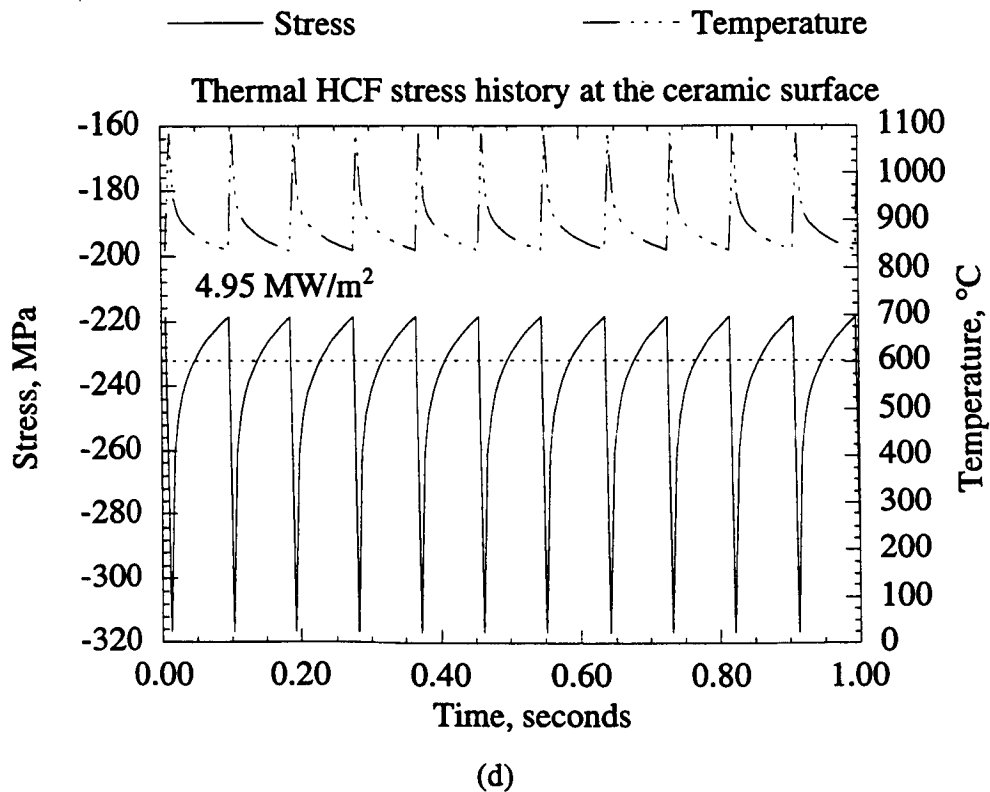
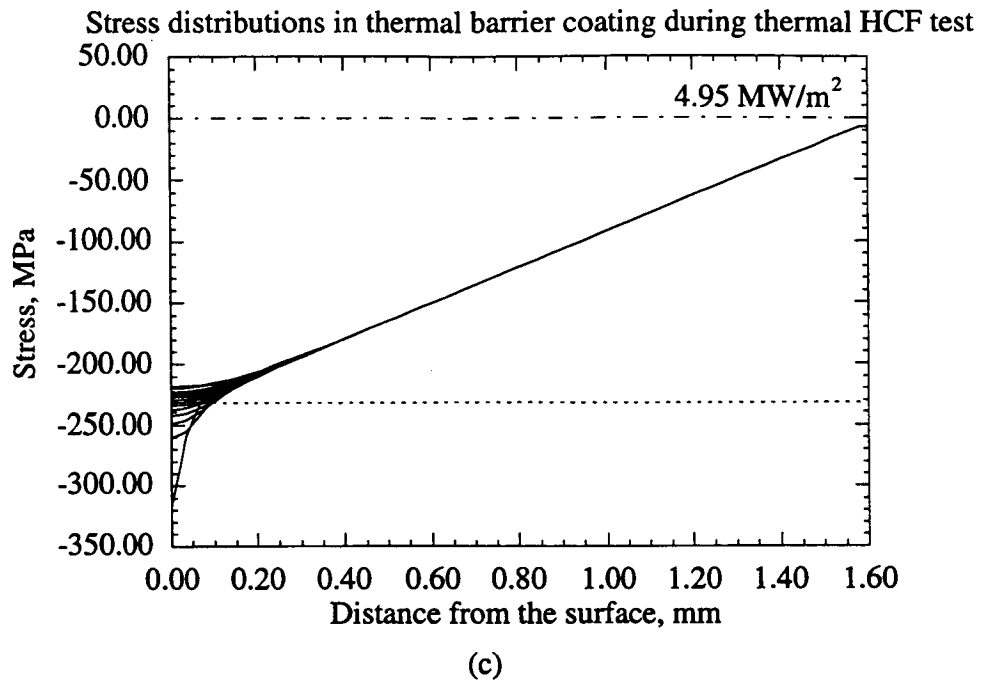


Fig. 5 Predicted thermal stresses induced by pulsed laser heating. Besides a constant stress gradient generated by the steady state heating, high frequency HCF cyclic stresses are present near the ceramic coating surface (continued). Peak power density 4.95 MW/m².

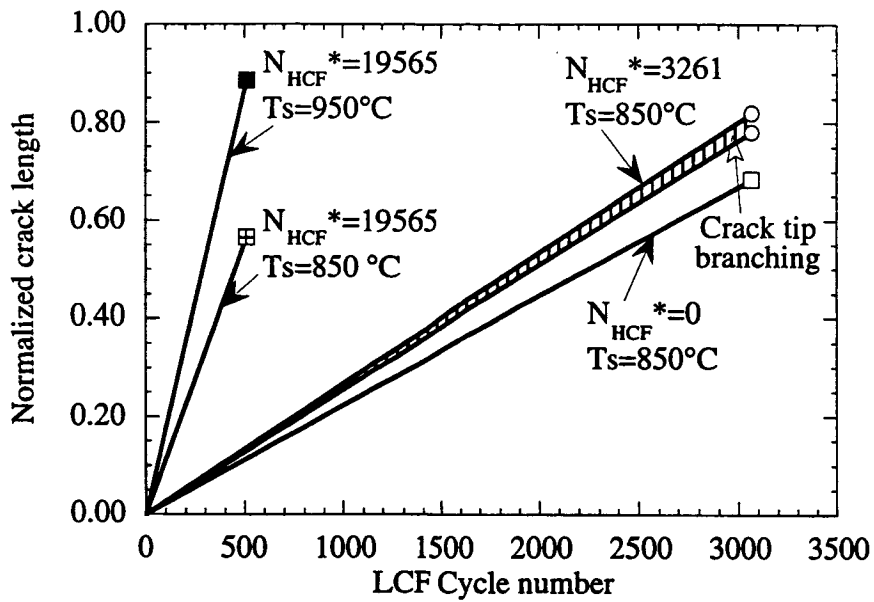


Fig. 6 The crack length (normalized to coating thickness) as functions of LCF and characteristic HCF numbers.

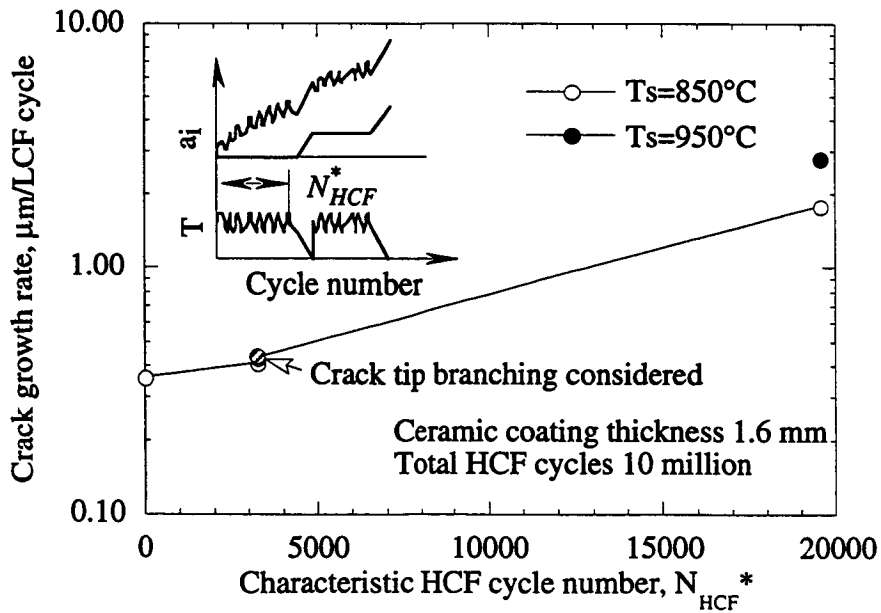


Fig. 7 Crack growth rate as a function of characteristic HCF cycle number (HCF numbers per LCF cycle), N_{HCF}^* .

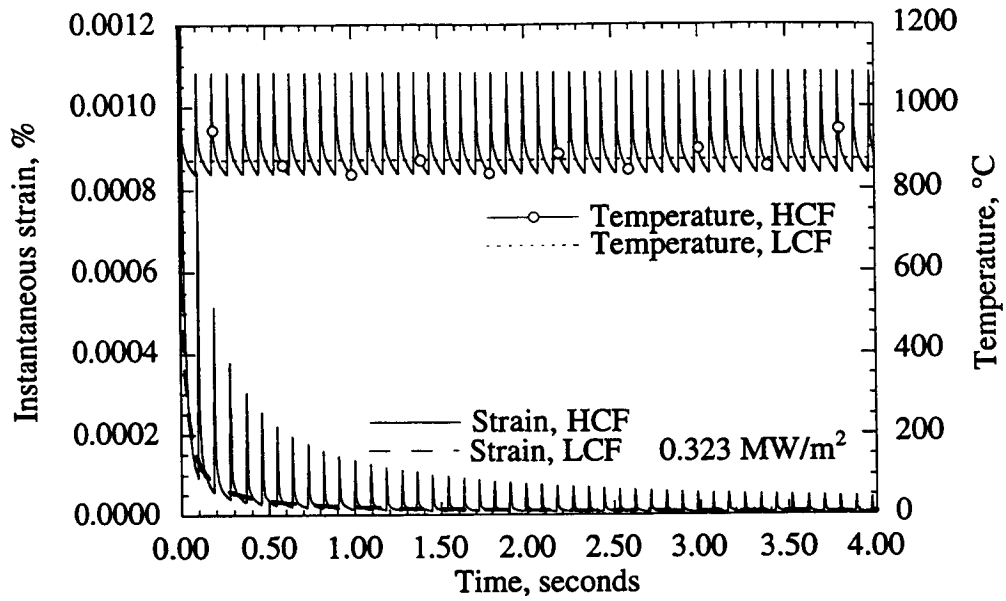


Fig. 8 Predicted instantaneous creep strains under LCF and HCF conditions (stress and time exponents are 0.48 and 0.82 respectively, activation energy 114 KJ/mol)

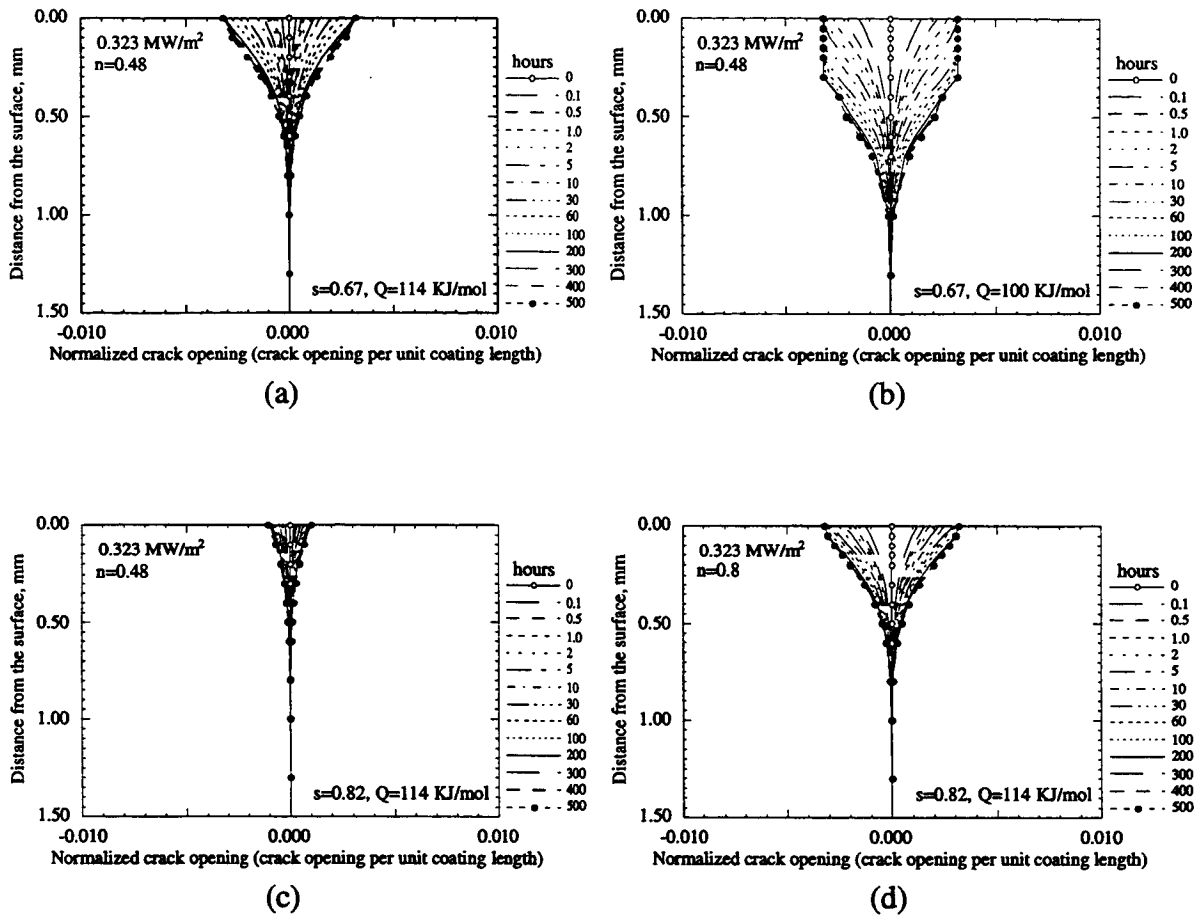


Fig. 9 Simulated LCF cracks showing the influence of coating creep behavior (ceramic surface temperature 872°C , n stress exponent, s time exponent, and Q activation energy)

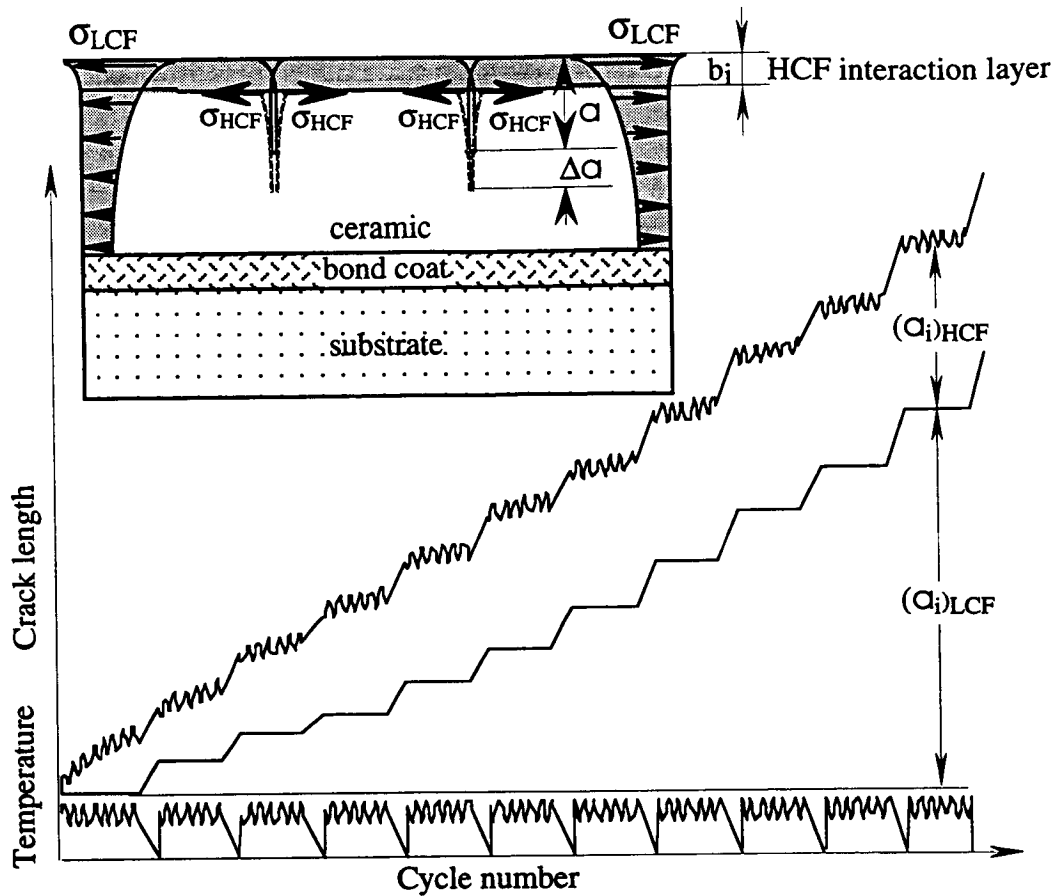


Fig. 10 Schematic diagram showing LCF and HCF mechanisms.

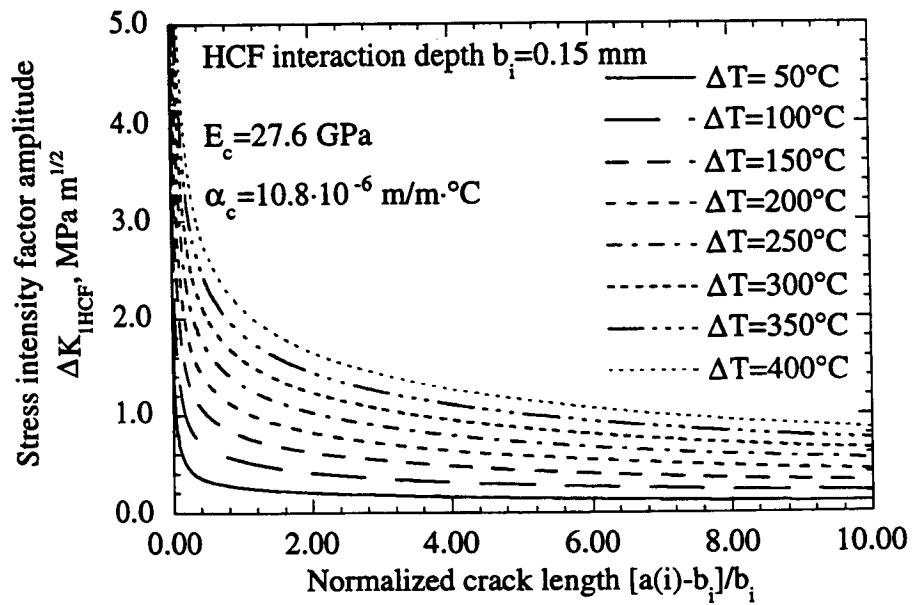


Fig. 11 The HCF stress intensity factor amplitude as a function of normalized crack length and temperature swing ΔT .

INTELLIGENT PROCESSING OF MATERIALS FOR THERMAL BARRIER COATINGS

**Y.C. Lau, Curtis A. Johnson, Dennis M. Gray, Paul Houpt, Murray Penney and
H.P. Wang**

GE Corporate Research and Development, Schenectady, New York

Introduction

Advanced land-based gas turbine performance is highly dependent on operating or firing temperatures, which has increased rapidly in recent years (Fig. 1) because of market needs and technology advances. High operating temperatures require improved material performance throughout the turbine hot sections. To meet this goal, state-of-the-art superalloy technology must be complemented with high-performance thermal barrier coatings (TBCs) with improved capabilities including maximum surface temperature, temperature gradient, life and reliability. Thermal barrier coatings are currently applied to many land-based turbine components by air plasma spray process. The standard air plasma spray process is an open-loop process with no feedback of the process and coating conditions during deposition. Thus on-line disturbances and the continuous wearing of the torch hardware during deposition may adversely affect the coating quality and create significant part-to-part, operator-to-operator and booth-to-booth variations. As a result, these coatings may not have the consistent quality and durability needed. The objective of this work is to develop a more knowledge-based and data-intensive "intelligent process" for air plasma spray that will improve the reproducibility, quality and reliability of TBCs, thus allowing the potential payoffs of TBCs, such as increased efficiency, reduced maintenance, and lower emission, to be optimized in future turbine designs. This "intelligent process" must also be capable of scaleup to industrial manufacturing operations.

Intelligent Processing of Materials (IPM) for TBCs

The IPM concept for the plasma spray process is illustrated in Figure 2. A suite of sensors serves as the "eyes" of the system controller, providing selected information for feedback control. The empirical database and physics-based process models provide a basis for designing the system controller, including both multivariable and rule based techniques to update the spray process parameters and ensure that the coating will meet specifications.

A three-year program has been funded in 1995 by NIST-ATP to develop intelligent processing methods for air plasma spraying of TBCs. This program is divided into five major technical tasks:

1. **Sensor Task:** development of a comprehensive sensor suite, and selection of optimum control sensors;
2. **Data base Task:** development of empirical data-base;
3. **Modeling Task:** development of plasma-particle process models;

4. Control Task: development of process control model using Tasks 2 and 3 results; and
5. Integration Task: integration of the system controller with the sensors and the plasma controller, and demonstration of the online process control.

Sensor Development

To better utilize resources, proven commercially available sensors are being utilized to the fullest extent possible. These sensors fall into three categories, as listed in Table 1. Also listed in Table 1 are examples of sensors that are being investigated in this work.

The part surface can interfere with particle and plasma properties measurements, therefore, the torch will be swung away from the part being coated to a suite of sensors at a reference station at specific intervals between coating passes. As an example of a particle sensor, a Tecnar DPV2000 particle sensor developed by NRC of Canada [1] is being investigated as a means of measuring local particle temperature, velocity, size and plume distributions.

The "target" sensors continuously monitor the part surface during TBC deposition for coating surface temperature and thickness distributions. The part surface temperature distribution is measured by an infrared imaging camera operated at a wavelength of about 10 μm . In-process coating thickness measurement is the most challenging objective of the sensor task. A number of techniques are being explored including laser-based noncontact ultrasound, x-ray fluorescence, microwave and laser triangulation [2] techniques.

Torch sensors may include standard instrumentation that measure torch current and voltage, plasma gas flow and average powder feed rates during deposition of TBCs.

Table 1: Sensor categories and respective measured process parameters

Sensor Categories	Measured process parameters
"Reference Station" Sensors	<ol style="list-style-type: none"> 1. Local particle temperature, velocity and size <ul style="list-style-type: none"> - DPV2000 particle sensor 2. Plasma properties <ul style="list-style-type: none"> - Enthalpy probe for off-line plasma model verification and database generation
"Target" Sensors	<ol style="list-style-type: none"> 1. Coating surface temperature <ul style="list-style-type: none"> - Long-wavelength infrared imaging camera 2. Coating thickness <ul style="list-style-type: none"> - Laser triangulation and other techniques
"Torch" Sensors	Torch current and voltage, gas flow rates and mean powder feed rates

Process Control Development

The process control development focuses on improving the control of the plasma torch, the repeatability of the coating process by using feedback of process and coating parameters as measured by a suite of process sensors. Using the results from the database and modeling tasks, process control models have been developed to control process parameters such as particle temperature and velocity. Figure 3 shows the particle temperature and velocity controller developed based on an empirical 'input-output' process model and an interaction matrix generated by the DPV2000. It has been demonstrated that on-line decoupled mean particle temperature and velocity control can be achieved with coordinated manipulation of torch current and plasma gas flow.

Acknowledgment

Much of the work reported in this paper is supported by the NIST/ATP Materials Processing for Heavy Manufacturing program under contract 70NANB5H1132 with Ms. Clare M. Alloca as the ATP program manager. The support is gratefully acknowledged.

References:

1. Moreau, C.; Gougeon, P.; Lamontagne, M; Lacasse, V.; Vaudreuil, G. and Cielo, P.: On-line Control of the Plasma Spraying Process by Monitoring the Temperature, Velocity and Trajectory of In-flight Particles, Proceedings of the 7th National Thermal Spray conference, Boston 1994, pp. 431-437.
2. Kuroda, S.; Fukushima, T. and Kitahara, S.: *In-situ* Measurement of Coating Thickness during Thermal Spraying using an Optical Displacement Meter, J. Vac. Soc. Technology, Jan/Feb 1987, pp. 82-87.

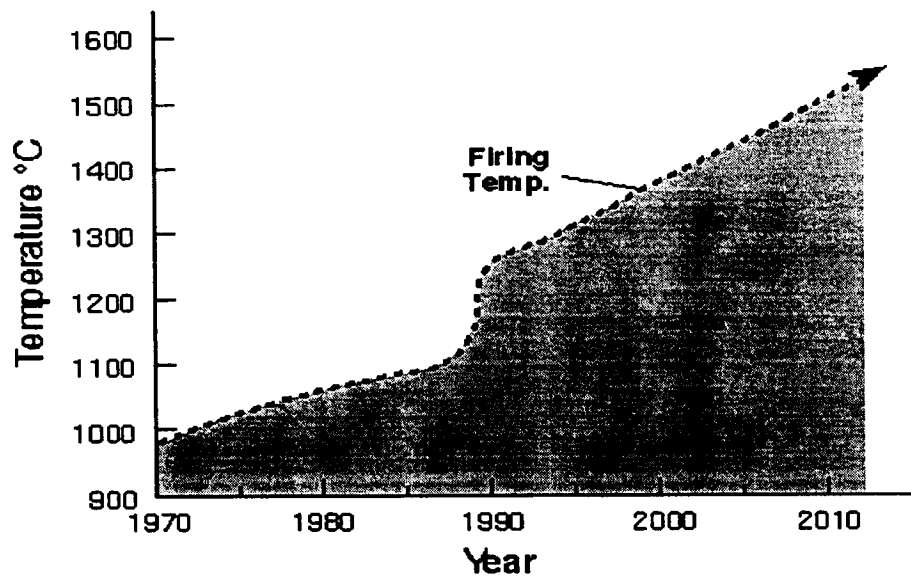


Figure 1: Gas turbine operating temperature trend. High operating temperatures require improved material performance throughout the turbine hot sections.

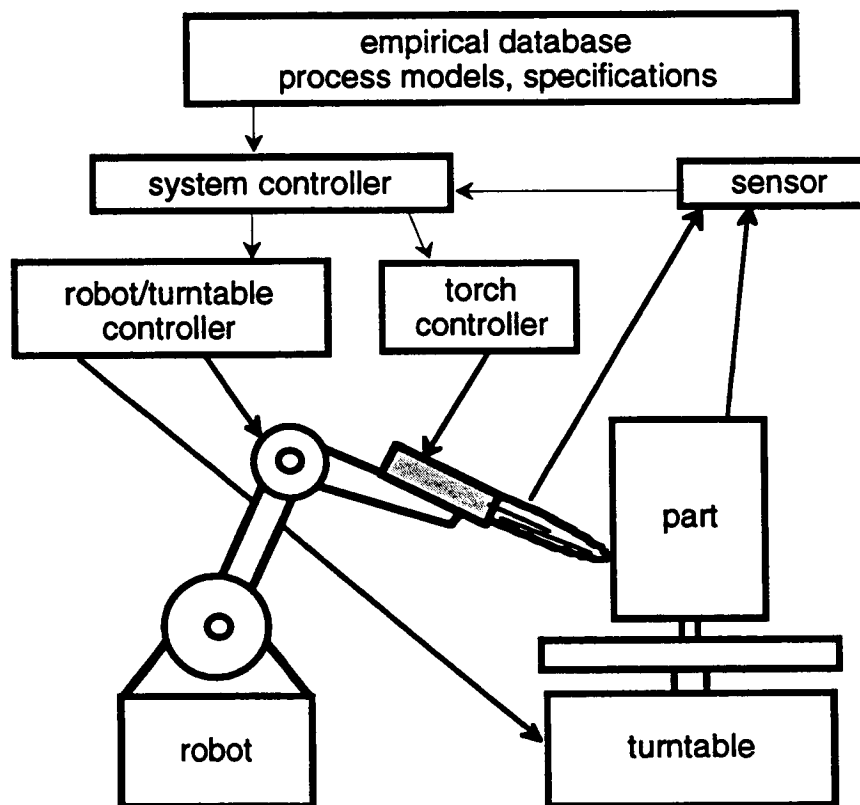


Figure 2: IPM for air plasma spray TBC process. The sensors provide feedback to the system controller that controls the torch and robot conditions. The empirical database and physics-based process model provide the set of rules for the system controller to control the spray process.

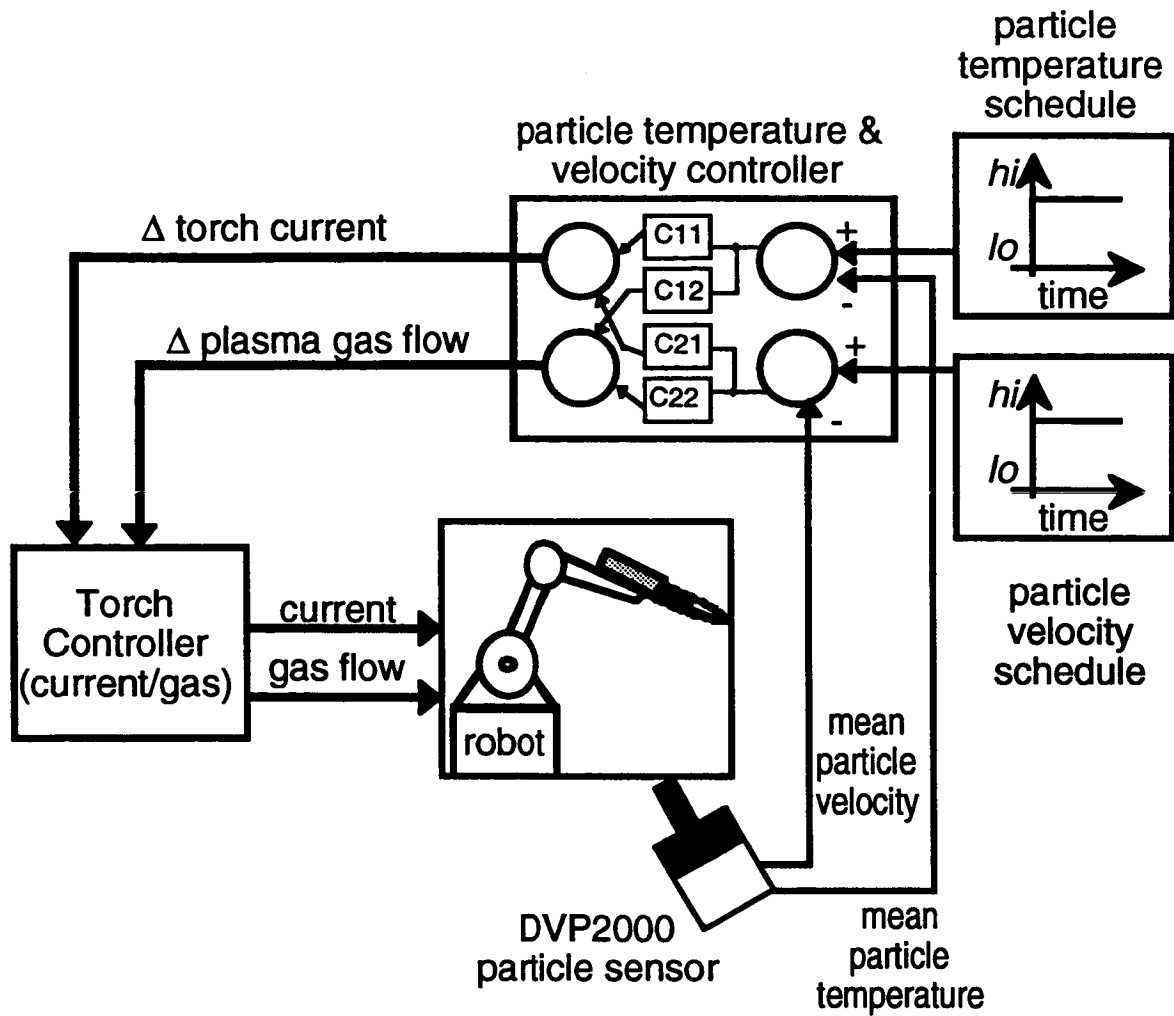


Figure 3: Particle temperature and velocity controller based on an empirical "input-output" process model and an interaction matrix generated by the DPV2000. On-line decoupled mean particle temperature and velocity control can be achieved with coordinated manipulation of torch current and plasma gas flow.

DYNAMIC MODEL FOR SIMULATION OF HEAT TRANSFER, VAPORIZATION, VAPOR TRANSPORT, AND DEPOSITION IN EB-PVD PROCESS

Farzin H. Azad
GE-Corporate Research and Development
(IPM-PVD Consortium¹)
Schenectady, NY

Introduction

The intelligent processing of materials (IPM) concept involves the integrated use of process models, sensors and control systems to achieve reproducible manufacturing processes and increased product quality. Detailed models provide in-depth process understanding by enabling extensive exploration of the process parameter space, but require large computation time and resources. The simplified or reduced-order models capture the key dynamics of the system and are suitable for control algorithm design and real-time implementation. These models are typically based on a combination of simplified process physics and selected empirical data. This paper describes a reduced-order model for dynamic simulation of heat transfer, vaporization, vapor transport, and deposition in an electron beam physical vapor deposition (EB-PVD) process for thermal barrier coating production.

Figure 1 summarizes the role of process models in the IPM methodology and indicates how a simplified or “reduced-order” dynamic model fits this structure. The physical phenomena that should be treated in an IPM implementation of the EB-PVD process, and the process models needed to accomplish this, are depicted in Figure 2. The reduced-order model—the overall scope and structure of which are shown in Figures 3 and 4—captures only a key subset of the elements shown in Figure 2.

From a control system design perspective, the key objective is to relate the dynamics of the melt temperature, deposition rate, and component surface temperature to changes in e-beam and over-source heater power inputs. A brief description of the reduced-order model and some sample results are presented below.

Model Structure

The feed material, which is introduced in the form of an ingot from the bottom of the PVD chamber (Figure 3), is heated by a scanning electron beam. Heat generation within the melt is caused by the fraction of incident electrons that are not back-scattered at the

¹ Sponsored by DARPA under Agreement MDA972-95-3-0039 Vapor Phase Intelligent Processing of Materials-Thermal Barrier Coatings

melt surface. Electrons penetrating the ZrO_2 melt are thermalized in a very short distance as compared to the melt thickness [1]. For example, the penetration depth in ZrO_2 melt for 50 keV electrons is about 5 μm . Thus, e-beam heating of the melt can be treated as heating by a scanning surface heat flux.

Electron beam back-scattering is governed by electron energy, target atomic number, and angle of incidence. Figure 5 depicts the variation of the back-scattered energy with e-beam energy and target atomic number [2]. The curve labeled "best fit to data" in Figure 5 is used for computation of the back-scattered fraction at normal incidence. The effective atomic number of ZrO_2 is computed based on mass concentrations of Zr and O [3]. A best fit to experimental back-scattering data at oblique incidence of 10 keV and higher electrons [4] is employed to relate absorption at oblique angles to that at normal incidence (Fig. 5).

Other key parameters affecting the transient behavior of heat generation are the e-beam spot size on the melt surface ("focus"), e-beam scan pattern, and pattern frequency. Slow scan rates, and small spot sizes (as compared to the thermal diffusion and convection scales within the melt), produce a transient temperature distribution under the beam footprint which is significantly higher than the average melt temperature. The detailed melt pool model is used to generate effective curves, relating the evaporation rate to the average melt temperature, for different scan patterns, frequencies and spot diameters.

An energy balance for a lumped-parameter [5] representation of the melt relates the rate of change of melt temperature to the net power retained by the melt (Figure 6). Heat transfer in the feed material is computed by modeling the ingot as a cylindrical fin. The corresponding geometry and formulation are shown in Figure 7.

Radiative exchange is the dominant mode of heat transfer in the PVD chamber. The chamber is modeled as a gray-diffuse enclosure [6] (Figure 8). The formulation yields a system of simultaneous equations relating the net radiative heat flux at each of the surface elements to the surface temperatures.

Simplified models of evaporation and vapor transport are summarized in Figure 9. The Clausius-Clapeyron equation [7] is used to relate the vapor pressure at the melt surface to the corresponding temperature. The vapor mass flux at the melt surface is obtained by assuming a Maxwellian velocity distribution in the vapor [8]. An estimate of the temperature of the vapor arriving at the component surface is obtained by assuming isentropic expansion of the vapor [9]. In Figure 9, subscript (1) represents the vapor conditions just above the melt surface (prior to expansion), and subscript (2) corresponds to the vapor conditions at the component location (after expansion).

The net deposition rate is the difference between the mass flux of the vapor that arrives at, and is intercepted by the part, and the back-vaporization mass flux at the coating surface. This is obtained, as shown in Figure 10, by assuming line-of-site vapor transport from the melt surface to the component location.

In order to derive a simple formulation for the rate of change of component surface temperature, the following assumptions are made:

- The coating is thin compared to typical part “thickness”. Thermal mass of the coating is much smaller than that of the part and can be neglected.
- Conduction and internal radiation in the coating can be represented by a single, “effective” coating thermal conductivity.
- Thermal conductivity of the part (component) is high enough (low Biot number) so that the part can be represented as a single “lump”.

The resulting formulation for the component energy balance is summarized in Figure 11.

Sample Results

Figures 12 through 14 depict computed steady-state dependence of the melt temperature, deposition rate, and component surface temperature on e-beam and over-source heater power inputs. The results are nondimensionalized with respect to a nominal operating point. The sensitivity of the component (substrate) surface temperature to changes in melt and chamber wall temperatures are compared in Figure 15. The high degree of radiative coupling between the component and chamber walls suggests the need for implicit computation of the wall temperatures in the next implementation of the reduced-order model. Figure 16 shows the sensitivity of the deposition rate to the melt pool temperature and indicates the required resolution for a melt temperature sensor. Typical transient responses are shown in Figure 17.

References

1. Flik, M.I. and C.L. Tien, “Intrinsic Thermal Stability for Scanning Electron Microscopy of Thin-Film Superconductors,” *J. Appl. Phys.*, Vol. 67, No. 1, 362-370, 1990.
2. Archard, G.D., “Back Scattering of Electrons,” *J. Appl. Phys.*, Vol. 32, No. 8, 1505-1509, 1961.
3. Bishop, H.E., “The Absorption and Atomic Number Correction in Electron-Probe X-Ray Microanalysis,” *Brit. J. App. Phys., Ser. 2.* Vol. 1, 673-684, 1968.
4. Darlington, E.H., “Backscattering Of 10-100 keV Electrons from Thick Targets,” *J. Phys. D: Appl. Phys.* Vol. 8, 85-93, 1975.
5. Kreith, F. and M.S. Bohn, *Principles of Heat Transfer*, Harper & Row, 1986.
6. Siegel, R. and J.R. Howell, *Thermal Radiation Heat Transfer*, 3rd ed., Hemisphere Publishing Corporation, 1992.
7. Wark, K., *Thermodynamics*, McGraw-Hill, 1983.
8. Langmuir, I., “The Vapor Pressure of Metallic Tungsten,” *Physical Review*, Vol. II, No. 5, 329-342, 1913.
9. Saad, M.A., *Compressible Fluid Flow*, 2nd ed., Prentice Hall, 1993.

IPM Methodology - Role of Process Models

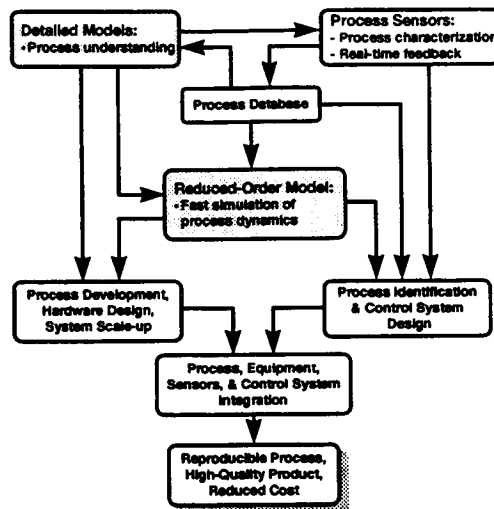


Figure 1. IPM methodology: role of process models

Application of IPM Methodology to EB-PVD Process

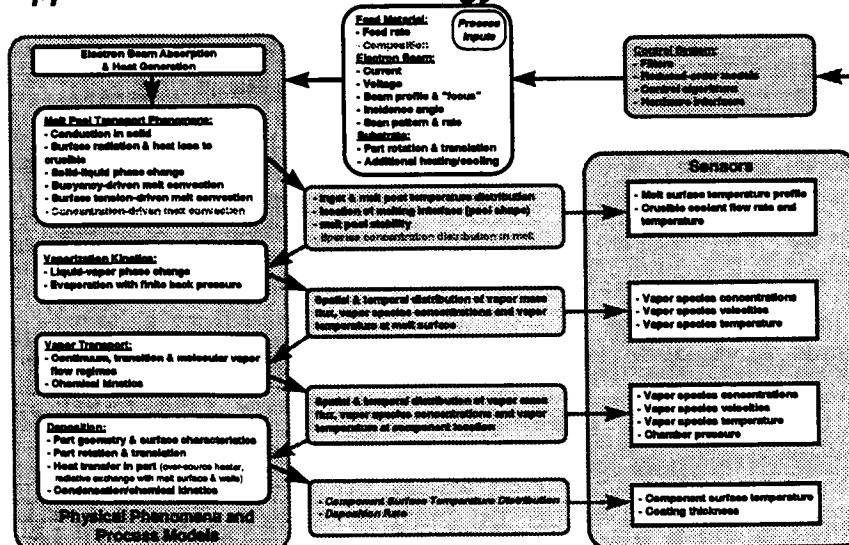
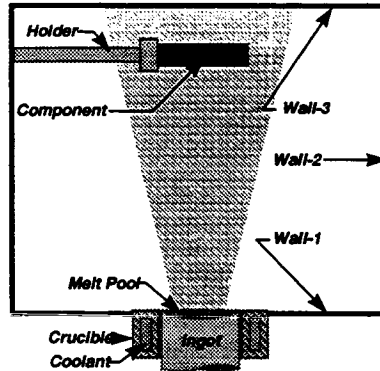


Figure 2. Application of IPM methodology to EB-PVD process

Model Scope

- Simplified, dynamic EB-PVD process model treating:
 - E-beam absorption & heat generation
 - Transient melt temperature & melt pool depth
 - Evaporation kinetics
 - Line-of-site vapor transport
 - Deposition rate
 - Over-source heating
 - Component surface temperature



Reduced-Order Model enables efficient control system design

Figure 3. Reduced-order model scope

Model Structure

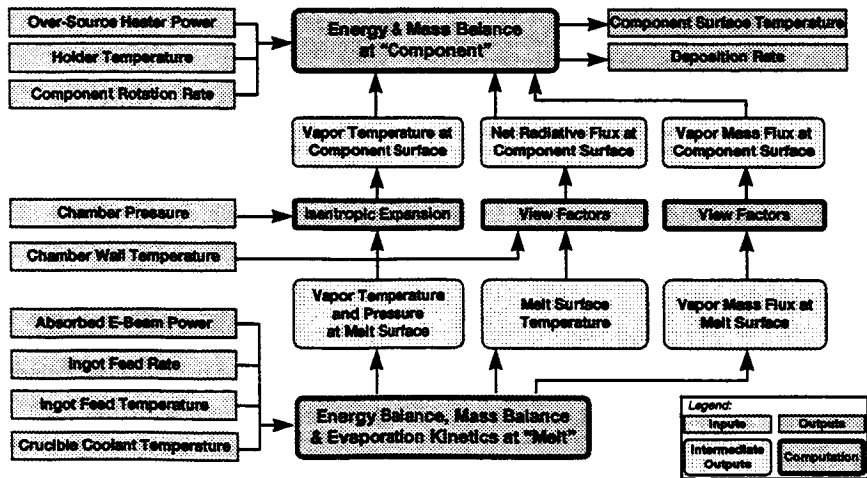
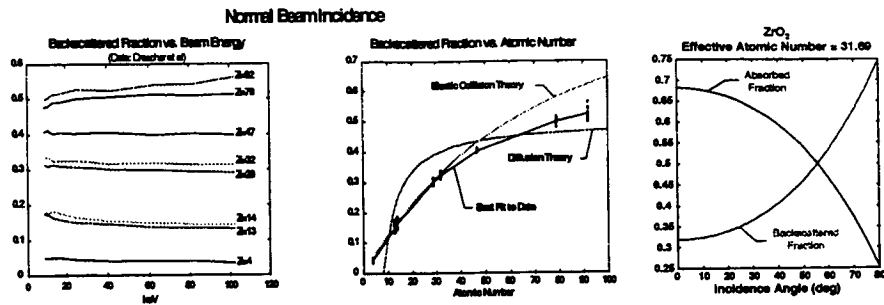


Figure 4. Reduced-order model structure

E-Beam Absorption & Heat Generation



- Effects of target atomic number, beam voltage and incidence angle on energy absorption are treated
- Influences of beam scan pattern and frequency are modeled in terms of the average power intercepted by the melt surface. ROM input is obtained from *Detailed Models*.

Figure 5. Electron beam back-scattering and absorption

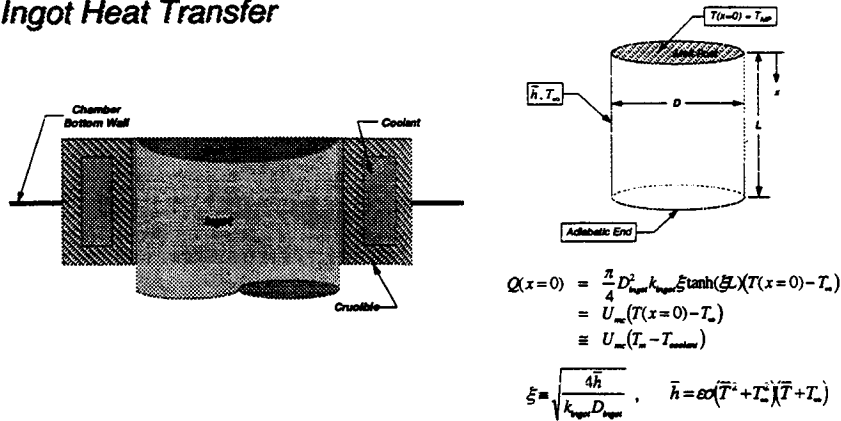
Melt Pool Energy Balance

$$\frac{d}{dt}(m_m C_m T_m) = \alpha_{em} F_{beam}^* Q_{beam} + Q_{radiation} + Q_{crucible} + Q_{conduction} + Q_{sensible} + Q_{melting} + Q_{evaporation} + Q_{dissociation}$$

- The rate of change of melt temperature is expressed in terms of the net absorbed e-beam power, radiative exchange with the chamber enclosure, heat loss to the ingot and crucible, and power used to supply the latent heats of melting, evaporation and dissociation

Figure 6. Melt pool energy balance

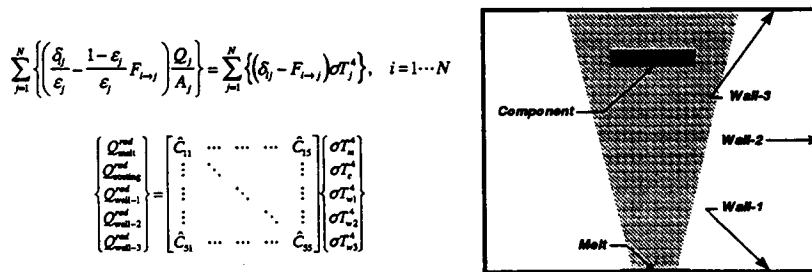
Ingot Heat Transfer



The ingot is modeled as a cylindrical fin, losing heat to the crucible by radiation from its curved surface

Figure 7. Ingot heat transfer model

PVD Chamber Enclosure Radiation Exchange



- Radiative exchange is governed by the emissivities, temperatures and the view factors of the enclosure elements
- View factors are computed a priori
- System of equations relates net radiative flux at each element to the temperatures of all other enclosure elements

Figure 8. Radiative exchange in EB-PVD chamber

Evaporation & Vapor Transport

Clausius-Clapeyron and Langmuir equations relate evaporation rate to melt pool temperature:

$$\dot{m}_1 = A_m \sqrt{\frac{W}{2\pi RT_1}} \left\{ P_{ref} \left(\frac{\Delta H_v W}{RT_{ref}} \left(1 - \frac{T_{ref}}{T_1} \right) \right) \right\} = A_m \sqrt{\frac{W}{2\pi RT_1}} \cdot P_1(T_1)$$

Vapor mass flux at component location is related to mass flux at melt surface using line-of-sight view factors:

$$G_2 = F_{melt \rightarrow component} \cdot G_1$$

Temperature of the vapor at component location is estimated from isentropic expansion equation:

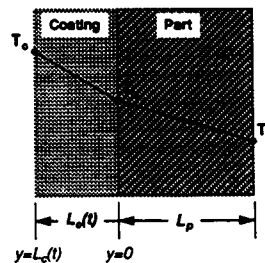
$$T_2 = T_1 \left(\frac{P_2}{P_1} \right)^{\frac{\gamma-1}{\gamma}}$$

Figure 9. Formulation of evaporation and vapor transport phenomena

Deposition Rate

The net deposition rate is the difference between the mass flux of the vapor intercepted by the part, and the back-vaporization mass flux:

$$\frac{dL_c(t)}{dt} = \frac{1}{\rho} \sqrt{\frac{W}{2\pi R}} \left(F_{melt \rightarrow part} \cdot \frac{P_1}{\sqrt{T_1}} - \frac{P_2}{\sqrt{T_2}} \right)$$



Part rotation is treated by computing the average vapor mass flux over the component surface

Figure 10. Deposition rate

Component Surface Temperature

Net heat flux at coating surface:

$$Q_{c,net} = F_{OSH} Q_{holder} + Q_{radiation} + Q_{skip} + Q_{resizable} + Q_{convection} + Q_{condensation} + Q_{recombination}$$

Using "lumped" thermal model for part:

$$T_c = T_b \approx T_p(t)$$

Assuming linear temperature profile in coating (thin coating):

$$T_c(t) = T_p(t) + \left(\frac{L_c(t)}{k_c A_c} \right) \cdot Q_{c,net}$$

Component energy balance:

$$m_p C_p \frac{dT_p}{dt} = Q_{c,net} - Q_{holder}$$

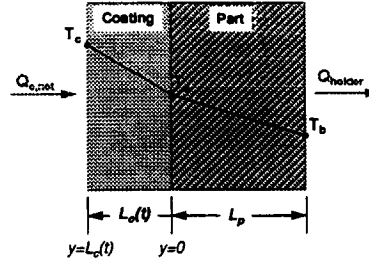


Figure 11. Component energy balance

Sensitivity Studies - Effect of e-beam power on melt pool temperature

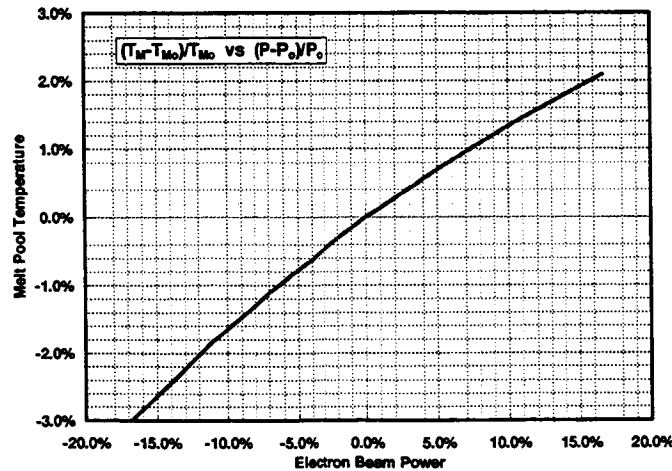


Figure 12

Sensitivity Studies - Effect of e-beam power on deposition rate

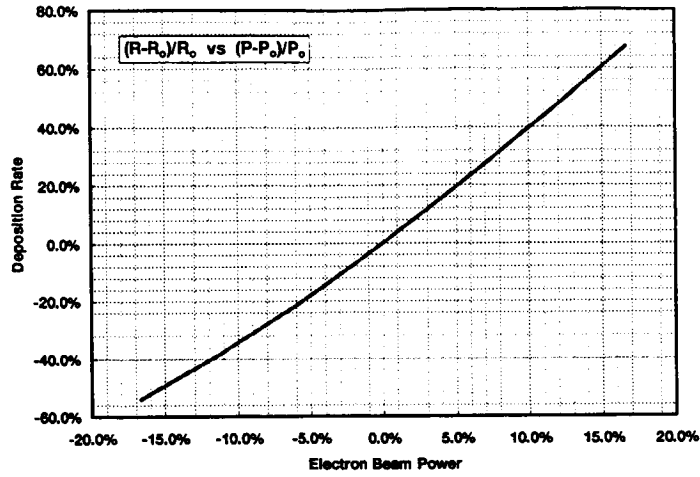


Figure 13

Sensitivity Studies - Effect of over-source heater power on component surface temperature

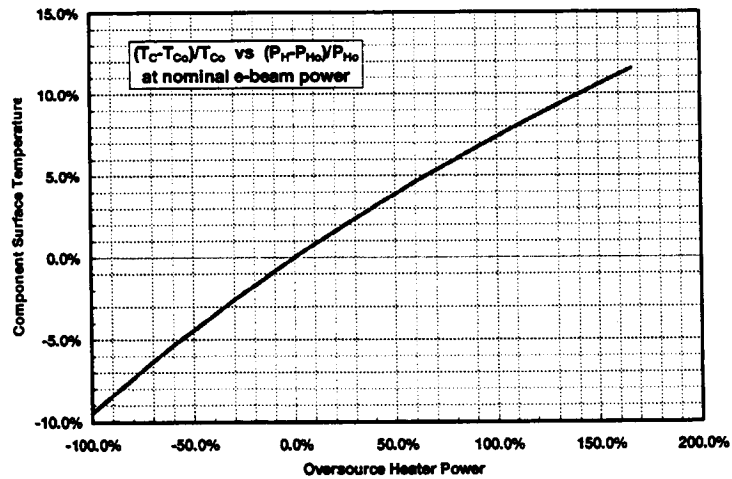
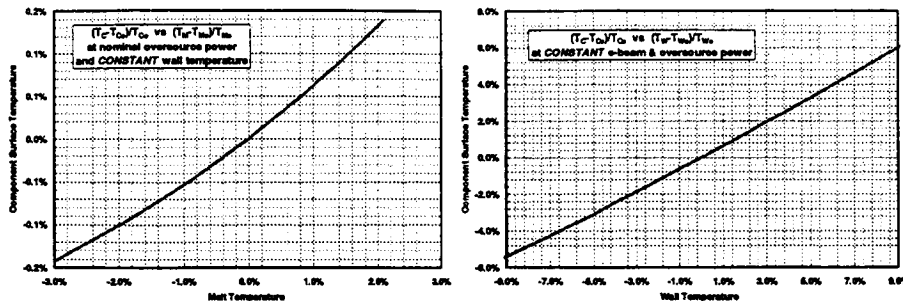


Figure 14

Sensitivity Studies - Effect of changes in melt and wall temperatures on component surface temperature



- At "nominal" melt-to-part distance, component surface temperature is largely determined by radiative exchange with chamber walls and over-source heater (not by direct melt radiation)
- Significant coupling exists between component surface temperature and wall temperature

Figure 15

Sensitivity Studies - Effect of melt pool temperature on deposition rate

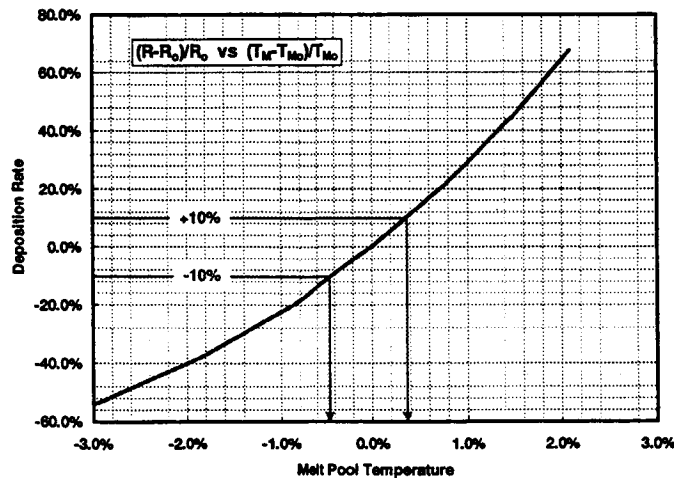


Figure 16

Sensitivity Studies - Typical transient responses

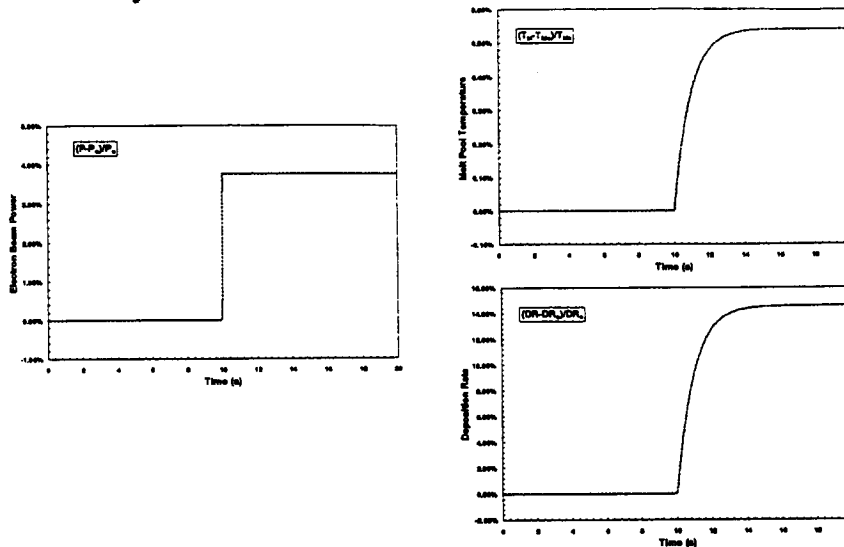
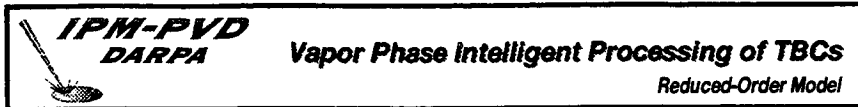


Figure 17. Transient responses of melt pool temperature and deposition rate to step change in electron beam power

Integration of Detailed Model Results – Examples

- **Melt Pool Model**
 - Use detailed models to determine the effect of e-beam focus, scan pattern & scan frequency on evaporation rate and melt pool stability; implement results as correlations or rules in ROM
- **Vapor Transport Model**
 - Use detailed models to establish deviation of vapor mass flux distribution from pure line-of-sight calculation; implement as correction curves in ROM
- **Deposition Model**
 - Add more physical detail to ROM deposition model based on detailed model predictions of part energy balance & deposition rate (*e.g. effect of complex part rotation*)

Figure 18



Conclusions

- **Integration of IPM-PVD Reduced-Order Model with control system design tools demonstrated**
- **Strategy for implementation of Detailed Model results in Reduced-Order Model established**
- **Initial parameter sensitivity studies completed**
 - need for implicit computation of wall temperature identified
 - measurements required for ROM refinement/validation specified

Figure 19

Poster Session Abstracts

SCANDIA, YTTRIA-STABILIZES ZIRCONIA (SYSZ): CANDIDATE MATERIALS FOR HIGH TEMPERATURE TBCs

R.L. Jones

Naval Research Laboratory, Washington, DC

This presentation summarizes a series of tests comparing SYSZ with $Y_2O_3(8wt\%)-ZrO_2$ - initially as plasma spray powders and then subsequently as air plasma sprayed (APS) coatings -- which show SYSZ to have substantially better high temperature (1400C) tetragonal phase stability than PYSZ. The data suggest that SYSZ could be a leading candidate as the new TBC needed for future, high efficiency gas turbines which will operate at gas temperatures too high (>1200C) for PYSZ.

LOW THERMAL CONDUCTIVITY IN GARNET CERAMICS, AND THEIR POSSIBLE NEW USE AS ADVANCED THERMAL BARRIER COATINGS

N.P. Padture, P.G. Klemens and M. Gell

University of Connecticut, Storrs, CT

Thermal conductivity of dense, polycrystalline Y-Al-Fe garnets was measured in the temperature range 23-1000 °C. The high-temperature thermal conductivity of some of these garnets was found to be as low as 2.4 W/m/K. The effects of temperature and composition on the observed thermal conductivity will be discussed with reference to thermal-conduction theories. It appears that the high oxygen diffusivity in the currently used TBC ceramics based on zirconia, and the attendant oxidation of the metal substrate, fundamentally limits the useful life of zirconia-based TBCs. In this context, yttrium aluminum garnet (YAG), in particular, with its high-temperature thermal conductivity comparable to zirconia but oxygen diffusivity about 10 orders of magnitude lower than zirconia, may offer a possible alternative to traditional zirconia in future TBCs for improved durability.

SPPS FOR ADVANCED THERMAL BARRIER COATINGS

K. T. Faber, D. E. Boss, T. F. Bernecki, J. Mawdsley, and J. Su

Northwestern University, Evanston, IL

Small-Particle Plasma Spray (SPPS) allows coatings with controlled porosity (>99% dense to graded porosity), controlled morphology, and/or numerous layers (nanometers to microns/layer) to be produced using conventional thermal spray equipment. With SPPS, it is possible to engineer thermal conductivity, strain tolerance, grain growth, and sintering rates for TBC. Thus, materials with the desired CTE and oxygen diffusion coefficients can be engineered to meet TBC requirements. Initial results of bond strength versus surface preparation and flaw tolerance by indentation methods will be presented. Candidate approaches to developing advanced TBC will be discussed.

LOW COEFFICIENT OF THERMAL EXPANSION BOND COATS FOR TBCs

D.R. Arenas¹, W.J. Brindley², L.B. Temples³ and D.A. Koss¹

¹The Pennsylvania State University, State College, PA

²NASA Lewis Research Center, Cleveland, OH

³Praxair Specialty Powders, Indianapolis, IN

Interfacial roughness combined with a bond coat-ceramic layer thermal expansion mismatch has been identified through finite element modeling as one cause for high delamination stresses in plasma sprayed thermal barrier coatings. Plasma sprayed coatings have been fabricated from NiCrAlY powders mechanically alloyed to contain a range of volume fractions of fine (<0.7 μm) alumina particles. A preliminary assessment of powder and coating microstructure has been conducted. Dilatometry demonstrated that the alumina additions successfully reduced coating thermal expansion, in agreement with previous work by T.A. Taylor, et al on oxidation resistant coatings. Burner rig thermal fatigue tests indicated substantial improvements in TBC life for some of the compositions examined.

RELATIONSHIP BETWEEN DEPOSITION CONDITIONS AND TEXTURE OF EB-PVD THERMAL BARRIER COATINGS

U. Schulz and M. Peters

DLR German Aerospace Research Establishment, D-51140 Cologne, Germany

Today the most durable TBCs are yttria PSZ coatings that are applied by EB-PVD. The EB-PVD process offers the advantage of a superior strain and thermoshock tolerant behavior of the coatings due to their columnar microstructure. Those TBC are highly textured because of the physical nature of film growth. Pole figure measurements and orientation distribution function (ODF) calculations are presented in order to show a clear relationship between deposition conditions and type of texture. Mainly the vapor incline angle and the movement of the substrate within the vapor cloud determine the preferred orientation of TBCs. Two different coaters have been used to vary the deposition conditions in a wide range. The technical importance of texture investigations originates from the anisotropy of elastic moduli and thermal expansion coefficient within the t' phase of YPSZ.

THE EFFECT ON MICROSTRUCTURE ON THE CREEP RESPONSE OF FUNCTIONALLY GRADED THERMAL BARRIER COATINGS

S.M. Arnold¹ M.-J. Pindera² and J. Aboudi³

¹NASA-Lewis Research Center, Cleveland, OH

²University of Virginia, Charlottesville, VA

³Tel-Aviv University, Ramat-Aviv, ISRAEL

The recently developed two-dimensional version of the higher-order theory for functionally graded materials (HOTFGM-2D) is employed to investigate the effects of microstructural architectures in graded zirconia-based thermal barrier coatings (TBCs) on the stress distributions in the presence of a through-thickness temperature gradient. In particular, the response of TBCs with different levels of functionally graded microstructural refinement and different arrangements is investigated under a thermal gradient that simulates a heat-up/hold/cool-down cycle, and the results for the through-thickness stress distributions are compared with those based on the standard micromechanical homogenization scheme. Single and multiple heat-up/hold/cool-down cycles with different thermal gradient magnitudes are considered. The examples presented illustrate the shortcomings of the standard micromechanics-based approach applied to the analysis of functionally graded TBCs subjected to cyclic thermal loading when creep effects are included in the analysis.

RESIDUAL STRESS MEASUREMENTS IN THERMAL BARRIER COATINGS

T. R. Watkins and C. R. Hubbard

Oak Ridge National Laboratory, Oak Ridge, TN

Understanding the residual stresses of the oxide scale growth is critical to enhancing the performance and reliability of thermal barrier coating systems. In this study, the residual strains were measured in an EB-PVD yttria stabilized zirconia top coat and a platinum aluminide bond coat at room temperature before and after heat treatment. Further, in situ measurements of a thermally grown oxide scale on a platinum aluminide bond coat on top of a René N5 superalloy substrate were performed at high temperature using x-ray diffraction. Experimental difficulties and future work will also be discussed.

*Research sponsored by the U. S. Department of Energy under contract number DE-AC05-96OR22464.

EFFECT OF POWDER SIZE AND DEPOSITION TEMPERATURE ON THE MICROSTRUCTURE AND PROPERTIES OF PLASMA SPRAYED ZIRCONIA

S.Sampath¹, J.Matijicek¹, C.C.Berndt¹, H.Herman¹, A.Vardelle², A.C. Leger²,
M.Vardelle², P.Fauchais², J.Ilavsky³, G.G.Long³ and S.Dapkunas³

¹State University of New York, Stony Brook, NY

²LMCTS, University of Limoges, Limoges, France

³NIST, Gaithersburg, MD

The thermal and mechanical properties of plasma sprayed zirconia are affected by several factors associated with the plasma spray process. The feedstock particle size, feedstock morphology, plasma parameters, injection parameters, and deposition temperature being some of the key variables. In this investigation, the effects of feedstock size and deposition temperature have been examined, while other variables have been kept constant. Partially stabilized zirconia powder (with 8% yttria) consisting of four different size distributions were examined. In addition, the study also examined the effects of deposition temperature on the nature of the interlamellar contact. Porosity, mechanical strength, thermal conductivity, and microstructural examination were conducted in an effort to develop a processing-structure-property relationship.

MICROSTRUCTURAL CHARACTERIZATION OF INTERFACIAL Al_2O_3 SCALES FORMED BY CYCLIC OXIDATION OF PLASMA SPRAYED TBCs AT 1150C

J.A. Haynes^{1,2}, M.K. Ferber² and E.D. Rigney¹

¹University of AL at Birmingham, Birmingham, AL

²Oak Ridge National Laboratory, Oak Ridge, TN

Growth, mechanical properties and damage accumulation of interfacial Al_2O_3 scales were evaluated by isothermal and cyclic oxidation of plasma-sprayed TBCs at 1150°C. Specimens consisting of Rene'N5 substrates, VPS Ni-22Cr-10Al-1Y bond coatings and APS YSZ were furnace cycled to failure (355 one hour cycles), and to 25%, 50% and 75% of failure. Microstructures and void content of Al_2O_3 scale fracture sections (exposed by YSZ spallation) differed in scales formed isothermally vs. cyclically. Metallographic cross-sections revealed the evolution of extensive scale fracture, buckling and layering beneath the YSZ during thermal cycling. Hardness and elastic moduli of the Al_2O_3 thin films were evaluated by nanoindentation.

*Research sponsored by the U.S. Department of Energy under contract DE-AC05-84OR21400, with Lockheed-Martin Energy Research.

RESIDUAL STRESS DEVELOPMENT IN THERMAL BARRIER COATINGS

R.T.R. McGrann¹, E.F. Rybicki¹, J.R. Shadley¹, J. Wigren², L. Pejryd² and W.J. Brindley³

¹The University of Tulsa, Tulsa, Oklahoma

²Volvo Aero Corporation, Trollhättan, Sweden,

³NASA Lewis Research Center, Cleveland, Ohio

Residual stresses are unavoidable in thermal barrier coatings (TBC's) applied by air plasma spraying (APS). An understanding of the development of residual stresses during processing and the changes during in-service loading is necessary for control and prediction of TBC performance. The Modified Layer Removal Method is used to determine through-thickness residual stress levels in TBC's of yttria stabilized zirconia applied by APS to B1900 and Hastelloy-X substrates. Residual stress distributions are determined for as-received, shot peened, as-sprayed bond coat, and as-sprayed top coat (preheat and no preheat) conditions. In-service changes in residual stresses due to thermal cycles, thermal shock, and long-term, high-temperature exposure are investigated.

PORE AND CRACK STRUCTURE EVOLUTION IN THERMAL BARRIER COATINGS DURING PROCESSING

A.J. Allen¹, G.G. Long¹ and J. Ilavsky²

¹NIST, Gaithersburg, MD

²Institute of Plasma Physics, Prague, Czech Republic

Anisotropically-oriented interlamellar pore and intralamellar crack void structures in plasma-sprayed ceramic TBCs have been characterized using small-angle neutron scattering. Results indicate that preferred intralamellar crack orientations depend on spray angle whereas interlamellar pore orientations do not; intralamellar cracks comprise a significant void fraction in gray alumina but are less significant in partially-stabilized zirconia; cracks that do form in zirconia are removable by sintering; and total specific surfaces within gray alumina deposits decrease with increasing porosity, with different characteristics for varying spray-distance and angle. Such studies relate TBC morphology to microstructural models involving the spray parameters.

ON THE SOLID PARTICLE EROSION BEHAVIOR OF PLASMA SPRAYED AND THERMALLY CYCLED ZIRCONIA COATINGS

J.Gutlebar, S.Usmani and S.Sampath

State University of New York, Stony Brook, NY

TBCs in aircraft engines and stationary turbines can experience solid particle erosion during service. These effects can enhance the degradation of the protective coating and accelerate their failure. Plasma sprayed TBCs due to their unique lamellar microstructure provide different erosion mechanisms as compared to bulk materials. In this study ambient and elevated temperature solid particle erosion behavior of plasma sprayed TBCs have been examined using the ASTM G76 test. Tests were conducted using alumina grit on as-sprayed and furnace cycled samples at different impact angles. The results show significant influence of processing and thermal cycling on erosion behavior. These results have been assimilated on the basis of microstructure and mechanical property differences.

PROCESSING AND CHARACTERIZATION ISSUES ASSOCIATED WITH THE SYNTHESIS OF "LOW - SULFUR" NiAl AND NiPtAl BOND COATS

W. Y. Lee¹, Y. Zhang², I. G. Wright¹, K. M. Cooley¹, and P. K. Liaw²

¹Oak Ridge National Laboratory, Oak Ridge, TN

²University of Tennessee, Knoxville, TN

Prior research clearly shows that the cyclic oxidation behavior of Ni-based superalloys is significantly improved when the level of sulfur impurities in the alloys is reduced below ~1 ppmw. However, the potential merits of lowering the sulfur content in bond coat materials have not been systematically assessed from manufacturing and performance perspectives. This presentation will address the feasibility of manufacturing "low-sulfur" NiAl and NiPtAl bond coats, with particular attention to characterization procedures for resolving sulfur effects as well as other microstructural and compositional influences on scale adhesion behavior.

Research sponsored by the Advanced Gas Turbine Systems Program, DOE under contract DE-AC05-96OR22464 with Lockheed Marietta Energy Research Corporation.

MONITORING DAMAGE EVOLUTION IN EB-PVD TBCs USING THERMAL WAVE IMAGING

S.Q. Nusier, T. Ahmed, Z.A. Chaudhury, R.L. Thomas and G.M. Newaz

Wayne State University, Detroit, Michigan

Progressive damage evolution was monitored in Electron Beam - Physical Vapor Deposition (EB-PVD) thermal barrier coating (TBC) samples subjected to thermal cycles using the thermal wave imaging (TWI) technique. The substrate was Rene N5 coated with PtAl bondcoat. The TBC was partially stabilized zirconia. The samples were subjected to thermal cycles between 200-1177C. They were then removed from the furnace and TWI was conducted on these samples simultaneously. The thermal wave signal amplitude continues to increase with number of imposed thermal cycles and appears to saturate near spallation life (similar characteristics as the Fick's Law). Results indicate that there is correlation of damage states from microscopy conducted on the same samples and their corresponding thermal wave amplitudes. Based on this study, TWI technique shows excellent promise in monitoring damage evolution in TBCs.

THERMAL TRANSPORT PROPERTIES AND INFRARED IMAGING OF THERMAL BARRIER COATINGS

R.B. Dinwiddie and H. Wang

Oak Ridge National Laboratory, Oak Ridge, TN

Thermal transport properties are a very important aspect in TBC applications. Thermal conductivities of Air Plasma Sprayed (APS) and Electron Beam Physical Vapor Deposition (EB-PVD) thermal barrier coatings were measured by standard laser flash diffusivity and DCS techniques. The effects of aging, light penetration, gas species and gas pressure have been investigated. TBCs from GE Aircraft Engines, GE CR&D and Westinghouse were measured. Thermal imaging technique was also used to study the quality of the TBCs. A high-speed, high-sensitivity infrared imaging system has been used to detect subsurface flaws and delaminations in TBCs.

A THERMAL GRADIENT TEST SYSTEM FOR THERMAL BARRIER COATINGS

G.R. Romanoski

Oak Ridge National Laboratory, Oak Ridge, TN

An energy efficient, low cost thermal gradient test system has been built at Oak Ridge National Laboratory to aid in the characterization of thermal barrier coatings. The rig employs an internally cooled tubular specimen. The heat flux is generated by an inductively heated zirconia susceptor concentric with the specimen. The maximum possible heat flux is greater than 50 w/cm^2 . The system is capable of generating turbine relevant temperatures and temperature gradients through a TBC coated superalloy specimen. The rig features precise control of the heat flux and forced convection internal cooling. TBC surface temperature, TBC / bond coat interface temperature, and internal surface temperatures can be measured and recorded. Provisions for introducing alternative gas environments are incorporated in the design.

ELASTIC OPTICAL SCATTER METHODS FOR NONDESTRUCTIVE INSPECTION OF TBCs

A. Ellingson¹, J. G. Sun¹, R. Orenstein² and J. Viertel²

¹Argonne National Laboratory, Argonne, IL

²General Electric Company Schenectady, NY

Low-power (<35 mw) visible-wavelength ($\lambda = 0.63 \mu\text{m}$) lasers were used with special detectors that utilized polarization optics, CCD cameras, and Fast Fourier Transform digital image processing to characterize variations in thermal barrier coatings (TBCs) that were obtained by air plasma spraying and electron-beam physical vapor deposition. The variables that were studied included thickness of the coating (e.g., 330 μm -2 mm), bond-coats, and substrates. The laser system allows fast scanning, adjustable depth of focus, and provides direct image generation. The method and results will be presented.

*Work supported by General Electric Power Generation Systems and U.S. DOE/Office of Fossil Energy/Advanced Research and Technology Development/Materials Program.

PIEZO-SPECTROSCOPIC CHARACTERIZATION OF THERMAL BARRIER COATINGS

M. J. Lance, J. A. Haynes, M. K. Ferber, and W.R. Cannon

¹Oak Ridge National Laboratory, Oak Ridge Tennessee

²Rutgers University, Piscataway, New Jersey

Plasma-sprayed and EB-PVD zirconia thermal barrier coatings were analyzed using Raman and fluorescence spectroscopy. These spectroscopic techniques allow the measurement of both stress and phase content in the zirconia thermal barrier and in the thermally grown oxide scale that forms between the zirconia and the bond coat. Damage was induced in TBC-coated superalloy buttons by isothermal and cyclic oxidation at various temperatures in air. Both plasma-sprayed and EB-PVD samples were initially in high compression but gradually reduced to zero during cycling suggesting damage accumulation can be monitored with this technique.

CATALYTIC COMBUSTION EFFECTS IN INSULATED IC ENGINES

R.L. Jones

Naval Research Laboratory, Washington, DC

Several catalytic combustion effects are identified that may occur in IC engines, especially if combustion chamber surface temperatures are raised by TBCs or other thermal insulation. Such effects can be simultaneously beneficial in aiding in fuel ignition, but detrimental by increasing the flame-quenching distance at combustion chamber surfaces. The anomalous increase in "heat rejection" to the combustion chamber wall that occurs after a certain critical wall temperature is reached (i.e., the Woschni effect) is shown to be probably a manifestation of catalytic combustion.

ASSESSMENT OF THERMAL CONDUCTIVITY OF THERMAL BARRIER COATINGS MADE BY PLASMA SPRAY DEPOSITION

K. S. Ravichandran¹, K. An¹ and R.E.Taylor²

¹University of Utah, Salt Lake City, UT

²Thermophysical Properties Research Laboratory, West Lafayette, IN

Accurate thermal conductivity data is required for proper design and reliability of gas turbine blades. In this study, thermal conductivities of Al₂O₃ and 8wt.% Y₂O₃ stabilized ZrO₂ plasma sprayed coatings were determined from thermal diffusivity and specific heat data, as a function of temperature. Thermal conductivities were found to be sensitive to porosity, interfaces between splats as well as the interface between the coating and the substrate. Thermal conductivity evaluations were limited by the choice of reference data on dense materials. Further, analyses of sensitivity of the laser flash technique to variations in the coating and the substrate parameters were also performed. The results are discussed in the context of coating characteristics, reference conductivity data for dense materials and the sensitivity of the measurement method to coating parameters.

RADIATION HEAT TRANSFER PROCEDURE FOR MATERIALS WITH DIFFERENT INDICES OF REFRACTION

J.C. Chai¹ and J.P. Moder²

¹Tennessee Technological University, Cookeville, TN

²NASA Lewis Research Center, Cleveland, OH

At elevated temperatures, the advanced materials used as thermal barrier coatings are partially transparent to radiant energy. The refractive index, n , of these materials can therefore have a significant effect on their internal temperature distribution. Within semitransparent materials, internal emission of radiant energy depends on n^2 . Since the radiant energy leaving a surface cannot exceed that of a blackbody, there is significant *internal* reflection at the interface when the refractive index of the material is significantly larger than unity. This paper presents a procedure for radiative heat transfer in semitransparent layers in which an angular-multiblock procedure is used to ensure the conservation of radiant energy across layers. The accuracy of the procedure is tested using a few standard benchmark problems.

IMPROVED POWDERS FOR THE PRODUCTION OF HIGH TEMPERATURE STRESSED PLASMA SPRAYED COATINGS

H. Meinhardt and H. Keller

I.

H.C. Starck GmbH & Co KG, Laufenburg/Germany

New platinum- and rhenium-modified MCrAlY test materials were developed in powder form. ZrO₂-based materials for heat-insulating top coats were also analyzed with regard to their degree of stabilization and the stabilized oxide. The life span of the coatings with the modified bond coats is substantially longer than with standard alloys. The newly-developed MCrAlY variants containing rhenium and platinum show an improved resistance to high temperatures compared with standard grades and are superior in terms of their mechanical-thermal behavior. The platinum-containing coating is very resistant, especially to hot-gas corrosion sulfidation. The Yb₂O₃ and Dy₂O₃ stabilized ZrO₂ grades proved to have a higher durability than the Y₂O₃ stabilized ZrO₂ and showed no difference to Y₂O₃ stabilized ZrO₂ in terms of oxidation behavior, phase structure or internal stress and porosity levels.

REPORT DOCUMENTATION PAGEForm Approved
OMB No. 0704-0188

Public reporting burden for this collection of information is estimated to average 1 hour per response, including the time for reviewing instructions, searching existing data sources, gathering and maintaining the data needed, and completing and reviewing the collection of information. Send comments regarding this burden estimate or any other aspect of this collection of information, including suggestions for reducing this burden, to Washington Headquarters Services, Directorate for Information Operations and Reports, 1215 Jefferson Davis Highway, Suite 1204, Arlington, VA 22202-4302, and to the Office of Management and Budget, Paperwork Reduction Project (0704-0188), Washington, DC 20503.

1. AGENCY USE ONLY (Leave blank)		2. REPORT DATE May 1998	3. REPORT TYPE AND DATES COVERED Conference Publication	
4. TITLE AND SUBTITLE Thermal Barrier Coating Workshop, 1997			5. FUNDING NUMBERS WU-523-21-13-00	
6. AUTHOR(S) William J. Brindley, compiler				
7. PERFORMING ORGANIZATION NAME(S) AND ADDRESS(ES) National Aeronautics and Space Administration Lewis Research Center Cleveland, Ohio 44135-3191			8. PERFORMING ORGANIZATION REPORT NUMBER E-11007	
9. SPONSORING/MONITORING AGENCY NAME(S) AND ADDRESS(ES) National Aeronautics and Space Administration Washington, DC 20546-0001			10. SPONSORING/MONITORING AGENCY REPORT NUMBER NASA CP-97-207429	
11. SUPPLEMENTARY NOTES Responsible person, William J. Brindley, organization code 5160, (216) 433-3274.				
12a. DISTRIBUTION/AVAILABILITY STATEMENT Unclassified - Unlimited Subject Categories: 23, 26, 27, and 39 Distribution: Nonstandard This publication is available from the NASA Center for AeroSpace Information, (301) 621-0390.			12b. DISTRIBUTION CODE	
13. ABSTRACT (Maximum 200 words) This document contains papers from the 1997 Thermal Barrier Coatings Workshop, sponsored by the TBC Interagency Coordination Committee. The Workshop was held in Fort Mitchell, Kentucky, May 19-21, 1997. The papers cover the topics of heat transfer and conductivity of thermal barrier coatings, failure mechanisms and characterization of the coatings as well as characterization of coating deposition methods. Speakers included research, development and user groups in academia, industry and government.				
14. SUBJECT TERMS Thermal barrier coatings; TBC; Oxidation; Failure; Conductivity characterization; Plasma spray; Electron beam-physical vapor deposition; EB-PVD			15. NUMBER OF PAGES 191	
			16. PRICE CODE A09	
17. SECURITY CLASSIFICATION OF REPORT Unclassified	18. SECURITY CLASSIFICATION OF THIS PAGE Unclassified	19. SECURITY CLASSIFICATION OF ABSTRACT Unclassified	20. LIMITATION OF ABSTRACT	